
THE UNIVERSITY *of* EDINBURGH

# Ultrafast Electron Dynamics in Thin Films of Prussian Blue Analogues

**Luke Benjamin Hedley**

**Thesis Submitted for the degree of**

**Doctor of Philosophy**

**School of Chemistry**

**2020**

THE UNIVERSITY *of* EDINBURGH
School of Chemistry

# Contents

# Chapter 1

# Abstract

The potentially complex energy redistribution processes that occur in inorganic transition metal complexes make the interpretation of their relaxation dynamics a significant challenge. Unlike in organic molecules, where rates for processes such as intersystem crossing can take up to and in excess of many nanoseconds, the timescales involved in inorganic materials are of picosecond / femtosecond timescales and therefore require a more advanced experimental setup to study them. The dynamic processes that are of interest are the evolution of the electron population after excitation through external stimuli, via the various charge transfer and decay processes. These processes can also induce changes in the population of the valence orbitals on the metal ion centres causing a change to the overall spin state. This work aims to develop techniques to monitor the redistribution of the electron population along with the magnetisation of the materials of interest.

The dynamic processes are much too fast to be captured using standard spectrometers and magnetic techniques, so a technique which can operate on these very fast timescales is required. Ultrafast laser spectroscopy allows study of the electronic dynamics using a technique called transient transmission which involves studying changes in the transmission spectrum as a function of time. Two laser pulses are employed, one to perturb the sample and another to interrogate

the sample. By varying the time delay between the two pulses a picture of how the spectrum changes over time can be constructed. This process allows a picture to be built, of how the electronic population redistributes and decays after excitation. In order to study the magnetisation dynamics of such materials the samples are required to exhibit a magnetic signal. To this end, a magnetically ordered family of inorganic compounds known as Prussian Blues were chosen as the system of interest. These materials consist of transition metal ions linked through cyanide bridging ligands in a rock-salt type structure. Laser spectroscopy was used to monitor the changes in the magnetisation of the sample through a technique called magneto-optical Faraday rotation. This involves monitoring the polarisation of the laser pulses after interaction with the sample, again, at various time delays to measure how the magnetisation of the sample changes over time. These techniques were applied to three chromium based Prussian Blues, vanadium-chromium (VCr), iron-chromium (FeCr) and the chromium-chromium (CrCr) analogues. Through the systematic substitution of the metal ion adjacent to the Cr sites, it was found that the rate of intersystem crossing could be influenced by the nature of the metal center. In the case of both VCr and FeCr analogues, the transfer of population to the final excited state occurred incredibly fast, within the temporal profile of the pump pulse. However, in the case of the CrCr analogue, this population transfer was slowed down sufficiently that a growth of the final excited state was observed over the course of the initial 0.5 ps after excitation.

The synthesis of these materials was carried out to optimise the morphology of the thin films for use in the laser measurements. During this work it was found that some of these materials exhibit electrochromic activity which was explored in isolated films and as part of multilayered heterostructures. This work was also incredibly helpful with understanding and predicting the spectral signatures of redox processes involved after photo-excitation.

This line of research offers the potential to gain a deeper understanding of the dynamic processes occurring in these functional materials which will serve as

model systems. The information gained can then be applied to a broader range of complexes. Functional materials which possess much higher magnetic ordering temperatures or larger magnetisation would have a greater potential to be used in future practical applications.

# Chapter 2

# Introduction

## 2.1 Ultrafast Charge Transfer Processes

The current availability of laser systems with ever improving temporal resolution and spectral tunability make studies of the photophysics of chemical species an incredibly informative technique. This allows the studying of the electronic structure and response of the samples upon exposure to external stimuli across a broad range of timescales. When a photon interacts with the bound electron system of a species, an electric dipole transition is induced which results in a new electronic state becoming populated. This excited electronic state possesses a different electronic configuration from that of the ground state which results in potentially different properties such as reactivity or changes to the optical absorption spectrum. There are different ways in which this excess energy can then be lost, as shown in Figure 2.1, such as radiative (fluorescence or phosphorescence) or non-radiative (vibrational relaxation) decays, these can be used to monitor the recovery of the ground state or the loss of the excited state absorption with complementary techniques which can operate on relevant timescales.

The phenomenon of intersystem crossing (ISC) involves the transition between two electronic states which are of different spin multiplicity. This change

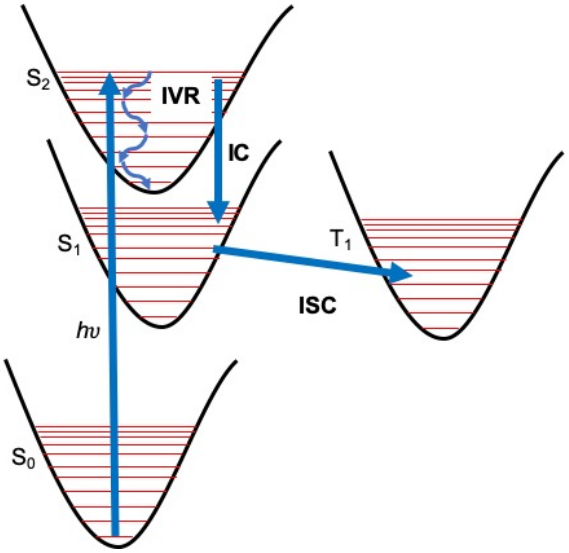


*Figure 2.1: A simplified energy level diagram illustrating the important processes where the states are considered harmonic for simplicity with inset vibrational levels in each state. IVR refers to internal vibrational relaxation which occurs within an excited state, IC is internal conversion which occurs between two electronic states of the same spin multiplicity and ISC denotes intersystem crossing which is a transition between two electronic states of different spin multiplicity (S and T refer to singlet and triplet states respectively).*

is associated with a modification of a material's spin-orbit coupling which is typically much higher in inorganic materials due to the presence of heavy metal atoms. By varying the wavelength of excitation, one can select from metal centred (MC) transitions, ligand to metal charge transfer (LMCT) transitions or metal to ligand charge transfer (MLCT) transitions amongst others. ISC has generated a large amount of literature over the past 20 years with the aim being the identification of any intermediate states involved in the transitions in order to understand what drives this forbidden direct transition. The ability to influence this phenomenon through the application of external stimuli combined with the development of ultrafast light sources allows the control over these materials to be developed to allow faster and more controlled switching.

The traditional picture for the order of the decay processes which occur

in molecules follows the following order, $k_{IVR} \gg k_{IC} \gg k_{ISC}$, these relative rates were first proposed by Adamson [1]. This picture, however, begins to break down with the introduction of heavier metal ions which possess significant spin-orbit coupling. The rate at which ISC occurs depends predominantly on two parameters, the spin-orbit coupling and the energy difference between the two states. The spin-orbit coupling parameter depends on the nuclear charge of the metal ion in question, as the metal ion grows in nucleus size the spin-orbit coupling increases. The energy mismatch between the two states of different spin multiplicities involved in the ISC also influences the rate at which it occurs, the larger the energy mismatch then the lower the rate of the transition occurring. The traditional way of considering the order of these processes was primarily based upon the fact that spin-allowed optical transitions such as IC will occur on a faster timescale than spin-forbidden transitions such as ISC. In turn, transitions which occur over multiple potential energy surfaces would occur on a slower timescale than single surface processes such as IVR.

Ultrafast studies were conducted by McCusker *et al.* into a family of low spin polypyridyl iron complexes in order to elucidate the nature of the ISC from the singlet metal to ligand charge transfer state, $^1$MLCT, to the quintet, $^5T_2$ state. [2] These materials were thought to be ideal model systems due to a large adiabatic energy difference between the low spin (LS) and high spin (HS) states. This work found that upon excitation at the MLCT, the system undergoes a fast ISC within approximately 700 fs. Thus the transfer of population into the $^5T_2$ state is considered a direct transition from the MLCT state despite being a spin-forbidden transition, and it was concluded that the various states of different multiplicities are all heavily mixed which facilitates these transitions.

This work signified a shift in the perceived method of the transfer of population into a final excited state, where there is no longer the need for an energy cascade through various vibronic states and this instead can be considered a direct, surface to surface, transition.

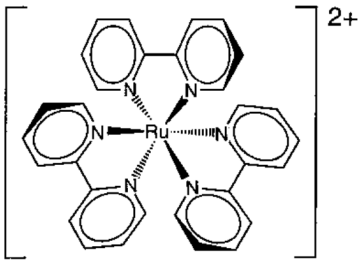


*Figure 2.2: The structure of the $[Ru(bpy)_3]^{2+}$ has been thoroughly studied as a model compound with respect to the photophysics of inorganic materials.*

Time-resolved absorption spectroscopy with femtosecond time resolution was also applied to $[Ru(bpy)_3]^{2+}$, which can be seen in Figure 2.2, to study the nature of the excited state and it's subsequent decay. [3] In this work, the system was excited at 475 nm which corresponds to the main ground state absorption feature attributed to a MLCT transition. This transition resulted in the triplet excited state $[Ru^{III}(bpy^{-})(bpy)_2]^{2+}$ being formed within approximately 300 fs. The rate at which this excited state is populated precludes the relaxation on the initial MLCT surface, but instead the population remains in region of direct overlap with the $^3$MLCT state to facilitate the ISC. It was determined in this work that the resulting species were generated within a very short amount of time after excitation due to the relative rate of ISC compared to IVR. Vibrational cooling is no longer considered the fastest process to occur which allows this excess energy in the system to facilitate further reactivity.

In 2007, a study on solution based $[Fe^{II}(bpy)_3]^{2+}$ was carried out by Chergui and co-workers [4] as an optimal spin crossover (SCO) model system due to the previously discussed large separation between LS and HS states. In previous SCO systems, the energy gap was small enough to be induced thermally which introduced further complications to the interpretation of the dynamics. The energy gap in $[Fe^{II}(bpy)_3]^{2+}$ is approximately 6000 $cm^{-1}$ which means that optical excitation is required to make the transition.

Subsequent studies of this material continue to elucidate more clearly

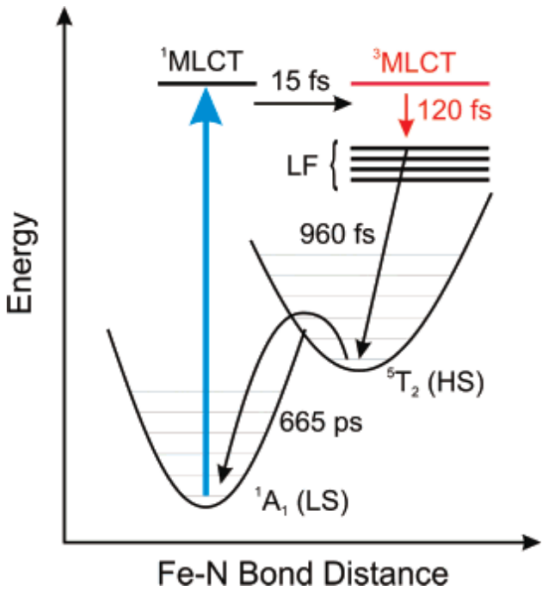


*Figure 2.3: Excited state diagram involved after the photo-excitation presented by Gawelda et al. to describe the dynamics of the $[Fe^{II}(bpy)_3]^{2+}$. The observed lifetimes are shown by each transition and the X and Y co-ordinates refer to the ground and HS states only. Figure reproduced from the literature with permission [4].*

the exact rates and identities of the states involved. In 2015, Aubock and Chergui revisited this study employing a temporal resolution of around 40 - 60 fs across the spectrum. The UV and visible regions of the spectrum correspond to absorption features for the $^5$T and the hot MLCT and $^5$T respectively, which were studied using transient absorption measurements. It was previously suggested [2] that there could be a direct $^1$MLCT to $^5$T conversion but this work revealed a very short-lived emission around 385 nm which has fully decayed within 50 fs which was attributed to the $^3$MLCT band. This is then followed by a multiple picoseconds vibrational cooling within the $^5T_2$ state. These dynamics are summarised in Figure 2.3. Crucially, this work has allowed a more complete picture of the electronic states involved in the very fast ISC transition, a greater understanding of the rates and properties which influence these rates will allow these systems to be employed in the application of functional materials.

Another system related to the work in this thesis is the chromium (III) tris-acetylacetonate [5], $Cr^{III}(acac)_3$, which was chosen due to the highly detailed body of work pertaining to the $Cr^{III}$ ion contributed by studies across many fields of science. The lowest lying excited state for the $Cr^{III}$ ions is typically the $^2E$ state which corresponds to an intra-configurational excited state of the ground, $^4A_2$ state.

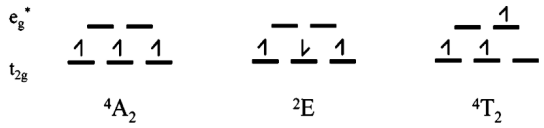


*Figure 2.4: The electronic configurations of the ground (left) and excited (middle and right) states involved in the ultrafast photo-induced study of $Cr^{III}(acac)_3$ carried out by McCusker et al. Figure reproduced from the literature with permission [5].*

This work was very important in the development of the current body of work discussed in this thesis due to the focus on the $Cr^{III}$ centred complex [6]. The main absorption feature of the material around 560 nm corresponds to the ground state to $^4T_2$ transition, which corresponds to the metal centred (MC) excitation of a $t_{2g}$ electron to the $e_g$ orbitals, Figure 2.4. At very early time delays, there is an instantaneous increase in the absorption at 480 nm which corresponds to the shoulder of the primary absorption peak observed in the excited state, Figure 2.5.

A narrowing and a blue shift of the excited state absorption spectrum is used to attribute the 1.1 ps mono-exponential decay to vibrational cooling within the $^2E$ state. Upon charge-transfer excitation into the $^4$LMCT state at 336 nm, there is an additional feature present which was attributed to the decay of this state to the $^2E$ state with a time constant of approximately 50 fs. The presented summary of the electronic states and dynamics is shown in Figure 2.6.

The most significant outcome of this study is the very fast rate at which

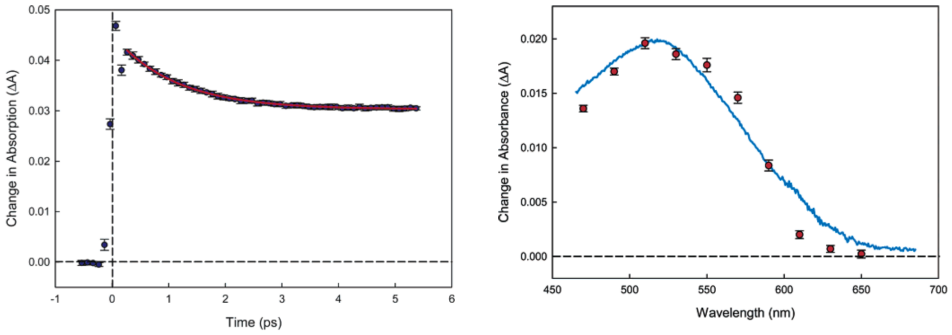


*Figure 2.5: The time-resolved measurements obtained by Juban et al. [5] which illustrate the change in the absorption measured at 480 nm after excitation at 625 nm (left). The difference absorption spectrum is also shown measured at 5 ps after excitation which corresponds to the absorption spectrum of the $^2E$ excited state (right). Figure reproduced from the literature with permission.*

the ISC occurs from the $^4T_2$ state to the $^2E$, relative to the vibrational cooling within the $^4T_2$. This information was attained by conducting measurements with varying pump pulse energies which resulted in a broadening of the transient absorption feature at very short (sub 1 ps) time delays. This implies that the population is generated in higher vibration levels in the quartet manifold, which results in the population being transferred into a higher lying energy level within the doublet manifold. From this it can be assumed that the rate of ISC is in excess of the rate of IVR within the quartet state. In 2012, this material was further probed using quantum chemical calculations of wave packet dynamics by Ando *et al.* [7] in terms of the potential energy surfaces and the spin-orbit coupling involved in the dynamics. It was confirmed that the initially populated $^4T_{2g}$ likely undergoes a very fast intersystem crossing (ISC) to the $^2T_{1g}$ which then undergoes internal conversion (IC) to the final $^2E$ state.

These studies relied on the change in the optical absorption spectrum as a function of time. The issue with this technique is that there is no inherent information on the spin states without the introduction of secondary species such as $O_2$, which acts as a quencher. This means that any changes in spin

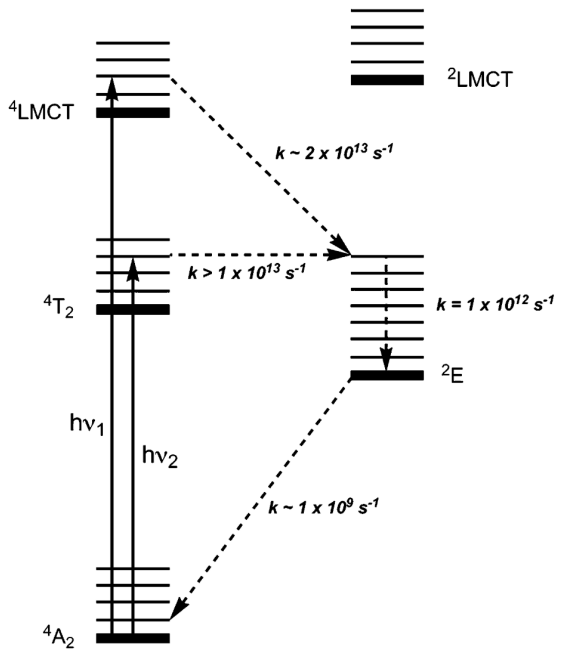


*Figure 2.6: A summary of the proposed electronic states and approximate decays obtained by McCusker et al. [5] for Cr(acac)$_3$ based on time-resolved measurements. Figure reproduced from the literature with permission.*

state are inferred from the timescales of the dynamics or from complementary computational efforts which can be used to determine the relative energies of other electronic states. The field of ultrafast magneto-optical spectroscopy could allow these studies to be made much more definitive with respect to the spin multiplicity and are able to operate on relevant timescales. This gives a direct handle on the magnetisation dynamics allowing the observation of changes in spin states to be studied in real time, and the evolution of the states, giving accurate timescales.

Time-resolved magneto-optical spectroscopy was employed to study the magnetisation dynamics in a thin film of magnetic nickel by the group of Jean-Yves Bigot in 1996. [8] This work involved the use of ultrafast optical pulses to study the optical and magneto-optical response of the metallic film. It was found that ultrafast demagnetisation of the sample occurs on a sub-picosecond timescale and this work allowed a model to be proposed. This model involves

three coupled energy reservoirs for the electron, the spin, and the lattice energies. Over the next few years there were further studies into this demagnetisation process [9–11]. Many of these papers describe a direct relationship between the MO signal observed and the magnetisation (M) observed. In particular the work of Koopmans *et al.* [11] employed time-resolved magneto-optical Kerr effect measurements with the aim to further study the contributions to the observed signal using MO rotation and ellipticity measurements.

Despite the large volume and breadth of work in this area which have been used to study this phenomenon, the nature of the underlying physics is still being debated. The work of Jean-Yves Bigot and co-workers in 2017 [12] employed a joint theoretical and experimental study of Ni and Co thin films in order to resolve the contentious nature of the ultrafast demagnetisation. Measurements were carried out on films of varying thickness using much shorter optical pulses of 10 fs. The magnetisation dynamics were probed at both the front and rear faces of the samples at different time delays. The two main models which had been proposed previously were spin flips of localised spins of the materials and superdiffusive spin transport. The spin transport model involves the generation of a spin current, where majority spins diffuse away from the sample and minority spins remain within the magnetic layer leading to an overall reduction of the moment. A study of the spin transport in bilayers of Au and Ni by Eschenohr *et al.* [13] illustrated that hot electrons generated in the non-magnetic gold layer influenced the magnetisation in the adjacent Ni layer, lending credence to involvement of superdiffusive transport of spins over relatively large distances. The joint theoretical/experimental work by Bigot *et al.* determined that it is in fact the spin flips which contribute the most to the process of demagnetisation of Ni and Co films and not the superdiffusive spin transport as previously thought. It was found that the rear face of the Co sample exhibited an inversion of the sign of the magnetisation at early time delays ($t > 50$ fs), whereas this was absent in the Ni film. These interesting differences were explained through theory which

surmised that at very early time delays there is a temporal separation between a significant amount of spin flips and the majority spin diffusion in the Co sample, on the other hand both of these processes occurred concurrently in the Ni film. This study is significant as it was able to pin down the exact nature of the demagnetisation process in these two metal thin film samples to a high degree of certainty. However the application of these techniques to metallic systems will only prove so useful when compared with the greater amount of information which could be obtained on the more complex inorganic transition metal systems with their richer range of photophysics.

In order to employ these techniques to study the ultrafast spin dynamics of an inorganic system, this system must be ordered, that is to say that the spin centres must appear in a periodic structure and be able to communicate with each other in order to produce a significant and measurable magnetic moment. To this end, the family of compounds structurally analogous to Prussian Blue (Prussian Blue analogues) have been chosen as the model system for which these techniques, prevalent in the field of solid state materials, will be applied to inorganic transition metal complexes which exhibit a much richer and varied photophysics.

## 2.2 Prussian Blue and its Analogues

Prussian Blue is a deep blue pigment that has been extensively used in paintings since its serendipitous discovery in the $18^{\text{th}}$ century. The discovery was attributed to the Swiss paint maker Johann Jacob Diesbach who was attempting to make cochineal red lake pigment [14]. The discovery of Prussian Blue was significant as it was both stable and resistant to light bleaching over time. More importantly, it offered a similarly coloured alternative to the extremely expensive ultramarine which was made from the semi-precious stone, lapis lazuli, was imported from northern Afghanistan into Europe for use in paintings. These colours were often reserved for the clothing of the central figure of a work, often

for subjects of religious importance such as the Virgin Mary.

*Figure 2.7: The deep blue pigment, Prussian Blue of the general formula $Fe_4(Fe(CN)_6)_3{\cdot}xH_2O$ which has been used extensively in the world of art since its discovery.*

Prussian Blue and its analogues (PBAs) are a fascinating family of materials which express a broad range of optical and magnetic properties. The stoichiometry varies, depending on the metal composition but in the most general form, Prussian Blue or ferric hexacyanoferrate(II), exists with the general chemical formula of $Fe_4(Fe(CN)_6)_3{\cdot}xH_2O$. The magnetic ordering temperature of Prussian Blue itself was measured to be $T_C = 5.6$ K [15] by Ito *et al.* in 1968. It was soon discovered that by substituting the $Fe^{III}$ and $Fe^{II}$ for other transition metals, a broad range of optical and magnetic properties could be obtained. Over the past 30 years or so, these properties have been explored, particularly the magnetic ordering behaviour of these materials.

The highest magnetic ordering temperatures and the understanding of the rational design used to create such materials is of great importance for the future of this field. The ability for molecular-based magnetic materials to function above room temperature is critical if they are to play a future role in the technologies of the future, primarily in the data storage devices in which they could improve data read/write speeds and storage densities.

A molecular approach was therefore taken when studying this family of materials as they could easily be synthesised by the addition of two separate

molecular sub-units, to generate the typical cubic structures exhibited by Prussian Blue analogues. With the aim of producing molecular-based systems with as high a $T_C$ as possible, one must consider the effect of the surrounding molecular field which was described by Neél in 1948 [16] for the susceptibility of a ferrimagnet composed of two magnetic centres,

$$kT_C = \frac{Z|J|}{N_A g^2 {\mu_\beta}^2}\sqrt{C_A C_B} \tag{2.1}$$

where $Z$ is the number of magnetic neighbours, $J$ is the value of the exchange interaction, $C_{A/B}$ are the Curie constants for A and B respectively, $N_A$ is Avagadro's constant, $g$ is a mean Landé factor which accounts for the degeneracy of energy levels in a magnetic field and $\mu_\beta$ is the Bohr magneton. Thus if one wishes to increase $T_C$, then it would be necessary to increase $Z$, $J$ or $C_{A/B}$.

One must also consider the nature of the exchange interaction between adjacent metal centres in an organometallic system as first described by Kramers [17] and Anderson [18] and which were later developed into the Goodenough-Kanamori rules developed in the 1950s [19,20]. This theory predicts that orthogonal orbitals give rise to ferromagnetic coupling and that overlapping orbitals will give rise to antiferromagnetic coupling. Thus depending on the d electron populations of the transition metal ions used in the M—CN—M' system, the behaviour of the resulting 3D structure can be estimated. How both the $J_F$ and $J_{AF}$ contribute to the overall magnetic properties such as coercivity, $H_C$ or the ordering temperature $T_C$ will optimised on a case by case basis depending on the desired magnetic properties.

In the early 1980's, Babel *et al.* [21] reported a ferrimagnetic system with formula $CsMn^{II}[Cr^{III}(CN)_6]\cdot 1H_2O$, with a Curie temperature of 90 K after a series of X-ray and magnetic characterisation measurements on perovskite-related materials. In this specific case, the material of interest was a Prussian Blue analogue containing Mn and Cr centres. It was thought at this time that the

superexchange interaction via the cyanide bridging ligands was responsible for the strong ferrimagnetism observed.

The group of Michel Verdaguer built upon this work to synthesise a system with short range ferromagnetic exchange interaction with a spontaneous magnetisation at $T_C = 90$ K [22]. The material, $CsNi^{II}[Cr^{III}(CN)_6]\cdot 2H_2O$ was synthesised by the slow addition of a $Ni^{II}$ salt into a concentrated solution of the hexacyanochromate (III) precursor in a 1:1 mole ratio. The use of these molecular precursors allowed the covalent 3D framework of spin-active species to be constructed. Using the hexacyanochromate (III) in place of the hexacyanoferrate (III) yielded an large enhancement in the observed $T_C$ over previously observed ferromagnetic molecular systems. In addition to this, the inclusion of Cs counter ions hinders the presence of B site vacancies which break up the long range order of the material by imposing charge neutrality of the 1:1 metal centred system. This ferromagnetic ordering was expected to be the case due to the orthogonality of the $Cr^{III}$ $t_{2g}$ and the $Ni^{II}$ $e_g$ magnetic orbitals, as illustrated in Figure 2.8, which block any correlation between ions.

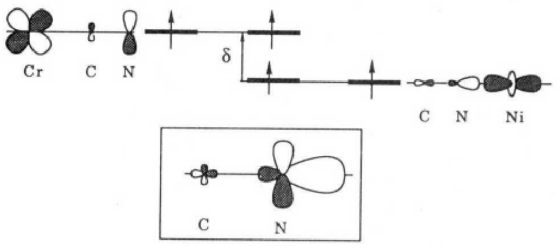


*Figure 2.8: The orthogonality of the $t_{2g}$ (xy) $Cr^{III}$ and the $e_g$ (z) $^2$ $Ni^{II}$ magnetic orbitals in the Prussian Blue analogue, $Cs^{I}Ni^{II}[Cr^{III}(CN)_6]\cdot H_20$, studied by Gadet et al. Figure reproduced from the literature with permission [22].*

The following year, the same group had developed a novel system [23] based upon the same principles used to analyse the $CsNi^{II}[Cr^{III}(CN)_6]\cdot 2H_2O$ system. Using the same orbital model it was predicted that the mixed valence chromium (II) and chromium (III) would exhibit an ameliorated magnetic ordering temperature. There are two kinds of interaction which were considered when

choosing the partner for the hexacyanochromate ions, if one ignores the next-nearest neighbour interactions of A-A or B-B couplings. In the case where the electrons on the $M^{II}$ site, typically in the nitrogen pocket of the PBAs, are of $e_g$ symmetry, then electrons on $M^{II}$ and $Cr^{III}$ are orthogonal and as such there is zero overlap. This results in a ferromagnetic interaction, as was the case for $CsNi^{II}[Cr^{III}(CN)_6]\cdot 2H_2O$, where $J = J_F > 0$. On the other hand, when the electrons on $M^{II}$ are of $t_{2g}$ symmetry then the $M^{II}$ and $Cr^{III}$ experience significant overlap which gives rise to two molecular orbitals with an energy gap, $\Delta$. The stronger the overlap, the larger the separation which results in a stronger antiferromagnetic interaction between $M^{II}$ and $Cr^{III}$ ($J_{AF} < 0$). In order to increase $T_C$, there are two options, increase the antiferromagnetic or decrease the ferromagnetic interaction. It was decided that $Cr^{II}$ would be a good candidate as it fulfils both criteria, the smaller ionic radius means that the $t_{2g}$ orbital electrons have a greater overlap with the $Cr^{III}$ and the single electron in the $e_g$ orbitals results in a weak ferromagnetic component. Using this model it was possible to synthesise two analogues of Prussian Blue containing mixed valence chromium ions, $[Cr_5(CN)_{12}\cdot 10H_20$ and $Cs_{0.75}[Cr_{2.125}(CN)_6]\cdot 5H_20$ which exhibited extremely high magnetic ordering temperatures of 240 and 190 K respectively.

This body of work culminated in a study of an analogue containing vanadium and chromium ions [24], and again employed the rational design of a Prussian Blue analogue to yield favourable orbital interactions to favour magnetic interaction between the two metal centres. The vanadium was selected due to well matched energies and significant overlap of the $t_{2g}$ electrons of the vanadium and chromium ions. There are also no unpaired electrons in the $e_g$ orbitals of the vanadium which would otherwise lead to ferromagnetic coupling between orthogonal orbitals. Therefore the high average number of magnetic neighbours and the strong antiferromagnetic interaction between adjacent, non-compensated spins explains the high $T_C$. The Curie temperature for the complex, ${V^{II}}_{0.42}{V^{III}}_{0.58}$ $[Cr^{III}(CN)_6]_{0.86}\cdot 2.8H_2O$, was recorded as 315 K, the thermal dependence of the

material showed a sharp increase of the magnetization at $T_C$ as shown in Figure 2.9.

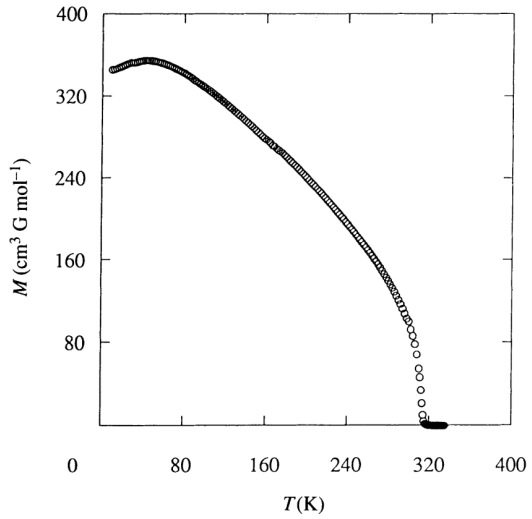


*Figure 2.9: The temperature dependence of the magnetisation, M, of the $V^{II/III}Cr^{III}$ in an low applied field of 10G measured by Ferlay et al. Of particular interest is the sharp increase in the magnetisation at $T_C$. Figure reproduced from the literature with permission [24].*

The experimental saturation magnetisation, $M_s$, of the material was measured to be 0.15 $\mu_\beta$ which is in good agreement with the theoretical value (0.16 $\mu_\beta$). This low value of $M_s$ was explained by the nature of the magnetic interactions involved. The proposed picture has the $Cr^{III}$ on one hand and the $V^{II}$ and $V^{III}$ on the other hand with their respective spins arranged antiparallel to each other. The spins of the $Cr^{III}$ and the $V^{II}$ are both $S = 3/2$, which means that these spins perfectly cancel each other out resulting in a zero net magnetisation. However the $V^{III}$ has a spin of $S = 1$ which means that these do not cancel out with adjacent $Cr^{III}$ ions. This results in a net magnetisation from the remaining excess magnetisation on the $V^{III}$ ions. This long range order of antiferromagnetically coupled centres is know as a ferrimagnet.

This material was shown to be highly air sensitive but when mixed with paraffin oil or sealed using super glue it showed good stability and maintains its optical

and magnetic properties for many weeks.

Over the course of the late 1990s, the group of Joel S. Miller published several papers [25–27] studying the nature of these materials. In particular, the paper published in 1999 [27] discusses the importance of the exact composition of the materials and the impact this has upon the magnetic properties. By varying the starting materials used in the wet chemical synthesis, either the ammonium salt of the vanadium precursor [24] or the simpler potassium salt [27], a significant increase in $T_C$ and a reduction of the coercive field was observed for the mixed valence $V^{II/III}$-$Cr^{III}$ Prussian Blue analogue. This increase in $T_C$ is attributed to the increased amount of $V^{II}$ S = 3/2 with respect to the $V^{III}$ S = 1 centres. The orbitals of the $V^{II}$ ions extend further from the nuclei due to the decreased overall charge of the metal, this increases the overlap and therefore the magnetic exchange interaction with the $Cr(CN)_6^{3-}$ moieties.

Concurrently with this, the groups of Shin-Ichi Ohkoshi and Kazuhito Hashimoto conducted studies on various analogues of Prussian Blue. These displayed the electrochemical control one could wield over the magnetic properties of the CrCr analogue [28], the reversible photo-induced magnetisation of the Co-Fe films [29] and the effect of interstitial cations upon the spin transitions of this material [30]. They also commenced studies which involve ternary Prussian Blue analogues, that is to say, analogues which contain 3 different metal ions to make up the 3D lattice structure. The $(Ni^{II}_xMn^{II}_{1-x})_{1.5}[Cr^{III}(CN)_6]$ material (where $0 \leq x \leq 1$) was used as a model system to manipulate the ferro- ($J > 0$) and antiferro- ($J < 0$) magnetic exchange interactions by adjusting the Ni:Mn ratio during the electrochemical synthesis [31]. This led to the application of these models to novel thin films of $(Fe^{II}_xCr^{II}_{(1-x)})_{1.5}[Cr^{III}(CN)_6]\cdot zH_2O$ where the target electrochemical synthesis of family of thin films which possess magnetic ordering temperatures and optical absorption spectra dependent on the stoichiometry [32]. The electrochemical potential applied during synthesis was the control used to determine the value of x in these films due to an increase in the amount of $Cr^{II}$

as the reductive potential is decreased to more negative potentials.

When the value of x is equal to 1 then the material produced is simply the FeCr Prussian Blue analogue, which was the focus of a subsequent paper where the magnetic and photo-magnetic properties in the electrochemically produced films were discussed [33]. The material exhibited ferromagnetic ordering at $T_C = 21$ K and the spontaneous magnetisation could be decreased under irradiation at the intervalence transfer band between $Fe^{II}$ and $Cr^{III}$. This effect would persist for several days after irradiation was removed and the sample was held at 5 K. The photoexcited state was thought to be a mixture of the $Cr^{III}$-CN-$Fe^{II}$ and $Cr^{II}$-CN-$Fe^{III}$ states in which the ferromagnetic interaction is too weak to maintain magnetic ordering. This state reverted back to the ground state upon heating to 40 K.

The ultrafast spin and charge transfer dynamics of the $V^{II/III}$-$Cr^{III}$ PBA were studied by Johansson *et al.* [34] which is the basis for the current studies into these materials. These studies also employed time-dependent density functional theory calculations (TD-DFT) of one monomeric unit, shown in Figure 2.10 of the Prussian Blue structure which consisted of one octahedrally coordinated vanadium and one octahedrally coordinated chromium surrounded by cyanide ligands and linked together through one bridging cyanide ligand.

These calculations used Gaussian 09 with the PBE0 hybrid functional [35]. The calculations were performed at a fixed geometry and the 6-311G(d) and 6-31G(d) basis sets were used for the metal ions and the cyanide ligands respectively. These calculations confirmed the presence of two charge transfer bands within the UV/visible portion of the spectrum, an LMCT from the $CN^-$ ligand to the Cr $t_{2g}$ orbital at 401 nm and a metal-to-metal charge transfer (MM'CT) transition at 780 nm from the Cr $t_{2g}$ to the V $t_{2g}$ orbital. The MM'CT transition was mixed with transitions from V to Cr and Cr to V and was found to occur around 570 nm.

Electrochemically synthesised thin films on fluorine-doped tin oxide (FTO) coated

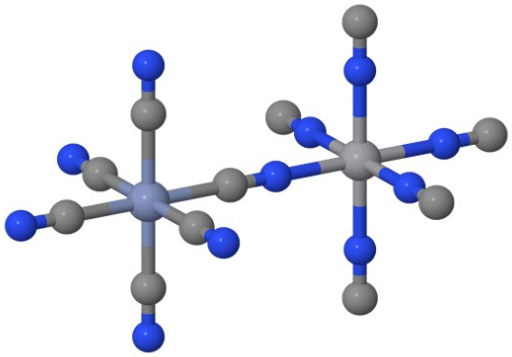

*Figure 2.10: The monomeric unit of Prussian Blue used by Johansson et al. to model the optical transitions (Chromium is in pale blue and vanadium is in light grey, nitrogen and carbon are blue and grey respectively).*

glass substrates were studied using femtosecond pump probe measurements which were used to observe the ultrafast transmission and magnetisation dynamics of the film. The temporal resolution of the experimental setup was approximately 250 fs. The sample was held within a temperature-controlled cryostat and the magnetic field was applied perpendicularly to the sample plane using a superconducting magnet at a strength of $\pm 0.5$ T.

It was found that when exciting the LMCT transition at 400 nm, an electron is transferred from the cyanide bridging ligand ($CN^-$) on to the Cr ion. This results in a change in the nature of the MM'CT transition which manifests itself as an increase in the transmission from 500 nm to 660 nm. A second portion of the laser beam was used to generate a supercontinuum which spanned wavelengths from 480 to 690 nm. This was used as a probe pulse to interrogate changes in the transmission spectrum and magneto-optical (MO) response of the sample as a function of time. Over this range of wavelengths, 8 wavelength specific bands of approximately 15 nm bandwidth were measured in order to build up a complete spectral picture of the dynamics.

Figure 2.11 was obtained by interpolation of the wavelength specific kinetic traces and illustrates the spectral response of the signal upon excitation

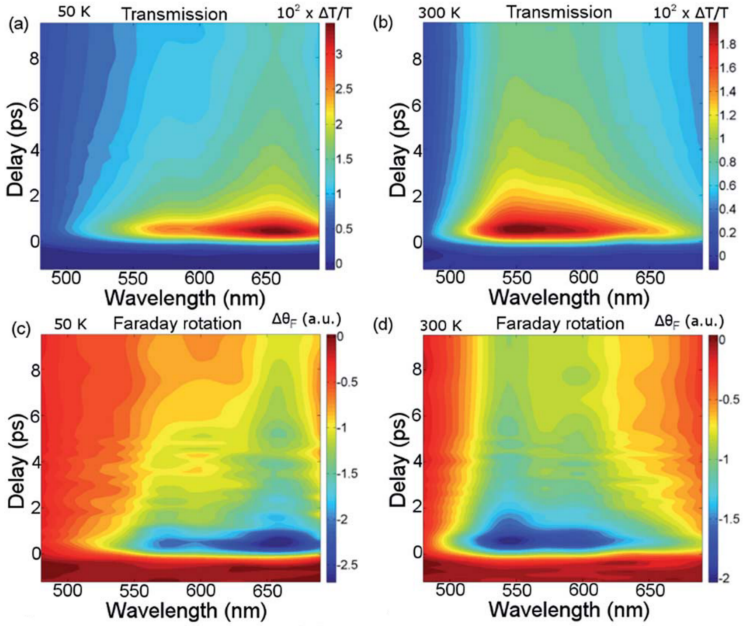


*Figure 2.11: The time-resolved transmission ((a) and (b)) and Faraday rotation ((c) and (d)) measurements carried out at temperatures of 50 and 300 K [34]. The transient transmission measurements exhibit a bleaching of the ground state absorption due to a modification of the MM'CT transition upon excitation. Changes in Faraday rotation appear at the same spectral positions and decay on the same timescales, suggesting the two processes are inherently linked. Figure reproduced from the literature with permission.*

at the LMCT. There appears to be a significant shift in the maxima of the two difference spectra as a function of the temperature, which was also observed in the static transmission spectra. The very fast increase in transmission and subsequent decay observed are due to the nature of the energy redistribution in these transition metal complexes. As was previously discussed with respect to the work of McCusker *et al.* on $Cr(acac)_3$ there is the possibility for a fast intersystem crossing to occur in the $Cr^{III}$ moiety. The fastest of the decay components found in this work was below 200 fs which, although below the temporal resolution of the experiment, gives a promising indication that there is a possible parallel to be drawn between the Cr present in the VCr PBA and the TM complexes studied by McCusker *et al.* The $^4$LMCT indeed appears to have a very short lifetime

which could be the result of a very fast intersystem crossing into a $^2$E excited state. These dynamics are summarised in Figure 2.12.

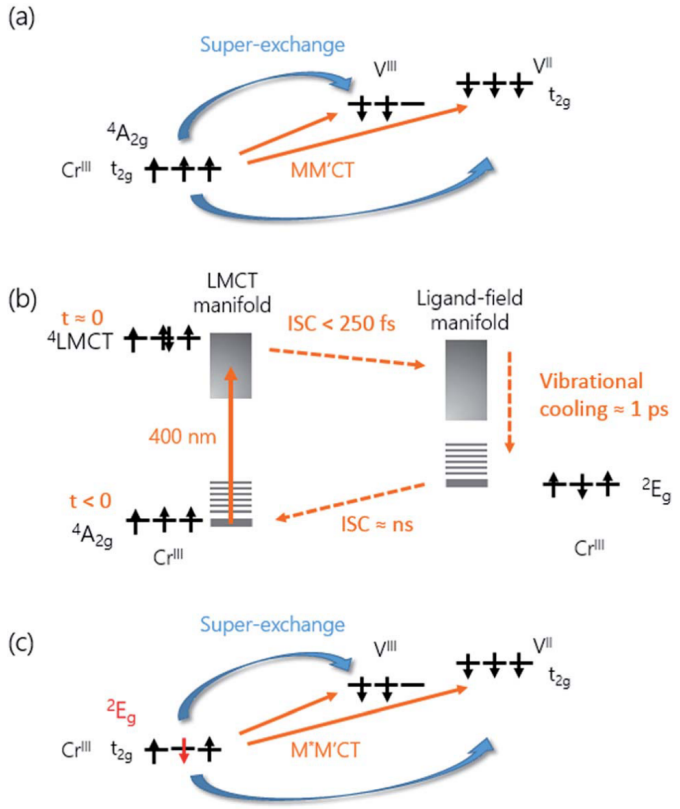


*Figure 2.12: The overall proposed model used to describe the electron and spin dynamics by Johansson et al. a) shows the ground state MM'CT transition between $Cr^{III}$ and $V^{II/III}$ [34]. b) After optical excitation the $Cr^{II}$ is transiently formed in the $^4$LMCT state before very fast ISC into the $^2$E state. Vibrational cooling then occurs within this state. c) The resulting modification of the MM'CT transition, denoted M*M'CT, after the $Cr^{III}$ is generated in the $^2$E state. Figure reproduced from the literature with permission.*

In the ground state, the MM'CT transition occurs between the Cr and V ions through the superexchange interaction mediated by the cyanide bridging ligands. After excitation at the LMCT, an electron is transferred from one of the $CN^-$ ligands on to the $Cr^{III}$, resulting in the transient reduction to $Cr^{II}$. This state subsequently undergoes very fast ISC into the ligand field manifold of the $^2$E state. This was attributed to the sub-200 fs decay constant found in the fitting

of the kinetic data, which does lie below the temporal resolution but does give an indication of the speed of the transition. After this, the vibrationally hot $^2$E state decays with an approximately 1 ps time constant which matches very well with the decay that was found by McCusker *et al.* [5].

It is important to note that the signals that were observed in the VCr Prussian Blue analogue in this study were simply the ground state bleach of the MM'CT transfer transition which is modified upon the addition of an electron to the Cr ion. This is the point at which the work carried out for this thesis began, with the development of an optical setup with the ability to carry out ultrafast transient transmission and magneto-optical measurements on thin films of Prussian Blue analogues. A commercial electromagnet and cryostat were used to apply a variable magnetic field and allow accurate temperature control of the material.

The application of these ultrafast techniques to inorganic functional materials will allow the study of ultrafast charge transfer and spin transitions with the aim to further the development of molecular based magnetic devices.

## 2.3 Aims

During this work, electrochemical synthesis will be used to synthesise thin films of the various PBAs which will be subsequently studied using the time resolved techniques. Electrochemical synthesis will give control over the thickness and morphology of the films in order to optimise the films for optical measurements. The analogues of Prussian Blue which are to be studied have been thoroughly characterised previously and exhibit a wide variety of spectral features. These are the VCr [24, 36–39], FeCr [33, 40–43] and CrCr [25, 26, 44] analogues. The influence of depositing one or more of these films on top of each other will be explored as these materials show a range of magnetic ordering temperatures and absorption spectra which could prove beneficial to one of the species involved.

It could be useful to consider the expected results from the ultrafast measurements before carrying them out, with respect to the relative rates of intersystem crossing from the three samples to be studied: the VCr, FeCr and CrCr Prussian Blue analogues. This will give an indication of the success of the measurements determine which parameters influence the intersystem crossing rates.

The two parameters which most impact the rate of intersystem crossing are the spin orbit coupling and the energy mismatch between the two electronic states. A larger spin orbit coupling parameter will result in a faster transfer of population between the two states.

The spin orbit coupling parameter depends on the nuclear charge of the atoms involved, meaning that larger metal atoms have a larger spin orbit coupling. Of the three samples studied here the Cr ion is consistent and the opposing metal ion is exchanged. Vanadium has the smallest nuclear size, followed by chromium and then iron has the largest nuclear size, this means that the spin orbit coupling increases as follows, V $<$ Cr $<$ Fe.

The second parameter to be considered is the energy difference between the initial $^4$LMCT state and the final $^2$E state. Due to the hybridisation of the metal-ligand orbitals it may be possible to estimate the relative energies of the $^2$E states based upon the amount of electron density localised on the cyanide ligands. The transition metals opposite the $Cr^{II}$ ion are in the $M^{3+}$ oxidation state in the FeCr and CrCr materials, however in the VCr analogue there is a varying percentage of $V^{II}$ also present. Metals in the +2 oxidation state generally have a larger ionic radius than their +3 counterparts as the lower charge results in a weaker attraction to the outermost electrons. This weaker interaction with the electron-electron repulsion therefore results in a larger overall ionic radius. The atoms with smaller ionic radii have a greater interaction with the adjacent ligands and therefore the bonding from the cyanide ligands is stronger. This results in a decrease in the electron density on the ligands, due to the dative nature of the

bonding in the nitrogen pocket, which detracts from the interaction with the Cr ions in the carbon pockets. This overall interaction reduces the metal-ligand interaction which results in a stabilisation of the $t_{2g}$ orbitals and a destabilisation of the $e_g$ orbitals. If this is the case then the VCr analogue would show the lowest energy $t_{2g}$ orbitals, followed by the chromium and the iron analogue. The vanadium should show a significant difference however the iron and chromium ions are much more similar in ionic radius and the differences will be much smaller. The spin orbit coupling is the dominant of the two influences and one would therefore expect the rate of intersystem crossing to be fastest in the FeCr analogue, followed by the CrCr analogue and the slowest is the VCr analogue. The influence of the energy difference is significantly different for the VCr analogue, in this case the energy after LMCT excitation is closer in energy to the overlap with the $^2E$ state, thus promoting intersystem crossing. Overall the expectation is that the rate of crossing for the FeCr PBA would be the fastest, followed by the VCr PBA and finally the CrCr PBA is the slowest.

The ultrafast electron dynamics of the Prussian Blue analogues will be studied using femtosecond time resolved transient transmission techniques which will allow the population and subsequent relaxation of the excited states to be followed. Where possible, measurements will be carried out as a function of the applied pump power to give insights into the photophysics of the materials. Also film thickness is varied in order to further study the nature of the thermal relaxation pathways available to these materials.

The construction of a new experimental setup will be discussed which will be capable of studying the ultrafast magnetisation dynamics of the materials. This will be very important when considering the different excited states which may be involved upon photo-excitation and during the transfer of population into the final excited state.

# Chapter 3

# Experimental

## 3.1 Optical Setup

### 3.1.1 Femtosecond Laser Pulse Generation

The whole optical setup is spread over two separate laser tables, the first of which holds the components which are responsible for the generation of the ultrafast laser pulses and the second laser table has been constructed to carry out the measurements presented in this thesis. A simplified schematic of the first laser table setup is shown in Figure 3.1.

#### Femtosecond Titanium Sapphire Oscillator

The generation of ultrafast laser pulses is achieved in a *Coherent Mantis* oscillator which uses a titanium-doped sapphire crystal (Ti:S) as the gain medium to generate the femtosecond laser pulses. There is a relationship the temporal and spectral width of a pulse called the Fourier relationship, where $\Delta$t is the pulse duration and $\Delta\nu$ is the bandwidth,

$$\Delta t \times \Delta\nu = 0.441 \tag{3.1}$$

This means that in order to generate a pulse of femtosecond duration, the pulse must have a sufficient spectral width in the frequency domain. The Ti:Sapph

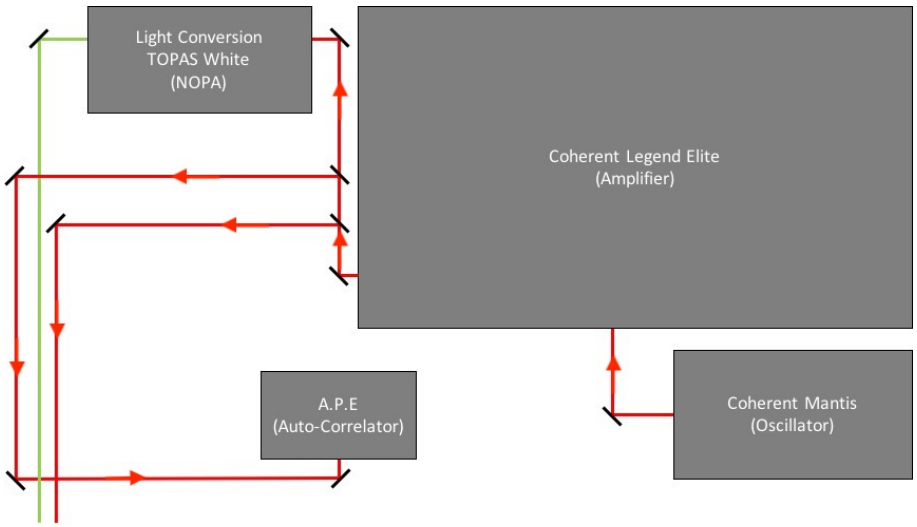


*Figure 3.1: A schematic of the first laser table where the ultrafast pulses are generated and divided up into various beams to be further modified or used in other experiments.*

oscillator therefore provides the fundamental 800 nm laser pulses with a sub-20 fs temporal profile with a bandwidth of 80 nm at a repetition rate of 76 MHz after mode-locking is achieved. The gain medium is pumped by a *Coherent OPS* quantum well laser to electronically excite the titanium ions. In order to generate the femtosecond laser pulses, the length of the cavity oscillates at a high frequency in order to induce power fluctuations. Once a threshold power is met, there is a Kerr lensing effect which occurs in the gain medium. This lensing results in this fluctuation being amplified and results in a single dominant pulse which forms the mode-locked laser pulse. This is referred to as passive mode-locking. The spectrum of the mode-locked output of the *Mantis* is shown in Figure 3.2.

The typical output power of the *Mantis* when mode-locked is around 500 mW. This is not sufficient to operate any of the non-collinear optical parametric amplifiers that are critical in the experiments to generate different wavelengths of light. To this end, the 800 nm, mode-locked beam from the *Mantis* is directed into a regenerative amplifier.

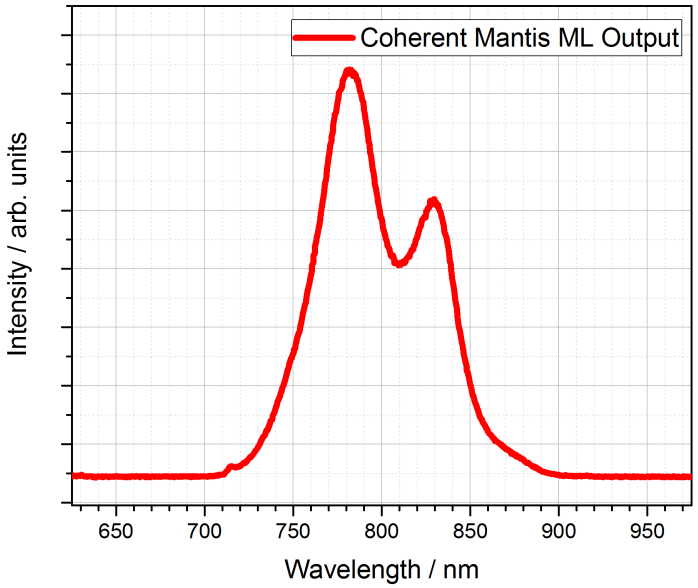


*Figure 3.2: The spectrum of the mode-locked output from the Mantis oscillator, centred around 800 nm at a repetition rate of 80 MHz.*

### Femtosecond Titanium Sapphire Regenerative Amplifier

The seed beam coming from the *Mantis* oscillator is directed straight into the regenerative amplifier unit with no further modification of the pulses. The *Coherent Legend Elite* regenerative amplifier system uses a Ti:S laser crystal as the gain medium which is held in a temperature and humidity controlled enclosure. The crystal is pumped by the frequency doubled output of a diode pumped neodymium-doped yttrium lithium fluoride (Nd:YLF) laser. To avoid damage to the optical elements, the incoming ultrafast laser pulses are first stretched in time to reduce their peak intensity, before they are amplified, by reflection from a dispersive grating. The stretched pulses are then passed into the optical cavity in which the gain medium is housed. Pockels cells are used to control the pulses entering and leaving by modifying the polarisation of the pulses. The polarisation of the incoming laser pulses are such that they are not allowed to pass, but when the Pockels cells are switched they enter the cavity. The timing

relative to the pump laser is controlled by a *SDG Coherent* delay generator to control the pulse build up within the cavity. The pulse is trapped within the cavity where it experiences amplification over 20 - 30 round trips through the cavity. Once the maximum amplification has been realised, another Pockels cell releases the pulse from the cavity. The time delay of this second Pockels cell is dictated by the same delay generator as the first cell which can be modified by the experimentalist. After the pulses have been sufficiently amplified, they are recompressed in time using another set of gratings to produce pulses with a central wavelength of around 800 nm with a bandwidth of 10 nm. The typical output power from the regenerative amplifier should be around 3.5 W at a repetition rate of 1 kHz and the polarisation is horizontal. The spectrum is shown in Figure 3.3.

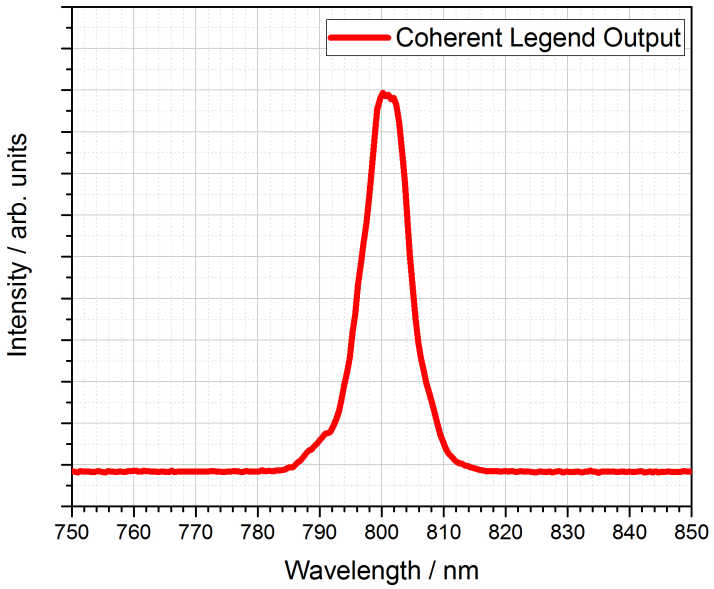


*Figure 3.3: The spectrum of the output from the Legend regenerative amplifier, the pulses are generated at 800 nm, 120 fs, 1kHz repetition rate with an overall power of 3.5 W.*

From the output of the *Legend* there are several beam paths dedicated to

the other experiments which use this laser source. Only the components pertinent to this project will be discussed here.

A commercial auto-correlator unit is used on this table to measure the pulse duration, this can help as a diagnostic tool when optimising the compressor in the regenerative amplifier or diagnosing problems with the system.

### 3.1.2 Optical Experimental Setup

The second laser table in the laboratory holds all of the optical elements specifically pertaining to the measurements presented in this thesis. The optical layout on this table is shown in Figure 3.4.

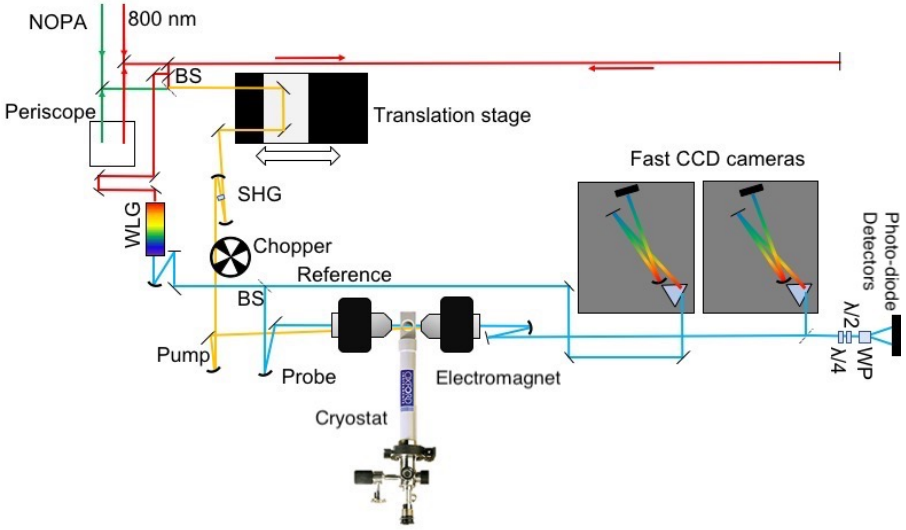


*Figure 3.4: A schematic of the optical setup specifically constructed to carry out the time-resolved magneto-optics and transient absorption measurements described in this work.*

A portion of the 800 nm beam from the *Legend* crosses from the first laser table and is brought down to the correct height using a periscope. From here the beam travels the length of the table and back again where it is then picked off at a slightly lower height by a mirror, this adjusts the relative time delay between this beam and the output of the *TOPAS-White* so that they arrive at the experiment at the same time. This allows the *TOPAS-White* to be used

as a pump pulses of different wavelengths of light.

After this delay line, the beam is split into two using a 90:10 beam splitter. 90% of the beam is used to generate our pump pulses by frequency doubling the 800 nm to give 400 nm pulses and 10% of the beam is used to generate a white light continuum as the probe. These two beams are then focussed into the same point in the center of the electromagnet and can be directed on to the two methods of detection, depending on the type of experiment carried out.

### White Light Continuum Generation

When a femtosecond laser pulse is focussed into an optically transparent material it is possible to generate a broad range of wavelengths through spectral broadening. The temporal variation of the laser intensity induces a variation in the index of refraction of the material. This effect is called self-phase modulation (SPM). Various materials can be used to generate a continuum with sufficient spectral width and stability, however in this work the continuum was generated in $CaF_2$.

As previously mentioned, 10% of the 800 nm beam which is reflected from the beam splitter forms the seed for the continuum generation. This beam is passed through a graduated neutral density (ND) filter and an iris, to allow the power and beam spot size to be modified. This is critical in order to be able to control the power density experienced by the $CaF_2$ plate to produce the most stable white-light continuum (WLC). No modification of the seed polarisation is carried out at this point so it remains horizontal as per the output of the *Legend*. The light is then focussed through a $CaF_2$ plate mounted in a 2-dimensional translational mount which continually moves the $CaF_2$ to avoid damage to the plate. This is because the damage threshold for the material is lower than the power required for continuum generation. The outgoing WLC is then immediately collimated using a spherical mirror before being passed through a 800 nm filter to remove any residual seed pulse in the beam. The use of a collimating mirror helps to

reduce the amount of material that the continuum passes through between the $CaF_2$ and the sample, in order to keep pulse chirp to a minimum. A typical spectrum of the white light continuum is shown in Figure 3.5.

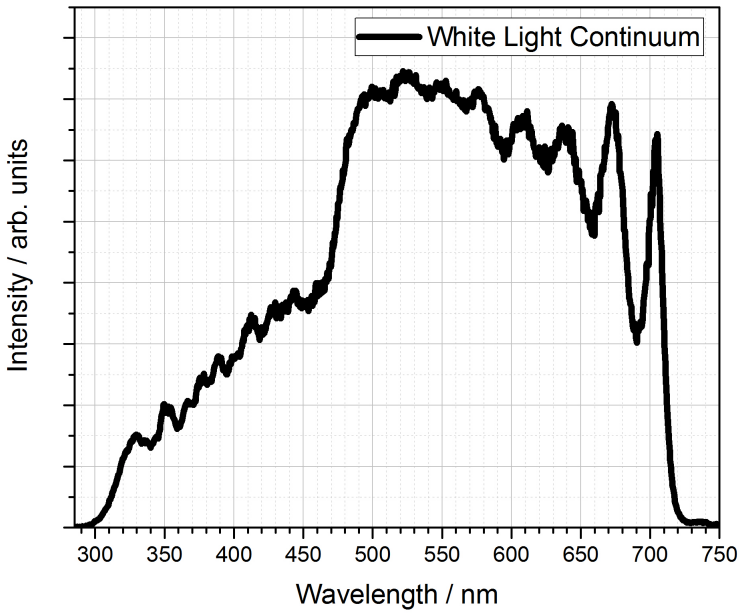


*Figure 3.5: The spectrum of the white light continuum which is generated by focussing 120 fs, 800 nm pulses in to $CaF_2$ which is being translated in two dimensions to avoid thermal damage. There is a cut-off filter placed shortly after the white light generation setup which is used to remove any residual 800 nm light. This is the cause of the modulations close to the cut-off around 750 nm.*

The optimum spectrum depends on the application on a given day, whether the spectrum needs to extend as far into the UV as possible or to achieve the highest stability across the breadth of the continuum. Iterative optimisation of the aperture, neutral density filter, focal position and pulse duration is necessary to produce the desired white light spectrum.

### Broadband Pulse Detection

In this section, the optical and electronic components which allow the measurement of transient absorption will be discussed. Two methods of detection are used to measure the difference in absorption as a function of time; a pair of balanced photodiodes (ThorLabs PDB210A) and two home-built spectrometers using CCD camera detectors. After interaction with the sample between the poles of the electromagnet, the beam is collimated using a spherical mirror, it is then aligned through a pair of apertures which ensures that the beam is travelling in a straight line from the electromagnet towards the detectors at the end of the table. The use of mirrors on flip mounts allows the probe beam to be directed to either method of detection, depending on the measurement being carried out.
The balanced photodiodes (PDs) are sensitive from around 400 nm to 1060 nm with wavelength-dependent responsivities, shown in Figure 3.6. These PDs can be used to measure the change in absorption over narrow wavelength ranges at once using 10 nm bandpass filters at particular regions of interest depending on the sample.

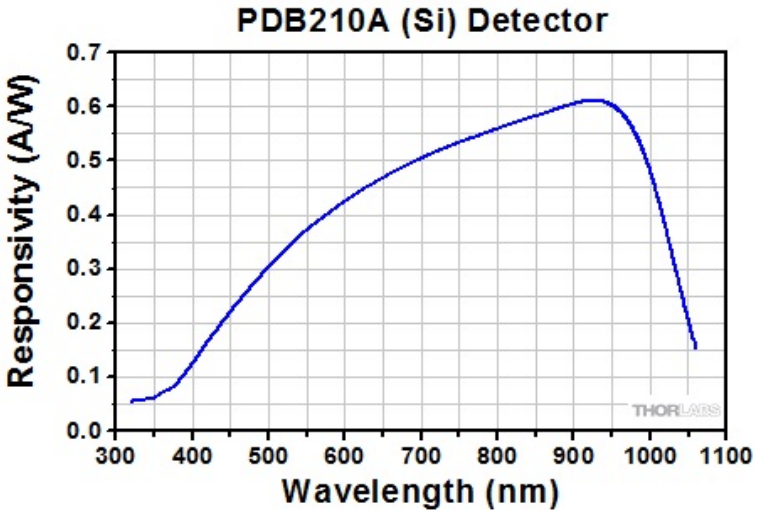


*Figure 3.6: The wavelength dependent sensitivity of the ThorLabs PDB210A balanced photodiode detectors used in the MO experimental setup.*

The cameras used to carry out time resolved broadband measurements

were supplied by Stresing, they contain two CCD detector heads (Hamamatsu, sensor S7030-0906) made up of an array of 512 x 58 pixels with each pixel measuring approximately 24 $\mu$m square giving an area of 12.3 x 1.4 mm. The beams enter the spectrometers, where they first pass through fused silica prisms to disperse the light. The light is then focussed down to a horizontal line which is directed to cover the width of the CCD chip. The actual width of the spectrum spans more than the 12.3 mm in order to retain resolution across the whole spectrum. Using the input mirror to the cameras, the angle of input to the cameras is optimised to pass through the prisms at the Brewster angle. The camera detectors are mounted on 3 dimensional translation stages so that they can then be moved horizontally in order to study the shorter or longer wavelengths generated in the continuum by scanning across the horizontally dispersed beam.

**Time-Resolved Transient Absorption Measurements**

Both methods of detection can be used to study the change in the absorption of the sample as a function of time. As previously described the balanced photodiodes are used for narrow wavelength region measurements and the cameras are used for broadband measurements. In order to study the change in absorption due to the pump excitation, the 400 nm beam is modulated at 500 Hz (half the repetition rate of the laser) meaning that every other pump pulse is blocked. The signals from the balanced PDs are passed through the lock-in amplifiers which filter out any signal which is not modulated at 500 Hz and this is then plotted using a LabView program which was written as this setup was being constructed.

In the case of the broadband measurements, the cameras are set up to monitor a wavelength range from around 300 nm to around 670 nm. In the presence of the pump laser pulse, there is a larger amount of light around 400 nm than without. The trigger signal from the chopper is then used to designate the 'Pump on' or 'Pump off' states in a separate LabView program, the change in absorption

spectrum is then plotted in the program. The reference beam is also used to clean up the observed signal by accounting for any changes in the intensity of the white light continuum itself [45].

### Faraday Rotation Measurements

Light is able to interact with the magnetisation of a sample as it is an electromagnetic wave. The effect comes from the interaction of a magnetised system's permittivity, $\epsilon$, and the electromagnetic field, E, generated by the light pulse and are related by the following equation: $\mathrm{D} = \epsilon_0 \, \epsilon \cdot \mathrm{E}$, where D is the electric displacement vector. The relationship between the angle of rotation of the polarisation, $\beta$, and the magnetic flux density in the medium, B, is the following: $\beta = \nu \mathrm{Bd}$, where $\nu$ is the Verdet constant for the material and d is the path length in meters. A positive Verdet constant corresponds to L-rotation when the magnetic field direction matches the propagation direction and R-rotation when the two vectors are anti-parallel. Right-handed and left-handed circularly polarised light causes charges within a material to rotate in opposite directions, where each polarisation contributes to the orbital angular momentum. A magnetic field then gives rise to a spin polarisation along the magnetic field direction which leads to an energy contribution to each of the two polarisations of opposite sign to each other. This leads to right-handed and left-handed polarisations having different refractive indices. Plane polarised light should be considered as the sum of right-handed and left-handed polarisations in this case. When passing through the material, these two polarisation components propagate at different speeds meaning that they emerge from the material out of phase, therefore the beam has a rotated plane of polarisation.

In an isotropic medium the dielectric tensor becomes

$$\epsilon = \epsilon \begin{pmatrix} 1 & iQ_z & -iQ_y \\ -iQ_z & 1 & iQ_x \\ iQ_y & -iQ_x & 1 \end{pmatrix} \tag{3.2}$$

where $\mathbf{Q} = (Q_x, Q_y, Q_z)$ is known as the Voigt vector which is aligned with the magnetic field and has a magnitude which depends on the nature of the material. The off diagonal terms in the matrix in the above equation give rise to magneto-optical effects. This leads to the two circular component normal modes which have the dielectric constants $\epsilon_\pm = \epsilon\ (1 \pm Q \cdot \hat{k})$, where $\hat{k}$ is the propagation direction of the light. The two circular components will travel with different velocities and are attenuated differently which results in the emergent light having a rotated plane of polarisation in the case of velocity difference or ellipticity in the case of a difference in attenuation.

In order to study the magnetisation dynamics of the samples we employ the magneto-optical Faraday effect (MOFE) which is analogous to the magneto-optical Kerr effect (MOKE) but is measured in the transmission geometry as opposed to reflection. The basis of the techniques is the same, when linearly polarised light interacts with a magnetised medium, the polarisation direction is rotated. The degree of rotation is proportional to the magnetisation of the sample, giving a direct handle on the magnetisation, and most importantly is able to operate on ultrafast timescales when used in a pump-probe type experiment.

After the sample, the probe beam is aligned through the apertures to ensure that the beam travels in a straight line, perpendicular to the polarisation optics (retarder plates and prisms). In order the measure the Faraday rotation we require a half waveplate, which is used to rotate the polarisation of the light by 45°, and a Wollaston prism, which is used to separate out the horizontal and vertical components of the polarisation.

Firstly, the waveplate is aligned perpendicularly to the beam propagation by overlapping the back reflection with the incoming beam. The probe light is

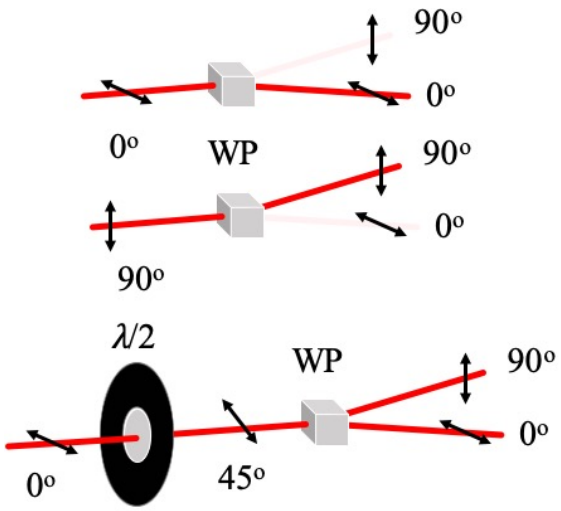


*Figure 3.7: A schematic representation of how the Wollaston prism in combination with the balanced photodiode detector allows the measurement of the polarisation. In the first two examples, the incident polarisations are horizontal and vertical which result in only one beam being produced of the initial incident polarisation. In the final case, a half waveplate is used to rotate the polarisation to 45° which then results in two beams of equal intensity to be produced, with horizontal and vertical polarisations.*

generated with the same polarisation as the seed pulse, this means the polarisation of the light at the sample is horizontal. The wave-plate is set to 22.5° inducing a 45° rotation of the polarisation. This results in a 1:1 ratio of the horizontal and vertical polarisations exiting the Wollaston prism, and the same fluence of photons incident on each detector of the balanced photodiodes.

When the light induces a change in the polarisation there is an instantaneous change in this balanced signal which may be due to a change in the magnetisation of the sample.

## 3.2 Electrochemistry

### 3.2.1 Electrochemical Deposition

The substrates (1.6 mm thick sodalime glass coated with a conductive fluorine doped tin oxide ($SnO_2$:F) layer. Substrates were bought from Solaronix and were not modified further) were sequentially cleaned using a water and detergent mixture, isopropanol ($^i$PrOH), and methanol (MeOH) in order to remove any impurities on the surface of the substrates. The films were then finally rinsed in distilled water as this is the solvent to be used in the synthesis. This is done on the day of synthesis in order to ensure that the substrates are sufficiently clean to produce homogeneous films of a sufficient optical quality. The general method for electrochemical deposition is fairly consistent over the various Prussian Blues, though the concentrations, potentials and deposition times vary. 1M KCl is used as an electrolyte in all of the syntheses and the precursors are chosen depending on the material that we wish to synthesise.

The general formula for these materials is; $X_xA_a[B(CN)_6]_b{\cdot}nH_20$, where X is an alkaline metal ion, in our case exclusively potassium, and A and B are first row transition metal ions. Therefore in order to synthesise analogues of Prussian Blue we are going to substitute both A and B for different free metal and hexacyanometalate ions. As precursors to these ions, metal (III) chlorides ($ACl_3$) and potassium hexacyanometallates (III) ($K_3B(CN)_6$) are used, where A can be Fe, V or Cr and B can be Fe or Cr to generate the materials that have been studied so far. This includes the VCr, FeCr, CrCr analogues and the FeFe Prussian Blue itself.

The electrochemical deposition works on the basis that the Prussian blue analogues are insoluble in water, which is exclusively the solvent used in the work presented here. Typically the precursor ions are not very reactive with one another, but when one of the species is electrochemically reduced they become much more reactive. As the reductive process occurs at the surface of the electrode, the

Prussian blue is formed and immediately precipitates onto the conductive face of the electrode. It is assumed that due to the labile nature of the chloride ions, they detach from the metal ion in solution whereas the more strongly bound cyanide ligands remain attached to the metal ion.

For the VCr analogue the precursor solutions are vanadium chloride ($VCl_3$) and potassium hexacyanochromate ($K_3Cr^{(III)}(CN)_6$) at concentrations of 50 and 75 mmol. Upon application of a potential of -1.15 V, the free vanadium ion is reduced.

For the iron/chromium analogue the precursor solutions are ferric chloride ($FeCl_3$) and potassium hexacyanochromate ($K_3Cr^{(III)}(CN)_6$) at concentrations of 50 and 75 mmol. Upon application of a potential of -0.7 V, the free iron ion is reduced.

For the CrCr analogue the precursor solutions are chromium chloride ($CrCl_3$) and potassium hexacyanochromate ($K_3Cr^{(III)}(CN)_6$) at concentrations of 5 and 7 mmol, according to the literature. Upon application of a potential of -0.85 V, the chromium ion is reduced.

In the case of the iron/iron analogue the precursor solutions are ferric chloride ($FeCl_3$) and potassium hexacyanoferrate ($K_3Fe^{(III)}(CN)_6$), however in this case the reduction potential of the cyanometallate species is lower than that of the metal chloride species meaning that the reduction occurs on the cyanometallate ion. The other difference here is that the electrochemical reduction is carried out galvanostatically, that is to say, at a constant current, in this case the current is set to -40 $\mu$A.

All materials are purchased from Sigma-Aldrich and are used without further purification.

The electrochemical setup is shown in Figure 3.8 and shows the electrochemical cell and the electrodes used to deposit the thin films which are all connected to the *Metrohm AutoLab III* potentiostat which controls the currents and potentials in the electrochemical cell.

The working electrode is the conductive surface where the reaction of

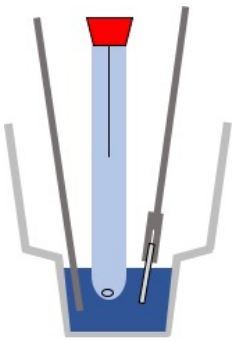

*Figure 3.8: A sketch of the electrochemical cell and the electrodes that are used to deposit the thin films. From left to right; the counter electrode, the reference electrode and the working electrode.*

interest occurs, in this case it is the conductive surface of the glass electrode which is contacted using a crocodile clip attached to a steel rod. The counter electrode is a simple platinum rod and along with the working electrode provides the circuit through which current can flow to carry out the electrochemical process of interest. Finally, the reference electrode is a Ag-AgCl electrode which provides a stable half-cell potential to allow the potential of the other half-cell (the difference between the working and counter electrodes) to be determined.

### 3.2.2 Spectroelectrochemical Studies

Spectroelectrochemistry has allowed the redox processes involved to be identified by correlating the peaks that are observed in the cyclic voltammogram with changes in the optical spectra. This combination of techniques works in both directions; giving information on the optical signatures of redox processes and allowing the identification of redox processes by their accompanying changes in the absorption spectra. The samples are placed in a 10 x 10 mm cuvette which is housed in a mount which allows the use of optical fibres to couple the halogen light source (Ocean Optics HL-2000-FHSA) to the spectrometer (Ocean Optics HR2000+) as shown in Figure 3.9.

This setup is easy to operate adjacent to the electrochemical setup

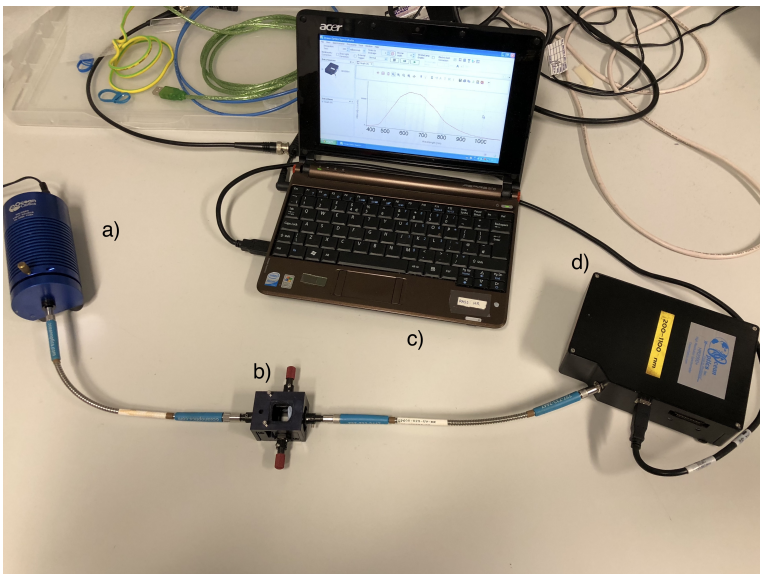


*Figure 3.9: The spectroelectrochemical setup which is used to study the transmission spectrum of the sample as a function of the potential. The light is contained within optical fibres for the majority of the beam path to remove the need for optical alignment. a) is the Ocean Optics light source which generates white light from around 400 nm to the IR. b) is the sample housing which uses a 1 $cm^2$ cuvette and coupled optical fibres. c) is the laptop used to run the spectrometer program used to store the transmission spectra. d) is the Ocean Optics spectrometer used to measure the spectra.*

previously described, and the coupling of the light using optical fibres means there is no alignment required at any stage. Due to the size constraint in the cuvette, the Ag-AgCl reference electrode is replaced with a Pt wire electrode which was found to have a negligible impact on the observed potential [46]. Samples are mounted in the cuvette and the electrodes are positioned such that no direct contact is made with the other electrodes, the electrolyte is then added to submerge the electrodes.

The potentials are then applied using the potentiostat and an auxiliary laptop is used to control the spectrometer and acquire the spectra. For the plots of absorption against time the absorption at a single wavelength was monitored at 0.2 s intervals. In the case of the spectra measured at each potential, this was

done manually and the potentiostat was set to hold at each potential for 30 s.

## 3.3 Characterisation

A broad range of analytical techniques are used which give information on various properties of the films including optical absorption, cyanide stretching frequency, film morphology and thickness and elemental analysis. This is important as there is a lot of variability with site defects and material stoichiometry which is highly dependent on the synthetic conditions, particularly for the VCr analogue [37]. The reproducibility of the films can therefore be an issue so all of these techniques were used together in order to build up a complete picture of the films.

### 3.3.1 UV-Visible Spectroscopy

Prussian Blue and many of its analogues are strongly coloured due to metal-to-metal charge transfer transitions occurring in the visible region. This means that investigation of the absorption spectrum is a simple method to study the nature of the material. The films are almost always of a sufficient thickness that one can see, by eye, if the correct colour has been formed but the use of absorption spectroscopy allows more subtle differences to be quantified. The strength of the absorption is directly proportional to the amount of material, or path length, so this can also be used as a simpler measure of the film thickness, once a calibration is carried out by measuring the thickness of various films. The relative energies of the d-electrons in the two metal ions is an important factor in the energy of the MM'CT and therefore the wavelength of light which is absorbed. During the spectroelectrochemical measurements, this absorption spectrum is modified due to a change in the relative energies of these electrons. All measurements of static absorption spectra are measured using the spectrometer and light source described in the spectroelectrochemical measurements. The

measurements were typically obtained using the spectroelectrochemistry setup described in the previous section unless stated otherwise.

Prussian Blue itself is strongly coloured blue and the absorption spectrum is shown in Figure 3.10, the single broad peak at 690 nm corresponds to a charge transfer transition between the adjacent $Fe^{II}$ and $Fe^{III}$ metal centres present in the PB lattice [47].

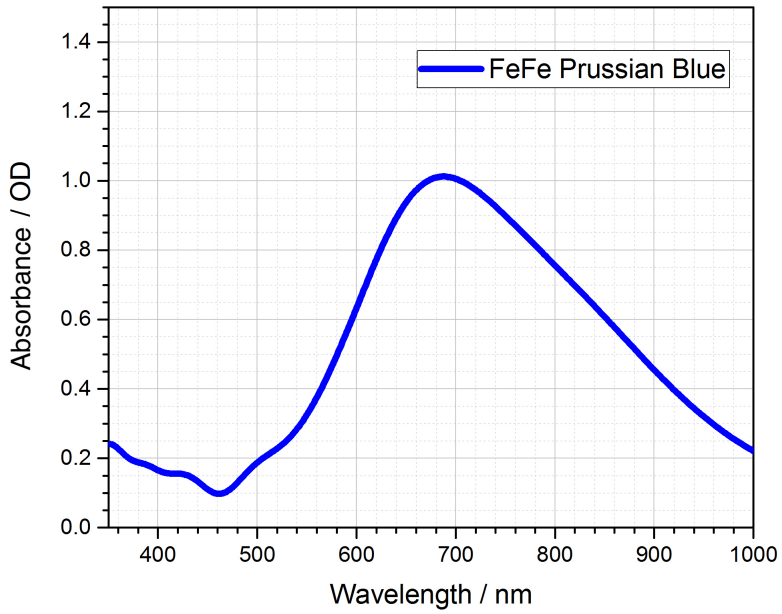


*Figure 3.10: The UV-Vis absorption spectrum of the FeFe Prussian Blue showing an absorption band from the $Fe^{II}$-$Fe^{III}$ MM'CT transition. This absorption spectrum was measured on a Shimadzu UV-1800 UV Spectrophotometer to obtain better signal-to-noise ratio across the whole spectrum.*

The VCr analogue is also coloured blue with a strong absorption from 500 to 700 nm, this broader band in this analogue is due to there being two oxidation states of the vanadium present in the lattice. These two different oxidation states, $V^{II}$ and $V^{III}$, are present in different ratios depending on the synthetic conditions. The effect of this ratio has been previously studied [27] with the aim to increase the observed $T_C$, but this is not the focus of this work.

The absorption spectrum of a VCr PBA film is shown in Figure 3.11, the MM'CT band in this material is made up of two bands, one at 540 nm and the second at 690 nm which correspond to the $Cr^{III}$-$V^{II}$ and the $Cr^{III}$-$V^{III}$ respectively [37,48,49].

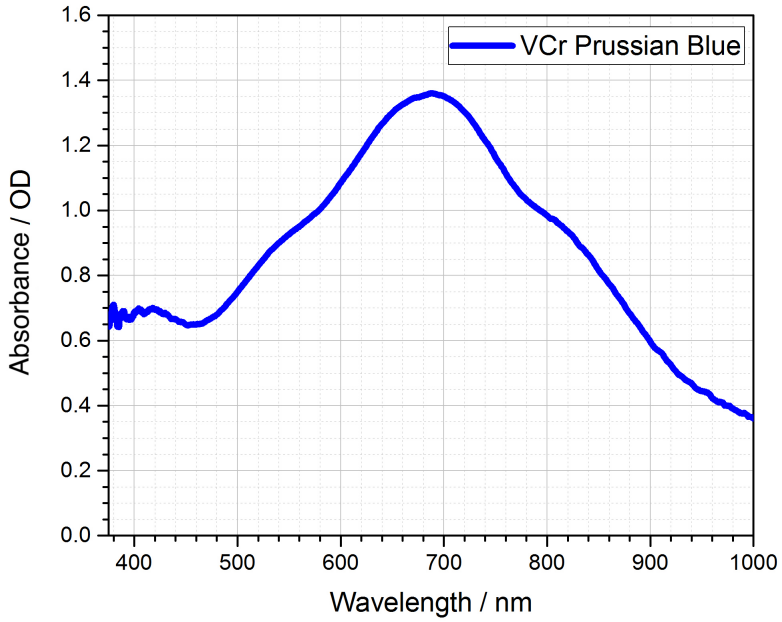


*Figure 3.11: The UV-Vis absorption spectrum of the VCr Prussian Blue showing a broad absorption from the two MM'CT transitions present due to the mixed oxidation state $V^{II/III}$.*

A previous study [34] of this material showed that time dependent density functional theory (TD-DFT), using the 6-311G(d) basis set, could be used to confirm the identity of bands in the visible. To simplify the infinite PB lattice, only a dimer of one $V(NC)_5$ unit and one $Cr(CN)_6$ unit which share a cyanide bridging ligand were considered. These calculations confirmed the presence of two non-zero oscillator strength transitions in the visible part of the spectrum, which are assigned to the two MM'CT transitions previously described. There was another transition which was found at 401 nm which corresponds to the $CN^-$ to Cr $t_{2g}$ orbitals, this transfers an electron from the cyanide bridging ligand onto the Cr ion, reducing it to $Cr^{II}$.

The FeCr Prussian Blue analogue is orange in colour due to a significant blue shift of the MM'CT transition. The absorption spectrum for a FeCr film has a single band at around 450 nm and is shown in Figure 3.12 [32, 33, 50].

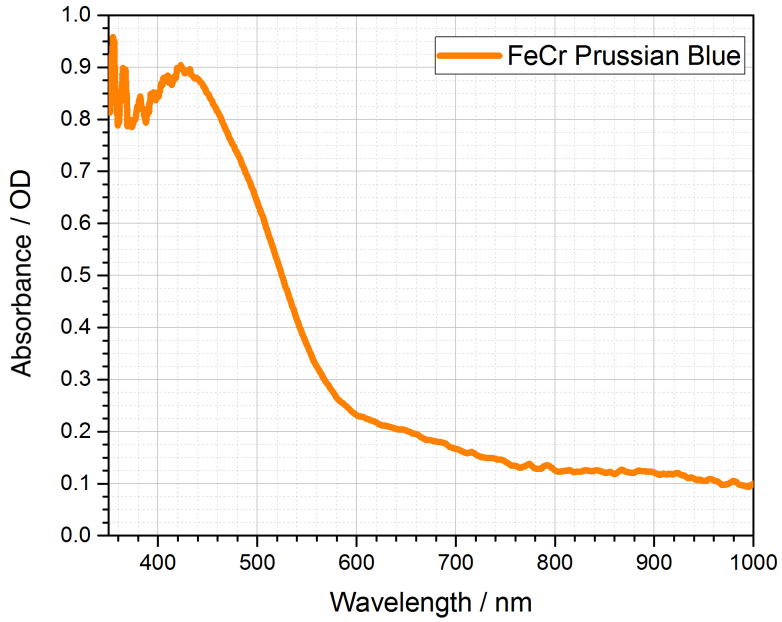


*Figure 3.12: The UV-Vis absorption spectrum of the FeCr Prussian Blue showing the absorption from the MM'CT transition at 450 nm.*

The CrCr Prussian Blue analogue is not strongly coloured at all with no significant structure to the absorption spectrum, implying that the MM'CT transition is shifted completely out of the visible and down into the UV region of the spectrum [32, 49, 51].

The relative energies of the MM'CT transitions observed in the optical absorption spectra show that the CrCr PBA (MM'CT in the UV) has the largest energy gap, followed by the FeCr PBA (MM'CT at 450 nm), then the VCr PBA (MM'CT at 540 - 670 nm) and finally the smallest energy gap of the FeFe PB (MM'CT at 690 nm). These are summarised in Figure 3.14. There is a large stabilisation afforded to the $Cr^{III}$ ion as this corresponds to a half-filled $t_{2g}$ set of orbitals relative to the $Cr^{II}$ resulting in the largest MM'CT transition energy.

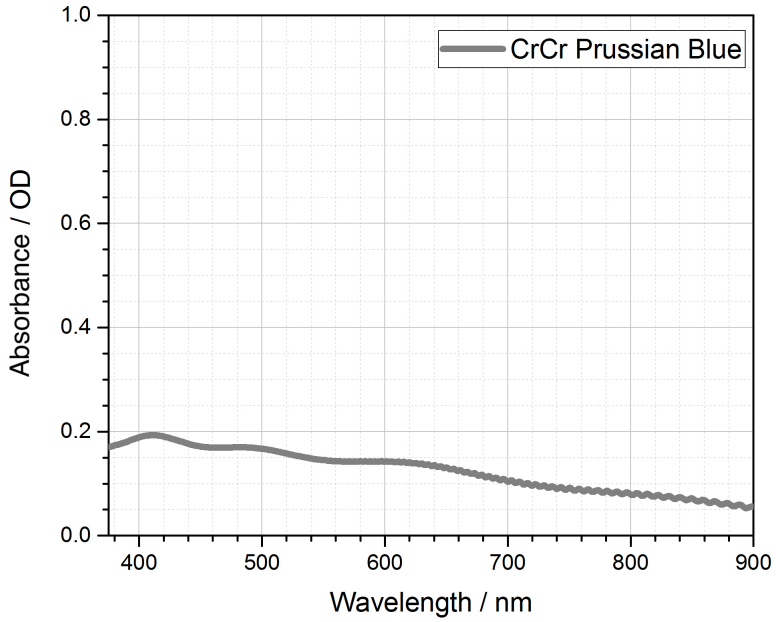


*Figure 3.13: The UV-Vis absorption spectrum of the CrCr Prussian Blue shows some poorly resolved peaks in the visible region. The oscillations in the near-IR are due to interference from the alignment of the sample and substrate in the spectrometer.*

The $Fe^{II}$ orbitals lie higher in energy than the $V^{II/III}$ due to the population of the orbitals, the 5 electrons in the $t_{2g}$ orbitals repel each other more than the 3 or 2 electrons in the $V^{II/III}$ orbitals. Then finally, the MM'CT for the FeFe PB has the smallest transition energy, this is due to a large stabilisation afforded to the full $t_{2g}$ set of orbitals for the $Fe^{II}$ ion. All of the spectra observed are in agreement with the available information from the literature.

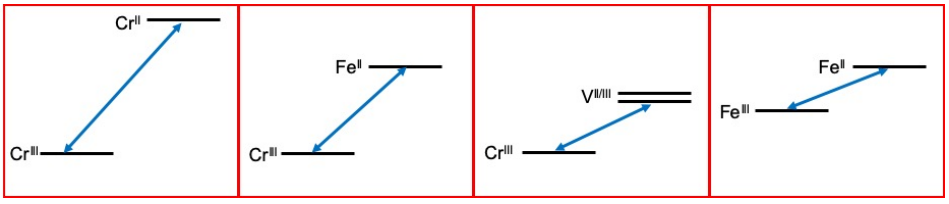


*Figure 3.14: A schematic of the relative energies of the MM'CT transitions according to the optical absorption spectra.*

### 3.3.2 Infrared Spectroscopy

The use of infrared spectroscopy has been a crucial first step in confirming the identity of the films that have been synthesised electrochemically. Infrared spectroscopy probes the stretching mode of the cyanide bridging ligand present in the Prussian Blue lattices. The strength of the cyanide stretch is used to inform on the electronic character of the metal ions at either end of the ligand, such as the electronegativity and the oxidation states. The available electron density on the metal ions is transferred to the ligand via $\pi$ back-donation which changes the bonding character of the cyanide bond. The region of interest for the cyanide stretch is 2000 - 2200 $cm^{-1}$ and does not overlap with any other vibrational modes present in the films so is a good choice for characterising the films. Each of the materials has a unique stretching frequency which allows them to be identified when compared with the literature values. All measurements were carried out on a Perkin Elmer Spectrum Two - UATR spectrometer for powdered samples, scraped from the surface of the electrode.

The VCr analogue has stretching frequencies [24] of around 2105 $cm^{-1}$ for the $V^{II}$-NC-$Cr^{III}$ moiety and 2115 $cm^{-1}$ for the $V^{III}$-NC-$Cr^{III}$ moiety, under aerobic conditions these shift to around 2165 $cm^{-1}$ where the vanadium ion is further oxidised to give the $V^{IV}O$-NC-$Cr^{III}$.

This oxidised band is typically always seen in these measurements, as shown in Figure 3.15, as it is often not possible to measure the spectrum within the time it takes the thin film to oxidise, so the band at lower frequencies is used to confirm that synthesis was successful.

The orange FeCr analogue of Prussian Blue has a cyanide stretching frequency around 2165 $cm^{-1}$ for the, as deposited, $Fe^{II}$-NC-$Cr^{III}$ moiety. However, this changes over time as a peak grows in at 2100 $cm^{-1}$ over the course of several hours, this corresponds to a rearrangement of the cyanide ligand to produce a mixture of this original configuration and the $Fe^{II}$-CN-$Cr^{III}$ moiety. This sample does not appear to be air sensitive so there is no issue with further oxidation.

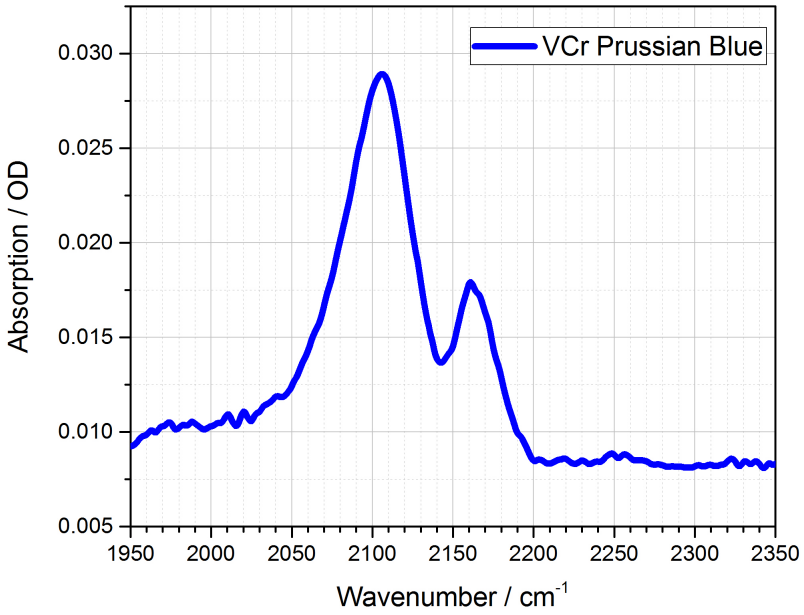


*Figure 3.15: The IR spectrum of the VCr Prussian Blue analogue showing the two peaks attributed to the cyanide stretching frequencies. The primary peak at around 2110 $cm^{-1}$ is from the $V^{II/III}$-$Cr^{III}$ stretch and the second peak at 2165 $cm^{-1}$ is due to the oxidised $V^{IV}$ species.*

This sample was studied by Coronado *et al.* [40] as a function of the applied pressure which resulted in a modification of the linkage isomerisation by inducing a lattice contraction. The resultant magnetisation is decreased.

The colourless CrCr analogue of Prussian Blue has a single cyanide stretching frequency, shown in Figure 3.17, of around 2185 $cm^{-1}$ corresponding to the $Cr^{II}$-NC-$Cr^{III}$ moiety. There is no indication of any air sensitivity or ligand isomerisation with this analogue.

### 3.3.3 Atomic Force Microscopy

Optimisation of the thickness and therefore optical density of the films was necessary for the spectroscopic measurements. The thickness of the films was measured with atomic force microscopy (AFM) as this technique is sensitive at the

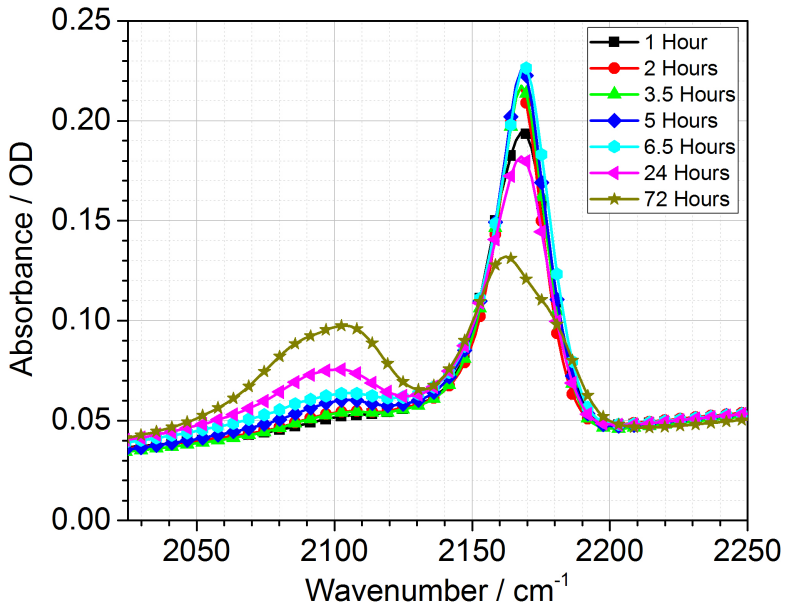


*Figure 3.16: IR spectra of the FeCr Prussian Blue analogue shows the decrease over time of the band at 2165 $cm^{-1}$ and the growth of the band at 2100 $cm^{-1}$ due to the isomerisation of the cyanide ligand. This has been studied as a function of pressure by Coronado et al. [40].*

range of thicknesses being produced, from 10's of nanometres up to a micrometer. AFM acquires an image by raster scanning the tip of the cantilever across the surface of the sample and measuring deviations in the height by monitoring the reflection of a laser from the back side of the cantilever with a position sensitive detector.

In this work, a Veeco Nanoman VS with Dimension 3100 controller was used to carry out the measurements and analysis was carried out using the NanoScope Analysis 1.5 program which allows the images to be viewed and various analytical procedures to be carried out such as smoothing, height profiles and roughness analysis. The sample is held in place on the surface of the instrument by a weak vacuum from below.

AFM allows the homogeneity of the films to be assessed on an individual crystal

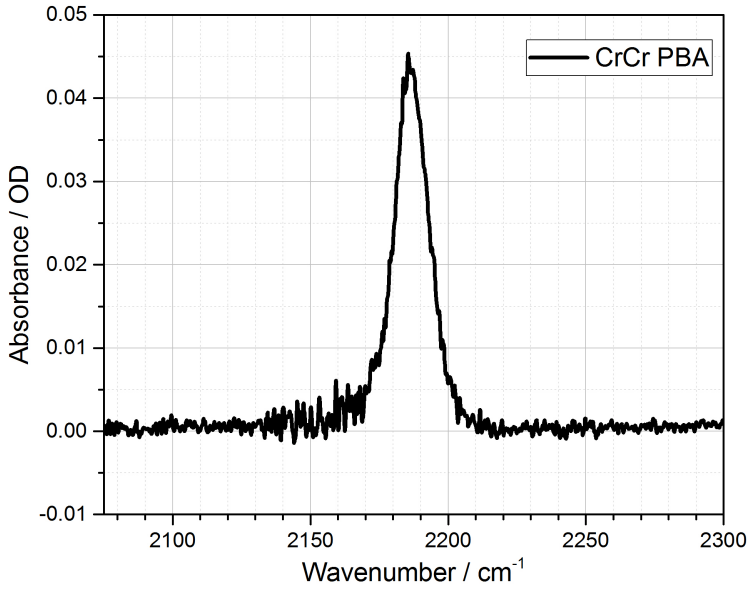


*Figure 3.17: IR spectra of the CrCr Prussian Blue analogue shows the band at 2185 $cm^{-1}$.*

scale; the average crystal size, crystal structure, film thickness and overall film coverage can be quantitatively studied in order to compare the different materials. The thickness analysis is carried out by drawing a razor blade across the surface of the film in order to remove the electrochemically deposited film, this 'valley' is then studied using the AFM tip. The difference in height between the surface of the substrate and the top of the crystals gives an estimate of the thickness of the film, this is typically studied over several cross-sections to increase accuracy. Figure 3.18 shows an AFM image obtained of the CrCr analogue.

For the VCr analogue it was not possible to prevent the films from oxidising so the AFM is carried out on oxidised films. We assume no significant changes in the film thickness due to this oxidation and the absorption of the films is measured before fully drying and being exposed to air. The other analogues are not air sensitive. The dependence of the absorption strength of all films as a function of film thickness was studied and shows a similarly linear relationship.

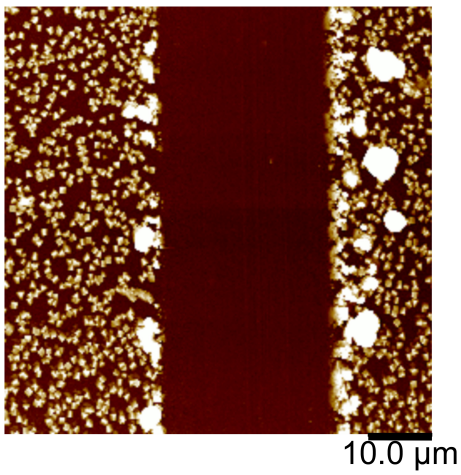


*Figure 3.18: An image obtained using AFM shows the 'valley' which is created by drawing a razor blade across the surface of the film with the crystals of CrCr PBA at either side.*

### 3.3.4 X-Ray Photoelectron Spectroscopy

X-Ray photo-electron spectroscopy (XPS) is a technique which allows the chemical composition of the synthesised films to be analysed. This method is sensitive to the oxidation states of the metal ions involved which is critical in terms of the properties that can be expected of a particular film.

Unlike the AFM, XPS is carried out under ultra-high vacuum which means that complete oxidation of the VCr film can be avoided by mounting the sample into the chamber when freshly made and allowing the film to dry under vacuum. Any small amount of oxidation which occurs at the surface of the film may be removed using ion bombardment. High energy argon ions ($Ar^+$) are focussed onto the surface of the film to ablate sections of the film. This can be carried out multiple times and the spectrum can be monitored after each bombardment to study the chemical depth profile of the structure. The elemental analysis of the VCr film does not show anything unexpected and all elements that are expected to be observed are seen.

The measurements we initially carried out on an XPS setup located at the University of Edinburgh, however measurements were subsequently carried

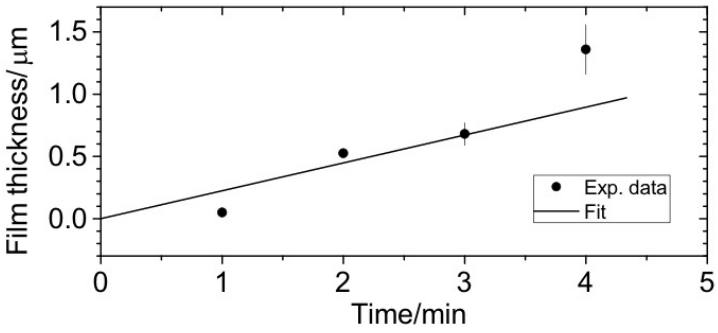


*Figure 3.19: A graph illustrating the linear relationship between the deposition time and the thickness of the deposited VCr film at the prescribed potential of -1.15 V.*

out at the NEXUS facility at the University of Newcastle. The CasaXPS software was initially used to aid with peak identification, subsequent analysis and fitting was carried out in Origin to determine relative abundances. Further analysis of the area under the curves can give us an indication of the elemental ratios and the positions of the peaks are indicative of the oxidation states present. This will allow us to assign a molecular formula to the deposited VCr material in order to interpret subsequent results. Each element has a specific sensitivity factor which must be taken into account before this comparison is made and the areas under the peaks are scaled relative to these factors.

## 3.4 Development of Time Resolved Magneto-Optical Faraday Effect Measurements

In this section the development of the experimental apparatus which was designed to allow the measurement of the time-resolved magneto-optical properties of the thin films samples will be discussed. The development of the optical setup will be described here first and then initial measurements that were carried out as proof of principle will then be discussed. The magneto-optical (MO) setup is built into the same beam path as the transient transmission, with

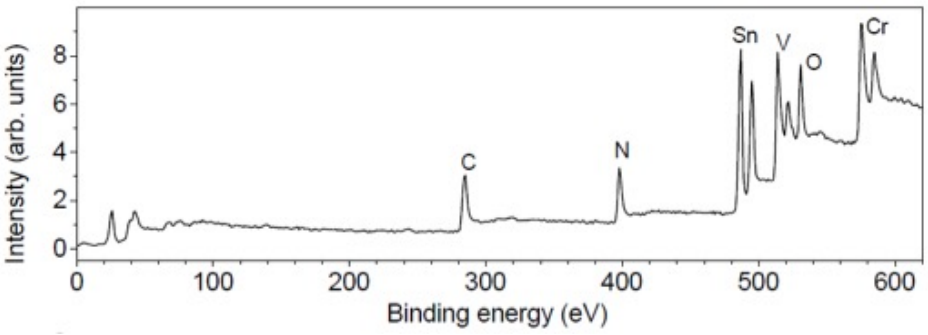


*Figure 3.20: The X-ray photo-electron spectrum of the deposited VCr material illustrates the elemental composition of the film. C and N are present as the cyanide ligands, V and Cr are the transition metals ions in the film and O is present as interstitial water in the lattice. Sn is seen due to the exposed FTO layer of the substrate which contains tin. The primary peaks for fluorine are found at higher binding energies than were studied in these measurements and the peaks for K are much smaller but can be found just above the C peak around 300 eV.*

a small number of important modifications to allow measurements of both types to be carried out with no realignment or rearrangement of optics required. The setup can simultaneously measure the transient transmission and magneto-optical response of a sample.

Figure 3.21 shows the beam paths of both the time-resolved and static MO measurements which use the femtosecond and CW laser outputs respectively (the preceding optics such as the delay line and the non-linear crystals are omitted for simplicity). In order to switch between these two laser sources a mirror on a flip mount is employed just in front of the focussing mirror for the probe beam path. In order to overlap the two beams as closely as possible between the poles of the electromagnet while using one directing mirror, the two beams must be spatially overlapped as closely as possible. This means that if the probe beam and the CW beam follow the exact same beam path then there is no realignment necessary after flipping the mirror.

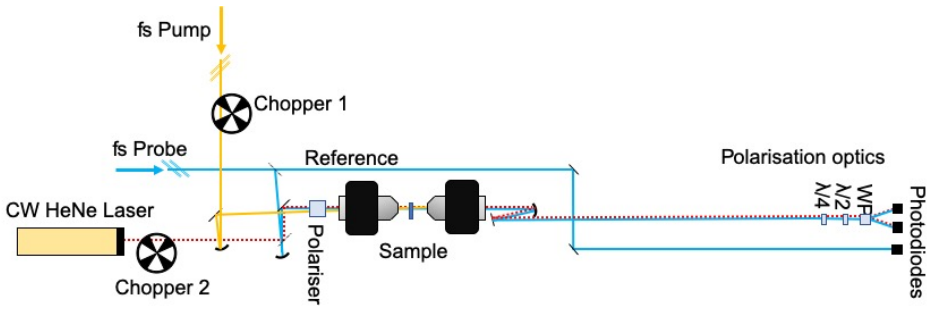


*Figure 3.21: The beam path and apparatus used in measuring the magneto-optical response of the samples. The blue/yellow lines correspond to the femtosecond laser beams and are used in the time-resolved experiments whereas the red dotted line is the (chopped) CW output of a HeNe laser which is used in the static measurements. (The polariser used to clean up the polarisation before the electromagnet is a Glan-Laser prism polariser (ThorLabs GL15) as this has a high extinction ratio. The half and quarter waveplates (ThorLabs AQWP05M-600 and AHWP05M-600) were achromatic waveplates with operating wavelengths of 400 - 800 nm.)*

The synchronisation of the optical chopper (ThorLabs MC2000B-EC) and the lock-in amplifiers (Zurich Instruments MFLI) is critical in order to be able to measure the relatively small variations due to the transient transmission and magnetic responses relative to the background variations in the intensity of the light sources. The chopper is used to modulate the pump beam to a given frequency, typically 500 Hz for the time-resolved measurements and approximately 995 Hz for the static MO measurements. This means that for the transient transmission measurements only every other pulse both the probe and pump pulses are present, only when these two beams are present should a 'signal' be considered. Conversely for the static MO measurements only light from the HeNe laser which passes through the sample in the magnetic field should be considered, at a frequency of 995 Hz. The frequency reference signals for these two measurement are passed on to the lock-in amplifiers which are used to isolate only these frequencies and therefore remove any noise, or scattered light from

other sources which could interfere with the measurements. The lock-in amplifier performs a multiplication of its input with a reference signal, a low-pass filter is then applied to the resulting waveform. This phase-sensitive detection isolates the signal at the frequency of interest and removes any signals at other frequency components. This reference signal is generated by the controller for the optical chopper and is sent directly to the lock-in amplifier for use in both the time-resolved and static MO measurements.

A CW HeNe laser source is used to measure the static magnetic response of the sample, this is used as a characterisation of the sample and its magnetic properties. Through the use of a variable magnetic field, generated by controlling the current passed through an electromagnet, it is possible to sweep the magnetic field experienced by the sample in order to measure the magnetisation versus field of the sample. In this way it is possible to measure the hysteresis loops of the magnetically ordered samples, this can be carried out at various temperatures in order to give an indication of the $T_C$ of the material. This is a non-destructive method of measuring these properties which hitherto would have been carried out in a SQUID magnetometer which requires the destruction of the electrochemically produced thin films.

The magnet is a GMW 3470 Electromagnet, which was purchased from the supplier with holes bored through the center of the poles with a diameter of 10 mm. The diameter of the holes was kept as small as possible as to not alter the magnetic field, yet to also allow the beams enough space to pass through the poles. The pump and probe beams are not parallel going through the magnet to allow for independent optimisation and overlap between the poles of the magnet. The spacing between the poles of the electromagnet can be varied from 0 to 75 mm but for this application was set to 26 mm. This allows the head of the cryostat to fit between the poles with the minimum amount of extra space, to maximise the strength of the magnetic field produced between the poles. Calibration of the strength of the magnetic field was carried out using a HGCA-3020 Hall probe

sensor which was placed in the center of the two poles. The sensor generates a voltage depending on the strength of the magnetic field and this can be monitored in order to study how the magnetic field varies with the current applied to the electromagnet. Linear sweeps of the field were carried out to mimic the field experienced by the sample during the hysteresis loop measurements. It was found that the greatest divergence of the observed magnetic field from the linear relationship was found around zero field and this decreased towards the maximum field strengths. At its maximum, the error was approximately 20 Gauss, or 2 mT which is less that 5% of the width of the VCr loop and this variation will not be taken into account given the inherent variability in the magnetic properties of the films. The power supply for the electromagnet is controlled by a LabView program which allows the current to be varied and the output from the lock-in amplifiers to be monitored and plotted immediately. This allows the user to instantly tell if the measurement is working correctly and assess viability of the sample and parameters used.

Once the light has passed through the sample it is then directed towards the photodiode detectors which have been discussed in a previous section.

Using a Glan-Laser polariser (ThorLabs GL-15), the polarisation of the light passing through the sample was cleaned up by removing any stray light at different polarisations. This polariser was selected as it possesses the highest extinction ratio of the available optics in the lab at 100,000:1.

The second polariser, or analyser, was placed after the electromagnet to study the polarisation of light that passes through the poles of the electromagnet. The analyser was gradually rotated and the intensity of the light was monitored using a laser power meter. The calculated ratio was approximately 1.5 x $10^4$ using this polariser, shown in Figure 3.22. This is the highest extinction ratio that was attainable using optics in the laboratory, so this will be used to clean up the polarisation of the light.

Before any measurements of Prussian Blue analogues were attempted, it

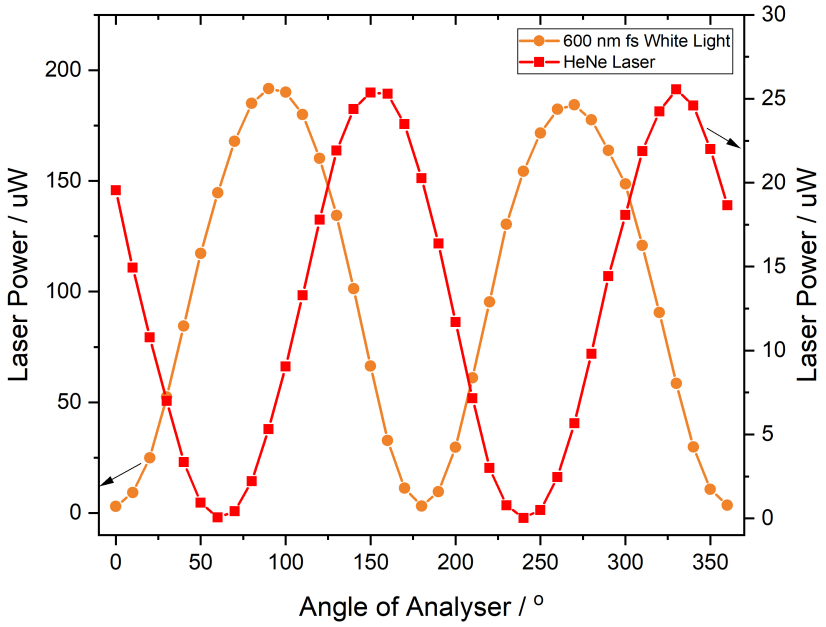


*Figure 3.22: The measured power of the femtosecond white light (600 nm filter) and the HeNe laser after passing through the Glan-Laser polariser as a function of the rotation of the analyser. The extinction ratio is defined as the ratio between the highest and lowest intensity.*

was important investigate the 1 mm thick FTO coated glass which may also show a magneto-optical response. The measurements which require cryogenic cooling were carried out within the cryostat, so the response of the cryostat windows was also characterised. The measurements were set up and carried out using the same parameters as used for the samples.

Figure 3.23 illustrates the magneto-optical response of the substrate and the cryostat windows. These materials display some paramagnetic response which is a linear dependence on the applied magnetic field. As this background is linear, it can be easily subtracted from the rotation measurements in order to more clearly observe the magnetic response of the sample. Crucially, the magneto-optical ellipticity response of the background is orders of magnitudes smaller than that of the rotation, for this reason the ellipticity often proved more

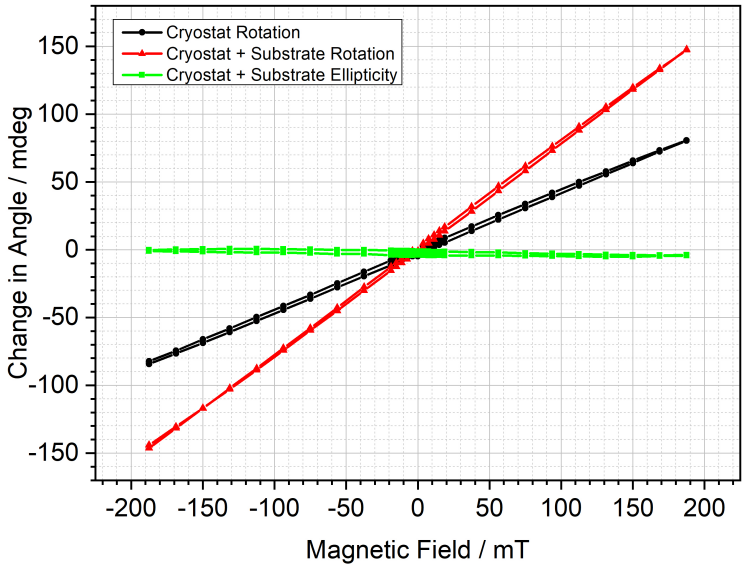


*Figure 3.23: The observed magneto-optical response from the substrate and the cryostat windows. These measurements were used to confirm the behaviour before the Prussian Blue analogues were introduced.*

useful for studying the samples.

In order to characterise the setup been built in the University of Edinburgh laboratory, a pre-characterised sample was sent by a collaborator at the University of Leeds, Dr Oscar Céspedes. The samples were two multilayered thin films comprised of four metallic layers of a few nanometer thickness, Ta (4 nm) | Pt (3.5 nm) | Co (X nm) | Pt (5 nm). The difference between the two samples was the thickness of the Cobalt layer, sample 1 had X = 1.04 nm and sample 2 had X = 1.2 nm. These samples were fabricated in order to maximise the perpendicular magnetic anisotropy (PMA). This means that the magnetic moment of the sample is favoured out of the plane of the sample. Given that the measurement was set up to operate in transmission with the magnetic field in the direction of beam propagation, this would mean that the experiment is best suited to measure a sample of this nature. The samples were independently characterised in terms of their coercive field, $H_C$, at the University of Leeds by magneto-optical Kerr effect

spectroscopy. $H_C$ was determined to be 10.2 ± 0.5 mT and 11.5 ± 0.5 mT for sample 1 and 2 respectively.

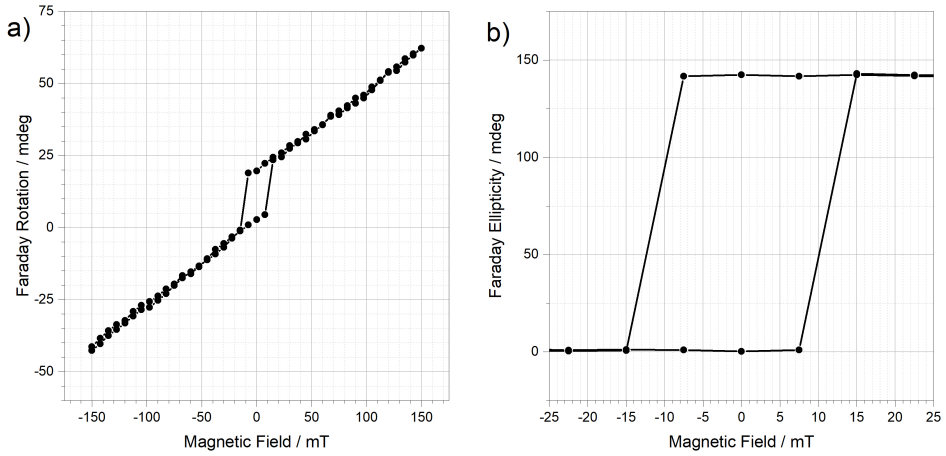


*Figure 3.24: The magneto-optical response of the second Ta | Pt | Co | Pt PMA calibration sample measured using the magneto-optical Faraday rotation, a), and ellipticity, b), techniques carried out in the lab at the University of Edinburgh. The $H_C$ of the sample was measured to be approximately 11 mT using a scan rate of 1.5 mT $s^{-1}$ and no subtraction of background contributions were made.*

The measurements was carried out by first thoroughly aligning the HeNe beam, particular care was taken to make sure that the beam was perpendicular to all of the polarisation optics and the sample. It was found that the alignment of the beam is critical to the measurement working correctly and the correct response being recorded. The measurement was carried out using the HeNe laser as this is easier to set up and was used to characterise unknown samples. The HeNe laser power was attenuated to approximately 5 $\mu$W to reduce the amount of scattered light from the sample. The observed $H_C$ of approximately 11 mT was very close to that which was measured by our collaborators in Leeds. The hysteresis loop for this sample is shown in Figure 3.24. This gives confidence that the values that are obtained with this newly constructed magneto-optical setup are indeed accurate and the setup is functioning as intended.

As a next step, a thin film of Ni was created by electron beam evaporation on to the surface of a glass cover slide. The film was approximately 10 nm thick, measured using a quartz crystal balance employed during the deposition of the sample under a constant deposition rate. The static Faraday rotation and ellipticity as a function of the applied magnetic field were then measured.

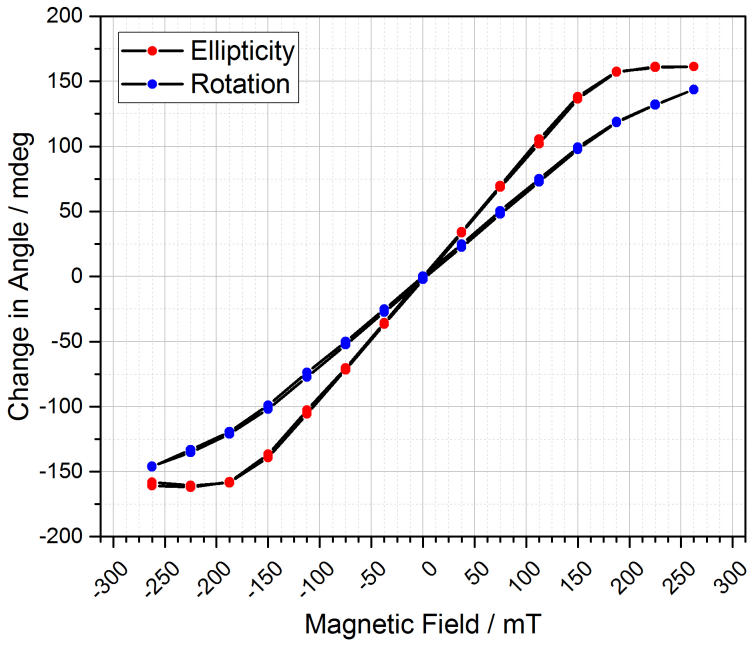


*Figure 3.25: The observed Faraday rotation and ellipticity response of the Ni thin film with variation of the magnetic field. There is clearly a magnetic response in the ellipticity measurement however there is no observed coercivity, indicated by the loop not opening up.*

The MO signal of the Ni film did not exhibit a hysteresis loop which was thought to be due to the magnetisation resting primarily in the plane of the film, which is perpendicular to the direction of the applied magnetic field. There appeared to be some contribution from the underlying substrate due to the relatively thin sample compared to the thickness of the substrate. There was however some magnetic response that was observed in this work, seen as the non-linearity of the magnetisation versus field plots, which suggests that a time-

resolved response of the ultrafast demagnetisation could possibly be observed. This was next attempted with the aim to reproduce the observed response seen by the group of Jean Yves Bigot in 1996 and in subsequent work.

Once the beam had been satisfactorily aligned onto the PD detectors, the sample and a bandpass filter were introduced in order to study the intensity of light at one wavelength of interest. In this case the measurement was carried out at 632.8 ± 2 nm (ThorLabs FL632.8-10, FWHM = 10 ± 2 nm) as this most closely matches the 620 nm that was used in the literature. The magnetic field was off while the zero signal was set on the photodiodes by rotating the wave-plate to generate polarisation at 45°. This leads to an equal intensity of light being generated in both arms which are output from the Wollaston prism. From here, a magnetic field of 250 mT was applied in one direction. This results in a non-zero signal which is caused by a shift in the rotation of the polarisation due to the magnetic field (this is confirmed by reversing the field direction to give a signal of opposite sign). This new signal which was seen when the magnetic field is applied constitutes the time zero signal, then when the 400 nm pump pulse was applied with a power of 5.3 mW the magnetisation is modified.

The Faraday rotation measurement shown in Figure 3.26 appears to show an influence of the magnetic field on the direction of the observed signal, but in order to obtain the demagnetisation, the signal for one field direction should be subtracted from the other in order to remove any non-magnetic signal. The measurement in zero field was carried out to confirm the absence of a response when the material is demagnetised out of the plane of the sample. The corrected Faraday rotation response is shown in Figure 3.27 with a fast sub-picosecond demagnetisation of the sample followed by a slow decay.

The decay dynamics were able to be fitted with a single exponential decay plus an offset, $\tau_1$ in this case was approximately 2.5 ps. With respect to the magnitude of the loss of magnetisation, the change in angle measured by the difference between the two field directions is approximately 190 mdeg. From the

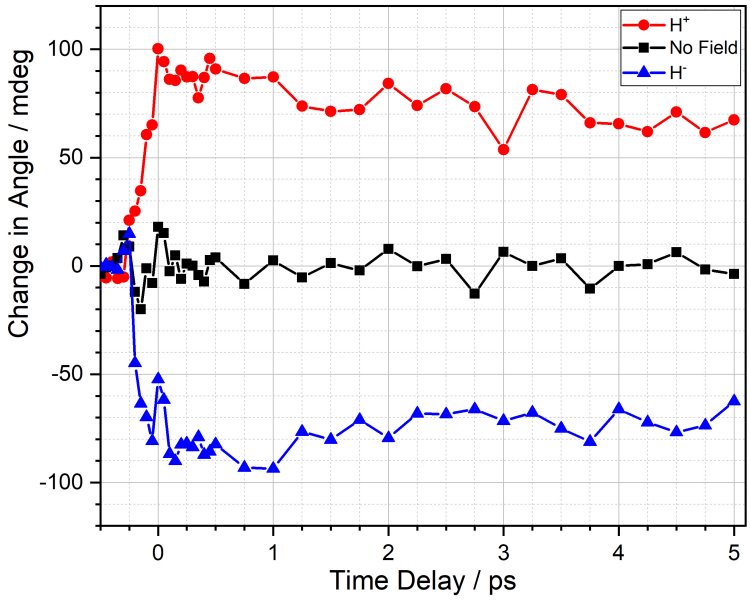


*Figure 3.26: The observed time-resolved magneto-optical response of the Ni thin film in a field strength of ±260 mT which equates to a current of ±3.5 A. A measurement was also carried out in zero field which shows no significant response.*

static measurement in Figure 3.25 a total magnetisation is able to be determined to be 330 mdeg, by subtracting one field direction from the reverse field. This means that when pumping with 400 nm light at 5.3 mW, a loss of magnetisation of around 57% of the total signal is achieved. Measurements in the literature typically see a faster recovery of the magnetisation than is observed in these measurements. This could not be visible in these measurements as the effective pulse duration is much longer than expected due to the introduction of the Glan-Laser polariser before the sample. This inhibits the ability to determine processes which occur on very fast timescales such as the initial demagnetisation. The experimental procedure however appears to be sound as the results are generally in good agreement with the literature. This technique can then be applied to functional inorganic materials such as the Prussian Blues.

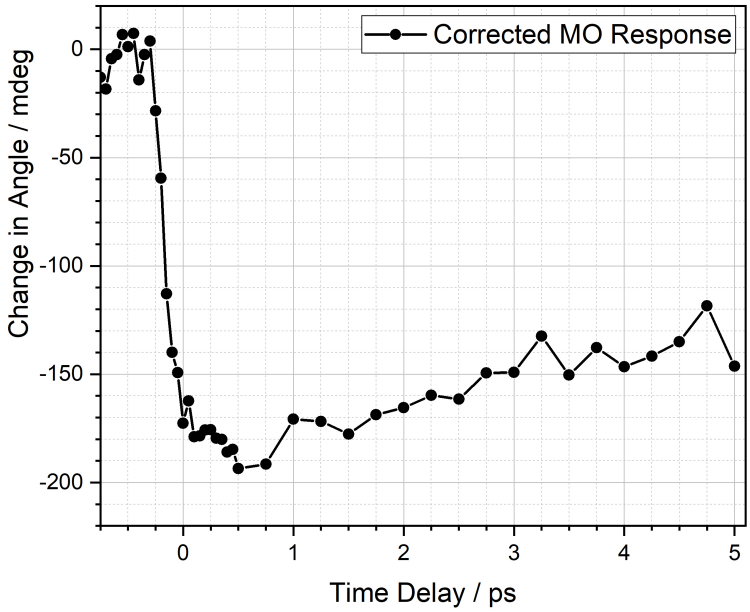


*Figure 3.27: The corrected time-resolved magneto-optical response of the Ni thin film in a field strength of 260 mT. The difference between $H^+$ and $H_-$ transients in Figure 3.26 is the true signal that remains is the true magnetic response to the excitation.*

In order to test these measurements on the functional materials which are of interest in this work, a further test measurement was carried out on the VCr PBA. This material has been previously studied by Johansson *et al.* [34] and this will serve as a proof of principle that these techniques can successfully be applied to inorganic materials which require cryogenic cooling in order to observe a magnetic response. This also allowed the films that were synthesised at the University of Edinburgh to be fully characterised using magneto-optical measurements which study the magnetic properties of these materials in a non-destructive way.

Magnetic hysteresis was measured using the same experimental parameters as for the Ni thin films to determine the magnetic coercivity of the films prior to using time resolved techniques. The static measurement of the Faraday rotation at 77

K yields the response shown in Figure 3.28, which shows a magnetic coercivity, $H_C$, of approximately 50 mT.

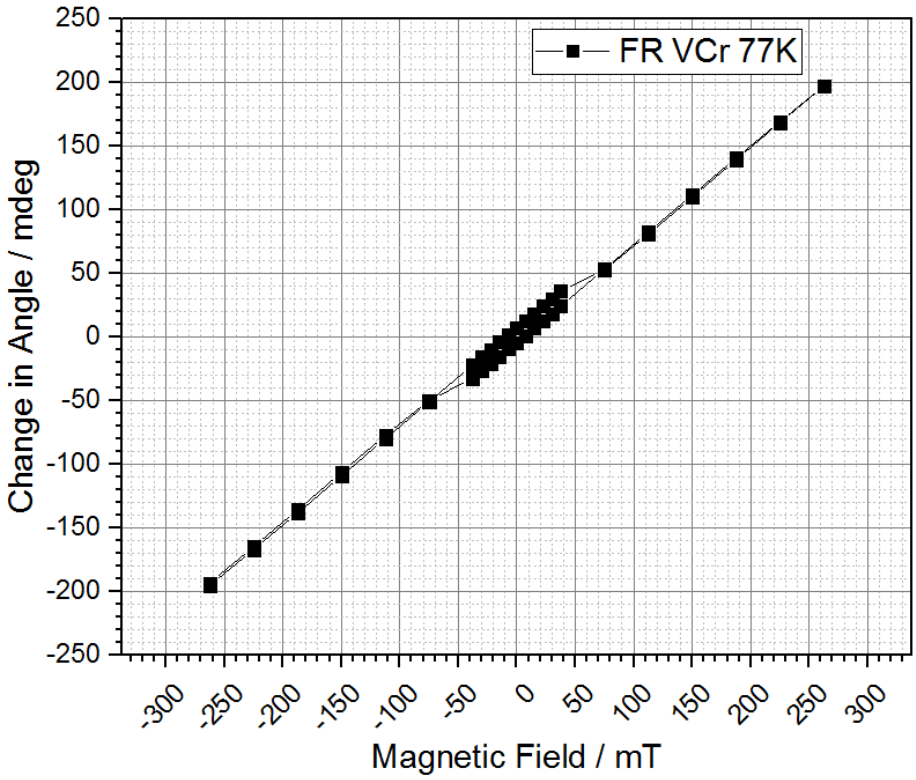


*Figure 3.28: The Faraday rotation of the thin film VCr sample measured at 77 K as a function of the applied magnetic field. The hysteresis loop is superimposed on a linear background which is thought to originate from the substrate, this can be subtracted to yield the loop.*

At this point, the experimental parameters were optimised in order to measure the magnetic properties more closely. The measurement step size was first varied, which affects at what point the magnetic response is recorded but also impacts the effective scan rate experienced by the sample.

The smaller step size appears to more closely track the changes in signal, as displayed in Figure 3.29, but this must be balanced with the time it takes to carry out the measurement and the waiting time of the lock-in amplifier. The waiting time for the measurement (and in turn the lock-in amplifier) was studied separately in order to determine the optimum speed to carry out these

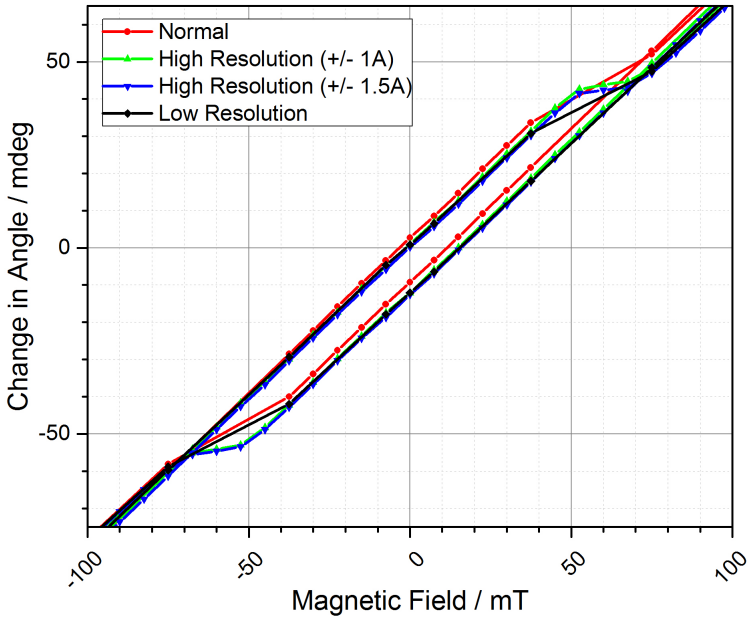


*Figure 3.29: The observed Faraday rotation measurement as a function of the step size controlled by the LabView program used to automate these measurements. This allows the value of the hysteresis to be obtained more accurately. These settings however, vary with the identity of the sample being studied and must be adjusted to fit the observed response.*

measurement. The balance between a fast measurement which minimises the long term drift of the setup due to temperature fluctuations and a slow measurement where the scans are prohibitively slow and time consuming. The measurements were started at a very long waiting time of 10 seconds per point, this gave a very clean measurement of the magnetic response around 50 mT but introduced a diversion from linearity at the very end of the measurement. This was often more obvious when the experimental apparatus had not been give sufficient time to settle and was helpful in determine the correct amount of time given for equilibration. However these measurements took over 5 minutes, especially when a wider range scan was required, and it was found that this very long term drift could be avoided by increasing the scan speed, with no discernible deterioration

in the observed signal. This held true until the waiting time was taken below 3 seconds per point at which point the signal began to deviate from the previous measurements significantly.

Due to the large linear contribution from the glass substrate measured with the Faraday rotation, it proved beneficial to measure the Faraday ellipticity of the sample. The basis of the two measurements are slightly different, the Faraday rotation signal results from a change in the index of refraction of left- and right-handed polarisation whereas the Faraday ellipticity comes from a change in the relative absorption of left- and right-handed polarisations. As the substrate shows a comparable refractive index to the sample, relative to the background air this signal can be lost in the signal from the substrate. The difference in the absorption however, between the sample and the substrate/background is much larger and therefore this offers greater sensitivity when studying the response from the sample itself.

The Faraday ellipticity is shown in Figure 3.30 and shows a much stronger magnetic response relative to the linear background, with a simple subtraction of this background it is possible to observe a clear hysteresis loop with a coercive field of approximately 60 mT. This value was interestingly among the largest value of $H_C$ that has been previously recorded in the literature, with previous values ranging from 1 mT [48], 2.5 mT [24] and up to around 10 - 20 mT [52] with the use of different alkaline metal cations (in this case Cs in place of K). The origin of this augmented coercivity is attributed to the electrochemical cycling of the films in a solution of KCl immediately after deposition.The insertion of the additional $K^+$ could introduce some anisotropy into the crystal structure which may cause some strain in the system. It has been found that the survival rate of these films was improved significantly following electrochemical cycling, the irreversible oxidation of the films appears to be slowed which facilitates the sealing of the films using super glue. This was then noticed that over the course of many separate measurements on different occasions there was a significant

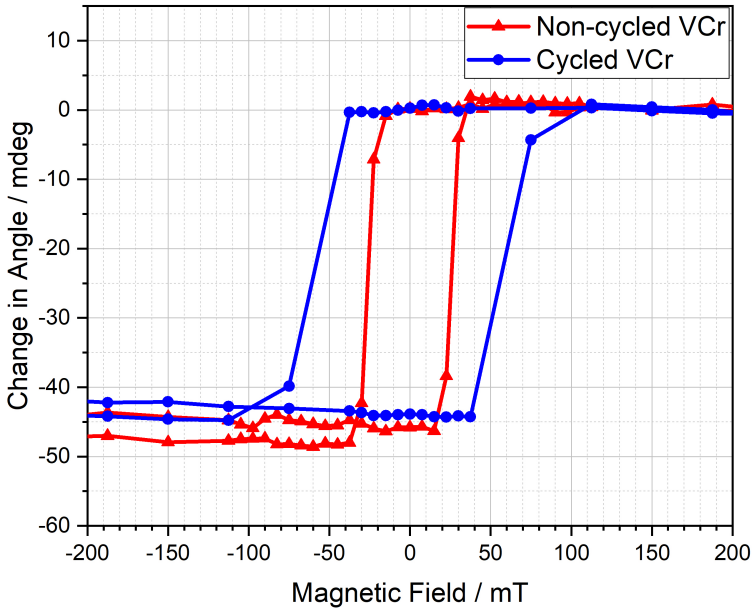


*Figure 3.30: The static Faraday ellipticity of two VCr samples measured at 77K. One of the films was cycled in KCl post synthesis in order to incorporate more potassium counter ions into the structure. The observed coercivity, $H_C$, is increased after the insertion of more potassium ions.*

improvement in the $H_C$ of the films that had been cycled versus those that had not. This became evident during an undergraduate project student's work and is currently undergoing a more methodical analysis to study this as a function of cycling and the resulting oxidation state ratios of the films produced.

Again, the waiting time of the measurement was varied in order to study the impact this had on the observed response to the magnetic field, shown in Figure 3.31. The width of the hysteresis loop is shown to depend strongly on the measurement waiting time.

The optimum waiting time for these measurements appears to match with what was determined for the rotation measurement also. At longer waiting times, the measurements are influenced by a greater long term fluctuations due to thermal drift in the laser.

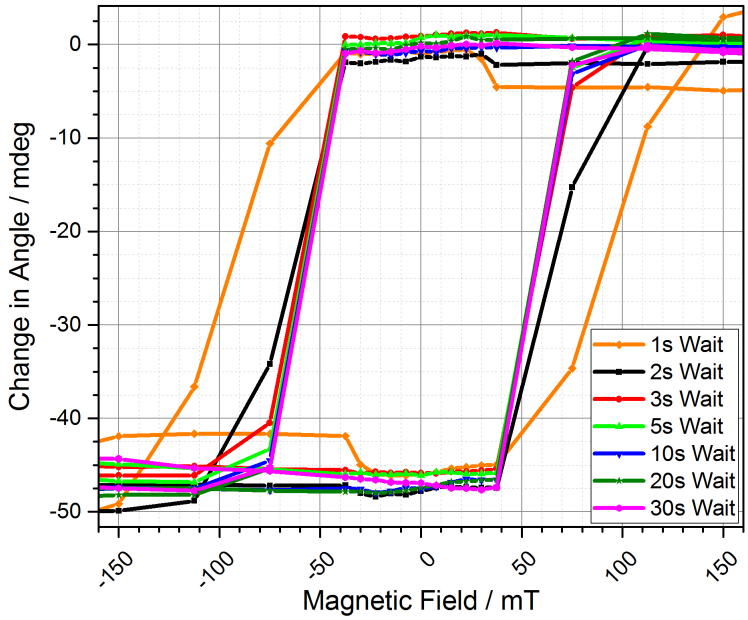


*Figure 3.31: The variation of the observed hysteresis loop measured using Faraday ellipticity of the VCr PBA.*

At this point, the experimental setup could be used to characterise the films, in terms of the coercive field ($H_C$) and Curie temperature ($T_C$). The ability to reliably measure these parameters in situ allows for a much easier optimisation of synthesis condition and more usefully the characterisation of brand new samples which have unknown magnetic properties. These studies were carried out by measuring the hysteresis loops at increasing temperatures. This allowed a measurement of the magnetic response as a function of temperature to be obtained to give an idea of the magnetic properties of the films.

Figure 3.32 shows the temperature dependence of the $M_S$ of typical VCr PBA films synthesised at the University of Edinburgh. The $T_C$ of these films has never been observed at room temperature which is due to the exact ratio of $V^{II}$:$V^{III}$. It was not a priority to reach the highest ordering temperatures in this work, only to use the VCr as a model system for the time resolved studies.

In a similar fashion to the Ni thin films, once it had been shown that

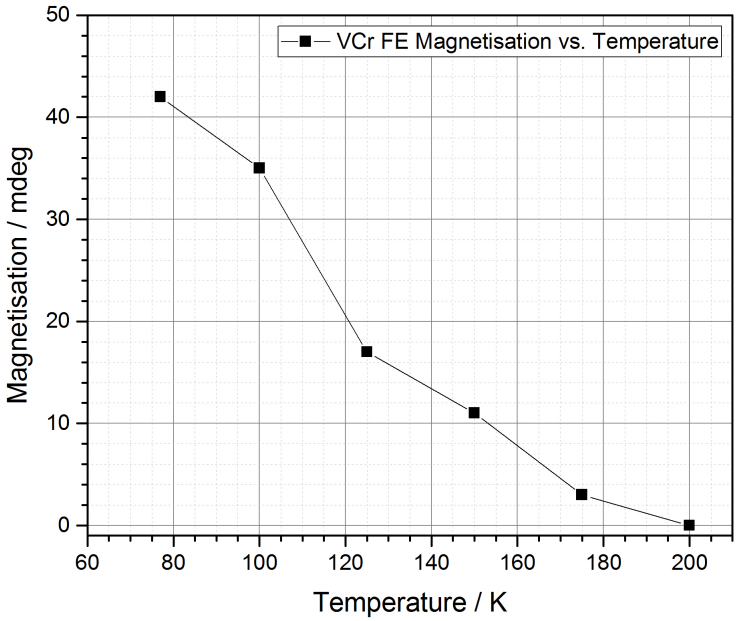


*Figure 3.32: The temperature dependence of the saturation magnetisation, $M_S$, of the VCr PBA thin film appears to show a $T_C$ of around 200 K. This is significantly lower than the highest values observed for this material but a higher $H_C$ has been recorded in this work.*

a clear, reproducible magnetic response could be measured using the magneto-optical setup, it was decided that it would be a useful exercise to reproduce the time-resolved MO study of this material that was carried out by Johansson *et al.* [34].

The alignment of the laser was checked before and during all of the measurements in order to measure the response correctly, the measurements of Johansson *et al.* were kept in mind at all times but also the time-resolved transmission measurements that have been conducted independently and more recently on this same optical setup. Typically a transient transmission measurement was carried out first in order to optimise signal of the sample, given that there is a long-lived bleach of the ground state that can be used to easily find the spatial and temporal overlap more easily than attempting this with the MO measurement. The probe

light was again balanced after inserting the sample and the red bandpass filter (632.8 nm) using the half wave-plate. The magnetic field was then applied at the maximum strength of 300 mT and the measurement was carried out.

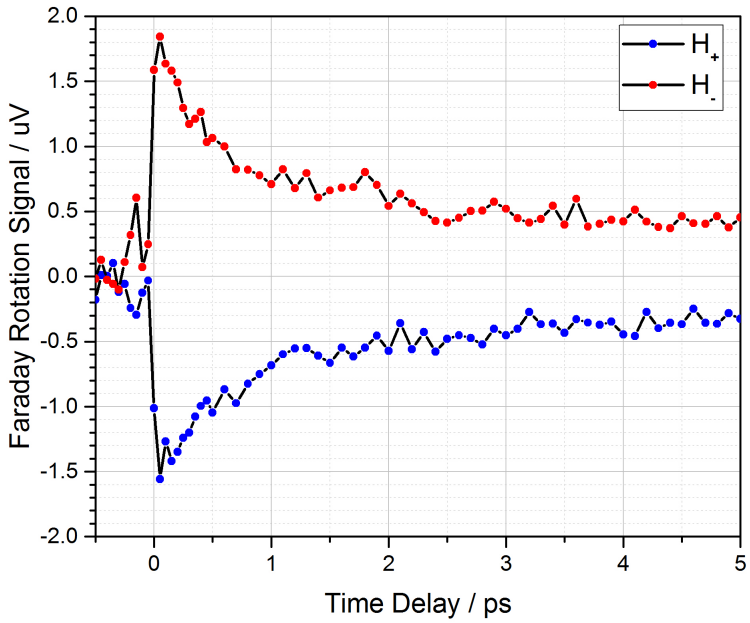


*Figure 3.33: The initial time resolved magneto-optical Faraday rotation response of VCr PBA upon excitation at 400 nm and probing at 632 nm. The transients show a signal of the opposite sign when the field is inverted, the magnitude of the two signals is approximately the same in each field.*

Figure 3.33 shows the time resolved magnetic response of the Faraday rotation upon excitation at 400 nm and 0.8 mW. The polarisation used was vertical. The sample that was studied was approximately 150 nm thick in order to reduce scattered light as much as possible. The initial signal rise and the subsequent decay of each of the signals appears to resemble the kinetic traces presented in the literature and transient transmission kinetic traces observed in our own measurements. If the origin of the magnetic signal is a result of the super-exchange interaction between the $V^{II/III}$ and the $Cr^{III}$ then the decay dynamics should follow the recovery of the ground state as observed in the

transient transmission measurements. There also appears to be an additional feature during the rise time of the signal which has been typically seen when the film is damaged due to the intensity of the light.

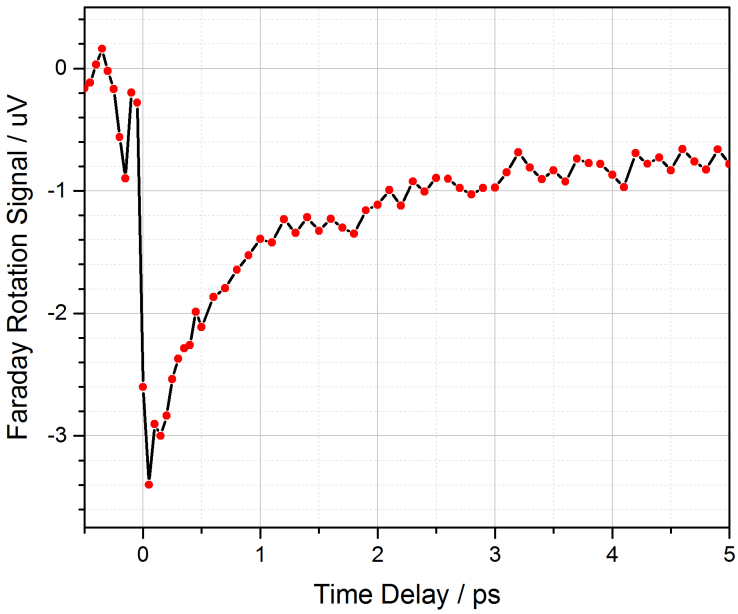


*Figure 3.34: The corrected magneto-optical Faraday rotation response of VCr PBA upon excitation at 400 nm and probing at 632 nm as a result of subtracting one field direction from the other. The small spike which appears before the main signal rise is indicative of the start of the degradation of the sample.*

Figure 3.34 shows the real magneto-optical response of the VCr PBA once the correction has been made by subtraction of one field direction from the other. There is a fast initial decay followed by a slower second decay constant which is visible over the time range that was measured in this experiment. The decay appears to match the observed ground state bleach of the MM'CT transition, previously reported for this material and more recently studied in the work outlined in this thesis. This indeed corresponds to the recovery of the ground state which would correlate to the recovery after photoinduced demagnetisation.

These techniques were also applied to the CrCr analogue as this material

possesses a $T_C$ of approximately 200 K, depending on the exact stoichiometry. This crucially also allowed measurements to be more easily carried out using liquid nitrogen as opposed to the much larger expense when using liquid helium. The static Faraday rotation measurement was carried out in order to measure the hysteresis loop of the sample at 77 K.

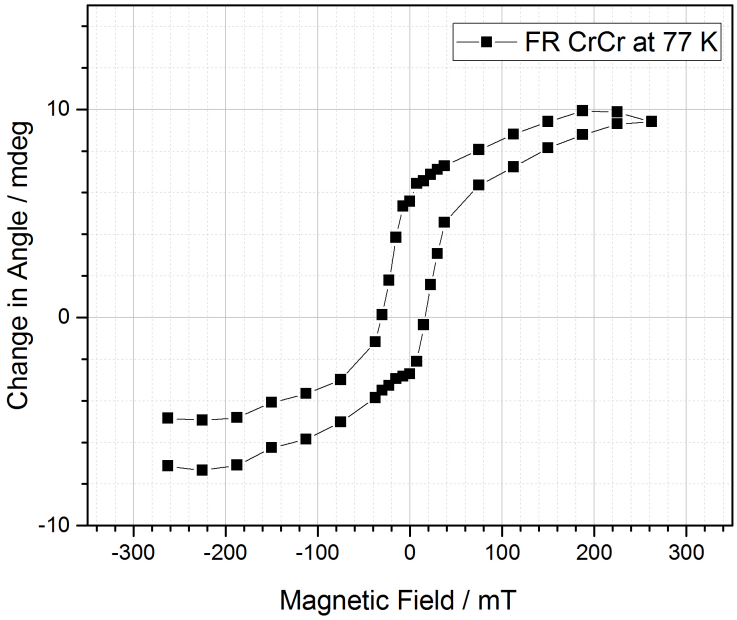


*Figure 3.35: The magneto-optical Faraday rotation response of CrCr thin film measured at 77 K. There is a significant amount of drift in this measurement which makes the extraction of exact values unreliable but the setup is definitely able to measure these samples to a relatively high degree of accuracy.*

The M vs field measurement of the CrCr analogue is shown in Figure 3.35 and shows a much narrower coercive field when compared with the VCr, but the value matched well with the literature value for the CrCr analogue. The separation of the start and finish of the measurement is due to a thermal drift in the laser polarisation. The thermal stability of the laser is improved through the use of the laser enclosure which was constructed to this end. When measurements are being carried out, as much of the laser enclosure as possible is closed to combat

air currents and scattered light.

The ability to measure the magnetic properties of these materials therefore allowed the characterisation of the temperature dependence of the magnetisation to be studied. The Faraday rotation measurements were carried out as a function of the temperature, this was carried out on a single day where the stability of the cryostat was favourable. The saturation magnetisation was measured for each of these measurements at intervals of approximately 25 K from the base temperature of liquid nitrogen, 77 K.

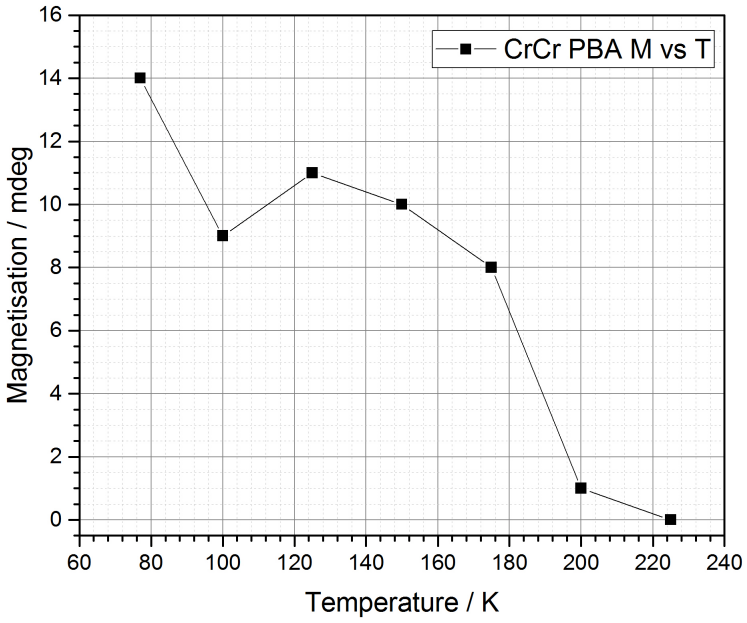


*Figure 3.36: The observed temperature dependence of the saturation magnetisation of the CrCr Prussian Blue analogue.*

Figure 3.36 shows the CrCr analogue's temperature dependence of the saturation magnetisation of the CrCr PBA. The observed $T_C$ was found to be approximately 220 K which is well within the range of Curie temperatures reported by [25] of 135 to 260 K which vary as a function of the Cr oxidation states.

The same measurements were attempted on the FeCr PBA, however

these attempts were unsuccessful. The much lower expected Curie temperature of these materials, around 20 K, means that it is not possible to use liquid nitrogen in these measurements, but liquid helium instead. This added a greater expense and complexity to the measurements which meant that many repeat measurements were not possible. Studies of the FeCr analogue are ongoing now with an improved understanding of materials and particularly of the measurements.

Unfortunately the measurements subsequently became very unreliable and did not appear to be working correctly. The main issue with the measurements was that the effect of reversing the magnetic field was no longer visible. Instead of the expected behaviour the first field direction applied would exhibit the usual response, ie. a demagnetisation recovery as was previously seen. However when the magnetic field was switched off and applied in the reverse direction, then the measurement exhibited a zero magnetic response or in much rarer cases there was an identical response but at a lower magnitude. In order to resolve this issue then a variety of attempts were made to find the root of the issue.

The first thing that was investigated was the method employed for balancing the photodiodes before a measurement is carried out. Instead of the usual method of balancing in zero field and subsequently applying the field, the measurement was balanced in one field direction. In this way the balancing was done for certain in a given field, as opposed to when balancing was carried out in the absence of a magnetic field where it was unknown what remnant magnetisation remained in the sample after removal of the external field. This unfortunately did not resolve the issue, so testing was continued.

The measurements were carried out again but this time the strength of the applied magnetic field was reduced, it was thought that an excessive magnetic field could lead to complications when the field is reversed, making it more difficult to observe reversal of the magnetisation. Again this was found to offer no resolution to the issue, there was however a reduction in the magnitude of the signal that was observed in one field direction as was expected. There remained no reversal of

the magnetisation for this measurement.

At this point it was considered that there may have been a change in the nature of the film and it's magnetic properties which resulted in the change in the magnetic response under changing magnetic fields. The measurements were repeated using freshly deposited samples being careful with the synthesis to follow the protocol as closely as possible. There was again no change with the behaviour of the time resolved measurements, so further critical analysis will be continued to understand the origin of this issue.

Unfortunately this issue was not resolved within the scope of this work but was attributed to natural defects in the films which result in the trapping of the spin states within, measurements were attempted using freshly made samples but this issue was not changed. To understand these problems and hopefully to solve them, efforts are ongoing employing new samples in order to thoroughly characterise the experimental setup.

# Chapter 4

# Results

## 4.1 Electrochemistry and Spectroelectrochemistry

### 4.1.1 Electrochromic Switching in the Vanadium-Chromium Prussian Blue Analogue

#### Introduction

The VCr PBA is of great interest as a functional material due to the high $T_C$ and as a member of the Prussian Blue family of compounds it was thought that the VCr analogue may exhibit electrochromic properties. From the literature it was known that a colour change does occur when the film is exposed to air for any period of time. It was assumed that this was due to the oxidation of one or more of the metal centres present in the material; the $V^{II/III}$ or the $Cr^{III}$ ions. In order to understand the redox chemistry at work here, a spectroelectrochemical study was conducted as part of understanding the electrochemical deposition of the material. It was shown that the redox chemistry of the metal centres, and therefore the optical properties of the films can be modulated using electrochemical potentials. This work has been published [46] and the paper is presented in Appendix 1.

The colour of the film can be reversibly switched from blue to black, as shown in Figure 4.1, through the application of alternating electrochemical

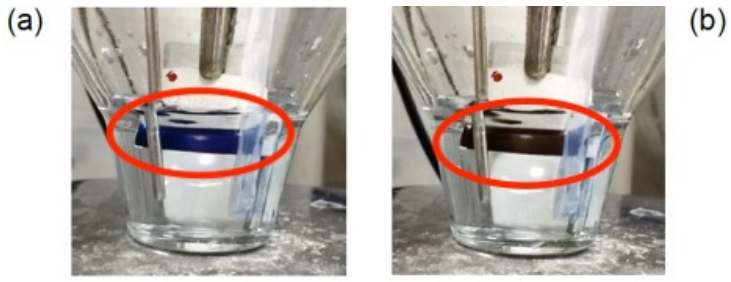


*Figure 4.1: The reversible change in colour from blue to black of the VCr PBA by electrochemical reduction, caused by a red-shift in the MLCT transition. The film is exposed to electrochemical potentials vs. a saturated calomel electrode (SCE) of 0 V (a) and −1.2 V (b).*

potentials.

The ability to control the colours of these functional materials shows the potential for them to be used in devices such as electrochromic windows, mirrors, sensors or light modulators. In the latter case, additional magnetic ordering of the materials would allow for modulation of the polarisation of the transmitted light via the Faraday effect. This would also require the materials to be transparent and deposited on to a transparent substrate. In this work, transparent thin films of the VCr PBAs were deposited on conductively coated glass substrates and the spectroelectrochemical properties of the material were studied in order to further understand the charge-transfer processes occurring in this family of molecule-based functional materials.

**Synthesis and Characterisation**

The synthesis of the VCr thin films was carried out in the same way for these studies as for those used in the ultrafast measurements, described in Section 3.2.1, earlier in this thesis.

During the analysis of the electrochemical deposition of the VCr PBA it was observed that when a reducing potential of approximately −1.2 V or more is applied to the material, the colour is switched from blue to black. This process

was reversible, by alternating between values of −1.3 V and 0 V vs. SCE to drive the redox process in either direction. Little to no degradation of the films was observed over the course of approximately 20 reduction-oxidation-reduction cycles with a waiting time of 15 seconds at each potential. Previously it had been noted that when an oxidising potential was applied, or even exposure to air, the material lost its strong blue colour and became colourless [52]. For this reason, the films are considered unstable in air and are sealed using super glue and glass cover slides and are then stored in a glove box.

During the synthesis of the VCr PBA, cyclic voltammetry was first carried out on each of the reagents, the results are shown in Figure 4.2 (a). These measurements allow the electrochemical deposition conditions to be optimised for production of the films. The cyclic voltammogram (CV) of the $VCl_3$ allowed the reduction potential to be characterised with respect to the reference electrode being used. The CV of the $K_3[Cr(CN_6)]$ solution shows negligible activity between 0.8 and −1.2 V in comparison to the CV of the $VCl_3$ and is mainly attributed to impurities in the salt.

The reduction peak seen in (a) as the potential is swept from right to left, around −0.7 V, is attributed to the reduction of the hydrated $V^{III}$ ion to $V^{II}$. The oxidative peak in the return direction as the potential is swept from left to right, at around −0.1 V, is due to the re-oxidation of $V^{II}$ back to $V^{III}$. This constitutes the simplest case, where there is one main redox couple involved, the CV becomes more complicated when extra processes are introduced. The shape of the CV is somewhat skewed from the expected shape due to the fact that the scan is ended prematurely when scanning to negative, or reductive, potentials. If the potential is taken too negative then additional processes begin to occur.

Figure 4.2 (b) illustrates what happens to the CV of the $VCl_3$ when the potential is swept past −0.8 V, this now involves multiple reduced oxidation states of the vanadium. The first reduction process, at −0.7 V, is presumably the same single electron reduction of $V^{III}$ as that in (a). After that we attribute the second peak

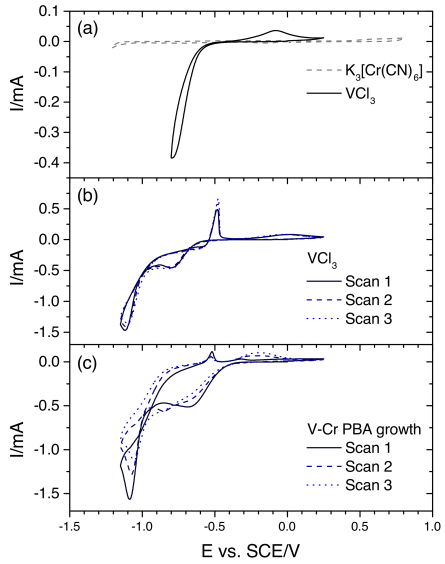


*Figure 4.2: The cyclic voltammograms for the various reagents and product film in the electrochemical cell in an aqueous solution of 1M KCl. (a) shows the CVs for the individual reagents in isolation across the region of interest. (b) shows the increasing complexity in the CV of the $VCl_3$ over a larger region of interest, where the scan is taken to a more reductive potential to induce further reduction. (c) illustrates the processes which occur when the film is grown under a cycling potential between $-1.15$ V and 0.25 V.*

at $-1.1$ V to further reduction and nucleation of vanadium containing species on the surface of the electrode. This is further implied by the structure of the first oxidative peak around $-0.5$ V which is sharp and indicative of material being stripped from the surface in a non-diffusion limited fashion. The shape of the loop gives important information on the nature of the processes which occur and can be used to rationalise what is going on in this more complicated situation. As the potential is swept from 0 V to more reductive potentials the current does not increase until $-0.65$ V when the first reduction occurs, however in the reverse direction the current flowing remains high up to $-0.55$ V before the stripping peak begins. This feature is called a nucleation loop and indicates that the potential required to initially reduce the species, in this case the $V^{III}$, is not equal to the

potential required to re-oxidise the species, $V^{II}$. This is thought to be based on the nature of the substrate involved, a larger potential is required to reduce the species on the surface of the FTO substrate than to oxidise the material from a layer of $V^{II}$.

This is then followed by the same re-oxidation of $V^{II}$ back to $V^{III}$, this process is gradually dampened by the loss of some material in the previous nucleation and stripping process. The appearance of the loop is not the most straightforward example of a cyclic voltammogram, as there appears to be what looks like a nucleation loop around $-0.6$ V where the wave in the reductive direction crosses over the with the oxidative wave.

The redox processes which occur when the two reagents are both present in the cell were then analysed, this is shown in Figure 4.2 (c). Again the first process to occur is the reduction of $V^{III}$ to $V^{II}$ around $-0.6$ V, followed by the further reduction and nucleation of species onto the surface of the electrode at $-1.1$ V. The magnitude of this peak, and therefore the frequency of this reduction occurring, decreases with each subsequent cycle. This implies that the process is not fully reversible, as some loss of species occurs. The oxidative peaks, first at $-0.5$ V due to the stripping of the nucleated deposits and then at $-0.2$ V due to the oxidation of $V^{II}$ back to $V^{III}$ also show changes over the course of the 3 scans carried out. First of all, the stripping peak decreases over time in agreement with the decrease of the reductive peak at $-1.1$ V indicating that less material is being nucleated on to the surface as it is instead reacting with the hexacyanochromate ions to form the VCr PBA. This is further evidenced by the increase over time of the second oxidative peak, indicating that more of the $V^{II/III}$ redox couple is incorporated into the structure over time.

The CV of the final product film, deposited potentiostatically as in Section 3.2.1, is shown in Figure 4.3 and was carried out in 1 M KCl as is standard in these measurements. The first peak, which starts around $-0.7$ V, corresponds to the reduction of $V^{III}$ ions to $V^{II}$ ions that are encorporated into the framework

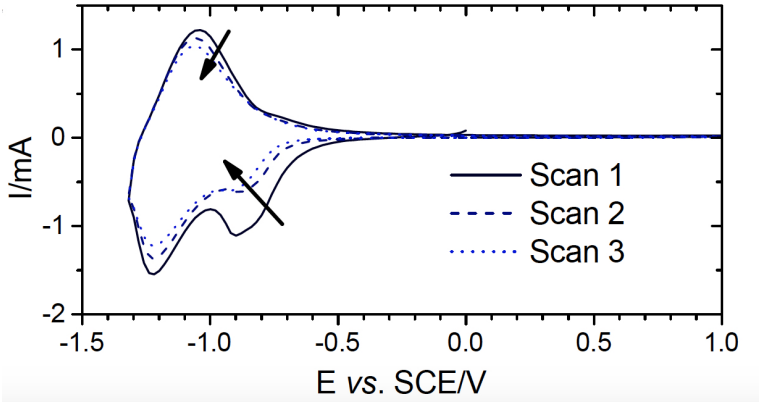


*Figure 4.3: The cyclic voltammogram for the final product film of the VCr PBA. As the potential is swept from right to left, the two peaks on the lower half of the plot correspond to the single electron reduction of $V^{III}$ and $Cr^{III}$ respectively. The single peak as the potential is swept from left to right is the re-oxidation of $Cr^{II}$ to regenerate the $Cr^{III}$ species.*

of the PBA, which is why the potential is shifted slightly from those in Figure 4.2. The second peak, which begins to appear below −1.0 V, is attributed to the single electron reduction of the $Cr^{III}$ in the PBA lattice. The only significant peak in the reverse direction is attributed to the re-oxidation of the $[Cr^{II}(CN)_6]^{4-}$. The assignment of the redox peaks associated with the chromium (III) ion are in agreement with the literature, where it has been shown that the $[Cr^{III}(CN)_6]^{3-}$ moiety in the Fe-Cr PBA, is reduced at a similar potential (−1.15 V vs SCE [33]). The arrows in Figure 4.3 illustrate how the current decreases with each cycle of the potential, particularly for the first reductive peak, this is due to an overall loss of $V^{III}$ species as they become trapped in lower oxidation states in the lattice. During the cycling of the potential, the balance of charge is maintained by the insertion and extraction of potassium counter ions. This can be studied using element specific techniques such as XPS before and after cycling of the film in order to study the differences that this induces in the film composition.

Figure 4.4 shows two XPS measurements carried out on two films made using the same deposition conditions, on the same day, but one of the films was

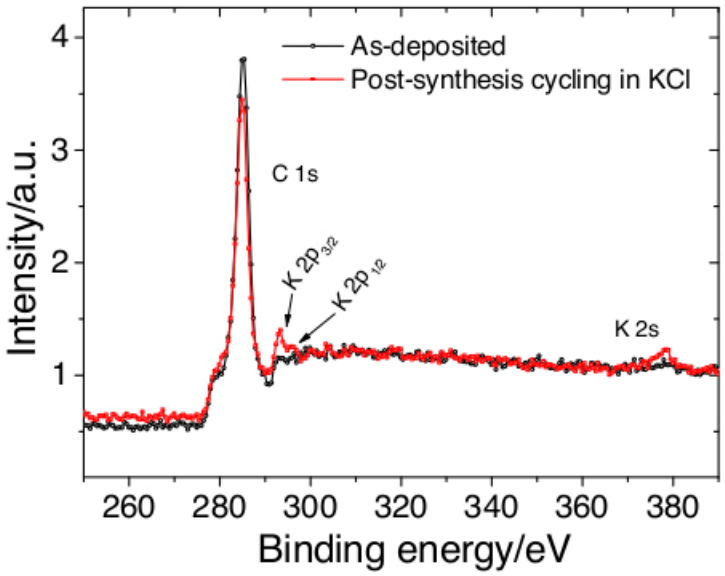


*Figure 4.4: Two XPS measurements illustrating the difference in the potassium ion content of two films, differing only by one having been cycled in KCl after deposition (red).*

cycled in KCl after deposition. The two small peaks, present in the red dataset, at 293 and 378 eV are attributed to the increased presence of potassium ions in the sample due to the cycling of potentials to incorporate ions into the film to counterbalance the change in charges on the V ions.

### Spectroelectrochemistry

In order to assign these observed redox peaks with greater certainty, a technique called spectroelectrochemistry was employed to give more information on the redox processes involved. From the literature [34] it is known that when incorporated into the V-Cr PBA lattice, the $V^{II}$ to $Cr^{III}$ MM'CT process occurs at 540 nm and the corresponding MMC'T process between $V^{III}$ and $Cr^{III}$ occurs at 660 nm. This gives us a handle on the critical redox processes involved in this material if we can observe changes to the absorption spectrum in these spectral regions.

As previously described, the sample was analysed in a cuvette, which is directly

connected to both the light source and spectrometer via optical fibres. The counter and pseudo-reference electrodes were arranged in the cuvette such that there was no contact when the substrate is introduced.

In order to precisely measure the absorption spectrum at a given potential, the potentiostat was programmed to scan the potential in steps, pausing every 0.1 V for 30 seconds to allow the spectrum to be measured manually using the computer controlled spectrometer, from 0 to −1.3 V. This ensures that the spectrum is measured at a specific potential as there is some time taken to measure the spectrum and this can change faster than the spectrum can be recorded as the potential is varied. The first reductive peak was analysed over the range from 0 to −0.8 V where any changes in the absorption spectrum could be assigned to this process alone, subsequently the second reductive peak was analysed from −0.9 to −1.3 V.

According to the computational studies by Rogers and Johansson [49], there should be two bands in the visible region of the spectrum corresponding to the MMC'T transitions from the two vanadium oxidation states present in the VCr PBA to the $Cr^{III}$ sites. These peaks are not usually resolved in the transmission spectra. If a sufficiently thin film is deposited, it was found that it is possible to observe the $V^{II}$-$Cr^{III}$ transition band as a shoulder on the side of the $V^{III}$-$Cr^{III}$ band, as seen in Figure 4.5. The sample in Figure 4.5 with a transmission of approximately 80% corresponds to a VCr film thickness of below 100 nm, this is typically achieved after only 60 seconds of deposition at -1.15 V. The shoulder is no longer visible at a thickness of 500 nm which is achieved after only 120 seconds of deposition.

The spectroelectrochemical measurements presented in Figure 4.6 show the changes seen in the transmission spectrum as a function of the electrochemical potential as it is swept from 0 V down to a maximum reductive potential of −1.3 V. As the potential is swept through the first reductive peak, assigned to the reduction of $V^{III}$ to $V^{II}$, the most prominent change in the transmission

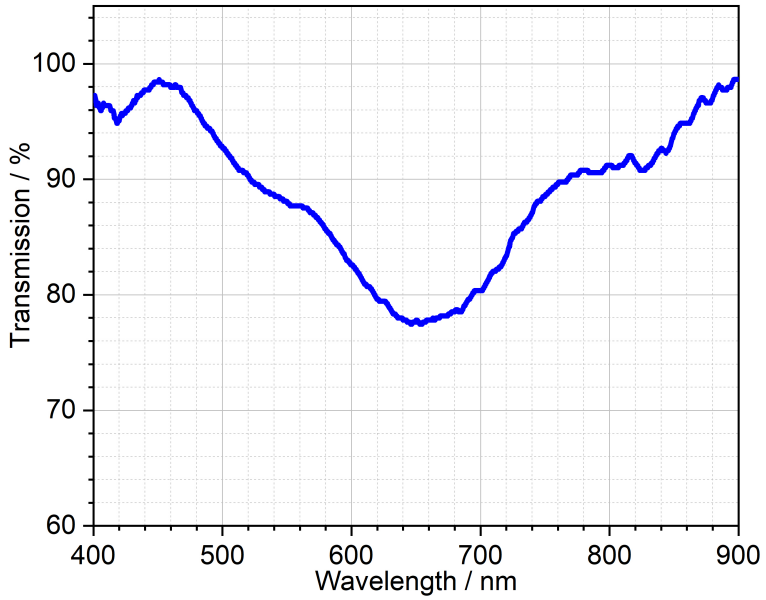


*Figure 4.5: The transmission spectrum of a particularly thin film of VCr PBA which is allows both vanadium MM'CT transition bands to be seen, at 540 and 660 nm. Deposition time of 60 seconds at −1.15 V using the standard reagent concentrations.*

spectrum is a decrease in the transmission around 540 nm, indicated by the arrow in (a), which appears to begin around −0.5 V in agreement with the cyclic voltammogram. Comparison of this spectral change with the static transmission spectrum in Figure 4.5 suggests that this loss in transmitted light is due to a generation of $V^{II}$ species in the PBA film.

The second process that occurs after −0.9 V, Figure 4.6 (b), corresponds to the second reduction peak in Figure 4.2 c) which is attributed to the reduction of the $[Cr(CN)_6]^{3-}$ moiety, as previously discussed. This results in a sharp decrease in transmission around 465 nm, meaning a species is being generated which has an absorption feature in this region. When assigning the redox process associated with the loss of transmittance at 465 nm, one has to consider that the total energy of the Cr site will increase when an extra electron is added through the process

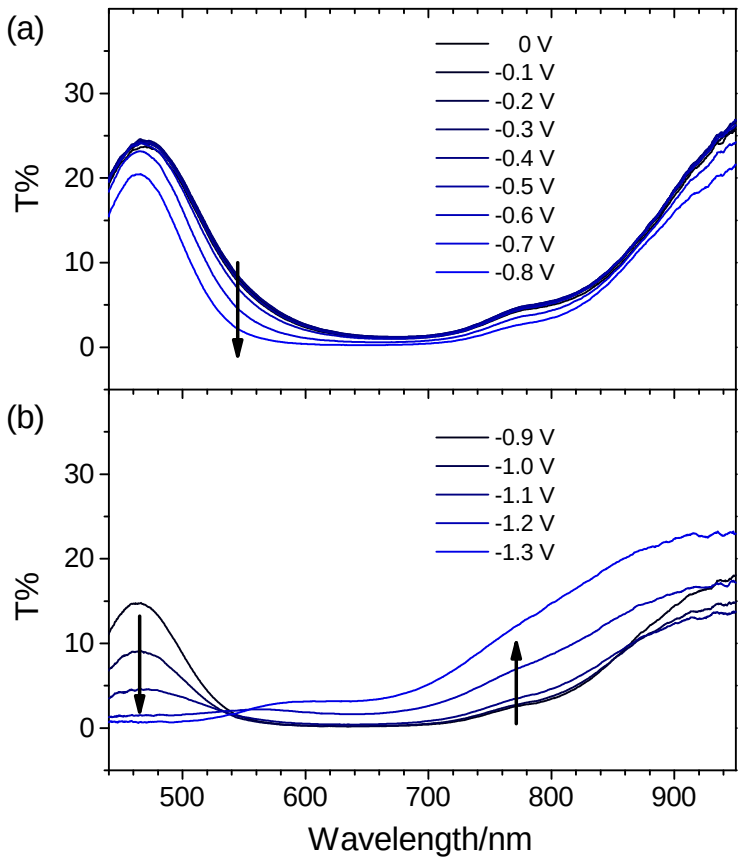


*Figure 4.6: The spectroelectrochemical measurements on the V-Cr Prussian Blue analogue showing the change in the absorption spectrum as a function of the electrochemical potential.*

of electrochemical reduction. An increase in energy of the Cr ions will cause a red-shift of the MM'CT transitions that occur at 540 and 660 nm. It is therefore not plausible that this new absorption is due to a shifted MM'CT transition. The slight increase in transmission at the MM'CT transition wavelengths do support this red-shift, as a loss of chromophores absorbing in this region would result in an increase in transmittance in this spectral region. The shifted MM'CT transition is probably pushed to wavelengths longer than 900 nm, where our detection system and light source are not effective. Likewise, the LMCT states around 400 nm would be shifted to even shorter wavelengths if the energy of the Cr ion is increased, further away in energy from the ligand states. We can also rule out metal-centred (MC) transitions, based upon the strong absorption

coefficient associated with the new absorption feature which are at least the same order of magnitude as the MM'CT transitions. The increase in energy of the Cr ion upon reduction will shift it closer to the energy of the empty $\pi^*$ orbitals of the cyanide ligands. The new absorption feature at 465 nm is therefore assigned to an MLCT transition from $[Cr^{II}(CN)_6]^{4-}$ to the empty $\pi^*$ ligand states. The peak at 800 nm has previously been assigned to a forbidden metal-centred absorption on the $[Cr^{III}(CN)_6]^{3-}$ unit [37]. When Cr(III) sites are reduced, there is an increase in transmission at 800 nm, which is consistent with a loss of absorption from this transition.

**Electrochromic Switching**

The colour change, from blue to black, which occurs as a result of the electrochemical reduction of the $Cr^{III}$ sites was clearly noticeable while carrying out the CV scans described in the previous sections of this thesis. It was noticed that this process was reversible and could be repeated at least 20 times without significant loss or degradation of the sample. The electrochromic properties of the films were therefore characterised using spectroelectrochemistry. The potential was swept between 0 and $-1.3$ V and the total charge passed was recorded. Simultaneously the transmittance was recorded at 465 nm as this is where the largest change in the transmission of the film in relation to the reduction of the $Cr^{III}$ sites was observed. These results are shown in Figure 4.7 where the amplitude of the transmitted light is clearly modulated as a function of the electrochemical potential applied.

From this measurement it is possible to determine a colouration efficiency ($\eta$) for the process. The colouration efficiency is a measure of the efficiency of the switching process and is defined as, $\eta = \Delta$ OD / $\Delta$ Q [53]. This relates the change in the absorbance, or optical density ($\Delta$OD), to the amount of charge ($\Delta$Q) passed through the system per unit area. The convention for defining $\eta$ in terms of absorbance (and therefore OD) instead of transmittance was followed

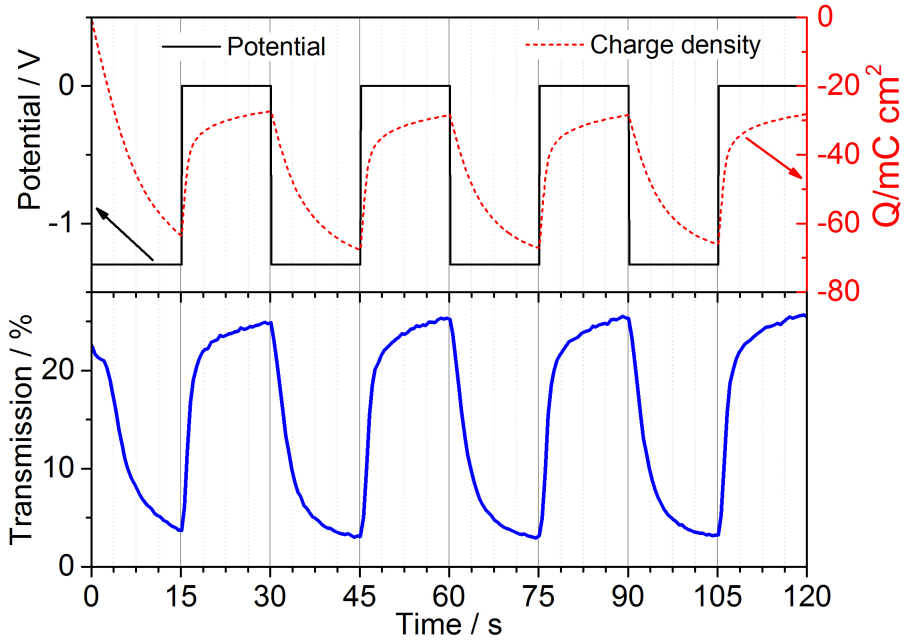


*Figure 4.7: The spectroelectrochemical measurements on the V-Cr Prussian Blue analogue showing how varying the potential effects the charge density and the transmitted light.*

here so the measurements were converted into absorbance. Therefore a plot of the absorbance against the supplied charge density will yield $\eta$ as the initial gradient. The initial gradient is used as at this point the rate it not limited by the relative abundance of any of the species involved. This follows the definition used in the literature. In the case of the film being under a resting potential of 0 V, there is a large number of the vanadium sites in the +3 oxidation state due to gradual re-oxidation in air while the samples are measured. When the reductive potential is then applied, the rate of reduction occurring is at its maximum. As the vanadium sites are reduced, there is an increasingly smaller number of available ions to be reduced. This site saturation is the reason that the plot in Figure 4.8 is not linear after the first initial period. This plot is shown in Figure 4.8 with the linear fit carried out on the initial change after the potential is first applied.

The value of $\eta$ was found to be -32 $\pm$ 1 cm$^2$ C$^{-1}$ for the black to blue switching process. This value is within the range of Prussian Blue containing

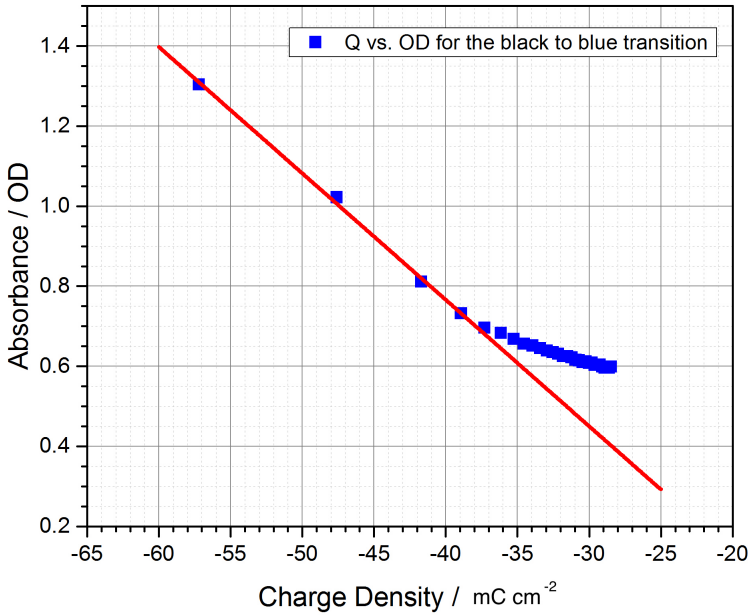


*Figure 4.8: The plot of the charge density, Q, against the absorbance, OD, to allow the value of the colouration efficiency, η, to be determined.*

electrochromic systems in the literature [54–57] where the magnitude of these values range all the way up to around 1000 $cm^2$ $C^{-1}$ when ameliorated by charge transfer species. This study however, constitutes a characterisation of a new compound in isolation with additional functional properties. The switching time for this process was found to be 4.7 seconds, this value is comparable with related work in the literature. This is defined as the time taken to reach 90% conversion from one state to the other. The electrochromic efficiency was also characterised, this follows the convention in the literature, for the blue to black switching process and was found to be -25.2 ± 0.2 $cm^2$ $C^{-1}$. This switching time was found to be 6.6 seconds for the same 90% conversion. The slower speed is attributed to the chemical process which is occurring in the film. In order to maintain overall charge neutrality over the course of the redox process (overall charge of the film remains zero), potassium ions diffuse in and out of the film, via the interstitial sites of the PBAs. This slower switching process occurs with the diffusion of ions

into the lattice, limiting the overall rate of the process. The hypothesis is that the rate at which potassium ions can diffuse in to the film is slower than the rate at which the ions can diffuse out of the film as it is more thermodynamically favourable to diffuse from a high concentration to a lower concentration than to do the opposite.

The VCr PBA exhibits room temperature magnetic ordering, as was previously discussed, which originates from the super-exchange interaction. Presumably the electrochemical modification of the metal ion oxidation states influences this super-exchange interaction and therefore has an impact on the magnetic ordering. This effect has not been characterised in this work due to not being able to measure both the magnetic and optical responses simultaneously. This would be of interest to future work in order to study and correlate these responses.

### 4.1.2 Electrochromic Switching of the Iron-Iron / Iron-Chromium Bilayered Heterostructure

#### Introduction

The synthesis of bi-layers composed of multiple PBAs could allow for a large spectrum of tuneability of the magnetic and optical properties of such heterostructures. Electrochromic bi-layer films of FeCr and FeFe Prussian Blues have been explored in this work as they have distinct optical spectra which allow us to monitor each layer individually during the electrochemical process. Prussian Blue itself, containing $Fe^{II}$ and $Fe^{III}$, is a well known electrochromic material. Therefore, this was a good starting place for understanding these investigations. This work has been published [58] and the paper is presented in Appendix 3.

In this work it was shown that a layer of the FeFe PB was successfully deposited on top of a layer of the FeCr PBA in order to produce a bilayered film composed of a blue and an orange film, which appeared green in transmission. The two individual films along with the bilayered sample are shown in Figure 4.9. By

applying a reducing potential, it was possible to electrochromically switch the colour of the FeFe layer off, from blue to transparent resulting in the film changing from green to orange overall. This switching process was fully studied using spectroelectrochemistry in order to characterise both the switching time and colouration efficiency.

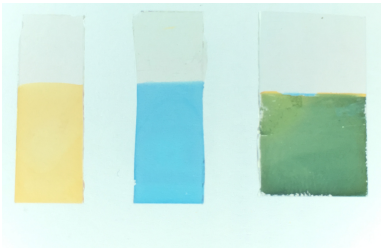

*Figure 4.9: An image showing the FeCr (left) and FeFe (center) Prussian Blues and the multilayer material (right) formed by sequentially depositing FeFe PB on top of the FeCr PBA. The substrates here are approximately 25 mm in height and 8 mm in width (left and center) to allow the films access to the cuvette used in the electrochemical measurements.*

### Synthesis

The synthesis of the multilayer structure was carried out in a sequential fashion, based upon the relative reductive potentials required to deposit the materials. In this way, the layer that was first deposited is not electrochemically affected by the reduction potential applied in order to deposit the subsequent layer. The reduction peak in the CV of the synthesis cell, Figure 4.10, suggests that the FeCr analogue is to be deposited at a potential of around -0.7 V (vs Ag/AgCl) and the FeFe to be deposited galvanostatically using a current of -40 uA (resulting in a potential around -0.2 V vs Ag/AgCl). From these values the FeCr will be synthesised first and the FeFe deposited on top, in order to minimise any unwanted redox processes in the underlying layer by applying a potential outside of the electrochemical range of the material. These values are in agreement with the literature values for these processes.

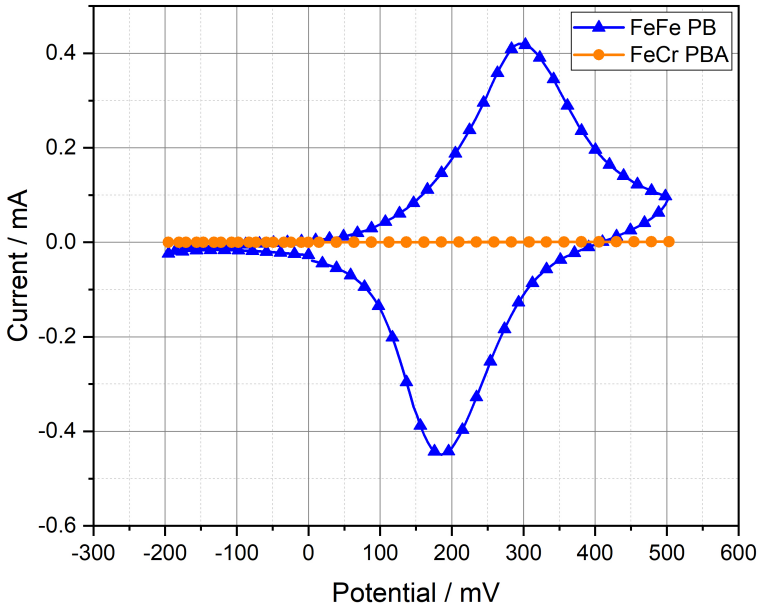


*Figure 4.10: The CV scans for the individual FeFe (blue) and FeCr (orange) Prussian Blues which were carried out in order to check the electrochemical activity over the range of potentials used. The FeCr analogue shows negligible activity over the potentials required to induce redox processes in the FeFe PB.*

To facilitate the spectroelectrochemical measurements, the two layers were also deposited individually in order to obtain films of similar optical densities. This allowed both absorption features to be clearly visible when studying the absorption spectrum as a function of the electrochemical potential during the measurements.

The FTO substrates were cut to 8 x 25 mm in order to fit into the cuvette for the spectroelectrochemical measurements with enough excess substrate on the top for attaching the electrode and handling the films after synthesis. These substrates were then cleaned in the usual fashion: sonication in $H_2O$/detergent then isopropanol and finally in methanol, the films were then rinsed with distilled water and dried under a flow of nitrogen gas.

The FeCr film was first deposited using concentrations of 37.5 and 25 mM of

the $FeCl_3$ and $K_3[Cr(CN)_6]$ respectively. The deposition was carried out at a constant potential of -0.7 V for 300 s. The resultant orange film was washed with deionised water and allowed to dry under a constant flow of $N_2$ gas. After deposition, the FeCr film was cycled in KCl, shown in Figure 4.10, in order to confirm that no electrochemical activity took place over the potentials of interest for the FeFe deposition or redox processes. The subsequent deposition of the FeFe was carried out galvanostatically at a constant current of -40 $\mu$A in order to produce a second film of approximately the same OD as the FeCr film below, this corresponded to a deposition time of 60 s. The colour of the resulting films ranged from orange (at very short deposition times), to green (at intermediate deposition times), through to blue (at long deposition times). The CV of the individual FeFe PB was carried out prior to the multilayer deposition to confirm the behaviour and for comparison with the multilayer structure, both CV are shown in Figure 4.11.

The cyanide stretching frequencies of the two films seen in the IR spectra, Figure 4.13, are in agreement with the literature and indicate that the FeFe film had indeed been deposited on top of the surface of the FeCr and the layers remained predominantly independent in terms of structure and chemical composition.

Both of the voltammograms in Figure 4.11 were carried out using Pt pseudo-reference and counter electrodes as this replicates the conditions which were used during the spectroelectrochemical measurements. The general behaviour of the FeFe layer is maintained when incorporated into the multilayer structure by depositing it on the surface of the FeCr material, but a shift is observed in the potential at which the reduction and oxidation peaks appear. This shift in the potential is likely due to the FeCr 'electrode' exhibiting a different electrochemical behaviour to the FTO substrate layer below. There is also a significant difference in the width of the peaks, the broader peaks which are seen in the isolated FeFe film indicate that the redox processes are limited by the diffusion of counter ions in the solution. The redox peaks in the multilayer suggest that the switching of

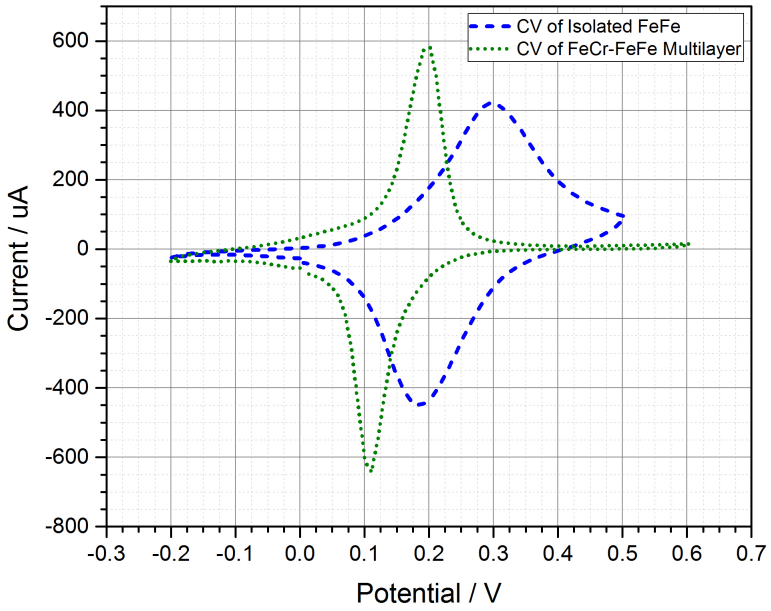


*Figure 4.11: The cyclic voltammogram of the FeFe PB showing differences between the isolated film (deposited directly on the clean FTO substrate) and the film deposited as part of the bilayer structure (deposited on top of the FeCr PBA). The expected single redox couple between $Fe^{III}$ and $Fe^{II}$ is retained but is shifted to lower potentials in the ML structure and the peak structure is also sharper in the multilayer.*

the FeFe layer is limited by the charge passing through the underlying FeCr layer.

### Characterisation

Optical transmission spectra were recorded using a Shimadzu UV-1800 UV Spectrophotometer and Figure 4.12 shows the absorption spectra of the individual FeCr and FeFe films and the multilayer FeCr-FeFe film. These spectra demonstrate that the structure of the individual films are retained and are in agreement with what has been described previously. It was found that for a given % transmission of FeCr, in order to achieve a similar % transmission of the FeFe film, the FeFe film needed to be much thinner suggesting that the MM'CT

oscillator strength for the two materials is very different, this is illustrated in Figure 4.15. All of the further measurements were carried out on films which possessed a comparable OD of both the FeCr and FeFe layers.

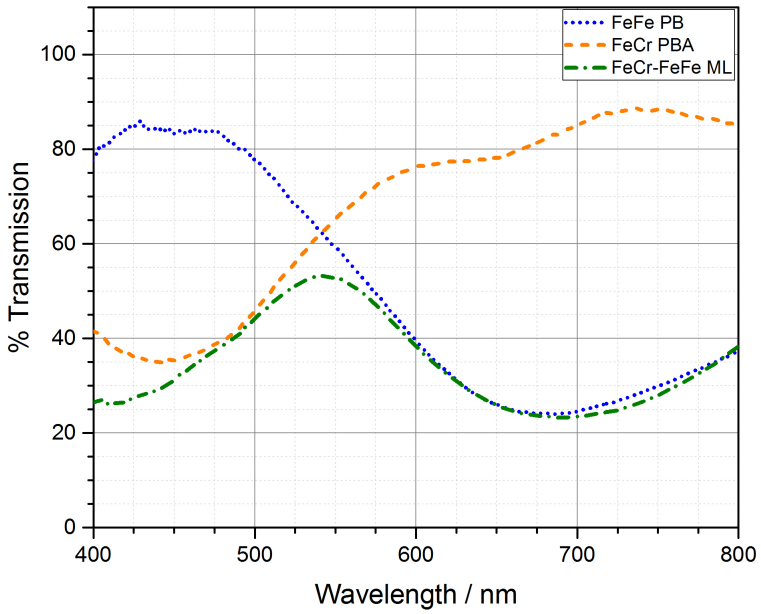


*Figure 4.12: The UV-Vis absorption features for the individual layers are clearly visible in the spectrum of the multilayer.*

IR spectra were measured using a Renishaw InVia Raman Microscope equipped with a reflection FTIR intrument. It was found that the reflectivity of the FTO layer allowed for more sensitive measurements to be taken than using an attenuated total reflectance (ATR) instrument. Figure 4.13 shows the measured IR stretching frequencies of the two individual Prussian Blue layers and the measured spectrum of the multilayer material. The fresh FeCr film shows a stretching frequency of 2168 $cm^{-1}$ and the FeFe film shows a peak at 2077 $cm^{-1}$. These peaks are maintained when the IR spectrum of the multilayer material is measured.

Information on the film thickness and crystal morphology was obtained using various techniques. Atomic force microscopy (AFM) was used to measure

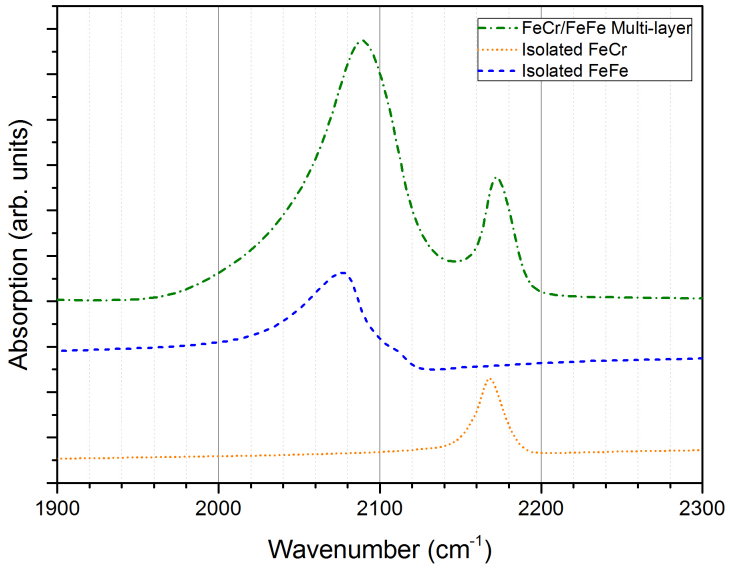


*Figure 4.13: The infrared absorption features for the individual layers are clearly visible in the spectrum of the multilayer.*

the thicknesses of the films. A comparison of the optical density of the FeFe and FeCr analogue versus the film thickness was carried out in order to construct a calibration curve from which we can estimate the film thickness from the OD of the films without the need to repeat the AFM measurements on each subsequent film. In order to do this, the behaviour of the individual layers must first be studied, and how the thickness of the film results in different observed OD. As was previously mentioned, the thickness measurements were carried out by drawing a razor blade across the surface of the film to create a 'valley' down to the FTO layer which will allow us to accurately measure the height of the layer from top to bottom. The analysis of the AFM images was performed using the NanoScope Analysis 1.5 program (Bruker Corporation) which allows for various manipulations of the 3D image generated by the AFM. The most useful of these tools is the 'step' analysis which plots the height profile along a straight line which is manually drawn by the user. Figure 4.15 shows the linear dependence of the film thickness against the resultant film absorption.

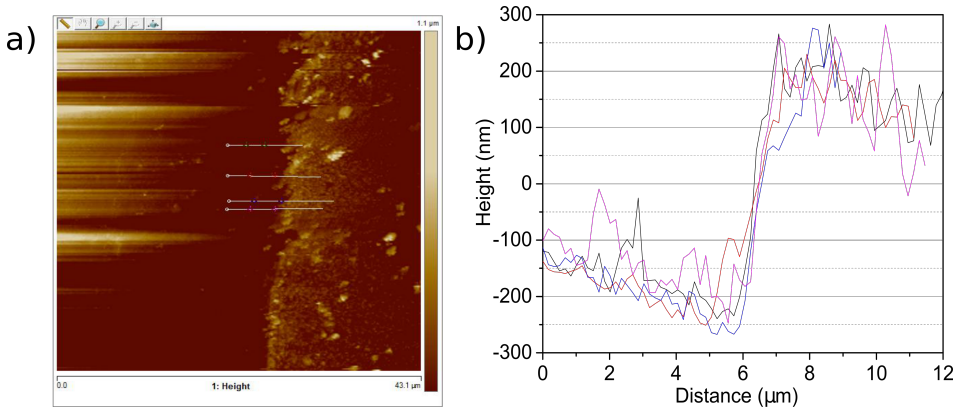


*Figure 4.14: The method by which the AFM images were used to determine the thickness of the films. a) The raw AFM image showing the clean region (left) of the film created by the razor blade and the area of the film densely populated with PBA crystals (right). The height profiles defined by the user can also be seen as four horizontal white lines superimposed on the image. b) The output of these height profiles are plotted as a function of height along the drawn line.*

The relationship between the OD of the FeCr material and the thickness of the film shows a different gradient than the FeFe counterpart. The gradient of the fit is smaller, indicating that the oscillator strength for this transition is weaker than in the FeFe material. This is an interesting observation which is further highlighted in SEM measurements carried out externally by collaborators at the University of the West of Scotland. All of these measurements utilised several of these height profiles through crystals in order to give a reliable measure of the true height of the thin layer, as there can often be a piling up of material at the edge of the valley if there is a sufficient density of PB crystals. Also note how the error seen in Figure 4.15 in the both the absorption data and the thickness measurement increase with film thickness due to the higher amount of scattered light and rougher film topology. The two PBA films of approximately 30% transmission, or 0.5 OD, correspond to thicknesses of 80 nm and 250 nm for the FeFe and FeCr materials respectively. These thickness films were used in the bilayer studies presented here as this allows each feature to be studied without

the OD becoming too high.

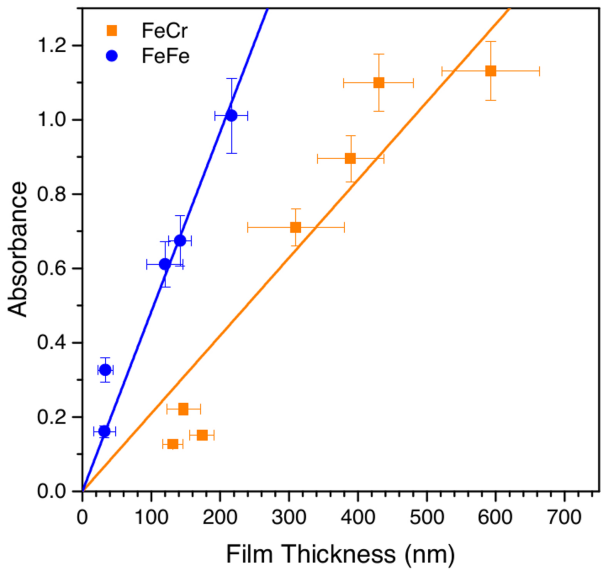


*Figure 4.15: A graph illustrating the linear relationship between the deposition time and the thickness of the electrochemically deposited FeCr and FeFe films.*

Finally, scanning electron microscopy (SEM) and energy dispersive X-ray spectroscopy (EDX) were used in combination to study the individual layers in terms of thickness and the elemental composition. The measurements were carried out at the Thin Films Institute based at the University of the West of Scotland in collaboration with Dr David Hutson and Dr Liz Porteous. Figure 4.16 shows the SEM images of the individual films and the multilayer structure. The film that was sent for EDX analysis was deposited using masking of parts of the substrate in order to produce a single sample which was composed of a single FeFe layer, a single FeCr and the FeCr-FeFe multilayer. This allowed all permutations of the films to be studied in one sample, after a single deposition process. This film was termed a 'tricolore' film due to the three different colours present. In order to achieve high image resolution, a thin layer of gold of approximately 10 nm was deposited across the surface of the sample in order to reduce charging up of the sample over the course of the measurement and to promote the emission

of secondary electrons to increase the signal-to-noise ratio.

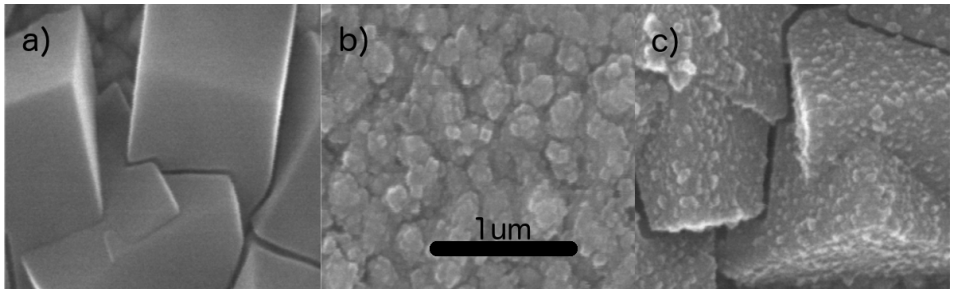


*Figure 4.16: SEM images of each of the individual layers, both at approximately 30% transmission, and the multilayer structure. The FeCr film on top of the FTO substrate is shown in a) and the FeFe crystals, which are a comparable size to the FTO substrate, are shown in b). The deposition of the multilayer in c) can be clearly seen as the small FeFe crystals are visible on the surface of the larger FeCr crystals.*

Figure 4.17 shows EDX data taken from an FeFe film deposited directly on FTO (denoted as 'blue square'), FeCr film (denoted as 'middle brown square') and a bilayer film (denoted as 'RHS brown square'). The peaks of interest are those coming from Cr and Fe ions at 5.4 and 6.4 keV respectively.

In the measurement of the individual FeFe layer, this area is highlighted in yellow, there is no Cr present in the film, evidenced by the lack of any peak around 5.4 keV. The measurements carried out on both of the other sections of the sample, the FeCr and the FeCr-FeFe multilayer, show both Cr and Fe at 5.4 and 6.4 keV, as expected. The presence of gold has been previous mentioned to facilitate SEM measurements and the tin peaks are present due to the FTO layer below the samples.

**Spectroelectrochemical Measurements**

The FeFe Prussian Blue is well known as an electrochromic material. Under certain reduction potentials the colour of the material is changed from blue to colourless. Crucially, at these same potentials the Fe-Cr Prussian Blue

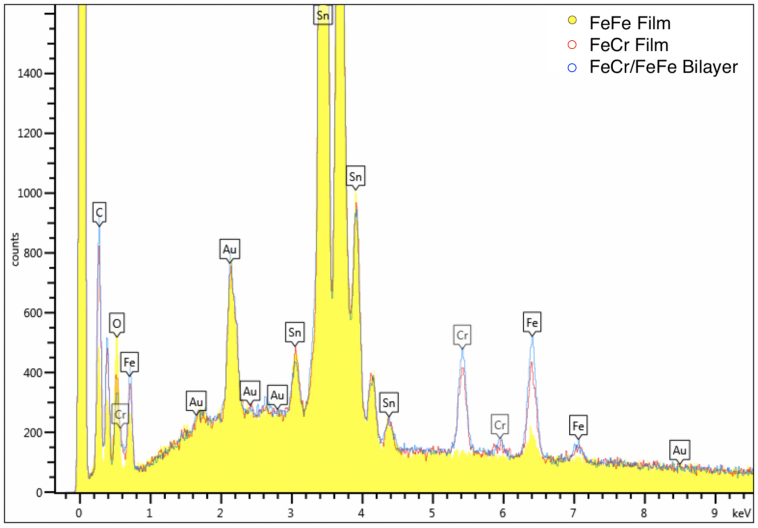


*Figure 4.17: EDX spectra measured of the 'tricolore' sample composed of isolated FeFe, FeCr and FeCr-FeFe multilayer films during SEM analysis by collaborators at the University of the West of Scotland.*

analogue undergoes no redox processes and therefore no spectroscopic changes. For the electrochromic switching, potentials of +0.5 V and -0.2 V were chosen based upon the information in the CVs presented in Figure 4.11 as this will drive the reduction and oxidation of the films to completion to allow accurate measuring of the switching.

During the CV scan, it was clear that the colour of the FeFe PB could be completely switched from blue to transparent. The peak of the absorption band of the FeFe is at 685 nm due to the MM'CT transition. This therefore constitutes the wavelength at which there will be the largest change in the transmitted light over the course of the electrochromic switching. The measurement was set up as follows: the sample was mounted into the 10x10 mm cuvette along with the pseudo-reference and counter electrodes and the spectrometer was set up to monitor the light intensity at 685 nm over the course of 300 seconds. During this time the electrochemical potential is swept between +0.5 V and -0.2 V in order to induce the electrochromic changes.

During the electrochemical cycling of the film, the current and the total

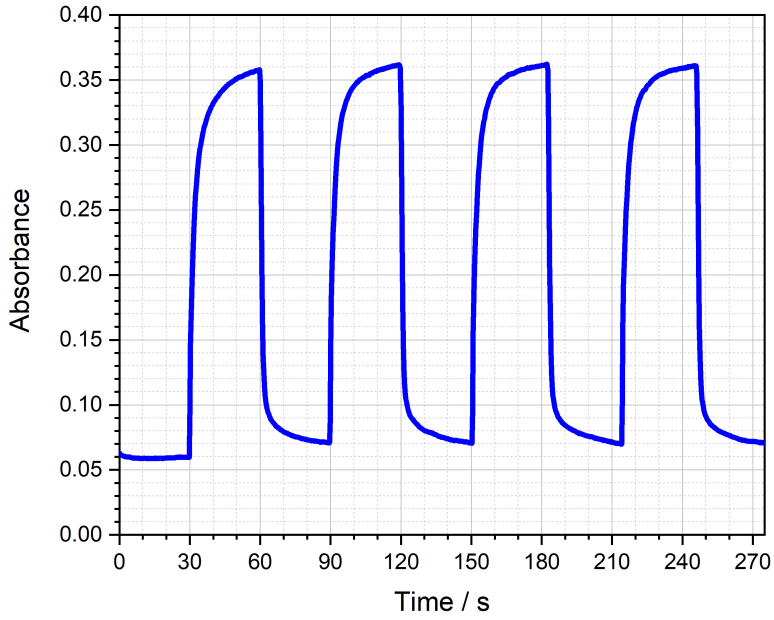


*Figure 4.18: The absorbance of the FeCr-FeFe multilayer is monitored at 685 nm, this corresponds to the reversible colour change of the FeFe layer from blue to colourless.*

charge passed through the system was also monitored in order to allow the determination of the efficiency of the switching, or the colouration efficiency (CE). The current and charge data is shown in Figure 4.19. There is an overall trend of the charge which is increasing over time, over the course of the measurement. This means that all of the charge that is passed through the system to reduce the FeFe layer is not passed in the reverse direction to re-oxidise the sample, but is instead building up in the sample. This may be due to the interface between the upper FeFe layer and the lower FeCr layer being inhomogeneous as both films are polycrystalline. This could result in charge building up in regions of the film which is not released when the potential is switched.

The second plot on this graph shows how the current varies as a function of time during the potential switching process. When the potential is switched at around 30 seconds to oxidise the FeFe layer, the current jumps up to a maximum

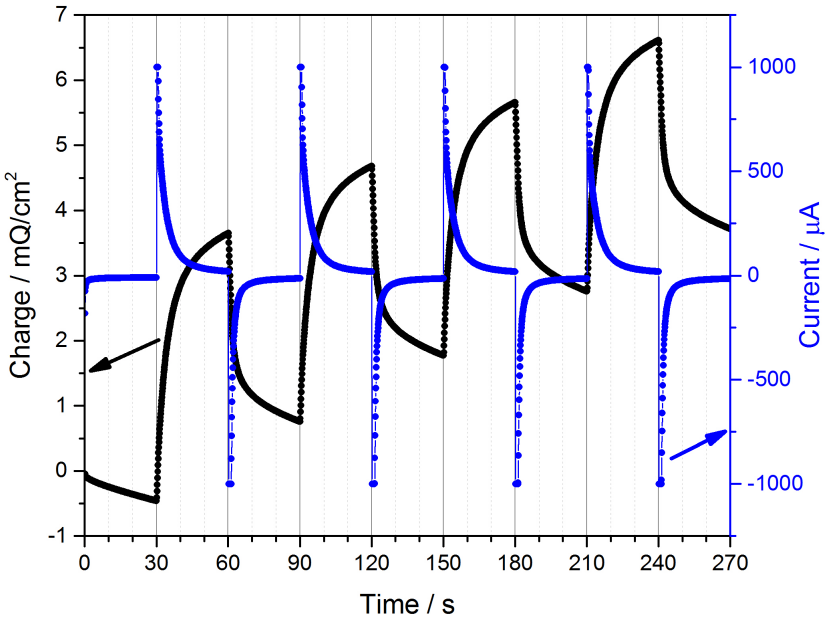


*Figure 4.19: The changes in the charge (black) and the current (blue) passing through the system during the electrochromic switching. The arrows indicate the axis to which each plot belongs. The sharp response of the charge and current is due to the initially large availability of redox centres.*

immediately. This current then decays very rapidly within the first 10 seconds, at which point the current slowly decreases to zero over the next 20 seconds. This indicates that the majority of the metal sites are switched within this first short period of time, suggesting a good overall contact between FeFe layer and the FeCr/FTO beneath. When the potential is then switched to reduce the FeFe layer, at around 60 seconds, the current peaks with the inverse sign which indicates that the current is flowing in the opposite direction. The flow of the current in this direction matches well with the previous switch, indicating that the process works equally in both directions.

From the plot in Figure 4.20 the value of $\eta$ was found to be 147.8 $\pm$ 0.8 $cm^2$ $C^{-1}$ for the transition from the coloured, blue state to the colourless, bleached state. This value is found to be the same order of magnitude as was reported in

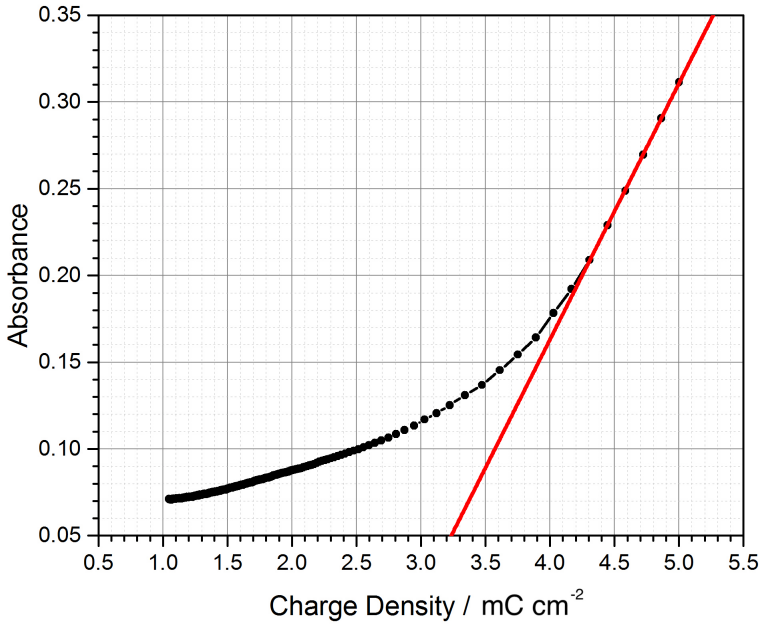


*Figure 4.20: A plot of the absorbance of the film as a function of the charge density passed through the system which yields the colouration efficiency as the initial gradient.*

other studies where the FeFe Prussian Blue was used as part of an electrochromic device [54–57]. The switching time for this process was determined to be 4.4 ± 0.4 s and is defined as the time taken for 90% of the switching process to be completed.

When bilayers of approximately equal absorbance were synthesised, polycrystalline films of around 250 nm and 80 nm of the FeCr and the FeFe materials respectively, were produced. It was possible to modulate the colour of only the FeFe layer within the heterostructure using electrochemistry to reversibly reduce/oxidise the material, as shown in Figure 4.21.

This study demonstrates the layer-sensitivity in multilayered heterostructures of Prussian Blue analogues and will allow the study electron charge-transfer processes in a range of related structures using Prussian Blue analogues. This is interesting because some of these materials, such as the CrCr, VCr and CoFe

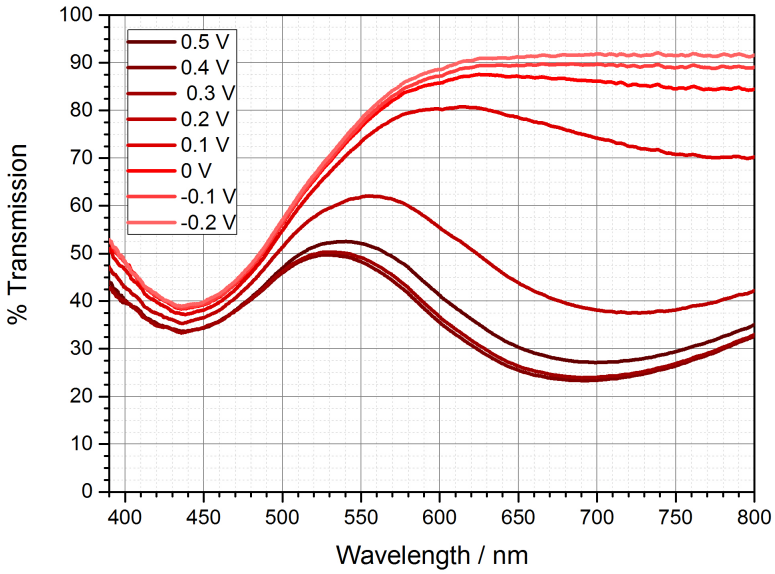


*Figure 4.21: The spectroelectrochemical measurements of the FeCr-FeFe bilayer structure; the transmission spectra are monitored as a function of the electrochemical potential. The band at 440 nm, from the FeCr material, remains mostly unchanged over the course of the measurement whereas the band at 690 nm, from the FeFe material, is entirely removed at more reducing potentials.*

analogues show a wide range of properties such as electrochromic activity, high-temperature magnetic ordering and exhibit strong and chemically tuneable colours. The further study of these functional materials in multilayered structures is of great interest for the development of novel photonic and spintronic devices.

## 4.2 Ultrafast Transient Transmission Spectroscopy

### 4.2.1 Overview

Functional, or smart, materials can be controlled by external stimuli such as temperature, pressure or laser light to modify their electrical, optical or magnetic properties. The interaction of light and matter in these kinds of systems is of particular interest, where the development of the understanding

of complex photophysical processes occurring in transition metal complexes is necessary if these materials are to become of use in future electronic devices. As previously mentioned, spin-crossover (SC) is of particular interest. This process can be optically induced which initiates a transition from a low-spin state to a high-spin state. It was previously found that a Prussian Blue analogue containing the -$Cr[CN]_6$- moiety undergoes intersystem crossing within 250 fs [34]. In order to study these ultrafast processes it is possible to employ femtosecond transient transmission spectroscopy. These measurements allow the evolution of the electronic excited states to be followed. In order to interpret the overall dynamic processes involved following laser excitation, a global analysis is carried out on the data.

Glotaran [59] is a free software program developed specifically to aid with global analysis of time-resolved spectroscopy measurements. It serves as a graphical user interface (GUI) to the R package 'TIMP', which is a problem solving environment for fitting superposition models.

Once our measurements have been carried out, the data is presented in the following way: two one dimensional arrays containing the time delays and the wavelength values, plus a two-dimensional array containing the resulting dataset. Using MATLAB, the 2D data array composed of the changes in transmission was combined with the time delay and wavelength information, into the first column and row, to allow it to be read by Glotaran. The array needs to be set up such that the first row contains the wavelength values and the first column contains the time delay values, this normally requires the values to first be transposed. Glotaran acquires the variables directly from the complete .ascii file containing the dataset. The import tool allows the variables in the data file to be automatically uploaded into Glotaran. It is important that the wavelength is expressed in nanometres and the time delays are defined in picoseconds.

Once the data has been successfully imported then it will be displayed as a 2-dimensional plot with the time delays on the vertical axis from top to bottom

and the wavelength on the horizontal axis from left to right. The change in transmission on the third dimension is displayed as a colour on a 'heat' scale from blue to red, where blue is the lowest value in the array and red is the largest value in the array. The data which is displayed has not been corrected for the chirp and as such the dispersion across the spectrum can be clearly seen as the time-zero occurs at later time delays as you move to longer wavelengths. Now that the data is ready to be analysed one must prepare the analysis scheme which will act as the template for the fitting protocol.

The kinetic parameters will be used to describe the decay dynamics so at this point an approximate first guess can be input if these are known. In the work discussed in this thesis, a local fit was first carried out in order to give reasonable starting parameters to allow the fit to converge with fewer iterations. Once the kinetic parameters have been decided on, then the instrument response function (IRF) can be set. The IRF uses a Gaussian pulse to describe the rise time of the signal such that the fit makes physical sense, ie. a laser pulse of finite duration will not induce an instantaneous signal rise but instead the signal will grow over a short amount of time. In order to assign values to these parameters, the data set itself must be inspected closely around the signal rise at time zero, Figure 4.22.

The value on the time axis at which the rise occurs is the first value which is required for the fitting parameter, at the specific wavelength chosen. Then the rise time for the signal is needed, this is inherently tied to the pulse durations used in the experiments, which gives a lower limit to this rise time. With these values, the fitting algorithm can incorporate this finite rise time into the fit across the whole spectrum.

The third set of parameters that are input to the analysis are the dispersion parameters. These parameters, 3 in our case, create a polynomial function which describes the chirp of the white light continuum across the spectrum, Figure 4.23. This is essential to ensuring that the signals are correctly calibrated with respect

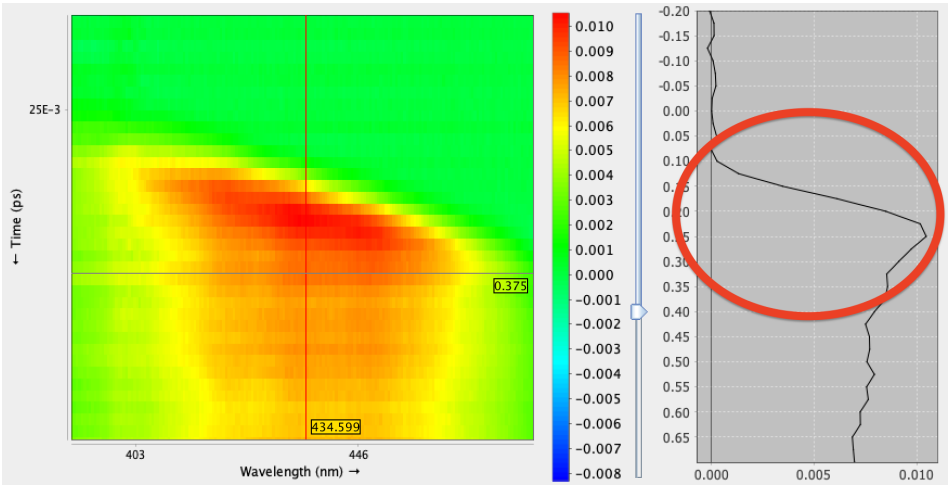


*Figure 4.22: The selected time trace on the right hand side (from the vertical line in the left hand panel) allows the important values to be extracted and then input to provide the fit with the IRF. Both the numerical position of the signal rise and the time the signal takes to grow are needed and can be input into the analysis scheme.*

to their relative temporal offset.

The quality of the fit of the fitting parameters is then judged using a three step process.

First of all, the convergence of the fit is determined by monitoring the progression of the sum of square errors (SSE), if the SSE has not yet converged then a higher number of iterations is required. Figure 4.24 shows the first 5 cycles of iterations in a test fitting protocol which indicates the fit has converged after the $4^{\text{th}}$ iteration.

Once a convergence has been established, then the second step of the fitting procedure is the inspection of the singular value decomposition (SVD) which is a matrix factorisation which is used to explore the number of spectrally and temporally independent components in the data matrix. The singular value gives an indication of the number of significant components that can be used to describe the data. The user can manually increase or decrease the number of the singular vectors until the point at which added vectors shows no ameliorated spectral structure. Finally, once a satisfactory SVD value is obtained and the fit

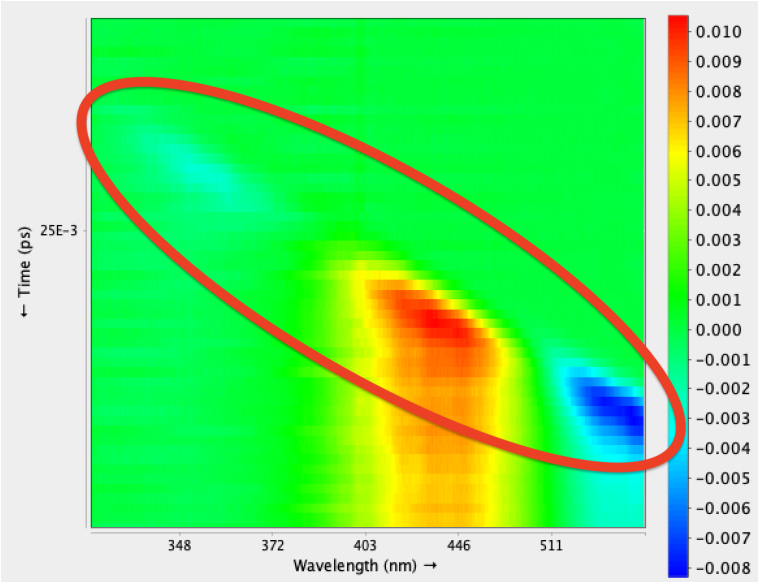


*Figure 4.23: The clear chirp of the white light continuum which can then be fitted to a polynomial expression to allow the actual time zero to be determined across the spectrum. The signal in the UV (left side) appears at around - 0.25 ps and the signal towards 600 nm (right side) appears at 0.5 ps giving the overall dispersion a temporal width of approximately 0.75 ps.*

appears to have converged then the fit can be visually inspected. It is possible to view the raw data with the fit as an overlay, Figure 4.25, which allows the fit to be closely scrutinised with respect to all of the spectral features.

Once the fit appears to match very well with the data then the number of iterations can be increased in order to give a more definitive convergence to the fit. The dynamical model used to describe these signals must then have a grounding in the photophysical processes which occurs in these such transition metal complexes. The previous work in this field of ultrafast studies of transition metal complexes and particularly the work of Johansson *et al.* were helpful in this endeavour. Subsequent measurements allowed an expansion of the knowledge of this material, was achieved by applying a spectrally broader probe pulse to investigate a wider range of wavelengths. The information gathered in this work then inspired further studies of analogues containing the hexacyanochromate

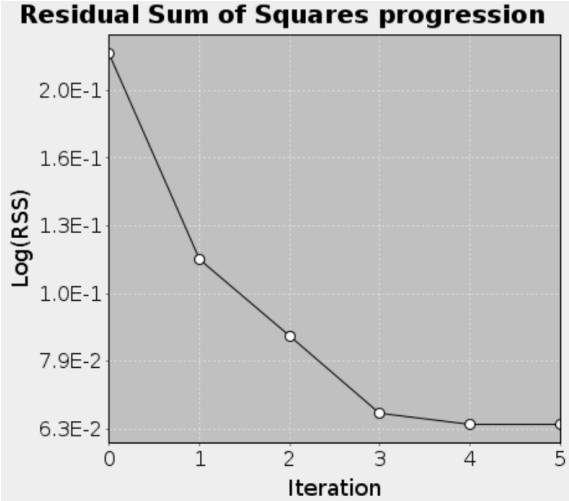


*Figure 4.24: The progression of the sum of squares of errors displayed in Glotaran. The constant value between the $4^{th}$ and $5^{th}$ iterations suggest that the fit has converged.*

moiety, to study the dynamics in these systems which appear to be predominantly chromium centred. These further studies were carried out on thin films of these analogues where the metal centre at site A was substituted for another transition metal. By modifying this metal-to-metal interaction, it was thought that one or more transitions within the decay dynamics would be influenced, potentially leading to some understanding of how this process could be influenced for future applications.

### 4.2.2 Vanadium-Chromium Analogue

#### Introduction

The vanadium-chromium analogue of Prussian Blue is a fascinating model system for studying the dynamics of functional materials due to its high magnetic ordering temperature recorded above room temperature [24]. The material has been the subject of various studies [27,36–39,48] of its static magnetic and optical properties which will aid in interpreting the results obtained for both these types of measurements.

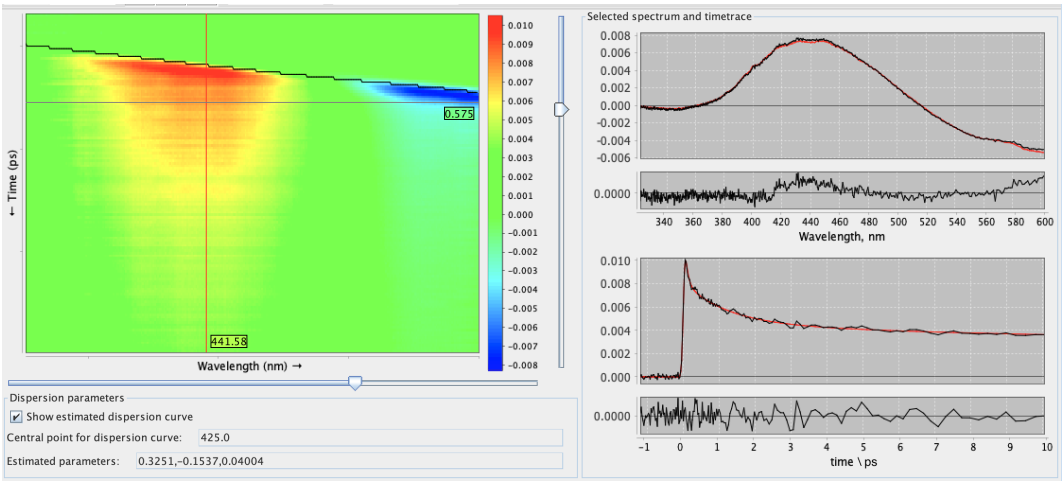


*Figure 4.25: The fitted traces which are overlaid on the raw dataset for the FeCr PBA. The left panel shows the raw data with the dispersion curve fitted along the proposed time-zero. The horizontal and vertical lines are cursors which can be moved manually and display the two traces on the right hand side of the screen. Top right is a difference spectrum taken at 0.575 ps after the pump pulse and bottom left shows a kinetic trace at 441.58 nm.*

The optical spectrum of the VCr PBA is dominated by MM'CT transitions in the visible, around 540 - 650 nm, and LMCT amd MLCT transitions in the UV, around 300 - 400 nm. The MM'CT transition takes place between $t_{2g}$ electrons on adjacent Cr and V metal centres. Previous work on the VCr PBA showed that when pumping at the LMCT (400 nm) the population ended up in the $^2$E state on the Cr ion, after very fast ISC, which corresponds to an intraconfigurational spin flip of the ground state [34].

The work presented here constitutes a development upon previous studies by employing a spectrally broader white light super-continuum probe pulse. This was generated in $CaF_2$, which can extend down as far as 300 nm, depending on optimisation. Transient transmission measurements were carried out using the broader probe pulse which allowed observation of an additional dynamic process. This new excited state absorption (ESA) was observed at room temperature in the UV portion of the spectrum, around 345 nm, which was attributed to excitation

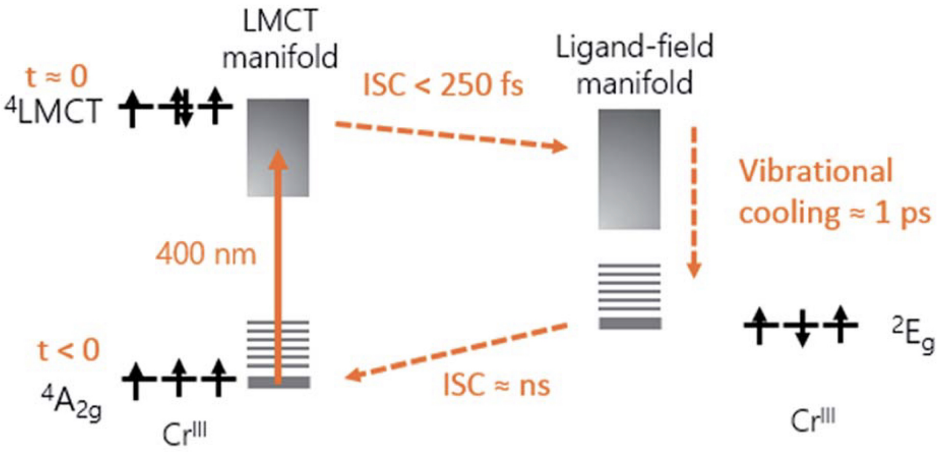


*Figure 4.26: The electronic excited state model used by Johansson et al. [34] to describe the dynamics which occur in the VCr PBA. After excitation at the ligand-metal charge transfer transition, the system undergoes very fast (sub 250 fs) intersystem crossing into the 'hot' ligand manifold. This then decays into the $^2E$ state which corresponds to an intraconfigurational spin-flip of the ground state. This figure is a subsection of Figure 2.12 concentrating on the dynamics which occur on the Cr centres following photoexcitation.*

directly from the $^2$E state. This importantly allowed the direct observation of this state, opening up the possibility to directly probe the growth and decay of this state instead of relying on the ground state bleach (GSB) signal.
These measurements were initially carried out at the University of Warwick's Chemistry department in the laboratory of Prof. Vas Stavros due to some down-time in the laser system at the University of Edinburgh. The measurements were subsequently repeated in the Edinburgh laboratory as a test of our setup for future measurements. This work has been published [60] and the paper is presented in Appendix 2.

### Sample Preparation

The film was prepared using the previously described synthesis at −1.2 V for 300 seconds. The glass substrates with a thin layer of FTO on one face

were cleaned and used as working electrode in an electrochemical cell containing an aqueous solution of KCl, $K_3Cr(CN)_6$ and $VCl_3$. This deposition produced a deep blue film of approximately 0.6 $\mu$m in thickness, this was estimated from a calibration curve constructed by measuring the absorption of the film and comparing it with its thickness measured with AFM. This corresponded to a percentage transmission of approximately 6 % at the peak of the absorption band, centred at 680 nm.

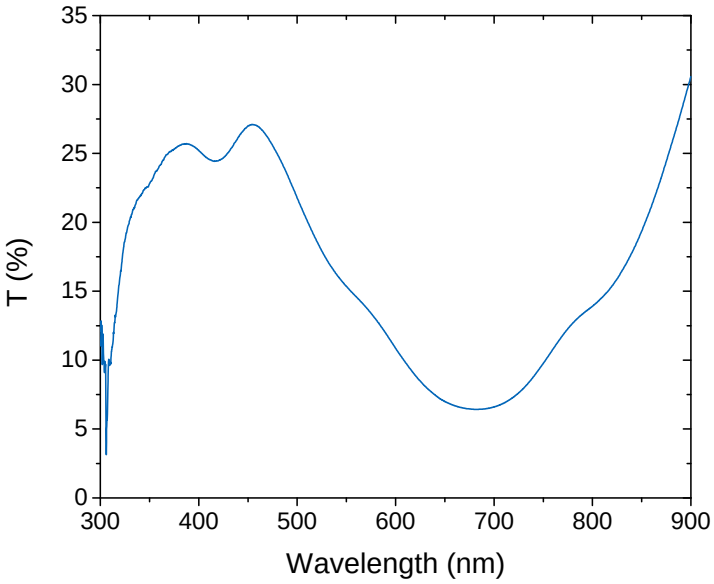


*Figure 4.27: The static transmission spectrum of the VCr sample that was taken to Warwick University for ultrafast pump probe measurements. The loss of transmittance in the visible region of the spectrum is due to the MM'CT transitions between $Cr^{III}$-$V^{II}$ at approximately 540 nm and $Cr^{III}$-$V^{III}$ around 680 nm in this particular film. The former transition is seen as a shoulder on the side of the main band, however this is not always clearly visible. (Structure below 320 nm is noise from the white light source used in this measurement.)*

### Ultrafast Transient Transmission Measurements of the VCr PBA

The sample was attached to a 1" optics mount where both the pump and the probe would interact with the sample in the foci of the two beams. The

white light continuum was generated in a $CaF_2$ plate and the probe spectrum was detected using an Avantes fibre-coupled spectrometer. The 400 nm pump beam was generated by frequency doubling the 800 nm fundamental of the laser system in a BBO crystal and was relatively defocussed at the point of interaction with the sample/probe. The diameter of the pump beam was approximately 1.5 mm and with a pulse energy of 400 nJ this corresponds to a fluence of 22 uJ/cm$^2$. This was determined to be below the damage threshold for the material for the duration of these measurements by checking the difference spectra at time zero and and a short time delay of 1 ps for any changes which may indicate film degradation.

The optimisation of the pump and probe overlap was carried out at a short positive time delay. Due to the long lasting bleach signal this was easy to find even out to much longer time delays. The following measurement was obtained over the course of 8 scans and the average of these scans was then studied. The pump probe time delays were scanned out as far as 1800 ps but after approximately 5-10 ps there only remained a constant offset in the signal.

Figure 4.28 shows the changes in the transmission spectra of the sample as a function of time delay. There is a clear dispersion in the white light spectrum as can be seen in the gradual change in the 'time zero', or onset of the signal across the spectrum. This has not been corrected for in this figure but was accounted for in the global fitting procedure and for all subsequent analysis. The data was analysed using a sequential global fit procedure and 3 time constants were assigned which were able to satisfactorily describe the dynamics. Two short timescales of 230 $\pm$ 40 fs and 1.38 $\pm$ 0.04 ps were found along with a third constant greater than 2 ns which is equivalent to a constant offset.

In agreement with the previous study of this material, there was a long-lived broad bleach signal between 500 and 700 nm as can be seen to the right of the plot in Figure 4.28. After pump excitation there is a loss in the population of the ground state Cr ion due to excitation into the $^4$LMCT manifold, meaning that

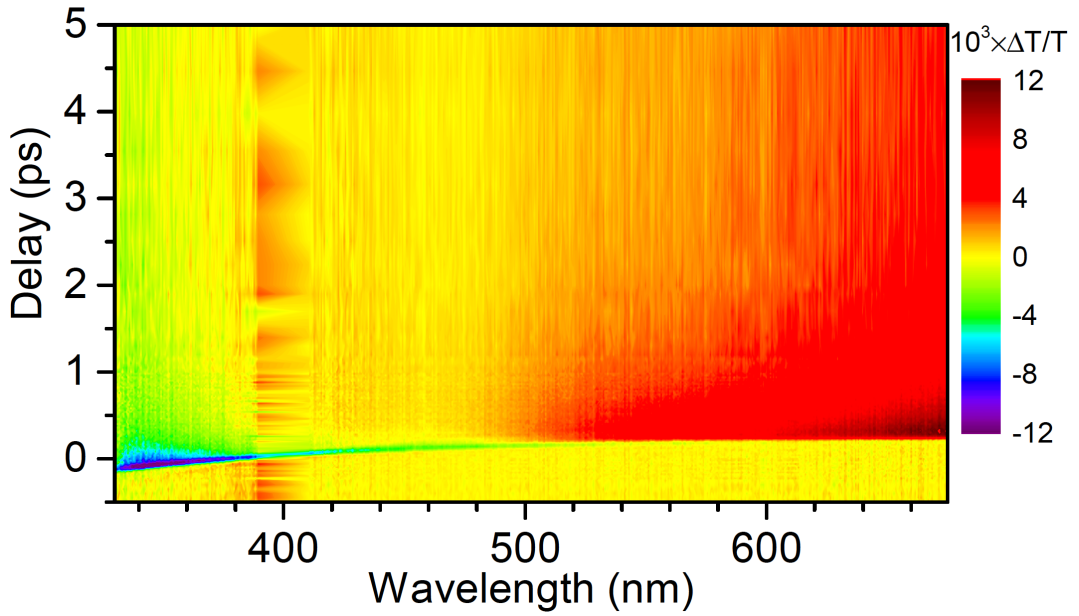


*Figure 4.28: The transient transmission spectra of the VCr PBA as a function of pump-probe time delay up to 5 ps. (The contribution from the pump signal, measured at - 1ps, has been removed from this plot for clarity as it significantly impacts the scaling on the z-axis. This is the anomalous signal around 400 nm.) The change in transmission is displayed on a colour scale. The excited state absorption can be seen to the left of the plot, from 330 nm to 390 nm, as a dark blue section. The bleach of the ground state is shown as the red section to the right, from 540 nm upwards.*

there are fewer sites available to absorb light of the wavelength corresponding to the MM'CT transitions, resulting in an increase in the transmitted light (or loss of absorption) at these wavelengths. There is a small red shift (20 nm) of the position of the ground state bleach signal in this measurement relative to the previous study (660 nm) which is attributed to the variability of the exact nature of these films. The position of the MM'CT can depend on the specific stoichiometry and morphology of the thin films which can vary as a result of slight differences in the conditions of the electrochemical deposition, this is thought to be an acceptable difference in the nature of the film.

The UV part of the spectrum was hitherto unexplored as the previous study

employed a sapphire-generated white light continuum which only spanned 480 - 690 nm. This region of the spectrum did prove to be very interesting as a completely new signal was observed with a negative change in transmission. Although it has not been possible to measure the complementary time-resolved reflectance, this signal has been attributed to a new excited state absorption. When attempting to assign the identity of the state which gives rise to this ESA in the UV part of the spectrum, the initial model which was shown in Figure 4.26 must be carefully considered. The spectral shapes of the ground state bleach and the excited state absorption are quite similar for each of the three time constants found by the global fitting analysis. This implies that there is no significant change in the electronic characteristics of the excited state after the initial dynamics induced by the pump pulse. This same rationale was used by Juban and McCusker to conclude that the $^2$E state was formed on very fast timescales (sub 100 fs) because their femtosecond spectrum matched that of their nanosecond spectrum. Based on the physical model that is being applied in this case, where the intermediate $^4$LMCT state decays to the $^2$E state within the temporal resolution of the experiment of ca. 40 fs, we can indeed attribute this excited state absorption to the $^2$E state.

When plotting these two signals on the same axis, as in Figure 4.29, it is clear that there is a difference in the decay timescales of these two signals which is a result of them probing different states within the dynamic pathway.
Due to the very fast $^4$LMCT decay relative to the available time resolution, we do not observe any evidence of a delayed offset of the excited state absorption and thus we conclude that the $^2$E state is populated within the rise time of the laser pulses. The magnitude of the change in transmission is comparable to the MM'CT bleach signal. This suggests that the nature of the transition, namely charge transfer, is the same in both cases as opposed to any metal-centred (d-d) transitions. This excited state absorption could therefore originate from a red shifted MLCT. This is analogous to what was found during a related

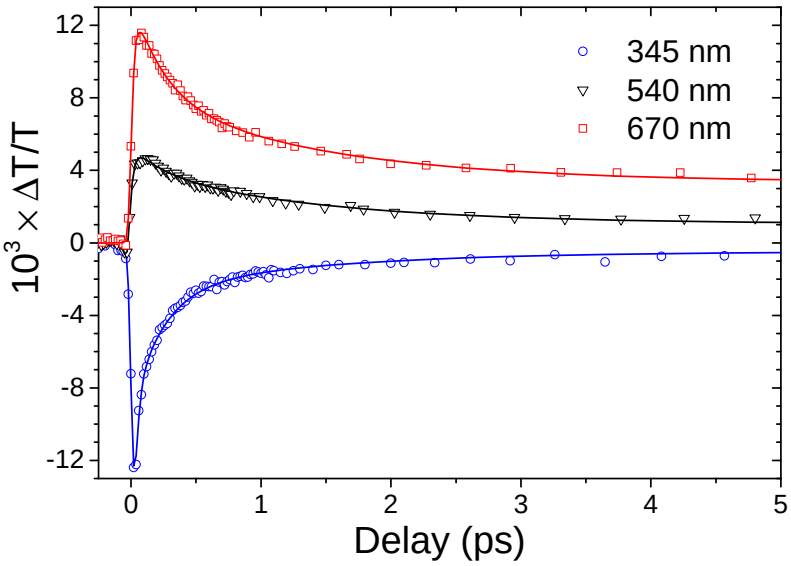


*Figure 4.29: The kinetic traces for selected wavelengths of interest up to 5 ps. The data points are experimental values and the solid lines are the result of the global analysis. These kinetic traces were averaged over a 10 nm bandwidth. It is immediately clear that there is a difference in terms of the initial decay of these two signals (ESA and GSB) as the blue excited state absorption decays much more quickly at short time delays.*

spectroelectrochemical study of the VCr PBA which is discussed in Section 4.1.1. The red shifted MLCT state found in $Cr^{II}$ in this spectroelectrochemical study was observed at 465 nm while the excited state absorption in this experiment is seen at 345 nm, this difference is entirely plausible as the $Cr^{III}$ $^2$E electronic state is expected to be lower in energy than the $Cr^{II}$ species.

A large fraction of the $^2$E state will decay back to the $^4$LMCT via back-intersystem crossing on a sub-100 fs timescale. The resulting EAS shown in Figure 4.30 shows a non-zero contribution of the nanosecond decay component, this corresponds to the fraction of the population which is trapped in the $^2$E state. This is smaller than expected given the plateau of the MM'CT bleach and the signal past around 100 ps is within the noise level. It is therefore difficult to extract information about the decay of this trapped population. The ratio of the first

and second decay component is large in this wavelength range which suggests that the majority of the population decays back to the $^4$LMCT manifold on a 230 fs timescale. The 1.38 ps timescale then corresponds to vibrational cooling of the population trapped in the $^2$E state.

This is further highlighted by the evolution associated spectra generated by the global fitting analysis shown in Figure 4.30 which help to describe the contribution of the time constants to the changes in the spectra. It can be seen that the 230 fs component dominates both regions, but crucially the ratio of the first and second time components is much larger in the UV region than in the visible. The spectral shapes of the three components can be seen to be very consistent across the spectrum which has been previously mentioned.

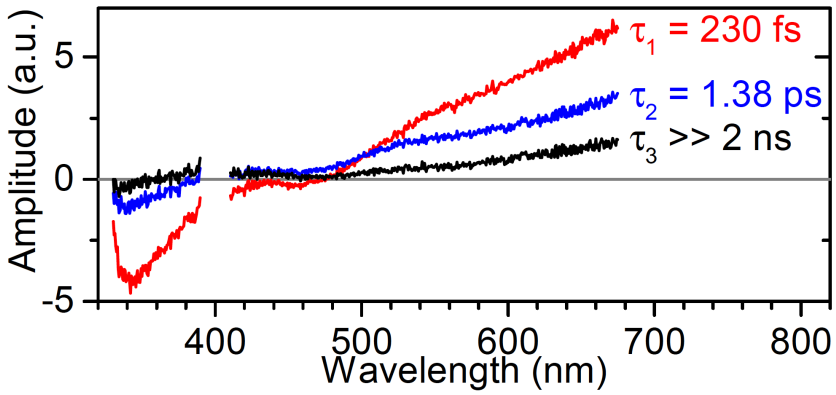


*Figure 4.30: Evolution associated spectra generated by the global fitting procedure. Each of the line plots shows the wavelength-dependant contribution of each of the three decay constants.*

The observation of the ground state bleach and the new excited state absorption means that, of the three electronic configurations presented in Figure 4.26, we now have a spectral signature of the ground $^4A_{2g}$ state and the $^2$E state decay (via the newly observed excited state absorption). This just leaves the intermediate $^4$LMCT state to be observed directly which would then allow us to fully characterise this system's electronic states and their spectral signatures.

In order to observe a signal in the blue region of the spectrum from the $^4$LMCT

state, the data at very short time delays must be scrutinised more closely in the range of 420 - 480 nm. Figure 4.31 shows an expanded plot of the evolution associated spectra for the first two decay constants in this narrow spectral range. Due to the very weak signal in this area the EADS were smoothed to allow the identification of any possible extra absorption features. At 455 nm specifically there is a clear decrease in the transmission of the signal for the shorter 230 fs component, while there is no such change for the 1.38 ps component.

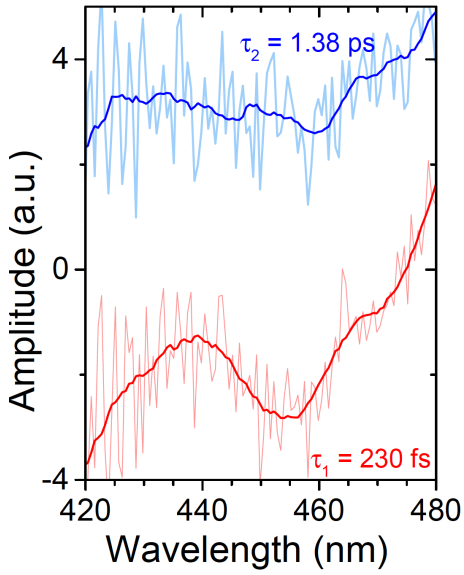


*Figure 4.31: Expanded evolution associated spectra in the region of interest from 420 - 480 nm appear to show an additional feature at approximately 455 nm in the 230 fs component which is absent in the 1.38 ps component. The feature is extremely short lived and therefore cannot be reliably fitted to a decay constant in these measurements.*

The main issues with observing an additional feature in this region are that the timescale appears to be shorter than the pulse duration used to measure it and that it is situated between the two relatively intense GSB to the red and ESA to the blue. We are however confident that this is the correct wavelength region as evidenced by the spectroelectrochemical study described in Section 4.1.1. The decay of this additional absorption feature is indeed very short lived so it becomes

increasingly difficult to extract any reliable dynamics from the coherent artefact from the glass substrate and the chirp of the white light continuum. Clearly a shorter time constant could be included in the global fit to account for this feature but based upon the aforementioned arguments this would be very unlikely to yield any reliable information. There is however something significant in this region which can be further investigated to inform future studies into this family of materials.

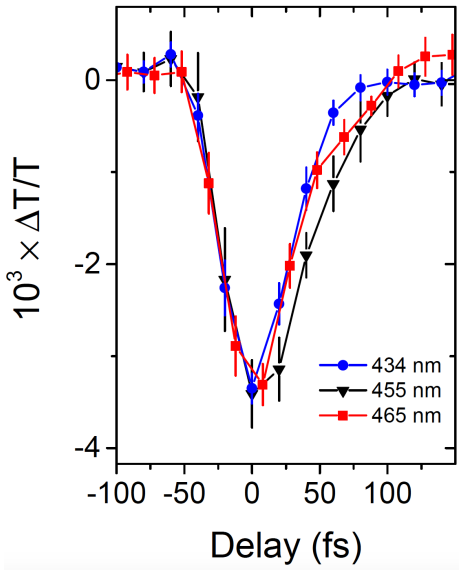


*Figure 4.32: Kinetic traces close to time-zero for three wavelength regions averaged over a 10 nm bandwidth. The error bars are the result of 10 nm bandwidth region averaging. The decrease in the transmission is predominantly due to the coherent signal in the glass substrate, however there is a lingering signal from the 455 nm band which is attributed to the $^4$LMCT.*

Figure 4.32 is a plot of the experimental data, averaged over 10 nm bandwidths, for 434, 455 and 465 nm. The main peak in each of these three plots is a result of the coherent signal from the glass substrate with a full-width half-maximum corresponding to the instrument response function of approximately 50 fs. For the transient at 455 nm there is a clear persistence of the signal for about 20 - 30 fs longer than solely the glass susbtrate signal in the other two channels. From the fact that this signal persists where the others do not and

it also featuring in the EAS, we can conclude that this is indeed an absorption feature of the $^4$LMCT and not simply an ultrafast artefact. To be certain of this, however, it would be necessary to conduct further measurements with even shorted laser pulses to allow these processes to be separated.

**Conclusions**

From this study of the VCr PBA we can conclude that the experimental results are consistent with the formation of a short-lived $^4$LMCT state upon excitation at the LMCT transition, which subsequently decays to the $^2$E state on a sub-100 fs timescale. This state is characterised by a bleach of the MM'CT in the visible (540 - 680 nm) and an excited state absorption in the UV (345 nm). The decay of the observed excited state absorption for the $^2$E state indicates that the majority of the $^2$E population undergoes back-ISC on a 230 fs timescale but that there is a small portion of the population trapped in this state.

We have also observed an additional excited state absorption feature at 455 nm which has been tentatively assigned to the $^4$LMCT state on the Cr ions which is directly populated by the pump pulse. This could be the result of a red-shifted MLCT transition, which is in good agreement with spectroelectrochemical measurements carried out on thin films of this material. Of course, the spectral position found during the ultrafast measurements and the spectroelectrochemical measurements are not necessarily the same due to the different means of reduction and the subsequent movement of potassium counter ions into the film to maintain charge when induced with electrochemistry. Conversely, during the photoinduced measurements, the sample is in the solid state and the electrons are transferred from adjacent cyanide ligands. These differences are also why one is so short lived and the other is much longer timescales due to the counter ion stabilisation. Overall, the very short time constant is in agreement with the work on $Cr(acac)_3$ by Juban and McCusker who noted an observed time constant of 50 $\pm$ 20 fs. The $^4$LMCT state very quickly decays into the $^2$E state. The rate of this decay implies

that the ISC happens on the same fast timescale limited by the instrument-response function of approx. 50 fs.

The ESA signatures for these two states will provide a direct handle on the excited state dynamics where measurements have, up until now, relied on the bleach of the ground state. These results also highlight the power of combining spectroelectrochemistry with ultrafast transient transmission measurements in elucidating femtosecond charge-transfer dynamics in these functional inorganic co-ordination polymers. Given the tunable nature of Prussian Blues, there exists a wide range of analogues with very different absorption spectra depending on the metal centres which can be substituted during the synthesis. Two potentially interesting materials are the FeCr and CrCr analogues which exhibit much lower Curie temperatures but show absorption spectra whose MM'CT band is shifted towards the UV (FeCr PBA) or even completely out of the visible (CrCr PBA) which will prove useful when exploring the changes in the absorption spectra as a function of time. Specifically, both of these analogues still contain the same hexacyanochromate moiety which may open up the direct observation of the $^2$E state in the same spectral region as the studies by McCusker *et al.*

### 4.2.3 Iron-Chromium Analogue

#### Introduction

The FeCr analogue of Prussian Blue was first reported by Ohkoshi *et al.* [33] using electrochemical deposition to generate thin films, which exhibited ferromagnetic ordering with a $T_C$ of 21 K. The FeCr PBA exhibits a strong orange colour due to a metal-to-metal charge transfer (MM'CT) band resulting in a broad absorption band centred at 450 nm. It was found that the magnetisation could be altered optically, by photoexcitation of the MM'CT transition between $Fe^{II}$ and $Cr^{III}$. Approximately a 10% reduction in the sample magnetisation was observed after irradiation for 8 hours under blue light, in a constant magnetic

field of 10 G. This photoreduced magnetisation was found to persist for several days when held at a temperature of 5 K. Mössbauer spectroscopy of the $^{57}$Fe centres showed no change in the spin state or the oxidation state of the iron centres, suggesting that there must have been a decrease in the strength of the ferromagnetic interaction between the $Fe^{II}$ and $Cr^{III}$ causing the change in magnetic behaviour. This resulted in a metastable paramagnetic state which reverted back to the original state upon heating to at least 40 K. Therefore the overall picture is as follows: upon excitation of the MM'CT transition, the excited state is formed which consists of a mixed valence $Fe^{II}$-CN-$Cr^{III}$ and $Fe^{III}$-CN-$Cr^{II}$ structure. This then decays into a metastable state in which the $J_F$ is too weak to maintain the spin ordering. This combination of optical and thermal methods has allowed the photoinduced change in the magnetisation of this functional material to be characterised.

If one wishes to control and utilise the properties of these materials then a more complete understanding of the photophysics at play should be obtained. As such, ultrafast transient transmission measurements have been carried out in order to study the electronic structure of this material in the form of thin films.

**Sample Preparation**

A range of thin films of the FeCr analogue were prepared with a variation of the deposition time in order to produce films over a range of absorbances from around 0.4 OD to approximately 1.0 OD. The optimum thickness of the films is a balance of the amount of signal that can be observed as a change in the static absorption spectrum, against the increasing amount of scattered light that is produced as the film grows in thickness. This range was decided on after some amount of trial and error attempting measurements on these films. The samples were placed in the focus of the beams, inside the electromagnet, and the scattered light was inspected by eye and by studying the spectrum recorded by the cameras. Absorption spectra were compared with static spectra measured independently.

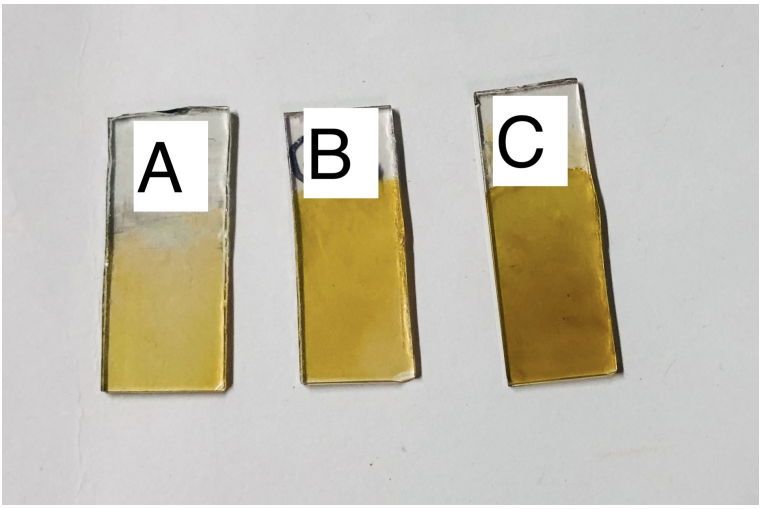


*Figure 4.33: The three FeCr samples of varying thickness and corresponding optical density that were studied in this work. Samples A, B, and C were shown to be approximately 200, 300 and 500 nm thick through AFM studies.*

As previously discussed, the FeCr films are not air sensitive but do undergo a ligand isomerisation over time, so the films were measured typically within a day or two of being synthesised. It was often necessary to make fresh films due to damage incurred when testing the measurements, meaning that the linkage isomerisation was rarely an issue of significant concern. Figure 3.16 shows the IR spectrum focussed on the cyanide stretching region, the peaks are shown to redistribute over the course of two to three days.

The films were synthesised using electrochemical deposition using $FeCl_3$ and $K_3Cr(CN)_6$ at concentrations of 37.5 and 25 mM respectively. Deposition times were varied in order to produce films of around 0.7 OD which was decided on being the optimal thickness. Three films of varying thickness were deposited in order to study the dynamics as a function of the film thickness, these were approximately 200, 300 and 500 nm thick which correspond to the spectra shown in Figure 4.34. As previously mentioned this material is not air sensitive so there is no need for the cover slip and glue on the top of the film, this results in more scattered light than was seen with the VCr sample.

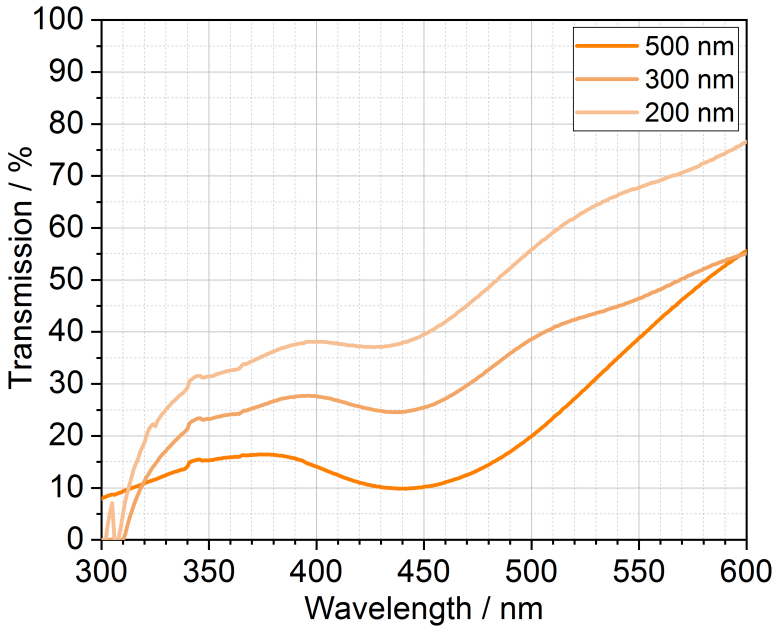


*Figure 4.34: Transmission spectra for three FeCr films which showed a clear signal in the time-resolved measurements in this work. Electrochemical deposition was used to create these films and the thickness was controlled by varying the duration of the applied electrochemical potential. Films of 200, 300 and 500 nm in thickness were deposited.*

### Ultrafast Transient Transmission Measurements of the FeCr PBA

The power damage threshold for this material was assessed independently from the other PBAs due to differences in the crystal structure, film thickness and heat dissipation properties which all presumably impact the power at which irreversible damage is done to the sample. This was achieved by series of transient transmission measurements carried out on different spots of the sample. The transmission spectrum of the sample before the measurement was compared with the spectrum after the measurement to look for any changes which would be indicative of sample degradation. When no damage occurred after a measurement at a given 400 nm pump power then an upper limit of fluence was determined. Measuring the dynamics as a function of the excitation energy gives information

on the nature of the photophysical processes involved in the absorption. The measurements as a function of the film thickness are potentially interesting when considering the slower decay dynamics where energy is dispersed from the lattice of the PBA into the substrate. Through the studies carried out in this work, it is believed that these PBA films, when made using electrochemical deposition, grow from isolated islands at the point of crystal nucleation. These islands then appear to predominantly grow laterally until the point at which the islands coalesce, the film then grows in thickness. If this growth pattern is indeed the case, then the energy dispersion into the crystal structure should significantly slow down when adjacent crystals are not in direct contact with the optically excited material. The growth of these PBA films appears to proceed in two stages; first the crystals grow from individual points of nucleation across the surface of the substrate and once these coalesce the film begins to grow vertically as seen in Figure 4.35.

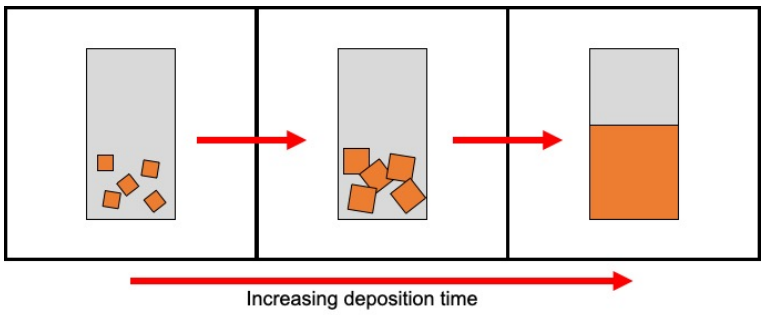


*Figure 4.35: The proposed method of the growth of the PBA films during the applied potential of the electrochemical deposition. From left to right; the crystals grow laterally from the points of nucleation until a continuous film is formed. From there the film grows vertically.*

Measurements were first carried out on a blank substrate in order to rule out any influence which is solely due to the substrate's response to the pump light. Figure 4.36 shows a sharp response around time zero due to the optical Kerr effect which is often termed the cross phase modulation. When this measurement was carried out the overlap of the pump and probe was optimised to be within the substrate which will result in an artificially larger response from the substrate

than would be the case for the response observed during a measurement. During the measurements of the PBAs, the pump-probe overlap is optimised for the film, this is still a useful indication of the reliability of the response around time zero. The width of the response from the substrate at the wavelength regions of 350 and 450 nm was approximately 350 - 400 fs and around 590 nm appears to last approximately 300 fs. This suggests that in these regions any decays which occur on these timescales may be slightly influenced by this signal.

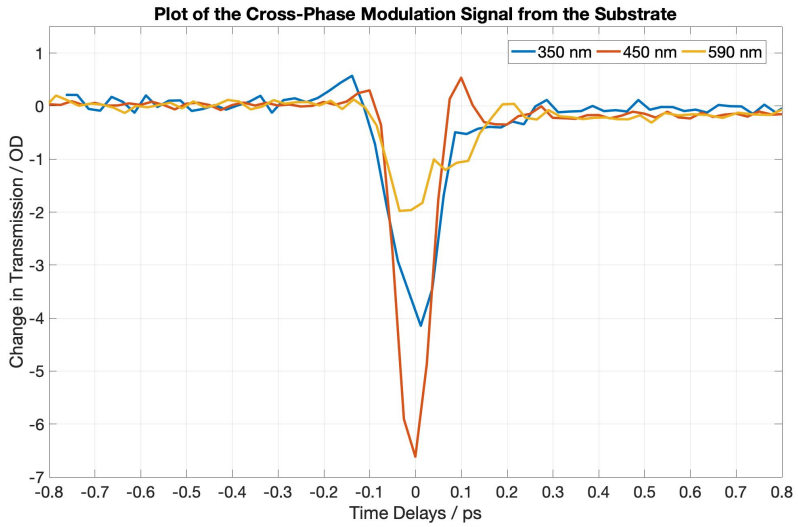


*Figure 4.36: The response of a blank substrate (1 mm thick aluminoborosilicate glass coated with a conductive FTO layer) that was measured in order to characterise the response of the substrate material to the laser pulses which may contribute to the overall signal that is observed during a measurement of the PBAs.*

The sample was secured on a 1" optics mount and placed centrally within the poles of the electromagnet, with the surface of the sample facing the against the laser propagation direction. This is to not introduce any further dispersion due to the white light continuum passing through any more material than is necessary. The polarisation of the white light and pump beams are perpendicular to each other, this has allowed the use of a polariser (ThorLabs - LPVISE100-A) after the sample in order to clean up the signal. The polariser was placed

after the collimating mirror before the light goes to the detectors and the output polarisation axis was aligned with that of the white light continuum. This will help to block out any pump light which has been scattered from the thin film sample and which is not horizontally polarised.

The mounting for the sample allows for easy translation in 3 dimensions to optimise the sample position and to allow the sample to be moved if any photo-induced damage occurs. Optimisation of the overlap was performed by setting the translation stage to several picoseconds after time-zero, at this point in time, the sharp response of the cross phase modulation is not longer visible and the optimisation is based solely on the response from the sample. In the case of the previously studied PBA the ground state bleach is typically the longer lived component and can be clearly observed even at the longest time delays used, which corresponds to a delay time of over 500 ps.

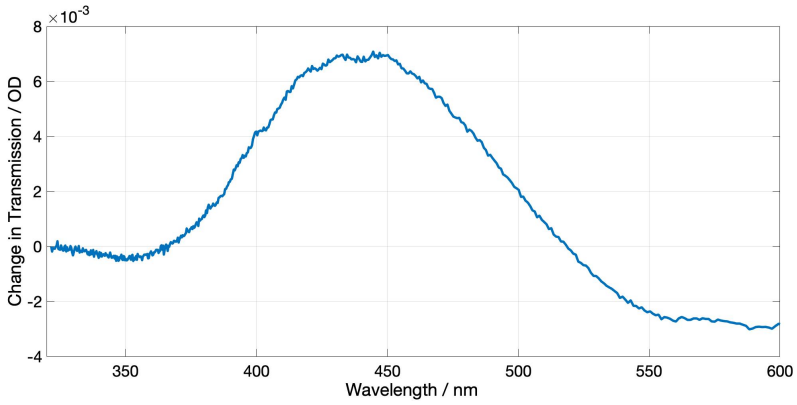


*Figure 4.37: Difference spectrum measured at 5 ps which is used to optimise the overlap of the pump and probe beams in the sample region. The MM'CT ground state bleach is seen as the broad positive signal at 440 nm flanked by two excited state absorption signals at 350 and 565 nm.*

### Results

The measurements as a function of pump fluence were carried out on the same day, on a single sample of 350 nm thickness, with different sample spots

selected for each measurement to avoid any long term damage to the films. The powers selected for these measurements were 600, 800 and 1000 $\mu$W which equate to fluences of 1.50, 2.00 and 2.50 mJ cm$^{-2}$ as these all fall below the estimated damage threshold of approximately 1200 $\mu$W. A single measurement constitutes 1000 shots at each time delay point, typically around 140 time points per full scan, this is then averaged over 3 iterations in order to reduce the noise of the measurement.

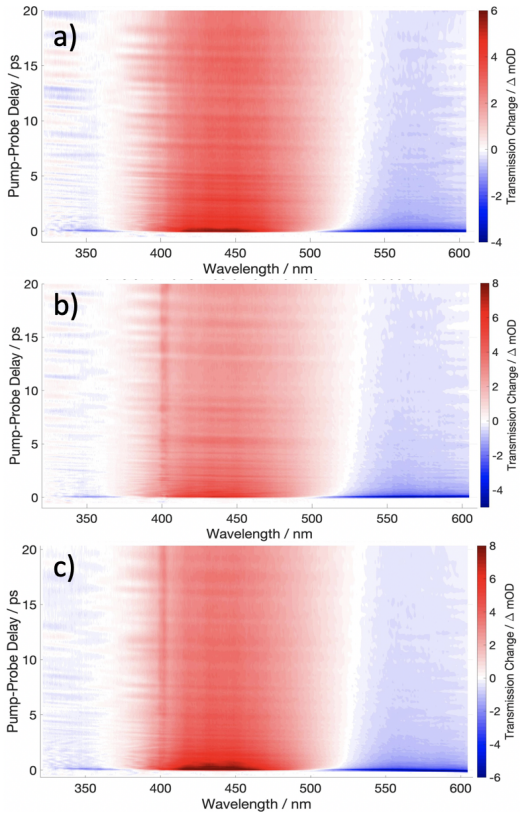


*Figure 4.38: The two dimensional contour plot of the first 20 ps of transient transmission of the FeCr PBA at 600, 800 and 1000 $\mu$W pump power for a), b) and c) respectively. Two excited state absorption signals around 340 nm and 560 nm, and a bleach of the ground state absorption around 440 nm were observed. (The dark vertical line around 400 nm is due to incomplete removal of pump scatter.)*

Figure 4.38 illustrates the signal recorded over the first 20 picoseconds

after photo-excitation of a 300 nm thick FeCr PBA film by the 400 nm pump pulse at the three different fluences. Around the region of the main absorption band at 450 nm, shown in Figure 4.34, a strong bleach of this absorption is seen, as was seen in the VCr PBA, which persists longer than a hundred picoseconds. There are then two excited state absorptions, one which appears in the UV part of the spectrum, around 340 nm, and another one in the visible, around 560 nm. Assuming that these signals originate from the excited state on the Cr moiety then the signals that are observed can be explained using the same model as used for the VCr PBA. For comparison, the measurements at lower powers are shown in Figure 4.38 where it can be seen that these measurements exhibit the same transitions regardless of the power of the pump pulses, as far as was studied in this work. There is an increase in the magnitude of the signals as the power of the pump pulse is increased, but in order to study any changes in the dynamics, the fits must first be studied in more detail.

The difference spectra as a function of time delay, ie. horizontal cuts through the 2D contour plots in Figure 4.38, are useful to illustrate the order of the processes occurring in the material by their spectral signatures. The first plot is taken before time zero and as such displays no signal in the difference spectra as the pump beam has not been applied to the sample yet. The first plot after time zero shows a maximum for each of the three bands in this material, the ground state bleach and the two excited state absorptions. This indicates that within the first 500 fs, the excited state populations are generated and decay from here as the time delay is increased. There is a significant drop in signal between 500 fs and 1 ps for the excited state absorption and between 1 ps and 5 ps for the ground state bleach which gives an approximate indication of the decay timescales for these processes.

The ESA which is found in the UV part of the spectrum is comparable in nature to the analogous signal found in the VCr PBA. The signal also exhibits a very fast initial decay, where approximately 90 % of the signal is lost within the

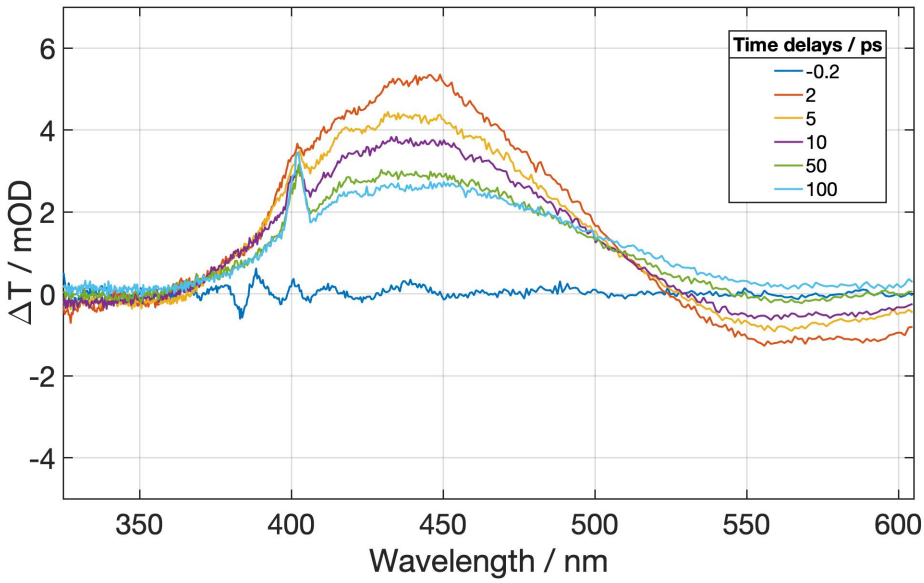


*Figure 4.39: The difference spectra of the FeCr measurement for various time delays plotted on the same axis in order to visualise the order of processes occurring. The spike observed around 400 nm is due to stray pump light which reaches the detectors.*

first few hundred femtoseconds after pump excitation which appears to be slightly faster than in the VCr analogue. This signal is therefore tentatively attributed to the same excited state absorption from the $^2$E state on the $Cr^{III}$ ion.

This signal appears to follow the same decay dynamics independent of the applied pump power, although there is a slight deviation with the two lower power measurements after the initial fast decay. There appears to be a less obvious difference between these compared with the highest power measurement. They all appear to follow the same very fast sub 100 fs decay immediately after excitation, the slower components of the decay also appear consistent.

In order to more closely study the nature of the decay, dynamics of this band were also fitted independently of the other spectral features, ie. no longer a global fit. This allows for greater control over the parameters and a closer fit to the data to be obtained.

The next signal that can be analysed is the bleach of the ground state absorption

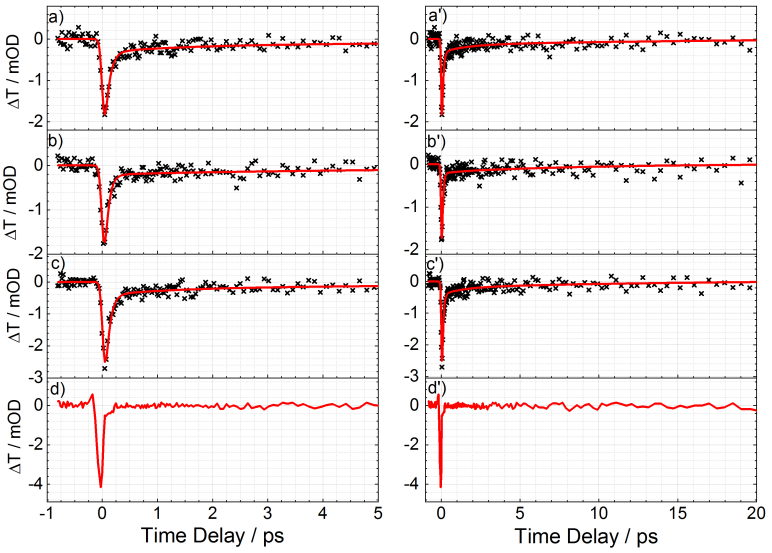


*Figure 4.40: The initial decay dynamics for the excited state absorption of the FeCr analogue at 350 nm as a function of the applied pump power. The plots in a) and a') correspond to a 400 nm pump power of 600 μW, plots b) and b') correspond to a 400 nm pump power of 800 μW, plots c) and c') correspond to a 400 nm pump power of 1000 μW. The plots in d) and d') are the corresponding substrate background measurements of the substrate.*

centred at 440 nm which is analogous to the ground state bleach seen in the VCr analogue which was centred around 540 - 660 nm. The position of this signal is obviously tied to the static absorption spectrum of the sample which in turn is a function of the MM'CT transition process. Figure 4.41 is a plot of the initial decay dynamics for this ground state bleach recovery over the first 5 picoseconds.

As was the case in the VCr PBA (and in the excited state absorption), there is a portion of the population which decays with a very fast time component, however in this sample a much larger percentage of the signal loss remains and recovers on a slower nanosecond timescale. This was also the case in the VCr PBA where an overall slower decay of the ground state bleach was observed when compared to the excited state absorption. The recovery of this ground state

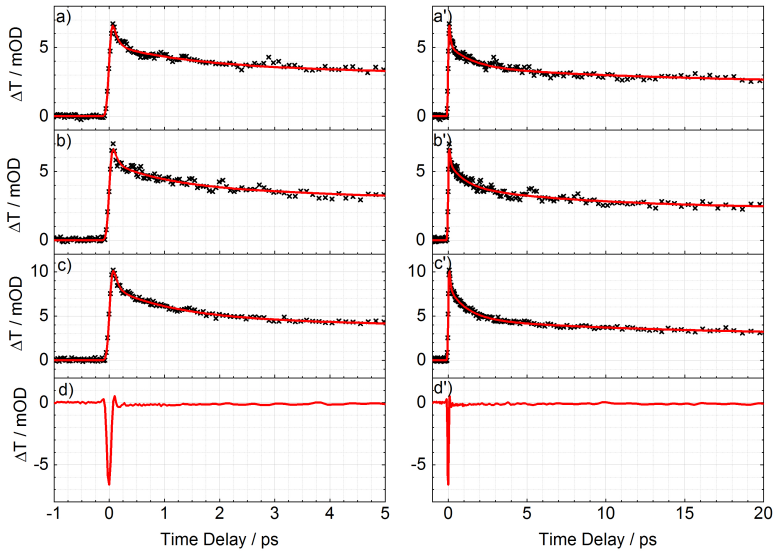


*Figure 4.41: The initial recovery dynamics for the ground state bleach of the FeCr analogue at 440 nm as a function of the applied pump power. The plots in a) and a') correspond to a 400 nm pump power of 600 μW, plots b) and b') correspond to a 400 nm pump power of 800 μW, plots c) and c') correspond to a 400 nm pump power of 1000 μW. The plots in d) and d') are the corresponding substrate background measurements of the substrate.*

bleach requires the excited state population to decay back to the $^4A_{2g}$ ground state, which is why this process has a much slower decay time when compared to the explicit signal from the $^2E$ state.

The third signal which is observed is in the visible region of the spectrum around 570 nm and is another excited state absorption. This signal is assumed to be an excited state absorption from the $^2E$ state which has previously been reported by [5] in analogous chromium centred complexes such as the $Cr(acac)_3$. This spectral signature was notably not observed in the VCr PBA due to the signal overlapping with the strong ground state bleach in this region of the spectrum. The FeCr analogue was one of the analogues chosen to further study this family of compounds because its static absorption spectrum was shifted sufficiently to

allow the $^2$E ESA signal to be observed.

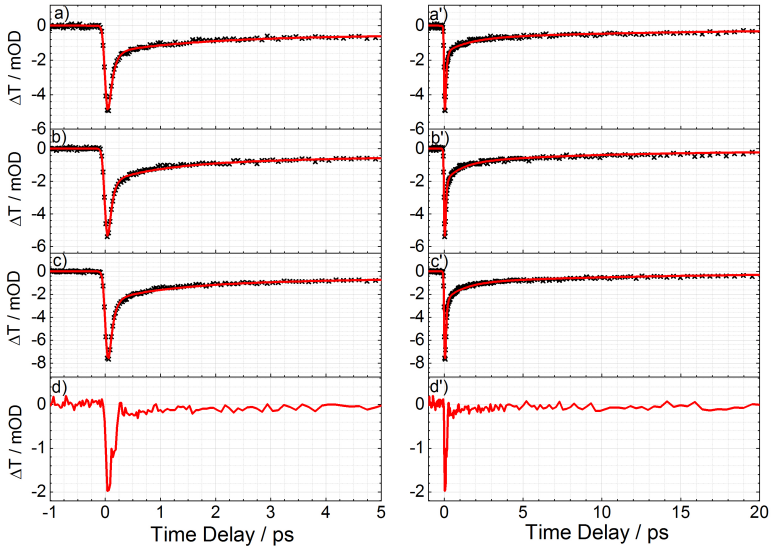


*Figure 4.42: The initial decay dynamics for the excited state absorption of the FeCr analogue at 580 nm as a function of the applied pump power. The plots in a) and a') correspond to a 400 nm pump power of 600 μW, plots b) and b') correspond to a 400 nm pump power of 800 μW, plots c) and c') correspond to a 400 nm pump power of 1000 μW. The plots in d) and d') are the corresponding substrate background measurements of the substrate.*

The decay dynamics of this channel in the visible follows very similar behaviour to the excited state absorption which was seen in the UV part of the spectrum in that the majority of the signal decays on a very fast, approximately 100 fs timescale. All three power measurements appear to follow the same, or very similar, dynamics through the first 5 picoseconds as has been the case for each of the other signals. There is again a more pronounced difference between the highest power measurement and the two lower power measurements, this could again indicate a non-linear signal response.

The global fitting analyses for these three measurements were carried out until a satisfactory fit was achieved which was able to describe all the dynamics of

the system with the minimum number of parameters across all wavelengths. The minimum number of variables was found to be 3 temporal parameters which were used to describe the shorter-lived dynamic processes and a fourth value which was constrained to be a 1 nanosecond decay which is the equivalent to a constant offset in the signal. This accounts for the slow recovery of the ground state bleach, which only recovers by the time the next laser pulse arrives approximately 1 ms later.

| Pump Power ($\mu$W) | $\tau_1$ (fs) | Error | $\tau_2$ (ps) | Error | $\tau_3$ (ps) | Error |
|---|---|---|---|---|---|---|
| 600 | 80 | 0.6 | 1.5 | 0.014 | 16.9 | 0.18 |
| 800 | 70 | 0.7 | 1.0 | 0.01 | 9.2 | 0.09 |
| 1000 | 70 | 0.08 | 1.2 | 0.04 | 13.3 | 0.06 |

*Table 4.1: The global fitting parameters found for the FeCr analogue as a function of the applied 400 nm pump power and the error values produced by Glotaran. In all cases there is also a 1 ns decay component which mimics the plateau which is seen past the end of the maximum time delay.*

The data shown in Table 4.1 shows the output of the global fitting procedures for the three data sets which have been discussed thus far. The errors for the three kinetic parameters are approximately 1 percent of the assigned value which was attained once converged, typically after approximately 10 optimisation iterations. There does not appear to be a trend within these values and they all appear to describe a similar decay dynamics across each of the three pump power measurements.

Figure 4.43 shows the decay associated spectra (DAS) for the global fit for the 1000 $\mu$W measurement. $\tau_1$ is by far the most dominant coefficient for the two ESA signals at 350 and 580 nm which matches well with what is observed in the kinetic traces. The bleach signal at 450 nm is much more a mix of shorter and longer timescale decays giving a more gradual decay over a longer period of

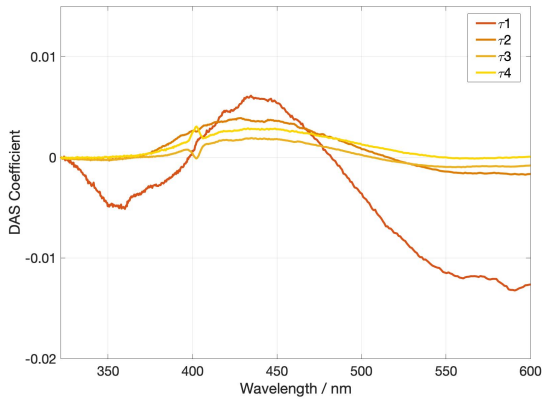


*Figure 4.43: The decay associated spectra which were output from the global fitting procedure of the FeCr vs 400 nm pump power, using the Glotaran software package. $\tau_{1\text{-}3}$ correspond to those shown in Table 4.7 and $\tau_4$ corresponds to the constant offset parameter.*

time. The constant offset parameter, $\tau_4$ only has a significant coefficient for the bleach signal which reflects there only being a significant long lived plateau for this band.

Given what has been discussed thus far with respect to the VCr and FeCr analogues, $\tau_2$ and $\tau_3$ are assigned to vibrational cooling on the $^2$E state and thermal dissipation of heat from the crystal structure respectively. This is thought to occur through transfer to the surroundings such as adjacent crystals or the FTO substrate itself. In order to test this hypothesis, another series of experiments were carried out.

From previous AFM analysis of the FeCr PBAs, particularly Figure 4.15, the thinnest of these films was estimated to be within the range of lateral growth as in the initial two frames of Figure 4.35. The two subsequent films reside well within the range of thicknesses where the growth appears more linear, and for this reason we believe that a more complete coverage of the films has been attained. Therefore of these three films, if the idea that the intercrystal coupling is faster than the coupling to the FTO substrate, we would expect the first film to show a slower decay component $\tau_3$. This slower decay would correspond to the

thermal redistribution of excess energy in the excited state into the substrate as opposed to into adjacent crystals. The $\tau_3$ for the two thicker films should then be similar to each other, but indicate a faster decay due to the close contact with the neighbouring crystals when compared with the thinnest film.

The measurements were set up in the same way as the pump power dependence measurements but were carried out on a separate day in order for these to be carried out in a single session to ensure consistency of the output of the laser. These measurements were all carried out at intermediate pump power of 800 $\mu$W to reduce the increased amount of scattered light that was produced when studying a film which is thicker than was deemed optimal for these optical measurements.

The first results for these are shown in Figure 4.44 which illustrates the initial decay dynamics of the excited state absorption which is located in the UV part of the spectrum around 350 nm. As has been previously observed in previous measurements of the FeCr and the VCr PBA the excited state absorption typically exhibits faster decay dynamics relative to the ground state bleach signals. This is also illustrated by the decay associated spectra which is used to assign the decay components to their spectral features.

The dynamics of the ground state bleach are shown in Figure 4.45 which exhibit a sharp increase in transmission followed by a slower signal recovery when compared with the ESA in the UV. This generally matches with what was seen for the VCr analogue. Again this can be related to the decay components by studying the DAS. There appears to be a slower, longer timescale decay in the thinnest of the samples (panels a) and a')) relative to the thicker samples.

The second excited state absorption, observed in the visible part of the spectrum, at around 590 nm, appears to show no dependence on the thickness of the film as seen in Figure 4.46. The three samples appear to follow the same dynamics with a sharp initial decay followed by a slower decay over 10 - 20 ps.

The most important difference to be considered between the VCr and

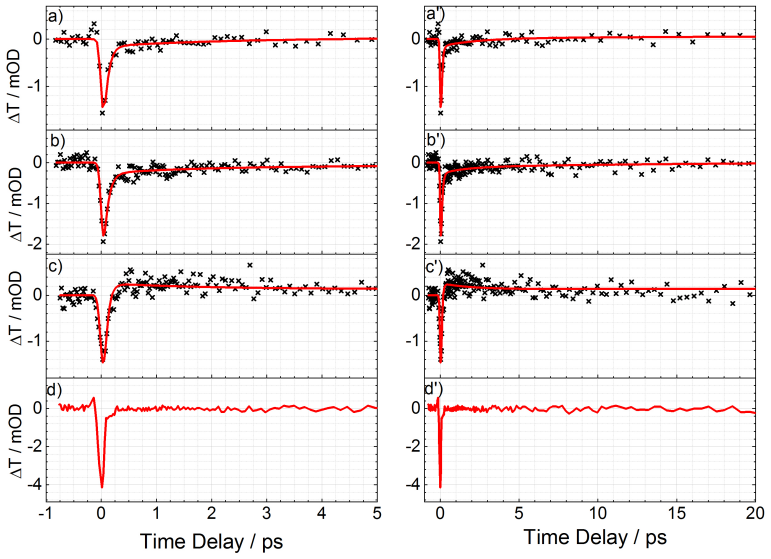


*Figure 4.44: The initial decay dynamics for the excited state absorption of the FeCr analogue at 350 nm as a function of the thickness of the thin films, after 400 nm excitation at 800 μW. The plots in a) and a') correspond to a film thickness of 200 nm, plots b) and b') correspond to a film thickness of 300 nm, plots c) and c') correspond to a film thickness of 500 nm. The plots in d) and d') are the corresponding substrate background measurements of the substrate.*

FeCr samples is the relative crystallinity of the samples. The VCr PBA is believed to be an amorphous film; no evidence of discrete crystal structures have been observed over the course of this project. Whereas the FeCr PBA is a highly crystalline film composed of many individual cubic crystals. The introduction of these crystal boundaries would inhibit the flow of thermal energy from the point of excitation to the surroundings. This third, slower decay constant is therefore attributed to this thermal dissipation of energy to the surroundings. If this is indeed the case then one may expect a significant difference in this decay constant as a function of the film thickness, given what has been recently discussed with respect to the two stage growth of the PBA films. If a film's deposition is stopped when the film is still in the first stage of growth, ie. the lateral growth of the

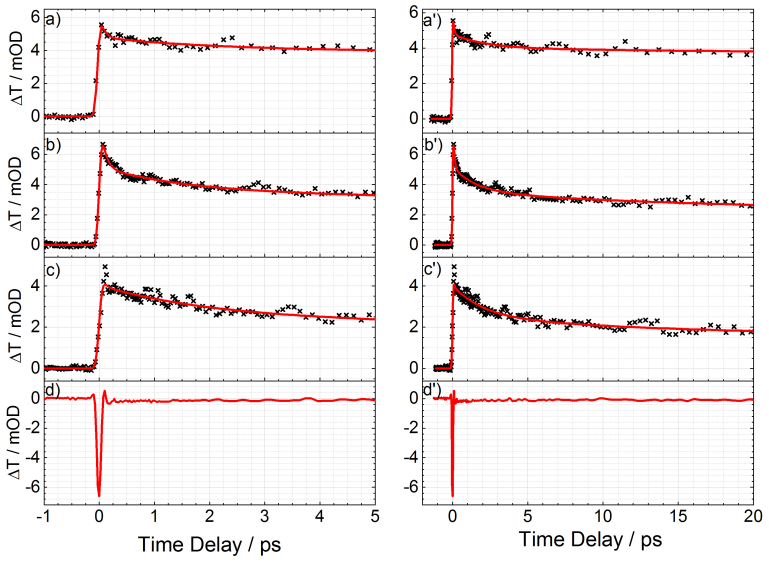


*Figure 4.45: The initial recovery dynamics for the ground state bleach of the FeCr analogue at 440 nm as a function of the thickness of the thin films, after 400 nm excitation at 800 μW. The plots in a) and a') correspond to a film thickness of 200 nm, plots b) and b') correspond to a film thickness of 300 nm, plots c) and c') correspond to a film thickness of 500 nm. The plots in d) and d') are the corresponding substrate background measurements of the substrate.*

islands formed at the points of nucleation, then the contact with adjacent crystals will be much lower than if the film has reached the second growth stage, where a mostly continuous film is formed which then grows vertically with continuing electrochemical deposition.

The very fast initial decay dynamics which are described by the $\tau_1$ decay constant in the model used to previously describe these dynamics appear to be very similar across the three sample thicknesses. The three samples have decay constants of 80, 80 and 60 fs respectively, while the errors for these fitting parameters are all small (approximately 1% of the parameter) these values all fall below the attainable time resolution of the experimental setup. This means that the exact value should not be scrutinised too closely but the fits all definitely

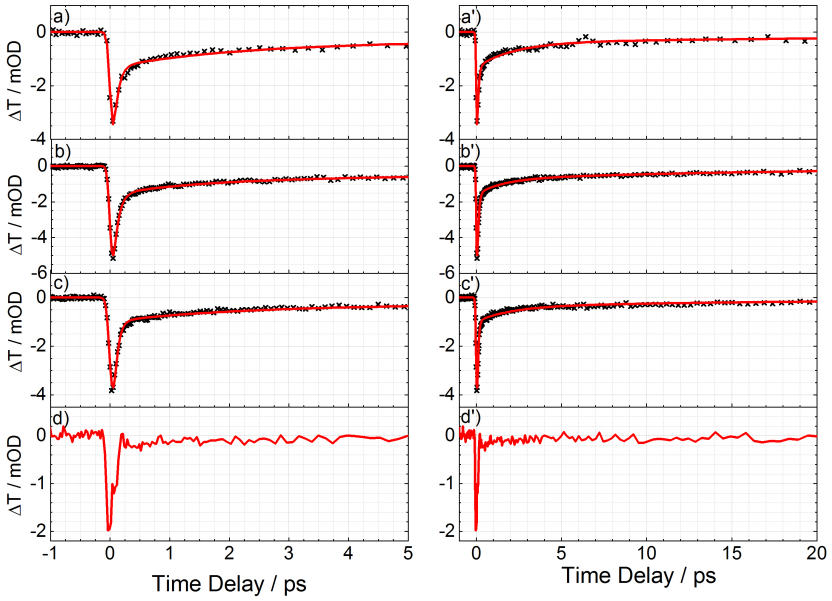


*Figure 4.46: The initial decay dynamics for the excited state absorption of the FeCr analogue at 590 nm as a function of the thickness of the thin films. The plots in a) and a') correspond to a film thickness of 200 nm, plots b) and b') correspond to a film thickness of 300 nm, plots c) and c') correspond to a film thickness of 500 nm. The plots in d) and d') are the corresponding substrate background measurements of the substrate.*

indicate a component in the sub 100 fs regime. This decay constant describes the very fast decay of the $^2$E state which is localised to single chromium ions and as such should not be effected by the variation in thickness of the films.

The next time constant to be considered is $\tau_2$ which was previously assigned to the vibrational relaxation of the ligand-field manifold of the $^2$E. Again, the values which are output from the fitting protocols are fairly consistent across the range of thicknesses, at 2.2, 1.5 and 2.0 picoseconds for the three samples respectively. Given the nature of the FeCr PBA crystal structure, the rigid octahedral arrangement of the ions is very consistent regardless of the size of the crystals when compared with the size of a single monomeric unit of the PBA.

It was found that there was a significant difference for the $\tau_3$ decay constant, unlike the values for $\tau_2$ and $\tau_1$. The values for each of the films were approximately 68, 9 and 15 picoseconds for the 200, 300 and 500 nm thick films respectively. Straight away it can be seen that the first of these values is significantly larger than in any of the other measurements and fits which have been obtained thus far. The $\tau_3$ decay constant for the film of approximately 200 nm thickness is approximately 6 times larger than the constants for the thicker films, but also for any of the power dependent measurement fits that have been obtained.

| Film Depth (nm) | $\tau_1$ (fs) | Error | $\tau_2$ (ps) | Error | $\tau_3$ (ps) | Error |
|---|---|---|---|---|---|---|
| 200 | 80 | 0.2 | 2.20 | 1.3 | 67.8 | 0.02 |
| 300 | 80 | 0.7 | 1.50 | 0.01 | 9.2 | 0.09 |
| 500 | 60 | 0.2 | 2.00 | 0.045 | 14.7 | 0.01 |

*Table 4.2: The global fitting parameters found for the FeCr analogue as a function of the film thickness and the error value generated by Glotaran. In all cases there is also a 1 ns decay component which mimics the plateau which is seen past the end of the maximum time delay.*

The overall fitting parameters for the varied thickness measurements are shown in Table 4.2, which allow the values to be easily compared across the three measurements. As previously discussed, the $\tau_1$ and $\tau_2$ parameters are consistent with each other through all of these measurements and those carried out previously when studying the dynamics as a function of the applied pump power. The only notable difference is seen in the $\tau_3$ parameter which is attributed to the thinnest of the films studied in this work, which is approximately 200 nm thick, where the decay constant is several times slower in this case. This is attributed to the lack of lateral connectivity with adjacent crystals within the film which inhibits the thermal dissipation of energy from the point of excitation to the surrounding material. This appears to be the preferred method of energy

transfer as the contact with the FTO coated substrate should be very similar across all samples.

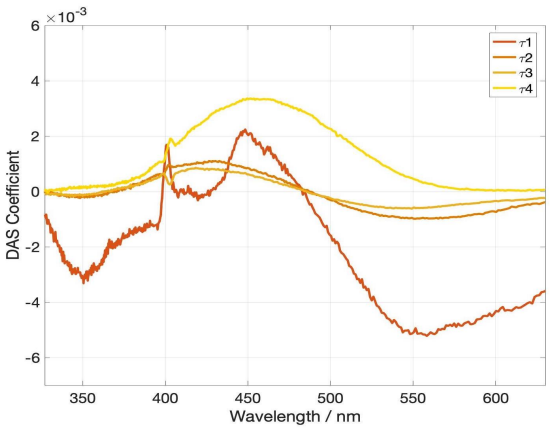


*Figure 4.47: The decay associated spectra which were output from the global fitting procedure of the FeCr vs 400 nm pump power, using the Glotaran software package. $\tau_{1\text{-}3}$ correspond to those shown in Table and $\tau_4$ corresponds to the constant offset parameter.*

Figure 4.47 shows the DAS for the measurement of the thinnest FeCr sample studied in this work. There appears to be some differences from the previously presented DAS plot, Figure 4.43. The $\tau_1$ component is still the dominant feature across the spectrum however the three other components are much more prominent across all wavelengths. Particularly $\tau_4$, which appears to be dominant at the wavelength region corresponding to the ground state bleach where the significant increase in the decay time is observed.

### Alternative Fitting Procedure

In order to be sure that the results obtained from the global fitting procedures were reliable, an alternative fitting was carried out on individual signals in order to more accurately fit each decay or recovery at the cost of requiring more parameters overall. The fitting was carried out using the MATLAB 'Curve Fitting' application which allows a custom equation to be selected by the user and all of the parameters individually changed in order to obtain a better fit

to the dataset. The equations which were used depended on the dataset and the characteristics that were needing to be fitted, an example of one such equation is:

$$(a0+(a1*e^{(\text{-(x-td)/t1})})+(a2*e^{(\text{-(x-td)/t2})})+(a3*e^{(\text{-(x-td)/t3})})).*(erf((x-td)/w0)+1) \tag{4.1}$$

The equation above consists of one constant offset (a0), which accounts for the fact that some of the measurements do not return to zero within the timescale of the measurement and three time dependent components which have an amplitude and a decay time associated with each one. There is finally an error function which performs a deconvolution of the fitting components that the observed measurement response is much longer than the length of the pulse itself due to the actual overlap of the pulses and temporal broadening. $\omega 0$ is used to characterise the measured temporal width of the pump laser pulse which controls the rise time of the signal to be non-instantaneous which is unrealistic of a pulse of finite width. The $a$ parameters correspond to amplitudes of each of the components in the fit, the $t_x$ parameters are the time constants for each of the components.

Fits were repeated for all of the samples in order to allow a more critical comparison of the obtained decay constants. It was possible to fit both of the FeCr excited state absorptions with the same parameters and the ground state bleach signal with a second set of parameters which were able to very closely match the dataset. For the measurements as a function of the applied 400 nm pump power then the following parameters were obtained:

The obtained parameters shown in Table 4.3 actually match fairly well with what was obtained using the global fitting parameters with values of around 100 fs, 1.1 ps and around 18 ps which are attributed to the fast decay of the $^2$E state, the vibrational relaxation on the $^2$E state and then the thermal dissipation of energy into the surrounding lattice and substrate.

| Pump Power $\mu$W | $\tau_1$ (fs) | A Coeff | $\tau_2$ (ps) | A Coeff | $\tau_3$ (ps) | A Coeff |
|---|---|---|---|---|---|---|
| 600 | 100 | -3x10$^{-3}$ | 1.2 | -4x10$^{-4}$ | 22 | -3x10$^{-4}$ |
| 800 | 75 | -3x10$^{-3}$ | 0.8 | -7x10$^{-4}$ | 14 | -3x10$^{-4}$ |
| 1000 | 100 | -5x10$^{-3}$ | 1.2 | -7x10$^{-4}$ | 19 | -5x10$^{-4}$ |

*Table 4.3: The fitting parameters found for the UV excited state absorption of the FeCr analogue as a function of applied pump power, using the same data as was previously presented. The pre-exponential coefficients for each of the decay constants are also given. In each case there is an a0 parameter which accounts for the fact that the signals remain offset to the maximum time delay of the measurement.*

The time constants which were obtained for the recovery of the ground state bleach, shown in Table 4.4 are generally longer than those obtained for the excited state absorption, this makes sense as the GSB looks to live much longer than the ESA. There is again a component around 150 fs which may correspond to the almost instantaneous loss of the $^2$E state which is seen in the ESA signals. There is another component around 2 ps which could be attributed to the recovery of the ground state after vibrational relaxation in the excited state. There is then another component around 20 ps which matches with all previous measurements and is attributed to the thermal dissipation of energy into the surroundings.
There do not appear to be any trends observed in the data as a function of the increasing pump power, instead the observed fits are fairly consistent across the three measurements. This could be further tested by increasing the range of the fluences studied, however the 1000 $\mu$W measurement was determined to be just below the damage threshold of the material.

The datasets for the measurements as a function of the film thickness were then refitted again, this will also allow a more accurate fit to be constructed but crucially will allow a more critical study of the perceived difference in $\tau_3$ with

| Pump Power $\mu$W | $\tau_1$ (fs) | A Coeff | $\tau_2$ (ps) | A Coeff | $\tau_3$ (ps) | A Coeff |
|---|---|---|---|---|---|---|
| 600 | 170 | -1x10$^{-3}$ | 1.5 | -7x10$^{-4}$ | 15 | -7x10$^{-4}$ |
| 800 | 180 | -2x10$^{-3}$ | 2.9 | -5x10$^{-4}$ | 25 | -4x10$^{-4}$ |
| 1000 | 100 | -2x10$^{-3}$ | 1.2 | -2x10$^{-3}$ | 21 | -1x10$^{-3}$ |

*Table 4.4: The fitting parameters for the ground state bleach of the FeCr analogue as a function of applied pump power, using the same data as was previously presented. The pre-exponential coefficients for each of the decay constants are also given. In each case there is an a0 parameter which accounts for the fact that the signals remain offset to the maximum time delay of the measurement.*

the thinnest of the samples.

| Film Depth (nm) | $\tau_1$ (fs) | A Coeff | $\tau_2$ (ps) | A Coeff | $\tau_3$ (ps) | A Coeff |
|---|---|---|---|---|---|---|
| 200 | 90 | -2x10$^{-3}$ | 1.1 | -5x10$^{-4}$ | 26 | -2x10$^{-4}$ |
| 300 | 75 | -3x10$^{-3}$ | 0.8 | -7x10$^{-4}$ | 14 | -3x10$^{-4}$ |
| 500 | 100 | -2x10$^{-3}$ | 1.3 | -2x10$^{-4}$ | 21 | -3x10$^{-4}$ |

*Table 4.5: The fitting parameters for the excited state absorption in the UV of the FeCr analogue as a function of film thickness. The pre-exponential coefficients for each of the decay constants are also given. In each case there is an a0 parameter which accounts for the fact that the signals remain offset to the maximum time delay of the measurement.*

The fitting parameters shown in Table 4.5 were obtained for the excited state absorption of the FeCr PBA and appear to show a similar behaviour to the previous fits. There is a fast component at <100 fs which is attributed again to the fast decay of the $^2$E state as previously discussed. There is again an approximately 1 ps component which matches well with the previously assigned vibrational decay in the $^2$E state. Finally there is again an approximately 20 ps component which has been assigned to the thermal dissipation of heat to the

surrounding crystals and substrate.

| Film Depth (nm) | $\tau_1$ (fs) | A Coeff | $\tau_2$ (ps) | A Coeff | $\tau_3$ (ps) | A Coeff |
|---|---|---|---|---|---|---|
| 200 | 80 | -3x10$^{-3}$ | 3.1 | -6x10$^{-4}$ | 363 | -7x10$^{-4}$ |
| 300 | 180 | -2x10$^{-3}$ | 2.9 | -5x10$^{-4}$ | 25 | -4x10$^{-4}$ |
| 500 | 100 | -2x10$^{-3}$ | 2.3 | -5x10$^{-4}$ | 13 | -7x10$^{-4}$ |

*Table 4.6: The fitting parameters for the ground state bleach of the FeCr analogue as a function of film thickness. The pre-exponential coefficients for each of the decay constants are also given. In each case there is an a0 parameter which accounts for the fact that the signals remain offset to the maximum time delay of the measurement.*

The fitting parameters in Table 4.6 were obtained to describe the ground state bleach dynamics in the FeCr PBA as a function of the film thickness.The values for $\tau_1$ and $\tau_2$ appear to match generally with what has been observed previously, however there is a significant difference observed in the value for $\tau_3$ in the thinnest of these samples which was approximately 200 nm thick. The value found was approximately 363 ps, which is at least one order of magnitude larger than anything which has been observed for the PBA samples thus far. This can be seen in Figure 4.45 a) and a') as a very slow decay after the initial loss of signal, this signal remains at this level out as far as the delay stage can travel (>500 ps) whereas the other signals always show a much greater loss of signal over the first 20-30 ps where they then reach a plateau.

These new fits generally show a similar behaviour to the global fits which were obtained using Glotaran but show closer fits to the dataset for each respective signal. The repeated fitting of the thickness measurements give credence to the observed difference in the recovery of the ground state absorption due to the thickness of the film. In the thinnest of these films the observed $\tau_3$ was significantly slowed down. This time constant has previously been attributed to the thermal dissipation of heat to the surrounding crystals. In the case of

this thinnest FeCr sample the crystals are considered isolated as was previously discussed in Figure 4.35. As such, the thermal dissipation of energy is slowed down due to the crystal isolation, the energy must therefore flow into the substrate instead which appears to be less efficient.

### 4.2.4 Chromium-Chromium Analogue

#### Introduction

The chromo-hexacyanochromate analogue has been reported to exhibit ferrimagnetic ordering with $T_C$ as high as 270 K but this was found to be heavily dependent on the exact composition of the material. [25, 26, 28] As such, these films fulfil multiple criteria for fitting into this study favourably; they possess magnetic ordering with a high $T_C$ and they also have a favourable absorption spectrum for observing the signature of the $^2E$ state. The MM'CT transition is shifted entirely out of the visible region of the spectrum and as such shows no significant structure in this region which would otherwise obscure observing the excited state absorption which may be present between 500 and 600 nm.

#### Sample Preparation

Again, a range of thin films of the CrCr analogue were prepared with a variation of the deposition time in order to produce films over a range of absorption levels from around 0.05 OD to approximately 0.7 OD. The range of thicknesses was decided on after some amount of trial and error when studying these films and was done independently from the trials that were carried out for the FeCr films due to the difference in oscillator strength of the two materials and therefore the difference in the relationship between thickness and OD.

Figure 4.48 shows the absorption spectra of the three films which were studied in this work, in a comparable fashion to the studying of the FeCr analogue in order to draw meaningful conclusions on the influence of the metal center

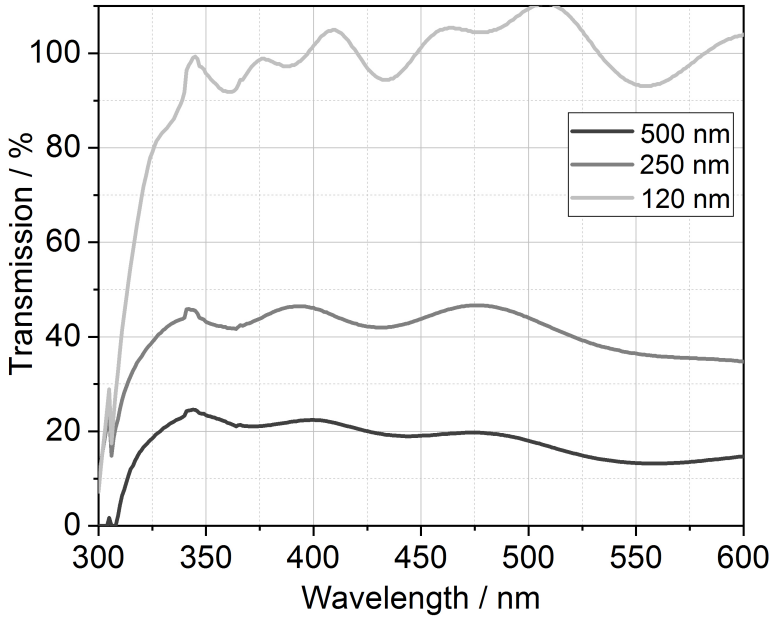


*Figure 4.48: Absorption spectra for the three CrCr films which were studied in this work. Electrochemical deposition was used to create three films of 120, 250 and 500 nm thickness. The thickness was controlled by varying the duration of the applied electrochemical potential.*

substitution or varying of the crystallinity of the material. The CrCr material is also not air sensitive like the FeCr material, which means that there is no need for any cover slides and glue which were used in the VCr material studies. This also means that the crystallinity of the material can be studied using AFM or comparable techniques in order to characterise the material to aid with result analysis.

### Ultrafast Transient Transmission Measurements of the CrCr PBA

The power threshold and optimal thickness was assessed independently from the FeCr and VCr analogues. During the setting up and optimisation of the measurements, a few test measurements were carried out to ascertain the optimal thickness. This turned out to be much thinner, below 300 nm, than had

been made for previous characterisation studies due to the CrCr PBA not being strongly coloured like the other analogues and thus it proved more difficult to estimate the correct thickness. It was again possible to estimate the thickness of these films after having created a calibration curve by comparing absorption measurements and AFM measurements.

To obtain the correct power threshold value, measurements were carried out and the difference spectra before and after the scans were compared to look for any differences induced by photophysical damage to the film in that particular spot. It is always possible to move the film to a new spot with the XY translation stages but it is impossible to know at what point the irreversible damage was caused to the film. When no significant damage was observed, over the course of a full length 3-scan measurement, an upper limit was set below which measurements could be safely carried out.

A series of time-resolved measurements were then carried out on a range of CrCr samples in order to study the decay dynamics as a function of the excitation power and the film thickness.

The sample was secured on the same 1" optic mount that was used for the FeCr measurements with the surface on which the sample was deposited facing the direction of the laser source. Optimisation of the overlap for this material was more complicated than the previous sample as there is no long-lived MM'CT bleach signal to locate, as such the delay line was set much closer to the time zero in an attempt to capture any short lived signal which will allow the overlap to be optimised. Once a signal was found which could not be attributed to the cross phase modulation, then the overlap was optimised using the final pump mirror before interaction with the sample and the beam profile after the sample was checked to ensure that the spot on the sample was not generating too much scattered light. Similarly to the FeCr measurements, a polariser was placed in the beam path before the detectors in order to help with removing scattered light from the pump beam.

**Results**

The measurements as a function of the pump power were carried out on the same day in order to aid with reproducibility of the measurements and were performed on different spots as to avoid damage over time to the film. The scattered light was always minimised when the spot on the film was adjusted between measurements. The powers selected for these measurements were 600, 900 and 1200 uW which equates to fluences of 1.5, 2.25 and 3.00 mJ $cm^{-2}$ as these all fall below the estimated damage threshold for a full measurement. The intermediate film thickness of 250 nm was selected for these measurements.
If the previous measurements are considered then an excited state absorption in the UV portion of the spectrum would be expected. This was seen in both the VCr and FeCr PBAs and was attributed to the $^{2}$E state on the Cr ion. Another excited state absorption was also observed around 570 nm in the FeCr analogue, this was not seen in the VCr due to overlap with the strong MM'CT bleach signal in this region. Finally, it was discussed in the VCr section that there may have been evidence of the $^{4}$LMCT at approximately 455 nm, this was however significantly obscured by the flanking excited state absorption and ground state bleach to shorter and longer wavelengths respectively.

Figure 4.49 illustrates the ultrafast transmission data over the first 20 picoseconds. Given that there is no ground state absorption in this material, there is no increase in transmission due to a bleach of this state. As such, all of the signals in these datasets are negative, ie. there is a decrease in the transmission after excitation, or an excited state absorption. The signals observed in this sample are of lower intensity than the signals in the VCr and FeCr, which is likely in part due to the thinner samples required for avoiding too much scattered light and differences in the oscillator strength of these transitions. The crystallinity of this material is comparable to that of the FeCr material as they both are comprised of many individual cubic crystals, the CrCr crystals are approximately 600 nm across when compared with the 1 $\mu$m sized crystals of the FeCr material.

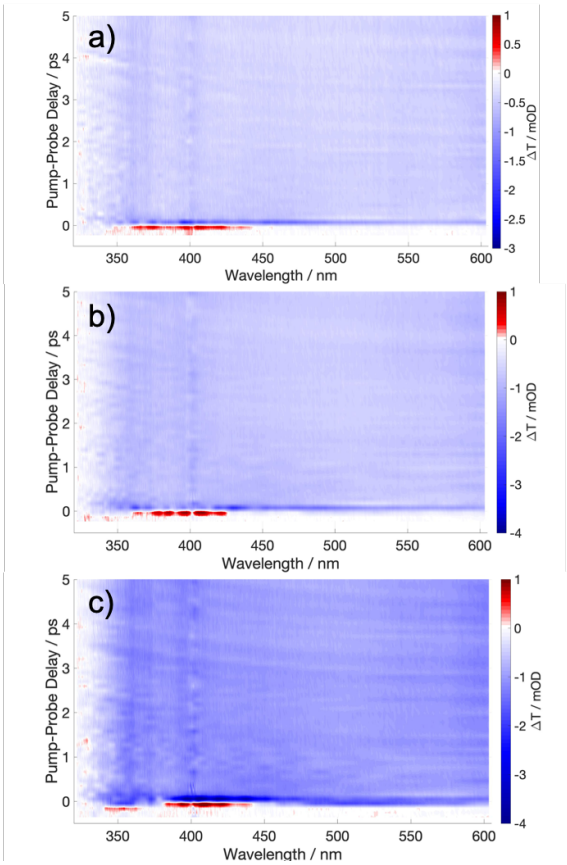


*Figure 4.49: The two dimensional contour plot for first 10 picoseconds of the transient transmission measurement of the CrCr PBA at pump powers of 600, 900 and 1200 uW for a), b) and c) respectively. The sample thickness was approximately 250 nm. The vertical line around 400 nm is scattered pump light which has been partially removed by background subtraction.*

The subsequent measurements at lower pump powers, shown in Figure 4.49, are also in accordance with the first measurement and exhibit very much the same behaviour.

There are a couple of key signals which can be see in all of these measurements; there is a clear signal at approximately 365 nm which persists throughout these plots and a slightly darker region of the two dimensional plot to the right, from approximately 500 nm upwards. This can be accentuated if the colour scale is biased to below zero, given that all of the signals are negative in these measurements and this is illustrated in Figure 4.50. This is not the standard

method for scaling used in this thesis as it can be misleading without properly studying the colour scale on each figure. For this reason the colour scales are typically scaled such that a value of 0 will be coloured white on the two dimensional plot.

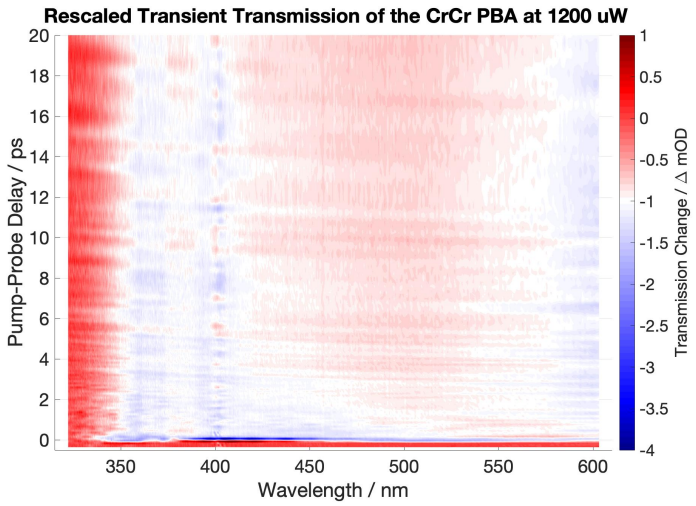


*Figure 4.50: The recoloured two dimensional contour plot for first 20 picoseconds of the transient transmission measurement of the CrCr PBA at a pump power of 1200 uW. This adjusted scaling highlights the signals of interest across the spectrum at 365 nm, 430 nm and 600 nm.*

The difference spectra at various time delays can be plotted on the same axis in order to visualise the progression of the electronic structure over time after pump excitation. Figure 4.51 shows this plot and the growth of the signals can be seen in the plots with increasing time delays. All of the signals in this measurement are of the same sign due to the lack of a significant structure in the ground state, this makes identifying any broad, overlapping signals difficult without any prior knowledge. Based upon the literature and after the previous measurements of the VCr and FeCr analogues, the signals that are seen can be attributed to analogous electronic states in the related materials.

The first difference spectrum after the cross phase modulation around time zero, at approximately 400 femtoseconds shows mostly the same signal structure as the rest of the time delays apart from the signal amplitude around 600 nm. This

signal appears to grow in over the course of the first picosecond, this behaviour is not seen in any of the other assigned regions of the spectrum. There is only a gradual loss of signal due over the course of the 100 ps measurement as the majority of the dynamics appear to take place within the first 5 - 10 picoseconds, this just leaves the very slow recovery of the ground state which results in a long-lived plateau, this has however recovered by the time the next laser pulse arrives within 1 ms. This behaviour was also seen in the VCr and FeCr PBAs, particularly in the recovery of the ground state bleaches.

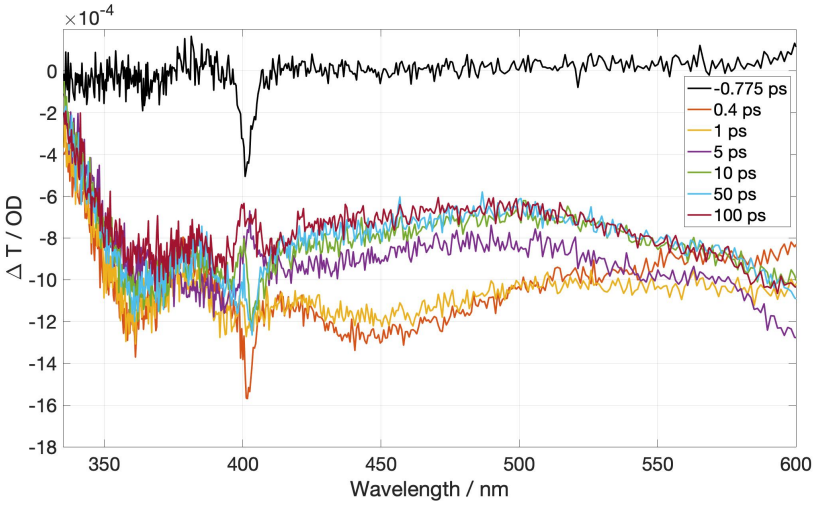


*Figure 4.51: The difference spectra as a function of the time delay for the CrCr PBA. The difference spectra show how the absorption spectrum of the material changes as a function of the time delay after pump excitation. All signals are negative, ie. excited state absorptions, due to the lack of a significant absorption band in the ground state.*

The first signal to be studied will be the excited state absorption observed in the UV part of the spectrum and this is shown in Figure 4.52. The three different measurements all appear to follow very similar dynamics whereby the majority of the signal decays during the first approximately 100 fs after excitation. This initial decay is assumed to be analogous to that which was observed in the FeCr analogue, which was attributed to the very fast decay of the $^2$E state back

to the ground state. In this case however, there is no direct comparison with a ground state bleach within the same measurement but the decay appears to follow much the same, faster behaviour as the excited state absorptions in the other two materials.

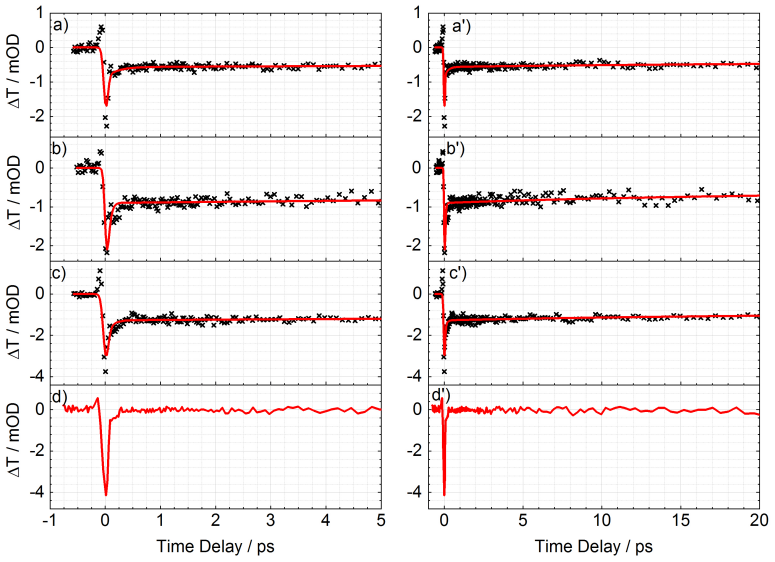


*Figure 4.52: The excited state absorption signals of the CrCr analogue at 360 nm as a function of the applied pump power. The plots in a) and a') correspond to a 400 nm pump power of 600 μW, plots b) and b') correspond to a 400 nm pump power of 900 μW, plots c) and c') correspond to a 400 nm pump power of 1200 μW. The plots in d) and d') are the corresponding substrate background measurements of the substrate.*

The next decay channel to be considered appears most clearly in this sample between 450 and 500 nm and corresponds to the location of the $^4$LMCT signal in the VCr PBA. This signal is placed in between the scattered pump light at 400 nm and the adjacent excited state absorption which is located to longer wavelengths. Figure 4.53 illustrates the decay of this state as a function of the applied pump power, which appears to proceed more slowly than the first excited state absorption, with the initial decay occurring over the first 200-300 fs and the

signal remaining after this initial decay being higher at approximately 50 %. This signal is also flanked by two other signals but the behaviour of the closest of these, the ESA to longer wavelengths shows a significantly different behaviour, thus no significant overlap is assumed. After this initial decay period there is again a very long lived plateau which persists for the full duration of the measurements (100 ps), long after all of the significant decay processes have already taken place.

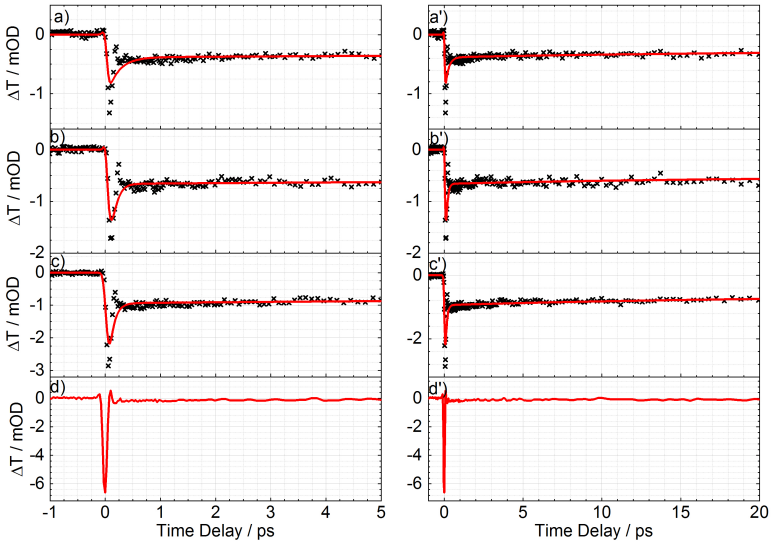


*Figure 4.53: The excited state absorption signals plotted of the CrCr analogue at 480 nm as a function of the applied pump power. The plots in a) and a') correspond to a 400 nm pump power of 600 μW, plots b) and b') correspond to a 400 nm pump power of 900 μW, plots c) and c') correspond to a 400 nm pump power of 1200 μW. The plots in d) and d') are the corresponding substrate background measurements of the substrate.*

The final decay process to be studied is that which is found around 600 nm and is assumed to be the same process which was observed in the FeCr material, and other examples in the literature containing the octahedral $CrL_6$ moiety, that is to say the decay of the $^2E$ state back to the ground state. There is, however, an interesting difference which is observed in this signal and which

has not been seen before in this family of compounds. There is a notable delay in the growth of this signal, after the first initial peak there is a small dip before the signal grows in to the plateau at which it remains for many picoseconds.

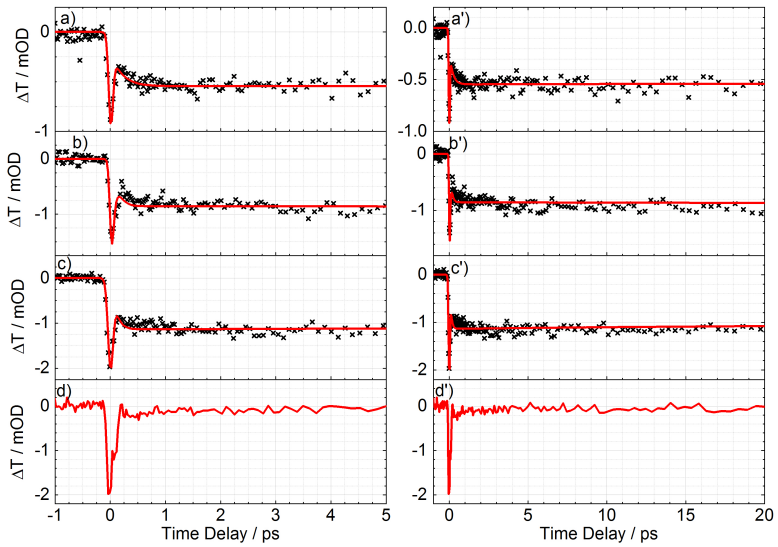


*Figure 4.54: The excited state absorption signals plotted of the CrCr analogue at 595 nm as a function of the applied pump power. The plots in a) and a') correspond to a 400 nm pump power of 600 μW, plots b) and b') correspond to a 400 nm pump power of 900 μW, plots c) and c') correspond to a 400 nm pump power of 1200 μW. The plots in d) and d') are the corresponding substrate background measurements of the substrate.*

When carrying out the global fitting analysis of the CrCr analogue the same model was used as was used for the FeCr analogue but the values of the parameters were adjusted in order for the fit to converge with an accurate overall modelling of the data. Table 4.7 shows the achieved fitting parameters for the global fitting of the CrCr material measured using increasing pump powers of 600, 900 and 1200 uW.

The fitting parameters for these measurements are much more varied than those obtained for the FeCr analogue, in particular the $\tau_1$ values are below

| Pump Power ($\mu$W) | $\tau_1$ (fs) | Error | $\tau_2$ (ps) | Error | $\tau_3$ (ps) | Error |
|---|---|---|---|---|---|---|
| 600 | $< 10$ | 24 | 200 | 2 | 21.9 | 0.9 |
| 900 | $< 50$ | 3 | 80 | 3 | 20.0 | 0.64 |
| 1200 | $< 10$ | 3x10$^6$ | 90 | 0.9 | 21.5 | 0.6 |

*Table 4.7: The global fitting parameters for the CrCr PBA as a function of the applied 400 nm pump power and the error values generated by Glotaran. The film thickness was approximately 250 nm.*

the limit for being reliable given the experimental time resolution of approximately 120 fs. This will make drawing comparisons within groups of measurements much more difficult but there may be some useful insights that this can give into the nature of this material.

As previously mentioned, the first constant, $\tau_1$, for each of the measurements are much too short to make physical sense and most likely pertain to the cross phase modulation signal around time zero.

The second time constant, $\tau_2$ appears to be a much more reliable duration at approximately 85 fs for the two higher power measurements and a longer value of 206 femtoseconds for the measurement carried out at the lower power.

The third time constant is very consistent across the three power measurements at around 21 picoseconds, there was no decay constant found with this value in the fitting of previous materials so this is a previously assigned decay process, such as the vibrational relaxation on the $^2$E state, which has been considerably slowed down in this material. Due to the growth which is seen in the excited state absorption, then there appears to be a slowing down of the intersystem crossing from the $^4$LMCT to the $^2$E manifold.

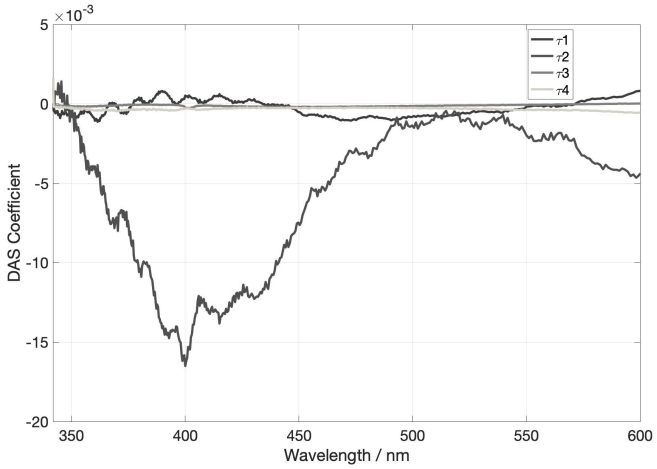


*Figure 4.55: The decay associated spectra which were output from the global fitting procedure of the CrCr PBA using the Glotaran software package. $\tau_{1\text{-}3}$ correspond to those shown in Table and $\tau_4$ corresponds to the constant offset parameter.*

The DAS plot shown in Figure 4.55 shows the decay associated spectra of the global fit carried out on the measurement at 600 $\mu$W pump power. The spectra for these measurements show much less structure than were observed for the FeCr fitting as the signals are much clearer in that case. However there is some information to be gained from this plot. As was predicted, the sub 100 fs component shows a very small coefficient across the whole spectrum but has very little structure. $\tau_2$ has by far the largest coefficient which corresponds to the approximately 200 fs time constant in this case, this is thought to come from the initial decay of the $^2$E state as soon as it is populated. This matches well with what is observed in the kinetic traces. There is a sharp initial decay straight into the long plateau. The other two components are negligible across the whole spectrum so no further information can be gained from those.

In a comparable fashion to the FeCr study, measurements were carried out at different film thicknesses in order to probe the slower, thermal decay of the excitons into adjacent crystals or the substrate below. The measurements were carried out on the same day in order to maintain consistency of the laser system. As has been previously mentioned, the films were difficult to optimise in terms

of the thickness as by the time that an appreciable optical density was deposited the crystals were already too large and caused a lot of scatter when inserted into the laser focus. This was a matter of trial and error until a reasonable range of thicknesses were found which did not produce too much scattered light on the detectors.

The first of the decay channels to be analysed is the excited state absorption in the UV part of the spectrum, these results are shown in Figure 4.56.

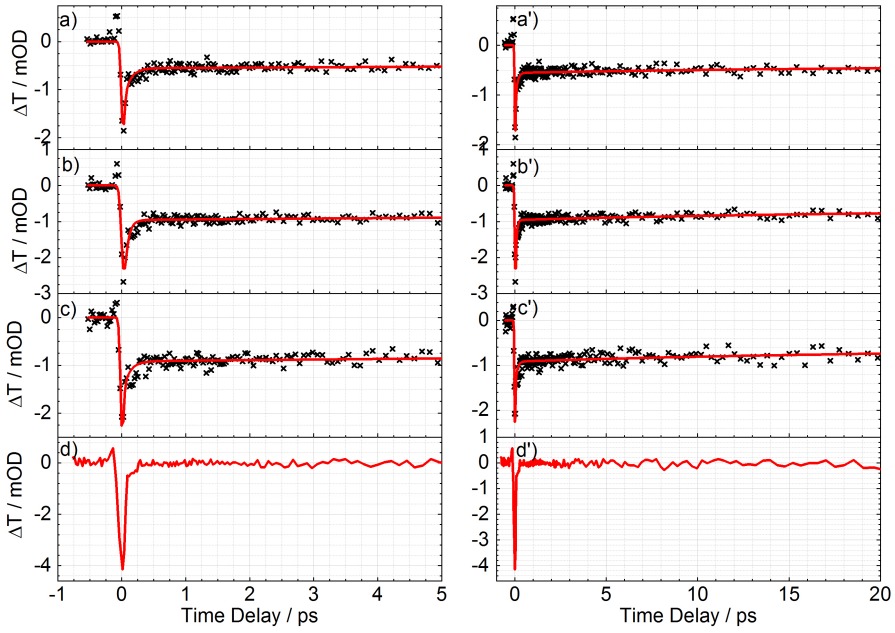


*Figure 4.56: The excited state dynamics of the CrCr analogue at 350 nm as a function of the thickness of the film. The plots in a) and a') correspond to a film thickness of 120 nm, plots b) and b') correspond to a film thickness of 250 nm, plots c) and c') correspond to a film thickness of 500 nm. The plots in d) and d') are the corresponding substrate background measurements of the substrate.*

There appears to be very little influence on this decay channel as one increases the thickness of the films. The hypothesis that was initially put forward suggests that the faster components of the decay would not be affected any

variation in lateral connectivity of the crystals. This is due to the assignment of the fastest component to the transfer of an electron via intersystem crossing. The slower decay processes have been assigned to thermal redistribution of energy to the substrate or surrounding crystals, where crystal connectivity may have an influence on the dynamics. All of the processes which are observed in this material are the result of excited state absorptions, and as such are dominated by the faster of the three fitting parameters which were previously unaffected by this change.

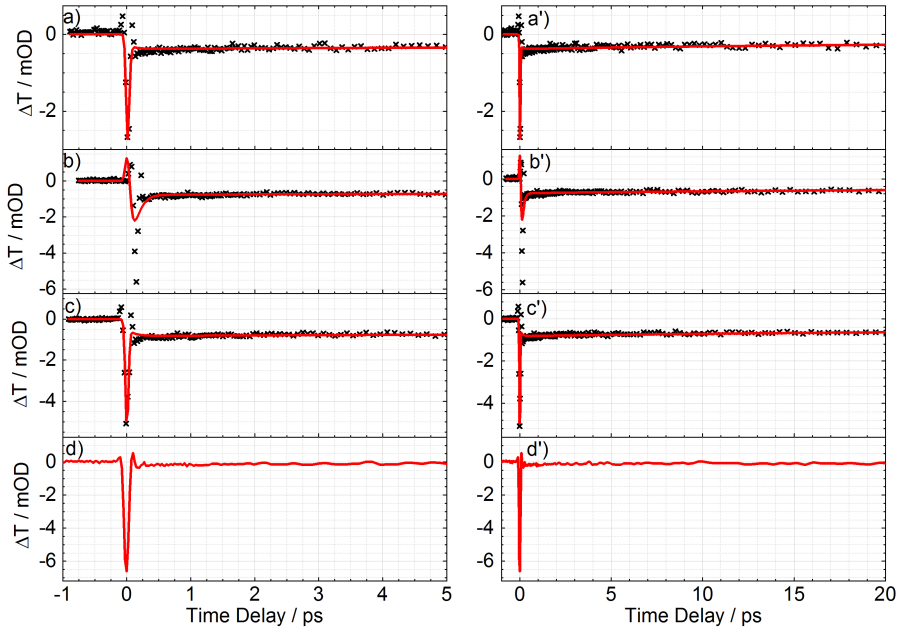


*Figure 4.57: The excited state dynamics of the CrCr PBA at 450 nm as a function of the film thickness. The plots in a) and a') correspond to a film thickness of 120 nm, plots b) and b') correspond to a film thickness of 250 nm, plots c) and c') correspond to a film thickness of 500 nm. The plots in d) and d') are the corresponding substrate background measurements of the substrate.*

The second of these decay channels is found at approximately 450 nm and is shown in Figure 4.57. This region of the measurements appear to be dominated by the cross phase modulation at this wavelength due to the proximity

to the pump wavelength, where the cross phase modulation signal is at its greatest. This is obscuring the subtle signal within the first 200 - 300 femtoseconds which appears to grow very slightly in the two thinnest sample measurements, this is not the case and manifests as the cross phase modulation shows a peak after the primary peak at 0 time delays.

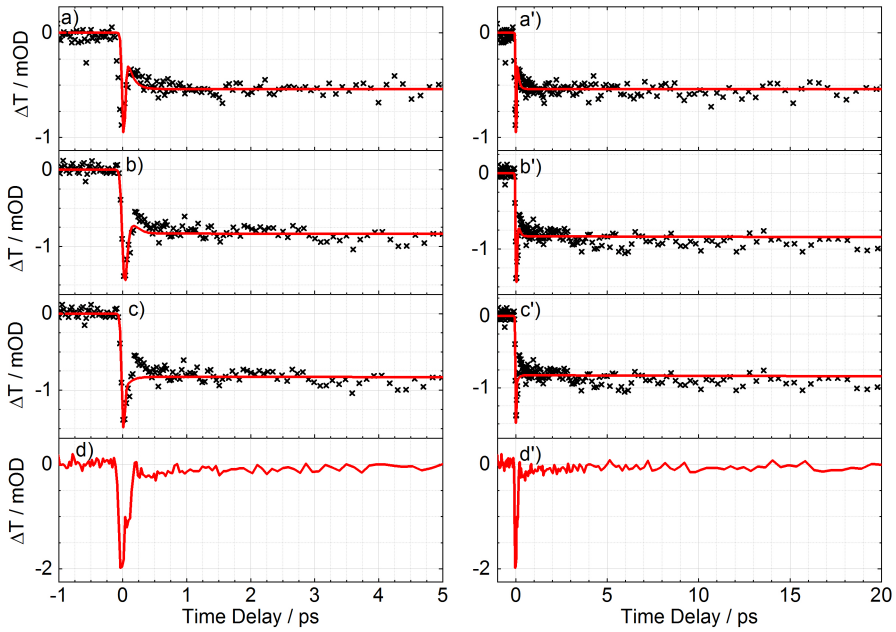


*Figure 4.58: The excited state dynamics of the CrCr PBA on the excited state absorption found around 600 as a function of the thickness of the films. The plots in a) and a') correspond to a film thickness of 120 nm, plots b) and b') correspond to a film thickness of 250 nm, plots c) and c') correspond to a film thickness of 500 nm. The plots in d) and d') are the corresponding substrate background measurements of the substrate.*

The final region to be studied is the excited state absorption attributed to the $^2$E state which appears just below 600 nm and are shown in Figure 4.58. It was in this region that significantly slower dynamics were observed, to the point where a growth of this excited state was seen after the initial cross phase

modulation. This behaviour is also seen in these measurements, where the only noticeable difference in this series of measurements is the signal rise which is seen in the thinnest sample. In the 120 nm thick sample the signal growth appears to be a larger proportion of the overall signal, this may be due to the further delaying of the intersystem crossing following internal relaxation within the $^4$LMCT state. The overall fitting parameters for the measurements as a function of film thickness are shown in Table 4.8. The parameters which were obtained were found when the fit appeared to completely describe the dynamics occurring in these systems. The growth of the excited state absorption observed around 590 nm was typically the final process to be fitted following various variations of starting parameters once a general model was decided on.

| Film Depth (nm) | $\tau_1$ (fs) | Error | $\tau_2$ (ps) | Error | $\tau_3$ (ps) | Error |
|---|---|---|---|---|---|---|
| 120 | $< 20$ | 0.5 | 100 | 900 | 20.6 | 0.4 |
| 250 | $< 50$ | 3 | 80 | 3 | 20.0 | 0.64 |
| 500 | $<< 1$ | $1.4\text{x}10^{-5}$ | 100 | 900 | 22.1 | 0.3 |

*Table 4.8: The global fitting parameters for the CrCr PBA as a function of the film thickness and the error values generated by Glotaran. The applied pump power was approximately 800 $\mu W$.*

The signals obtained from the CrCr analogue are much weaker than those observed for either the FeCr or VCr which means that the measurements were more difficult to optimise in the first place, primarily due to the lack of a structured ground state absorption. This has impacted the reliability of the exact values for the fitting parameters which have been obtained from the global fitting procedure. However, the approximate values are still useful and can be very constructive when compared within groups of measurements and across the family of hexacyanochromate Prussian Blue analogues studied in this work.

**Alternative Fitting Procedure**

As was the case for the FeCr analogue, a repeat fitting of individual signals in the CrCr PBA sample was carried out to more closely fit the dataset across the whole wavelength range. This is particularly important for the CrCr measurements as the signals are much smaller and there is a previously unseen growth signal around 600 nm. The same base equation was used as was discussed in the previous section, however in this case there were some additional terms added in to fit the data better.

$$(a0+(a1*e^{(\text{-(x-td)/t1})})+(a2*e^{(\text{-(x-td)/t2})})+(a3*e^{(\text{-(x-td)/t3})})).*(erf((x-td)/w0)+1) \tag{4.2}$$

$$a4*e^{(\text{-((x-td)/(w*}\sqrt{2}\text{))2})} \tag{4.3}$$

The first of the two equations above is the same as equation 3.1. The second of these equations is the equation for a Gaussian pulse which is used to characterise the sharp spikes from the cross phase modulation which are significantly more obvious in this dataset due to the smaller magnitude of the signal.

| Pump Power $\mu$W | $\tau_1$ (fs) | Coefficient | $\tau_2$ (ps) | Coefficient |
|---|---|---|---|---|
| 600 | 140 | -3x10$^{-4}$ | 31 | -8x10$^{-5}$ |
| 900 | 1100 | -1x10$^{-4}$ | 60 | -1x10$^{-4}$ |
| 1200 | 120 | -2x10$^{-3}$ | 31 | -2x10$^{-4}$ |

*Table 4.9: The fitting parameters for the excited state absorption of the CrCr PBA at 350 nm as a function of applied 400 nm pump power and the pre-exponential values used in the fits according to Equation 4.2. The film thickness was approximately 250 nm.*

Table 4.9 shows the parameters for this fit, in this case only two time constants were needed in order to satisfactorily fit the data as the data appeared

to be dominated by a short, sharp decay and a long, slow decay. In the case of these three fits, there were two Gaussian pulses used to describe the positive and negative amplitude spikes around time zero which means that the time constants only need to deal with the signal that remains. The first decay constant, $\tau_1$, is attributed to the analogous initial decay of the $^2$E state back to the ground state due to the spectral position and the time scale that was observed.

| Pump Power $\mu$W | $\tau_1$ (ps) | Coefficient | $\tau_2$ (ps) | Coefficient |
|---|---|---|---|---|
| 600 | 1.3 | -9x10$^{-5}$ | 50 | -7x10$^{-5}$ |
| 900 | 1.0 | -1x10$^{-4}$ | 53 | -1x10$^{-4}$ |
| 1200 | 1.5 | -1x10$^{-4}$ | 50 | -2x10$^{-4}$ |

*Table 4.10: The fitting parameters for the excited state absorption of the CrCr PBA at 460 nm as a function of applied 400 nm pump power and the pre-exponential values used in the fits according to Equation 4.2. The film thickness was approximately 250 nm.*

Table 4.10 shows the obtained fitting parameters for the excited state absorption observed at 460 nm. The $\tau_1$ value in this case is much slower and is attributed to the excited state absorption from the $^4$LMCT state which is populated after 400 nm excitation before ISC occurs into the $^2$E state. This was attributed to this state due to an analogous signal which was observed during spectroelectrochemical measurements of the VCr PBA where the electrochemically reduced Cr ion results in a significant loss of transmission around this wavelength, Figure 4.6 b). This signal was not observed in the FeCr analogue due to the overlap with the ground state absorption and corresponding bleach upon excitation.

The values shown in Table 4.11 are the result of the single band fitting of the excited state absorption of the CrCr PBA at 590 nm, where it was necessary to use 3 components in order to fit the data well. In this spectral region there was an obvious growth of the signal over the course of the first approximately

| Pump Power $\mu$W | $\tau_1$ (fs) | Coefficient | $\tau_2$ (ps) | Coefficient | $\tau_3$ (ps) | Coefficient |
|---|---|---|---|---|---|---|
| 600 | 300 | -2x10$^{-4}$ | 6.3 | -2x10$^{-4}$ | 24 | 2x10$^{-4}$ |
| 900 | 140 | -2x10$^{-4}$ | 5.3 | -1x10$^{-4}$ | 26.4 | 1x10$^{-4}$ |
| 1200 | 270 | -5x10$^{-4}$ | 5 | 2x10$^{-4}$ | 42.9 | -9x10$^{-5}$ |

*Table 4.11: The fitting parameters for the excited state absorption of the CrCr PBA at 590 nm as a function of applied 400 nm pump power and the pre-exponential values used in the fits according to Equation 4.2. The film thickness was approximately 250 nm.*

10 ps before the signal begins to decay away. The first two constants $\tau_1$ and $\tau_2$ are of positive amplitude, meaning they correspond to the growth of the signal. The third $\tau_3$ was then used to describe the subsequent decay. There is a sharp increase in the signal right after the Gaussian pulse which is described by $\tau_1$ which is followed by a slower growth which is clearly seen in the longer time scale plots which is described by $\tau_2$.
The origin of the growth of the excited state absorption of the $^2$E is thought to be due to a change in the relative energy between the $^4$LMCT and the $^2$E states.

This refitting of the data was also carried out on the measurements as a function of thickness, again in order to more closely fit the data to allow comparisons of the measurements to be carried out reliably.

The values shown in Table 4.12 correspond to the measurements of the CrCr PBA as a function of film thickness. In this case, $\tau_1$ is less that 200 fs which is attributed to the initial decay of the $^2$E state as has been discussed previously. There is then a second component, $\tau_2$. which appears to fit with the thermal dissipation of heat into the surroundings.

The decay parameters shown in Table 4.14 were then found to describe the excited state absorption at 460 nm of the CrCr PBA as a function of film thickness. The $\tau_1$ parameter in this case appears to match with the power

| Film Depth (nm) | $\tau_1$ (fs) | Coefficient | $\tau_2$ (ps) | Coefficient |
|---|---|---|---|---|
| 120 | 240 | -1x10$^{-4}$ | 22 | -7x10$^{-5}$ |
| 250 | 1100 | -1x10$^{-4}$ | 60 | -1x10$^{-4}$ |
| 500 | 100 | -5x10$^{-4}$ | 20 | -1x10$^{-4}$ |

*Table 4.12: The fitting parameters for the excited state absorption of the CrCr PBA at 350 nm as a function of the film thickness and the pre-exponential values used in the fits according to Equation 4.2. The applied pump power was approximately 800 $\mu$W.*

| Film Depth (nm) | $\tau_1$ (ps) | Coefficient | $\tau_2$ (ps) | Coefficient |
|---|---|---|---|---|
| 120 | 1.3 | -8x10$^{-5}$ | 74 | -9x10$^{-5}$ |
| 250 | 1 | -1x10$^{-4}$ | 53 | -1x10$^{-4}$ |
| 500 | 1.1 | -1x10$^{-4}$ | 28 | -1x10$^{-4}$ |

*Table 4.13: The fitting parameters for the excited state absorption of the CrCr PBA at 460 nm as a function of the film thickness and the pre-exponential values used in the fits according to Equation 4.2. The applied pump power was approximately 800 $\mu$W.*

dependence measurements and corresponds to a decay of the $^4$LMCT and then a much longer, $\tau_2$ parameter which is attributed to the thermal dissipation of energy to the surroundings.

The growth of the $^2$E ESA which was seen in the power dependence measurements was also seen in these measurements as a function of film thickness. The first two constants, $\tau_1$ and $\tau_2$ again correspond to the growth of this signal over the first approximately 10 ps. There is then a slow $\tau_3$ which describes the thermal loss of energy to the surroundings.

These single band fits appear to generally show similar dynamics to the global fits but they were able to give a more accurate fit to the data without the need

| Film Depth (nm) | $\tau_1$ (fs) | Coefficient | $\tau_2$ (ps) | Coefficient | $\tau_3$ (ps) | Coefficient |
|---|---|---|---|---|---|---|
| 120 | 180 | $2x10^{-4}$ | 10 | $6x10^{-5}$ | 35 | $-8x10^{-5}$ |
| 250 | 140 | $2x10^{-4}$ | 5.3 | $1x10^{-4}$ | 26 | $-1x10^{-4}$ |
| 500 | 330 | $1x10^{-4}$ | 6.2 | $2x10^{-4}$ | 24 | $-2x10^{-4}$ |

*Table 4.14: The fitting parameters for the excited state absorption of the CrCr PBA at 590 nm as a function of the film thickness and the pre-exponential values used in the fits according to Equation 4.2. The applied pump power was approximately 800 $\mu$W.*

for additional decay parameters. The aim is always to use the minimum amount of coefficients as possible which still make physical sense. Unfortunately, there does not appear to be any trends observed with either of the pump power or film thickness measurements. However it is very interesting that a growth of the $^2$E state was observed in the signal around 590 nm, which has been attributed to the modification of the energy of this state relative to the $^4$LMCT which occurred as a result of changing the metal center in the nitrogen pocket, linking together the hexacyanochromate moieties.

### 4.2.5 Overall Conclusions from Ultrafast Measurements

When all three of the samples studied in this work (VCr, FeCr and CrCr) are considered there are some interesting similarities and differences which are observed and can be rationalised. First one must review the electronic excited states involved in these materials using the scheme which has been previously presented in this work.

Figure 4.59 illustrates the assumed excited states of interest in these Cr-centric systems. In this case, after excitation the population does not have far to fall before experiencing significant overlap with the $^2$E state at which point the intersystem crossing occurs on a short timescale (<150 femtoseconds). If the

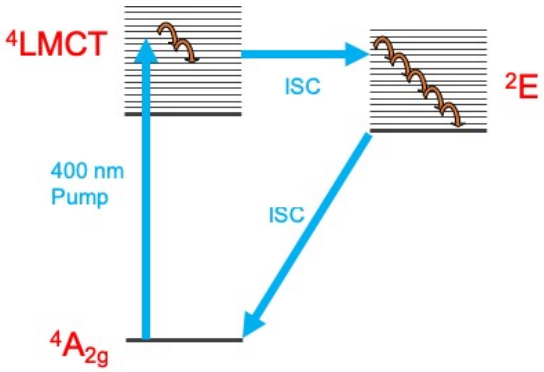


*Figure 4.59: The electronic excited states of the Cr ions which are the constant factor within all of the materials studied in this work. After excitation into the $^4$LMCT very fast intersystem crossing generally occurs and population is generated in the $^2$E, spin flipped state.*

energy of the $^4$LMCT state is shifted up or down in energy and the excitation wavelength is kept constant, then presumably the time taken to reach this overlap can be adjusted. The substitutions of the opposing metal ions do not affect the overall dynamics, thus allowing the timescales of the dynamics to be tailored.

In the case of the VCr and FeCr, where there is a ground state absorption and therefore a bleach of that state. The recovery of this bleach can be compared with the decay of the excited state absorption which is seen in the UV for the VCr analogue and both the UV and the visible for the FeCr analogue. In general, the decay of the excited state absorption occurs on faster timescales than the recovery of the ground state absorption. The recovery of the ground state absorption after excitation is dependent on the decay of the population all the way down to the ground electronic state. Conversely, for the ground state recovery to occur, the population in the $^2$E state must decay back down to the ground, $^4A_{2g}$, state via a back intersystem crossing which has been estimated to occur on the nanosecond timescale.

The excited state absorptions of the VCr and the FeCr are very consistent but there is a stark difference when looking at the dynamics of the excited state absorption of the CrCr analogue in the visible part of the spectrum. The excited

state absorption in the UV for the CrCr analogue appears to follow the same behaviour as the previous examples but this is believed to be due to a lower temporal resolution in this region.

The change in the relative energies of these two electronic states causes a slowing down of the transfer of population. This change in energy shifts the significant overlap between the two states to lower energies meaning that before the transfer can take place there needs to be some energy loss in the form of vibrational relaxation in the $^4$LMCT state.

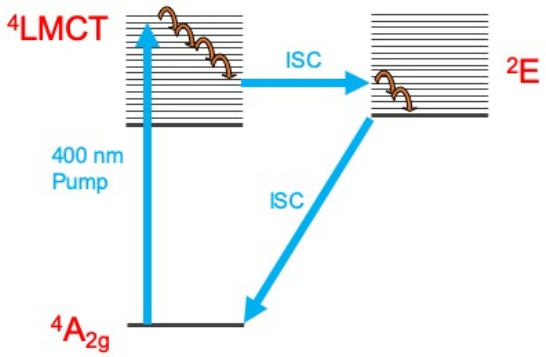


*Figure 4.60: The electronic excited states of the Cr ions which are the constant factor within all of the materials studied in this work. After excitation into the $^4$LMCT the fast intersystem crossing is delayed due to internal vibrational relaxation occurring until a significant overlap is found and population is eventually transferred to the $^2$E state.*

A modification of the energy of the $^4$LMCT state appears to be more likely than the $^2$E state after studying the literature of $Cr^{III}$ compounds. The energy of the $^2$E state appears to be largely independent from the surrounding ligand field effects, whereas the energy of the $^4$LMCT state is directly related to the surrounding ligand field. This effect has been previously studied in the literature and has resulted in an observed growth of the $^2$E state.

Studies of $Cr^{III}$ complexes in solution [61] have previously observed a growth in the $^2$E using transient absorption and flash photolysis. The system was probed at 540 nm which corresponds to the excited state absorption of the $^2$E state as

has been previously established. When pumping at 313 nm a clear growth is observed in the ESA over the first approximately 0.5 - 1 ps. The corresponding measurement with excitation at 628 nm shows no such growth.

A more recent study of the $Cr^{III}(AcAc)_3$ by McCusker *et al.* [62] allowed the observation of vibrational coherences following excitation into the first allowed, ligand field absorption, $^4T_2$. DFT calculations indicate that the oscillations in the $^4T_2$ is associated with Cr-O bond stretching vibrations, this hypothesis was confirmed by chemical substitution of the peripheral methyl groups for *tert*-butyl groups which have similar electronic properties but are much larger. This was found to have slowed the rate of intersystem crossing by over an order of magnitude by observation of the excited state absorption in subsequent studies. The vibrational coherences were also retained after the intersystem crossing which suggests that these vibrations define the reaction co-ordinate for the crossing event. This study exhibits the potential change in the rate of intersystem crossing by even a modest change in the steric and electronic structure of the complex.

A recent study of the $Co(AcAc)_3$ by Ferrari *et al.* [63] observed a growth in the excited state absorption in this system. The intersystem crossing of interest in this study is from a $^1$LMCT state to a $^3T_2$ state, this corresponds to a $\Delta_s$ of -2 which is the same as the equivalent transition in the $Cr(AcAc)_3$ study my McCusker *et al.*

When exciting in the UV there is a visible growth in the ESA bands at 500 and 700 nm with a characteristic growth time of 0.07 $\pm$ 0.04 ps. This growth is not observed when exciting at 580 or 650 nm, this is due to the initial excitation into higher lying electronic states using UV light. In order for the intersystem crossing to occur, then first there must be an internal conversion to the $^1$LMCT state with significant overlap with the $^3T_2$.

Figure 4.61 is a plot of the excited state absorptions for the FeCr and CrCr at their maxima of 580 and 595 nm respectively. The behaviour of the excited state absorption in the FeCr analogue follows the same dynamics as those

in the UV for this material but also the behaviour is the same as the excited state absorption in the VCr analogue in terms of the decay rate and amount of signal left to decay in the plateau. If the idea of varying the relative energy of the $^2$E manifold by changing the local environment of the ion is to be believed then there is no difference between the vanadium and iron hexacyanochromate materials.

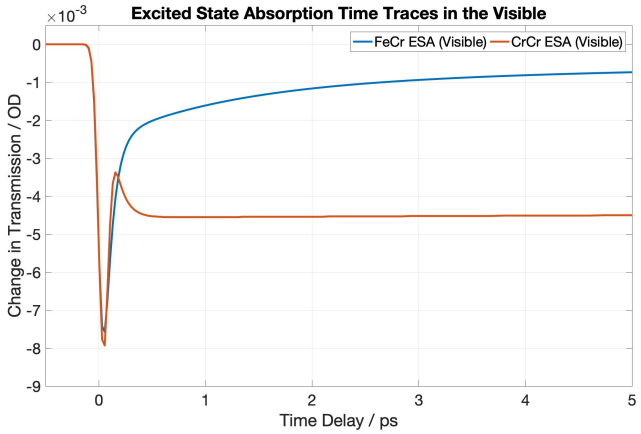


*Figure 4.61: The excited state absorptions from the $^2$E state in the FeCr (blue curve) and the CrCr (orange curve) analogues. The FeCr analogue the $^2$E state is only seen to decay whereas the CrCr signal appears to grow within the first 500 fs after excitation.*

The dynamics observed in the CrCr analogue differs significantly from those in the FeCr and VCr analogues, this is believed to be because the energy of the $^4$LMCT is lower in the case of the CrCr material. This means the laser pulse excites the electrons in the sample to higher lying vibrational levels within the $^4$LMCT and subsequently the internal relaxation required to find a significant overlap with the $^2$E state is increased before intersystem can proceed. In the CrCr material, this delay in the intersystem crossing is sufficient to observe the growth of the $^2$E excited state absorption.

The alternative fitting procedure which was used for both the FeCr and the CrCr was carried out because the viability of applying global fitting procedures to these dynamic processes was being questioned. In order for global fitting to form a reliable model then all of the signals across the spectrum must

follow the same dynamic processes, this allows all of the signals to be fitted to a minimum number of parameters which describe the complete dynamics. It was eventually decided that the dynamics of these materials was sufficiently complicated that a global fit was not the best way to approach this. This was evident when visually inspecting the fits which were output from the Glotaran procedure where there were regions of the dynamics which were not accounted for, when using the minimum number of decay constants which made physical sense.

The independent fitting protocol which was subsequently employed using MATLAB allowed greater control of the fits but also could simply account for the sharp cross phase modulation signal around time zero. This spike would often skew the short time scale decay constants used to describe the dynamics occurring within the first 500 fs after excitation. Depending on the appearance of the cross phase modulation then different numbers of Gaussian pulses could be used to model the positive and negative amplitude spikes. By defining the width of the Gaussian pulses then the decay of the signal could be modelled as soon as the cross phase modulation finished. The relative amplitudes of the decays were also important in deciding if the parameters were describing the dynamics well and allowed the comparison between data sets. The amplitudes were estimated and input to the formula but the output values were always considered when looking at the fits. The relative amplitudes of $\tau_1$, $\tau_2$ and $\tau_3$ indicate how significant the parameter is when describing the overall dynamics, if a parameter has a much lower amplitude this indicates that the value has very little impact on the fits and therefore is not always required.

The greater control afforded to the user when carrying out the fits manually in MATLAB and the doubt surrounding the applicability of global fitting procedures to these measurements meant that the single band fittings were of greater use than the global fits. The resulting fits more closely matched the datasets and the relative amplitudes of the parameters more easily allowed comparison between

datasets. For these reasons, the single band fitting procedure will be used from now on to analyse the decay dynamics of the Prussian Blue analogues due to the multi-decay process nature of the observed dynamics.

# Chapter 5

# Conclusions

## 5.1 Summary of Work

The complex photophysics involved in transition metal complexes has been studied in the family of compounds known as Prussian Blue analogues. This has been done to further the understanding of the factors which influence the decay dynamics and rates of the important photophysical processes which involve the transfer of populations between potential energy surfaces of the same, or different spin multiplicities. The combination of spectroelectrochemistry and ultrafast transmission spectroscopy has allowed the electronic dynamics to be tracked through changes in the transmission spectrum as a function of time. The ability to study the magnetisation dynamics of these functional materials requires a technique which is able to operate on relevant timescales but is also sensitive to the spin states of the materials involved. The other crucial caveat is that the sample itself exhibits a strong and persistent magnetisation. To this end, the Prussian Blue family of compounds were chosen as the model systems for these studies as the periodic nature of the PBA lattice promotes the long range ordering of the spins on the metal ions.

The application of a spectrally broader probe pulse and the broadband photodetection which have been applied to the VCr, FeCr and CrCr analogues of

Prussian Blue has greatly expanded the knowledge and understanding of the electron dynamics which occur in these materials. The discovery of spectral signatures for the $^2$E state, which corresponds to the intraconfigurational spin flip of the $^4A_{2g}$ ground state was of significant importance as this provided a direct handle on the growth and subsequent decay of this state. This state is of particular interest as it allows the rate of intersystem crossing to be studied more directly than in the previous attempt which relied on a bleaching of the ground state population implying transfer into the $^2$E state.

The use of the global fitting software, Glotaran, does not appear to have been the best option for modelling the systems as there are too many different signals with different origins to be able to describe the entire spectral dynamics with the same parameters. It appeared to work well for the FeCr system where the amplitudes of the signals are large and are spectrally separated. There was little evidence of the cross phase modulation signal here which simplifies the parameters required to attain a close fit to the data. In the case of the CrCr analogue, all of the signals are of the same sign and therefore establishing any spectral characteristics is very difficult. The signals are also very weak and there is a significant influence of the cross phase modulation which further complicates the fitting procedure. The presence of the growth signal at 590 nm requires a completely independent parameter as it is of a different sign to all the other signals. The fitting of the data in MATLAB using single wavelength kinetic traces allowed for a much tighter fit to be obtained as it was easier to determine the minimum number of parameters required. The signs of the coefficients could be easily constrained to make sure that all of the signals were accounted for. In the case of the FeCr PBA measurements it allowed a much closer fit to the data to be obtained. However in the case of the CrCr PBA the growth signal could be accounted for in a controlled fashion by restricting the temporal parameter and the sign of the coefficient for the band at 590 nm. The use of Gaussian pulses in the fitting of the CrCr allowed the complete cross phase modulation to be accounted for meaning that the fitting of

the actual dynamic signals was simplified and was more reliable. The use of global fitting is in principle a beneficial technique where the dynamics of the system are determined by a small number of processes meaning that a small number of decay constants can be used across the spectrum. However in transition metal systems such as the Prussian Blue analogues studied in this work, the dynamics are more complicated and therefore require a more independent fitting procedure which can account for the dynamics of the different signal independently.

The influence of substituting the transition metal center in the nitrogen pocket of the PBA lattice appears to have influenced the rate of intersystem crossing in clear way due to the different relative energies of the $^2$E states produced in the different electronic environments. It is hypothesised that in the case of the CrCr analogue, the $^2$E is shifted down in energy. This results in a delay of transfer of population into this state as there is a larger amount of internal vibrational relaxation required in order to produce a significant overlap between the $^4$LMCT and $^2$E states which facilitates the population transfer.

The ability to control the rates of intersystem crossings is of great interest in the field of functional magnetic materials which exhibit at least two different stable spin configurations. The ability to switch between these states is the basis for the development of future data storage technologies which will soon become a necessity with the continual growth and expansion of the data footprint we produce. A greater understanding of the processes that influence and control these dynamics is the bedrock upon which these developments can be made.

## 5.2 Outlook

The attempts made towards the development of a time-resolved magneto-optical experimental setup showed some very promising results with the ability to measure the ultrafast demagnetisation of these molecule-based magnetic materials. The sensitivity and accuracy of the optical setup has been tested using calibration

samples which had been independently characterised. The ability to measure the magnetic properties of these films in-situ without the need to destroy the sample is an important development in the continued development of these functional materials. The issues that were experienced with the time-resolved measurements will be the focus of future work in order to understand and correct to allow the application of this apparatus to new and varied samples.

# Chapter 6

# References

# Bibliography

[1] H. Kramer, A. M Adamson, and P. D. Fleischauer. *Concepts of Inorganic Photochemistry*, volume 80. John Wiley & Sons, Ltd, apr 1976.

[2] James K. McCusker, Kevin N. Walda, Robert C. Dunn, John D. Simon, Douglas Magde, and David N. Hendrickson. Subpicosecond 1MLCT 5T2 Intersystem Crossing of Low-Spin Polypyridyl Ferrous Complexes. *Journal of the American Chemical Society*, 115(1):298–307, 1993.

[3] N. H. Damrauer, Cerullo Giulio, Yeh Alvin, R. Boussie Thomas, V. Shank Charles, and K. McCusker James. Femtosecond Dynamics of Excited-State Evolution in [Ru(bpy)3]2+. *Science*, 275(5296):54, 1997.

[4] Wojciech Gawelda, Andrea Cannizzo, Van-Thai Pham, Frank van Mourik, Christian Bressler, and Majed Chergui. Ultrafast Nonadiabatic Dynamics of [Fe(II)(bpy)3]2+ in Solution. *Journal of the American Chemical Society*, 129(26):8199–8206, 2007.

[5] Eric A. Juban and James K. McCusker. Ultrafast dynamics of 2E state formation in Cr(acac)3. *Journal of the American Chemical Society*, 127(18):6857–6865, 2005.

[6] Eric A. Juban, Amanda L. Smeigh, Jeremy E. Monat, and James K. McCusker. Ultrafast dynamics of ligand-field excited states. *Coordination Chemistry Reviews*, 250(13-14):1783–1791, 2006.

[7] Hideo Ando, Satoru Iuchi, and Hirofumi Sato. Theoretical study on ultrafast intersystem crossing of chromium(III) acetylacetonate. *Chemical Physics Letters*, 535:177–181, 2012.

[8] Eric Beaurepaire, J. C. Merle, A. Daunois, and Jean Yves Bigot. Ultrafast spin dynamics in ferromagnetic nickel. *Physical Review Letters*, 76(22):4250–4253, 1996.

[9] J. Hohlfeld, E. Matthias, R. Knorren, and K. H. Bennemann. Nonequilibrium Magnetization Dynamics of Nickel. *Physical Review Letters*, 78(25):4861–4864, 1997.

[10] J. Güdde, U. Conrad, V. Jähnke, J. Hohlfeld, and E. Matthias. Magnetization dynamics of ni and co films on cu(001) and of bulk nickel surfaces. *Physical Review B - Condensed Matter and Materials Physics*, 59(10):R6608–R6611, 1999.

[11] B. Koopmans, M. Van Kampen, J. T. Kohlhepp, and W. J M De Jonge. Ultrafast magneto-optics in nickel: magnetism or optics? *Physical Review Letters*, 85(4):844–847, 2000.

[12] V. Shokeen, M. Sanchez Piaia, J. Y. Bigot, T. Müller, P. Elliott, J. K. Dewhurst, S. Sharma, and E. K.U. Gross. Spin Flips versus Spin Transport in Nonthermal Electrons Excited by Ultrashort Optical Pulses in Transition Metals. *Physical Review Letters*, 119(10):1–5, 2017.

[13] A. Eschenlohr, M. Battiato, P. Maldonado, N. Pontius, T. Kachel, K. Holldack, R. Mitzner, A. Föhlisch, P. M. Oppeneer, and C. Stamm. Ultrafast spin transport as key to femtosecond demagnetization. *Nature Materials*, 12(4):332–336, 2013.

[14] Jo Kirby and David Saunders. Fading and colour Change of Prussian blue: Methods of Manufacture and the Influence of Extenders. *The National Gallery Technical Bulletin*, 25:73–99, 2004.

[15] A. Ito, M. Suenaga, and K. Ôno. Mössbauer study of soluble prussian blue, insoluble prussian blue, and turnbull's blue. *The Journal of Chemical Physics*, 48(8):3597–3599, 1968.

[16] Louis Néel. Proprietes magnetiques des ferrites: ferrimagnetisme et antiferromagnetisme. *Ann. Phys.*, 3(2):137–198, 1948.

[17] H A Kramers. L'interaction Entre les Atomes Magnétogènes dans un Cristal Paramagnétique. *Physica*, 1(1):182–192, 1934.

[18] P W Anderson. Antiferromagnetism. Theory of Superexchange Interaction. *Physical Review*, 79(2):350–356, jul 1950.

[19] John B. Goodenough. Theory of the role of covalence in the perovskite-type manganites [La,M(II)]MnO3. *Physical Review*, 100(2):564–573, 1955.

[20] Junjiro Kanamori. Superexchange interaction and symmetry properties of electron orbitals. *Journal of Physics and Chemistry of Solids*, 10(2-3):87–98, 1959.

[21] W. D. Griebler and D. Babel. X-Ray and Magnetic Studies of Perovskite-Related Cyano Compounds CsM(II)M(III)(CN)6. *Zeitschrift Fur Naturforschung Section B-a Journal of Chemical Sciences*, 37(7):832–837, 1982.

[22] V. Gadet, T. Mallah, I. Castro, and M. Verdaguer. High-Tc Molecular-Based Magnets: A Ferromagnetic Bimetallic Chromium(III)-Nickel(II) Cyanide with Tc = 90 K. *Journal of the American Chemical Society*, 114:9213–9214, 1992.

[23] T Mallah, S Thiébaut, M Verdaguer, and P Veillet. High-Tc Molecular-Based Magnets: Ferrimagnetic Mixed-Valence Chromium(III)-Chromium(II) Cyanides with Tc at 240 and 190 Kelvin. *Science (New York, N.Y.)*, 262(1989):1554–1557, 1993.

[24] S. Ferlay, T. Mallah, R Ouahès, P Veillet, and M Verdaguer. A room-temperature organometallic magnet based on prussian blue. *Nature*, 378(6558):701–703, 1995.

[25] Wayne E. Buschmann, Scott C. Paulson, Charles M. Wynn, Mihai a. Girtu, Arthur J. Epstein, Henry S. White, and Joel S. Miller. Reversed (Negative) Magnetization for Electrochemically Deposited High- T c Thin Films of Chromium Hexacyanide Magnets. *Chemistry of Materials*, 10(c):1386–1395, 1998.

[26] Wayne E. Buschmann, Scott C. Paulson, Charles M. Wynn, Mihai A. Gîrtu, Arthur J. Epstein, Henry S. White, and Joel S. Miller. Magnetic field induced reversed (negative) magnetization for electrochemically deposited Tc= 260 K oxidized films of chromium cyanide magnets. *Advanced Materials*, 9(8):645–647, 1997.

[27] O Hatlevik, Wayne E. Buschmann, J Zhang, J L Manson, and Joel S. Miller. Enhancement of the magnetic ordering temperature and air stability of a mixed valent vanadium hexacyanochromate (III) magnet to 99 degrees C (372 K). *Advanced Materials*, 11(11):914–+, 1999.

[28] Osamu Sato, T. Iyoda, A. Fujishima, and K. Hashimoto. Electrochemically Tunable Magnetic Phase Transition in a High-Tc Chromium Cyanide Thin Film. *Science*, 271(5245):49–51, 1996.

[29] O. Sato, Y. Einaga, T. Iyoda, A. Fujishima, and K. Hashimoto. Reversible Photoinduced Magnetization. *Journal of The Electrochemical Society*, 144(1):L11, 1997.

[30] Osamu Sato, Y Einaga, T Iyoda, and a Hashimoto Fujishima K. Cation-Driven Electron Transfer Involving a Spin Transion at Room Temperature in a Cobalt Iron Cyanide Thin Film. *J. Phys. Chem. B.*, 101(20):3903–3905, 1997.

[31] S. I. Ohkoshi, Tomokazu Iyoda, Akira Fujishima, and Kazuhito Hashimoto. Magnetic properties of mixed ferro-ferrimagnets composed of Prussian blue analogs. *Physical Review B - Condensed Matter and Materials Physics*, 56(18):11642–11652, 1997.

[32] S. I. Ohkoshi, A. Fujishima, and K. Hashimoto. Transparent and colored magnetic thin films: (Fe(II)(x)Cr(III)(1- x))1.5[Cr(III)(Cn)6] [18]. *Journal of the American Chemical Society*, 120(21):5349–5350, 1998.

[33] S. I. Ohkoshi, Yasuaki Einaga, Akira Fujishima, and Kazuhito Hashimoto. Magnetic properties and optical control of electrochemically prepared iron chromium polycyanides. *Journal of Electroanalytical Chemistry*, 473(1):245 – 249, 1999.

[34] J. O. Johansson, J.-W. Kim, E. Allwright, D. M. Rogers, Neil Robertson, and Jean Yves Bigot. Directly probing spin dynamics in a molecular magnet with femtosecond time-resolution. *Chemical Science*, 7(12):7061–7067, 2016.

[35] Carlo Adamo and Vincenzo Barone. Toward reliable density functional methods without adjustable parameters: The PBE0 model. *Journal of Chemical Physics*, 110(13):6158–6170, 1999.

[36] Mikihisa Mizuno, S. I. Ohkoshi, and Kazuhito Hashimoto. Electrochemical synthesis of high-Tc, colored, magnetic thin films composed of vanadium(II/III)-chromium(II) hexacyanochromate(III). *Advanced Materials*, 12(24):1955–1958, 2000.

[37] Raquel Garde, F. Villain, and M Verdaguer. Molecule-based room-temperature magnets: Catalytic role of V(III) in the synthesis of vanadium-chromium Prussian blue analogues. *Journal of the American Chemical Society*, 124(35):10531–10538, 2002.

[38] Raquel Garde, Juan Manuel Herrera, F. Villain, and M Verdaguer. Molecule-based magnets with TC above room temperature: Improved synthesis of

vanadium-chromium Prussian blue analogues with inserted alkali cations. *Inorganica Chimica Acta*, 361(12-13):3597–3602, 2008.

[39] E Dujardin, S Ferlay, X Phan, C. Desplanches, C C D Moulin, P Sainctavit, F. Baudelet, E Dartyge, P Veillet, and M Verdaguer. Synthesis and magnetization of new room-temperature molecule- based magnets: Effect of stoichiometry on local magnetic structure by X-ray magnetic circular dichroism. *Journal of the American Chemical Society*, 120(44):11347–11352, 1998.

[40] Eugenio Coronado, Mari Carmen Giménez-López, Georgiy Levchenko, Francisco M. Romero, Valentín García-Baonza, Alla Milner, and Moshe Paz-Pasternak. Pressure-tuning of magnetism and linkage isomerism in iron(II) hexacyanochromate. *Journal of the American Chemical Society*, 127(13):4580–4581, 2005.

[41] Matthieu F. Dumont, Olivia N. Risset, Elisabeth S. Knowles, Takashi Yamamoto, Daniel M. Pajerowski, Mark W Meisel, and Daniel R Talham. Synthesis and size control of iron(II) hexacyanochromate(III) nanoparticles and the effect of particle size on linkage isomerism. *Inorganic Chemistry*, 52(8):4494–4501, 2013.

[42] Boris Le Guennic, Serguei Borshch, and Vincent Robert. Prussian blue analogue CsFe[Cr(CN)6] as a matrix for the Fe(II) spin-crossover. *Inorganic Chemistry*, 46(26):11106–11111, 2007.

[43] Wataru Kosaka, Kiyoshi Nomura, Kazuhito Hashimoto, and S. I. Ohkoshi. Observation of an Fe(II) spin-crossover in a cesium iron hexacyanochromate. *Journal of the American Chemical Society*, 127(24):8590–8591, 2005.

[44] Helena Prima-García, Eugenio Coronado, Juan P. Prieto-Ruiz, and Francisco M. Romero. Tailoring magnetic properties of electrodeposited

thin films of the molecule-based magnet Cr5.5(CN)12·11.5H2O. *Nanoscale Research Letters*, 7:1–7, 2012.

[45] M. Bradler and E. Riedle. Temporal and spectral correlations in bulk continua and improved use in transient spectroscopy. *Journal of the Optical Society of America B*, 31(7):1465, 2014.

[46] Luke Hedley, Neil Robertson, and J. Olof Johansson. Electrochromic Thin Films of the V-Cr Prussian Blue Analogue Molecular Magnet. *Electrochimica Acta*, 236:97–103, 2017.

[47] Melvin B Robin. The Color and Electronic Configurations of Prussian Blue. *Inorganic Chemistry*, 1(2):337–342, 1962.

[48] S. I. Ohkoshi, Mikihisa Mizuno, Guo jye Hung, and Kazuhito Hashimoto. Magnetooptical effects of room temperature molecular-based magnetic films composed of vanadium hexacyanochromates. *Journal of Physical Chemistry B*, 104(40):9365–9367, 2000.

[49] David M. Rogers and J. Olof Johansson. Metal-to-metal charge-transfer transitions in Prussian blue hexacyanochromate analogues. *Materials Science and Engineering B: Solid-State Materials for Advanced Technology*, 227(October 2017):28–38, 2018.

[50] Eugenio Coronado, Magdalena Fitta, Juan P. Prieto-Ruiz, Helena Prima-García, Francisco M. Romero, and Ana Cros. MOKE magnetometry as a probe of surface magnetic impurities in electropolymerized magnetic thin films of the Prussian blue analogue Fe3[Cr(CN)6]2·15 H2O. *Journal of Materials Chemistry C*, 1(42):6981, 2013.

[51] Eugenio Coronado, Magdalena Makarewicz, Juan P. Prieto-Ruiz, Helena Prima-García, and Francisco M. Romero. Magneto-optical properties of electrodeposited thin films of the molecule-based magnet Cr 5.5(CN) 12??11.5H 2O. *Advanced Materials*, 23(37):4323–4326, 2011.

[52] M Verdaguer, N Galvez, R Garde, and C Desplanches. Electrons at Work in Prussian Blue Analogues. *Electrochem. Soc. Interface*, 11(3):28–32, 2002.

[53] Paul Monk, Roger J. Mortimer, and David Rosseinsky. *Electrochromism: Fundamentals and Applications*. VCH, 2008.

[54] Roger J. Mortimer and John R. Reynolds. In situ colorimetric and composite coloration efficiency measurements for electrochromic Prussian blue. *Journal of Materials Chemistry*, 15(22):2226–2233, 2005.

[55] J Velevska, M Pecovska-gjorgjevich, N Stojanov, and M Najdoski. Electrochromic Properties of Prussian Blue Thin Films Prepared by Chemical Deposition Method. 4531(January):380–392, 2016.

[56] Kun Chieh Chen, Chih Yu Hsu, Chih Wei Hu, and Kuo Chuan Ho. A complementary electrochromic device based on Prussian blue and poly(ProDOT-Et2) with high contrast and high coloration efficiency. *Solar Energy Materials and Solar Cells*, 95(8):2238–2245, 2011.

[57] M S Roy. Complementary electrochromic display system based on prussian blue thin film. *Renewable Energy*, pages 505–507, 2006.

[58] Luke Hedley, Liz Porteous, David Hutson, Neil Robertson, and J. Olof Johansson. Electrochromic bilayers of Prussian blue and its Cr analogue. *Journal of Materials Chemistry C*, 6(3):512–517, 2017.

[59] Joris J. Snellenburg, Sergey P. Laptenok, Ralf Seger, Katharine M. Mullen, and Ivo H. M. van Stokkum. Glotaran : A Java-based graphical user interface for the R package TIMP. *Journal of Statistical Software*, 49(3):1–2, 2012.

[60] Luke Hedley, Michael D. Horbury, Florian Liedy, and J. Olof Johansson. Observation of excited state absorption in the V-Cr Prussian blue analogue. *Chemical Physics Letters*, 687:125–130, 2017.

[61] Gail E Rojas, Charles Dupuy, Douglas A Sexton, and Douglas Magde. Subpicosecond Flash Photolysis of Cr (III) Coordination Complexes. (2), 1986.

[62] Joel N Schrauben, Kevin L Dillman, Warren F Beck, and James K. McCusker. Vibrational coherence in the excited state dynamics of Cr ( acac ) 3 : probing the reaction coordinate for ultrafast intersystem crossing . *Chemical Science*, 2010.

[63] Luisa Ferrari, Mauro Satta, Amedeo Palma, Lorenzo Di Mario, Daniele Catone, Patrick O Keeffe, Nicola Zema, Tommaso Prosperi, and Stefano Turchini. A Fast Transient Absorption Study of Co(AcAc)3. *Frontiers in Chemistry*, 7(May):1–12, 2019.

# List of Figures

# Appendix A

# Publications

## A.1 Electrochromic Thin Films of the V-Cr Prussian Blue Analogue Molecular Magnet

Electrochimica Acta 236 (2017) 97–103

Contents lists available at ScienceDirect

Electrochimica Acta

journal homepage: www.elsevier.com/locate/electacta

# Electrochromic Thin Films of the V-Cr Prussian Blue Analogue Molecular Magnet

Luke Hedley, Neil Robertson, J. Olof Johansson*

*EaStCHEM, School of Chemistry, University of Edinburgh, David Brewster Road, EH9 3FJ, UK*

ARTICLE INFO

*Article history:*
Received 14 December 2016
Received in revised form 22 February 2017
Accepted 22 March 2017
Available online 24 March 2017

*Keywords:*
Electrochromism
spectroelectrochemistry
Prussian blue analogues
molecular magnetism

ABSTRACT

This paper describes spectroelectrochemical measurements of thin films of the $V^{II/III}$-$Cr^{III}$ Prussian blue analogue (V-Cr PBA). We show that we can electrically control the optical properties of this room-temperature molecule-based magnet and reversibly switch the colour of the films from blue to black upon reduction. The cyclic voltammogram of the films showed a weak wave at −0.85 V and a stronger wave at −1.22 V. The spectroelectrochemical measurement in KCl indicate that the wave at −0.85 V is related to the reduction of V(III) to V(II) because of a shift in the absorption band associated with the metal-to-metal charge-transfer band. The wave at −1.22 V occurred simultaneously with the growth of a new absorption feature at 465 nm and is attributed to the reduction of $[Cr^{III}(CN)_6]^{3-}$ sites to $[Cr^{II}(CN)_6]^{4-}$. We have assigned the change to the optical spectrum occurring at 465 nm after electrochemical reduction to a red-shift of a metal-to-ligand charge-transfer (MLCT) transition from $Cr^{2+}$ to empty $\pi^*$ ligand orbitals. The electrochromic coloration efficiency associated with switching from blue to black colour was found to be $\eta = -25.2 \pm 0.2\ cm^2\ C^{-1}$ with a switching time of 6.6 s at −1.3 V. These findings demonstrate the possibility to electrically control the optical properties of a room-temperature molecular magnet.



## 1. Introduction

The colour of electrochromic materials can be switched by applying a small electrical voltage [1,2]. These materials show large potential to be used in electrochromic windows and mirrors, sensors, or light modulators. For light modulators, additional magnetic ordering of the materials would also allow for modulating the light polarisation via the Faraday effect [3]. Here we have explored a family of molecular materials whose magnetic properties can be switched electrochemically and at the same time show electrochromic effects. In order to develop future multi-functional devices combining magnetic and electrochromic properties, there is an urgent need to gain a deep understanding of the spectroelectrochemical properties of these materials. An additional advantage of molecular materials is that they can be made transparent and be deposited on glass substrates. More generally, solution-processed electrochromic materials are gaining in popularity since they require less energy in the manufacturing process [4].

Some of the most studied molecule-based magnets are Prussian blue and its analogues, which comprise transition metal ions linked by cyanide ligands in a rock-salt structure [5]. The general formula is $C_cA_a[B(CN)_6]_b{\cdot}nH_2O$ (C = alkali cation, A,B = transition metal ions). Thin films of these magnetic materials have previously been electrochemically deposited on conductive glass substrates for a range of analogues [3,6–11]. The original Fe-Fe Prussian blue has been studied extensively for electrochromic applications [1,2]. Other PBAs, mainly containing hexacyanoferrate, have also been explored and an extensive summary is presented in Ref. [12]. Interestingly, some PBAs can be reversibly switched between a ferrimagnetic and paramagnetic state electrochemically [13–15]. For combining optical and magnetic functionality, the V-Cr PBA is promising because it is ferrimagnetic at room temperature [16] and has a clear blue colour. Verdaguer et al. have observed electrochromic behaviour of this material and showed that it is possible to change the colour from blue to colourless upon oxidation [17,18]. The aim of the work presented here was to expand the range of electrochromic switching capabilities of the V-Cr PBA and to understand the mechanisms involved causing the change to the optical spectrum as a function of applied potential. We have therefore studied the spectroelectrochemistry of the films at a more reducing potential than Verdaguer et al. and found that

* Corresponding author.
*E-mail address:* olof.johansson@ed.ac.uk (J. O. Johansson).

http://dx.doi.org/10.1016/j.electacta.2017.03.166
0013-4686/

we could reversibly switch the colour from blue to black. We have assigned the absorption giving rise to the black colour and determined the colouration efficiency and the switching time for the blue-to-black electrochromic response.

The oxidation state of the vanadium ions in the V-Cr PBA can vary depending on the synthetic conditions and often both V(II) and V(III) are found. Typically, the materials are to a large degree amorphous and characterisation is challenging due to the high air sensitivity. Nevertheless, oxidation states of the vanadium ions have been determined using X-ray absorption spectroscopy (XAS) [19], energy-dispersive x-ray spectroscopy (EDS) and x-ray photoelectron spectroscopy (XPS) [20], and elemental analysis [8] (based on charge-balance arguments). The visible spectrum of the V-Cr PBA is dominated by strong metal-to-metal charge-transfer (MMCT) bands, where an electron is optically transferred from a Cr ion to a V ion. More energy is required to transfer an electron from a Cr ion to a V(II) site than to a V(III) site. The spectral position of the MMCT therefore depends on the oxidation state of the vanadium ions. Garde et al. found that for V-Cr PBAs containing solely V(II), the main MMCT transition occurred at 540 nm, whereas in samples comprising only V(III), the absorption occurred at 650 nm [19]. For electrochemically produced films, Ohkoshi et al. [8] also noted that for certain conditions, they could produce predominantly V(II), which resulted in an absorption peak at 540 nm, in agreement with Garde et al. [19]. When Ohkoshi's films contained both V oxidation states, peaks at both 540 and 660 nm were observed. Another feature to note in the absorption spectrum of V-Cr PBA is a peak at 800 nm that has been assigned to a forbidden d-d transition localised on the $[Cr^{III}(CN)_6]^{3-}$ ions, which becomes partly allowed in the PBA network [19]. There are intense bands below 400 nm, which have been assigned to ligand-to-metal (LMCT) and metal-to-ligand (MLCT) charge-transfer transitions due to their energy and relatively strong oscillator strength [21,22].

The paper is organised as follows. In Section 2, the experimental approach is briefly explained and we discuss the synthetic methods and how to protect the air sensitive films. In Section 3.1, we present the cyclic voltammograms (CVs) of both the starting materials and the final films. The characterisation of these films is subsequently described in Section 3.2. We found that we can control the film thickness by varying the deposition time and interestingly we found that in thinner film it is possible to distinguish the V oxidation states in the transmittance spectrum. The dependence of the transmittance spectrum as function of applied voltage was studied in a spectroelectrochemical measurement and the results are presented in Section 3.3. We found that for lower voltages, we observe an increase in the MMCT associated with the Cr(III) to V(II) transition as a consequence of the reduction of V(III) to V(II). For more negative voltages, a MLCT absorption on the Cr ions is observed as a consequence of reducing $[Cr^{III}(CN)_6]^{3-}$ to $[Cr^{II}(CN)_6]^{4-}$. We have characterised the electrochromic performance of the films by investigating the colouration efficiency and switching time in Section 3.4. These results show a new electrochemical control of the optical properties of the magnetic V-Cr PBA.

## 2. Experimental

The films were electrochemically deposited on fluorine-doped tin oxide (FTO) coated glass substrates of 1 mm thickness. The substrates were sequentially cleaned in an ultrasonic bath in the following solvents: deionised water and detergent, isopropanol, methanol, and finally in deionised water, since water is used as solvent in the electrochemical cell. All electrochemical experiments were carried out using a Metrohm-Autolab μAUTOLABIII potentiostat with a saturated calomel reference electrode and a Pt counter electrode. Aqueous solutions of $VCl_3$ and $K_3[Cr(CN)_6]$ from Sigma-Aldrich were used without further purification at concentrations typically 10 mM and KCl (also from Sigma-Aldrich) was used as electrolyte at a concentration of 1.0 M. The V-Cr PBAs are air sensitive and so the electrochemistry was performed under $N_2$ flow. All solvents were thoroughly bubbled with $N_2$ and any $O_2$ in the reagent powders were removed using a Schlenk line. The films were made under potentiostatic conditions, typically at −1.15 V vs SCE. After the synthesis, the films were rinsed with $N_2$-bubbled $H_2O$ and allowed to dry under $N_2$ flow. Once dried, they were either sealed with cyanoacrylate glue and a 0.18 mm thick glass microscope coverslip or immediately used for CV scans without sealing. The film area typically ranged from 1.0 to 1.2 $cm^2$. Spectroelectrochemistry measurements were carried out in a standard 10 mm cuvette. A fibre-based halogen light source (Ocean Optics HL-2000-FHSA) and a fibre-coupled spectrometer (Ocean Optics HR2000+) were used. The films, together with reference and counter electrodes, were immersed in the cuvette. In order to fit all the electrodes, the saturated calomel reference electrode was replaced with a pseudo-reference electrode made from Pt wire. Any shift in potential of the pseudo-reference electrode was checked in a normal electrochemical cell with either the Pt electrode or the SCE electrode by carrying out a CV scan of a V-Cr PBA film. A shift smaller than 0.02 V was observed.

Electrochromic characterisation was carried out by setting the spectrometer to measure at a fixed wavelength at 465 nm and was synchronised with the potentiostat, which in turn was programmed to cycle the potential between 0 and −1.3 V at 15 s intervals.

The IR spectra were acquired using an attenuated total reflection IR spectrometer (Perkin Elmer Spectrum Two – UATR) by scraping off the films from the glass substrates with a razor blade. For the XPS measurements, the samples were freshly prepared and stored in $N_2$-bubbled water and were quickly transferred to the XPS where they were allowed to dry in the vacuum of the instrument. The sample was grounded by contacting the FTO-surface to ground using a metal support. The films were measured first without any surface treatment and subsequently after sputtering with $Ar^+$ ions for 30 min. The XPS instrument, VG Scientific with an Al Kα radiation source, was calibrated based on Cu $2p_{3/2}$ standard. Normally adventitious carbon would be used to further calibrate the spectrum for a specific sample. However, since there is probably a mixture of adventitious and cyanide carbon we did not further fine-tune the calibration. The C 1s peak positions before and after sputtering were 284.7 and 284.4 eV, respectively. Because the C 1s peaks were reasonably close to that expected for carbon (either cyanide or adventitious), the calibration was sufficiently accurate to distinguish Sn, V, and Cr. A Shirley baseline was subtracted from the XPS spectra and Gaussian functions were used to fit the peak area and positions. The AFM measurements were carried out on a freshly made sample that was immediately transferred to the AFM (AFM Veeco Nanoman VS with Dimension 3100 controller). However, it was not possible to purge the AFM with $N_2$ and so all AFM measurements were carried out on oxidised films.

## 3. Results and discussion

### 3.1. Electrochemical synthesis

When making the films, we followed the approach of Ohkoshi *et* al., who used potentiostatic conditions at a relatively large negative potential (−1.16 V vs SCE) [8]. We found that this method leads to the best optical quality and the clearest blue colour of the V-Cr PBA films. Aqueous solutions of $VCl_3$ and $K_3[Cr(CN)_6]$ were made and added to the electrochemical cell along with the electrolyte. When applying a negative potential to the working electrode, $V^{3+}$ ions are

reduced at the electrode surface to produce $V^{2+}$ ions. These ions subsequently react with $[Cr(CN)_6]^{3-}$ units in the solution to form the insoluble PBA film on the electrode surface. In order to understand the electrochemical synthesis, we first carried out the CV of the individual starting materials separately, *viz* $VCl_3$ and $K_3[Cr(CN)_6]$. The results are presented in Fig. 1 (a) and (b). In the CV for $K_3[Cr(CN)_6]$, shown in Fig. 1 (a), the weak reduction peaks at −0.7 and −1.1 V were negligible compared to the currents recorded for $VCl_3$ and are attributed to impurities. As can be seen in Fig. 1 (a), the reduction of the V ions appears around −0.8 V. The reverse process corresponds to the re-oxidation of V(II) ions. When scanning to more negative voltages (Fig. 1 (b)), which are used during the synthesis of the V-Cr PBA films, a more complicated CV is observed. We attribute the second reduction wave at −1.1 V to the nucleation of vanadium-containing deposit on the working electrode, which is an important step towards forming the insoluble PBA films on the substrate surface. The sharp re-oxidation peak at −0.5 V is then the stripping peak of the vanadium-containing deposit formed on the substrate, which is not observed when the potential is scanned only to −0.8 V. The oxidation of free V(II) ions can still be seen at the broad peak around 0 V. When the electrochemical synthesis is carried out in the presence of the two reagents together, the CV is different (Fig. 1 (c)). The stripping peak is significantly reduced in intensity, which is due to a kinetic effect where the $V^{2+}$ ions react more readily with the $[Cr(CN)_6]^{3-}$ rather than to continue to plate vanadium-containing deposits onto the substrate surface. This is therefore consistent with the formation of V ions attached to the substrate in order to form the insoluble PBA film. Note that we do not normally cycle the voltage when making V-Cr PBA films for optical applications since we found that the best optical quality, as

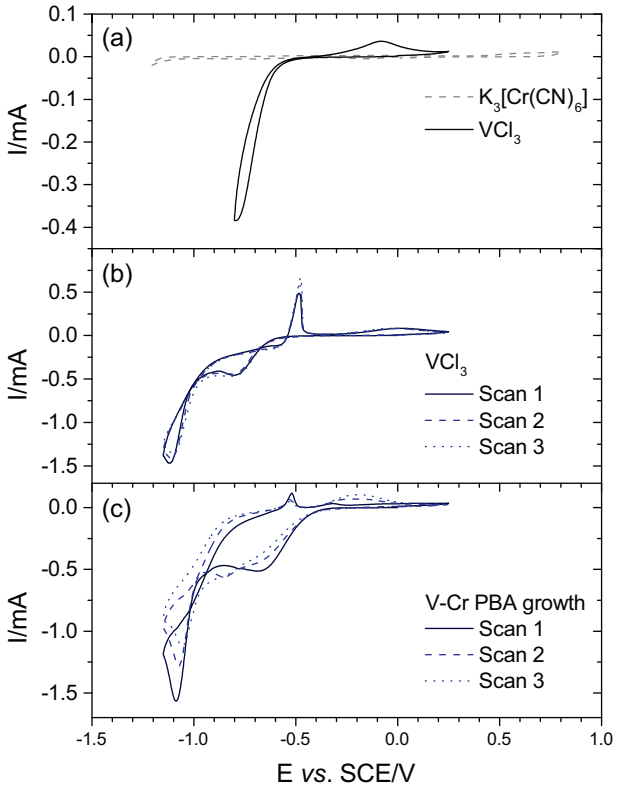


**Fig. 1.** Cyclic voltammograms of the starting materials. (a) CV of individual starting materials. Note that the voltage range for $VCl_3$ is smaller than $K_3[Cr^{III}(CN)_6]$ due to additional processes taking place at more negative potentials, which is presented in (b). The CV-growth of V-Cr PBA in the presence of both starting materials is presented in (c).

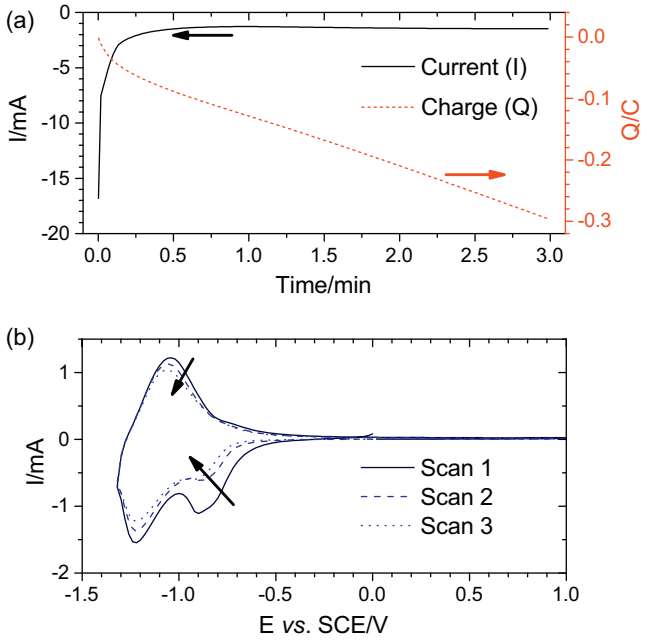


**Fig. 2.** Charge, current, and CV of potentiostatically synthesised films. (a) The charge and current recorded during the synthesis of a V-Cr PBA film at −1.15 V for 3 minutes. The CV of the film in (a) is presented in (b).

previously mentioned, is produced at potentiostatic conditions at as negative potential as possible (*ca.* −1.15 V). It should be noted however that Verdaguer et al. followed a different approach by using $VO^{2+}$ as a starting material and subsequently grew the films by cycling the potential between −0.6 and 0.1 V vs. SCE [17]. In order to distinguish processes involved in the film formation during the CV scan in Fig. 1 (c) and the CV of the final film produced potentiostatically, the CV of the potentiostatically produced PBA film was repeated in KCl electrolyte from 1.0 to −1.3 V. The results of the potentiostatic deposition and subsequent cycling in KCl are presented in Fig. 2 (a) and (b). For the measurements presented here, the films were made by applying a static potential at −1.15 V for 3 min. In the CV a wave at −0.85 V is observed and we attribute this to the reduction of V(III) present in the film. XPS measurements presented below indicate that V(III) is indeed present in the final film at a relatively high concentration. The reduction of V(III) sites is further supported by the spectroelectrochemical data presented in Section 3.3. The large wave at −1.22 V is attributed to the reduction of $[Cr^{III}(CN)_6]^{3-}$ to $[Cr^{II}(CN)_6]^{4-}$, with the corresponding re-oxidation taking place at −1.05 V. During the CV procedure, charge balance is maintained by the insertion and extraction of potassium counter ions (SI). The CV could be repeated several times. However, the peak current decreases slightly for each cycle due to film dissolution. This reduction process has not been discussed previously for the V-Cr PBA but it has been shown that $[Cr^{III}(CN)_6]^{3-}$ can be reduced at a similar potential in the Fe-Cr PBAs (−1.15 V vs. SCE) [23]. In Cr-Cr PBA, however, the reduction of $[Cr^{III}(CN)_6]^{3-}$ is thought to happen at a less negative potential (−0.85 V vs. Ag/AgCl) [9,11]. It is therefore possible that the first wave at −0.85 V is the reduction of $[Cr^{III}(CN)_6]^{3-}$. However, based on the spectral changes of the MMCT transition associated with this reduction wave, we attribute the first −0.85 V to the V(III) to V (II) reduction process, as is discussed below.

### 3.2. Film characterisation

The films were characterised with XPS, UV/VIS and IR spectroscopy. The XPS data are presented in Fig. 3 (a) for the

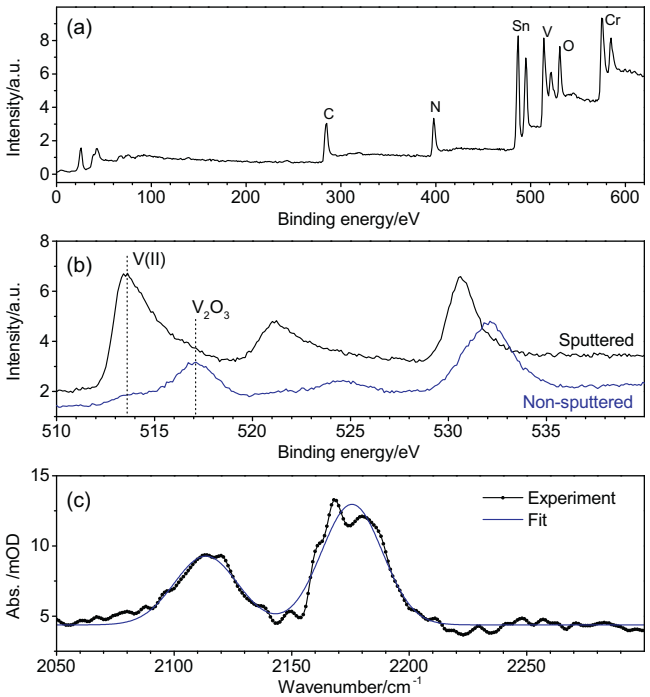


**Fig. 3.** XPS and IR characterisation of the V-Cr PBA films. (a) Full XPS scan of the sputtered surface, where peaks assignments are shown in the figure. The peaks to higher binding energies for Sn, V, and Cr are due to the spin-orbit splitting. XPS spectra were also collected with a higher resolution and the region of the V $2p_{3/2}$ and $2p_{1/2}$ are shown in (b). In this region the peak for O 1s is also observed. The O 1s binding energy for the sputtered sample is closer to what is typically observed for metal oxides whereas for the non-sputtered surface it is closer to what is typically found in organic molecules (resulting from impurities on the surface). Spectra for both the un-treated and sputtered surface are shown. The IR spectrum of a V-Cr PBA film is shown in (c). The peak at 2113.5 cm$^{-1}$ is due to the cyanide stretching mode in the $V^{II/III}$-$Cr^{III}$ PBA. During the measurement the sample was exposed to air and became partially oxidised, which is seen as a shift of the cyanide stretching peak to 2175 cm$^{-1}$.

full range of electron binding energies recorded. The expected elements such as C, N, O, Cr and V were observed, as well as the Sn peaks from the FTO layer. We did not observe any K or F peaks. The region around the expected vanadium peaks is shown in Fig. 3 (b). Here three peaks were used to fit the V $2p_{3/2}$ peaks in order to capture the relative intensities of the contributions from V(II), V (III), and the oxidised V(IV). The spin-orbit split peaks corresponding to $2p_{1/2}$ appear to ca. 7.5 eV higher binding energies. Unfortunately, the resolution of the measurement was not good enough to distinguish between V(II) and V(III), however the V(IV) peak at 517.1 eV could be distinguished from the two other valences. Because of the air sensitivity of the materials, it is natural to assume that a thin oxide layer is formed on top of the films. In fact, the band maximum of the V peaks is shifted towards the binding energy of 517.1 eV associated with oxidised vanadium. The film was therefore sputtered with $Ar^+$ ions for 30 min. After sputtering, the V band maximum has clearly shifted towards the range 513.6 eV (marked with a dashed line in the figure) to *ca.* 515.8 eV, associated with V(II) and V(III). The peak from oxidised vanadium at 517.1 eV is much less pronounced than in the spectrum from the non-sputtered surface. Despite the poor resolution, it is clear that the sputtered spectrum contains much less oxidised material than the non-sputtered spectrum (from the untreated surface). Since the relative V oxidation states could not be resolved, the composition of the V-Cr PBA film was determined based on the total area of V and Cr peaks in the XPS spectra. The peak areas were compared after correcting for the atomic sensitivity factors and taking into account the accuracy of the technique. A Cr:V ratio of 0.8 was found for the sputtered sample. Based on these findings, and assuming that the film should be neutral, we can determine the composition of the films as $V^{II}_{0.5}V^{III}_{0.5}\left[Cr^{III}(CN)_6\right]_{0.8}$. The composition of the non-sputtered film was $V^{II}_{0.1}V^{III}_{0.9}\left[Cr^{III}(CN)_6\right]_{0.9}$. In order to maintain the charge balance, potassium ions can be found in the lattice depending on stoichiometry. The XPS does not show any potassium ions although small amounts could potentially be difficult to detect since this peak is masked by the much stronger C signal. Nevertheless, we rule out any significant concentration of $K^+$ ions in the sample and so the charge balance is achieved by a slightly smaller amount of Cr to V and mixture of V oxidation states. The larger contribution of V (III) on the un-treated surface can be due to oxidised V(II). Furthermore, V(III), which is present in the solution, can react more readily with the already formed V-Cr PBA lattice. It is therefore likely that the majority of the V(III) sites are located at the surface of thicker films, as is indeed confirmed by the depth-dependent XPS measurements made possible with sputtering. The $2p_{3/2}$ Cr peak appears at 577.9 eV for the non-sputtered measurement and at 574.8 eV for the sputtered measurement (with a weak shoulder still observable at *ca.* 577 eV). The Cr $2p_{1/2}$ peak occurs at 584.9 eV for the sputtered measurement, giving a spin-orbit splitting of 10.1 eV. The Cr-peak binding energy is close in value to that reported by Hatlevik et al. (577.2 eV) [20] for non-sputtered films. However, in the spectrum for the sputtered surface we observe a binding energy closer to that expected for $[Cr^{III}(CN)_6]^{3-}$, which occurs at 576.2 eV [9]. Clearly the environment for the Cr ions at the surface is different from inside the bulk film. Because the Cr:V ratio ranges from 0.8 to 0.95 (sputtered or non-sputtered, respectively), it indicates that there are few vacant sites in the lattice.

The presence of the V-Cr PBA network is confirmed by the IR spectrum shown in Fig. 3 (c). The $Cr^{III}$-C≡N-$V^{II}$ peak has previously been reported to occur at around 2104 cm$^{-1}$ and the $Cr^{III}$-C≡N-$V^{III}$ peak at 2118 cm$^{-1}$ [16]. The cyanide stretching peak in Fig. 3 (c) can be seen at 2113.5 (4) cm$^{-1}$ (32 cm$^{-1}$ FWHM), which is in agreement with previously reported values for the V-Cr PBA [16]. Given the width of the peak at 2113.5 cm$^{-1}$, we can conclude that the IR data support the presence of both vanadium oxidation states. The peak at 2175.6 (2) cm$^{-1}$ (with 30 cm$^{-1}$ FWHM) is due to the presence of vanadyl and is an indication that the films are oxidised when they are exposed to air during the IR measurement. Powder X-ray diffraction patterns, obtained by scraping off the films from the substrate surface, were nearly featureless and so indicate that the films are mainly amorphous.

The film thickness was determined from the AFM measurements presented in Fig. 4 (a) and (b). The thickness could be controlled by the duration of the potentiostatic deposition process and four different deposition times were investigated (1 to 4 minutes). The AFM measurements were carried out with a freshly prepared sample which was transported from the synthesis lab to the AFM instrument in a sealed container. However, the samples oxidised during the measurement, as is apparent by the change in colour (the films become white/brown within 5 minutes in air). Ferlay et al. [24] have made structural measurements of the oxidised vanadyl analogue, and they observed a cubic structure with lattice parameter of ca. a = 10.490 (4) Å, similar to the non-oxidised V-Cr PBA sample. We therefore believe that the thickness measured on the oxidised sample is similar to the non-oxidised sample. For the thinnest film, a distribution of particles with a wide size distribution from *ca.* 25 to 90 nm was found (with an average size of 50 nm). However, for longer deposition times, a more continuous film was grown. The continuous films appear to crack when oxidised, which was observed for all films grown for longer

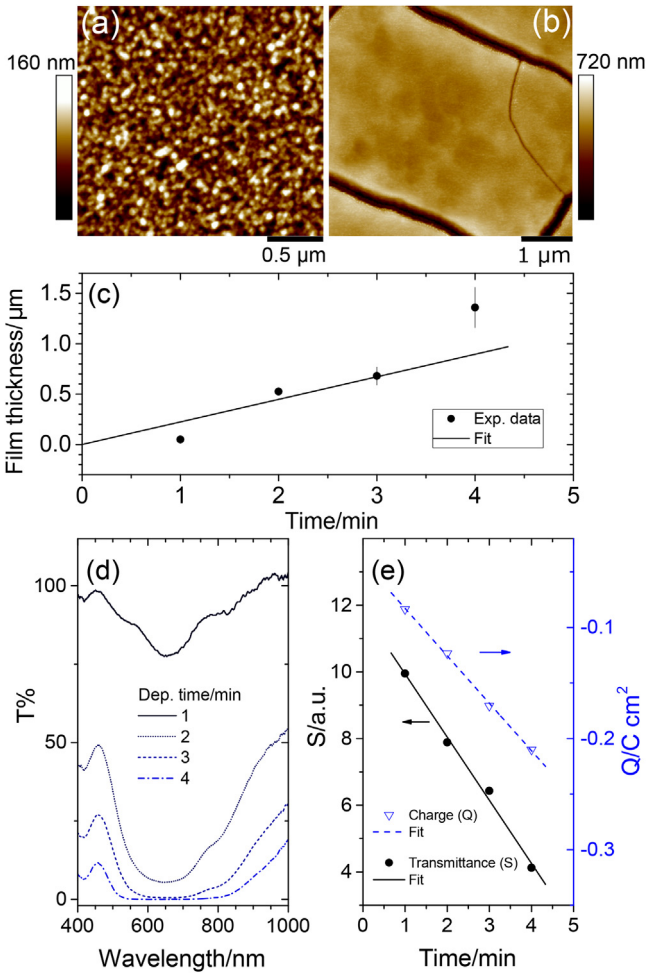


**Fig. 4.** Characterisation of film morphology and thickness as a function of electrochemical deposition time. All AFM measurements were carried out on oxidised samples. AFM images of films deposited for (a) 1 min and (b) 2 min are presented. The films cracked upon oxidation and the size of the crack was used to estimate the film thickness, which is plotted in (c) as a function of deposition time. Before the samples were oxidised, the optical transmittance spectra were recorded and are presented in (d). The dependence of the transmittance intensity on the film thickness is shown in (e). S is the natural logarithm of the total transmittance from 500 to 750 nm and is defined in Eq. (1). The total charge density Q used in the electrochemical synthesis is also presented in (e).

than 1 minute. This is shown in Fig. 4 (b) for the film deposited for 2 minutes. From the size distribution of the particle size in Fig. 4 (a) (film deposited for 1 minute) and the depth of the cracks of the thicker films, we could estimate the film thickness as a function of deposition time, which is presented in Fig. 4 (c). In order to relate the optical density to the film thickness, the transmittance was recorded for each film before they were oxidised. The results are presented in Fig. 4 (d). It is interesting to notice that for the thinnest film, the MMCT transitions to the two different vanadium oxidation states can clearly be seen as minima in the transmittance at 540 and 660 nm. However, for the thicker films, the two MMCT bands merge together. For the longest deposition time, the corresponding absorption reached an optical density of 4.0 (seen as zero transmittance on the scale in Fig. 4 (d)). In order to compensate for different ratios of V(II):V(III), which can depend on the film thickness as was discussed in the XPS section, the total transmittance over both MMCT peaks was integrated. According to the Beer-Lambert law, the transmittance scales exponentially with the optical path length and so the logarithm S of the integrated transmittance from 500 to 750 nm, should therefore produce a linear relationship with film thickness d according to

$$S = \ln\left(\int_{500nm}^{750nm} T(\lambda)d\lambda\right) \propto d. \quad (1)$$

We therefore plotted the natural logarithm of the integrated transmittance in Fig. 4 (e). A linear dependence is observed, in agreement with the AFM images of the oxidised films. We also plotted the total charge deposited for each film. In principle this should correlate with the total amount of material deposited. Based on an area of 1 cm$^2$ we would need *ca.* $10^{16}$ electrons to produce one sheet of the V-Cr PBA (assuming that each V ion is 10 Å apart). This estimation also assumes that all vanadium is present as V(II). Since the deposited films were grown with a total charge of *ca.* 0.1 C (Fig. 4 (e)), we can estimate that a total of $10^{18}$ electrons have been consumed in the film growth. The number of "sheets" is therefore $10^{18}/10^{16}$ and given that each sheet is separated ca. 10 Å, we can estimate that we should produce a 100 nm thick film. However, because some of the material crashes out in solution and the films also contain V(III) ions, this is difficult to estimate – not even taking into account the morphology of the films.

### 3.3. Spectroelectrochemistry

The spectroelectrochemical data are presented in Fig. 5 and the voltages should be referenced to the CV in Fig. 2 (b). At the onset of the first reduction wave at *ca.* −0.5 V in the CV in Fig. 2 (b), there is a decrease in the transmittance at 540 nm (Fig. 5 (a)). This decrease corresponds to an increase in the absorption associated with the Cr (III) to V(II) MMCT. This decrease in the transmittance grows up to −0.85 V, in agreement with the wave shown in the CV in Fig. 2 (b). This is the reason for assigning the first reduction wave in Section 3.1 to reducing V(III) to V(II). When changing the potential further to the second reduction peak at −1.22 V, the peak in transmittance at 465 nm, which gives rise to the blue colour of the V-Cr PBA, is significantly reduced in intensity (Fig. 5 (b)). As

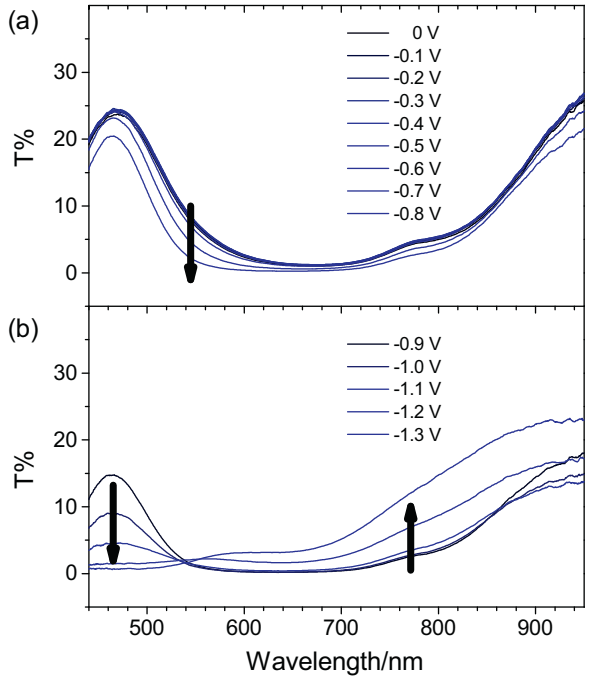


**Fig. 5.** Spectroelectrochemical measurements of the V-Cr PBA. For clarity the measurement is presented for two voltage regions, namely from 0 to −0.8 V (a) and from −0.9 to −1.3 V (b). Arrows indicate the direction of change in the spectra with increasing negative applied potential.

previously discussed, this is attributed to the reduction of the Cr sites. When assigning the transition associated with the loss of transmittance at 465 nm, one has to consider that the total energy of the Cr sites will increase when an extra electron is added in the reduction process. An increase in energy of the Cr ions will cause a red-shift of the MMCT transitions that occur at 540 and 660 nm. It is therefore not plausible that the new absorption feature is due to a shifted MMCT transition. The slight increase in transmittance at these wavelengths (540–660 nm) do support this red-shift because a loss of chromophores absorbing in the visible region would contribute to the increase in transmittance in this spectral region. The shifted MMCT is probably pushed to wavelengths longer than 900 nm, where our detection system and light source are not effective. Likewise, the LMCT states around 400 nm [21,22] would be shifted to even shorter wavelengths if the energy of the Cr ion increased. What is more, we also rule out metal-centred transitions based on the strong absorption coefficient associated with the new absorption feature (comparable to the MMCT transitions). The increase in energy of the Cr ion upon reduction will bring it closer in energy to the empty $\pi^*$ orbitals on the cyanide ligands. We therefore assign the new absorption at 465 nm to MLCT transition from $[Cr^{II}(CN)_6]$ to empty $\pi^*$ ligand states. The peak at 800 nm has previously been assigned to a forbidden metal-centred absorption on the $[Cr^{III}(CN)_6]$ unit[19]. When Cr(III) sites are reduced, there is an increase in transmission at 800 nm, which is consistent with a loss of absorption from this transition.

### 3.4. Electrochromic switching

The change in colour was noticeable while carrying out the CV scans in the voltage range where $[Cr^{III}(CN)_6]$ is reduced (Fig. 6 (a) and (b)). The colour could be cycled between blue and black repeatedly and we therefore characterised the electrochromic

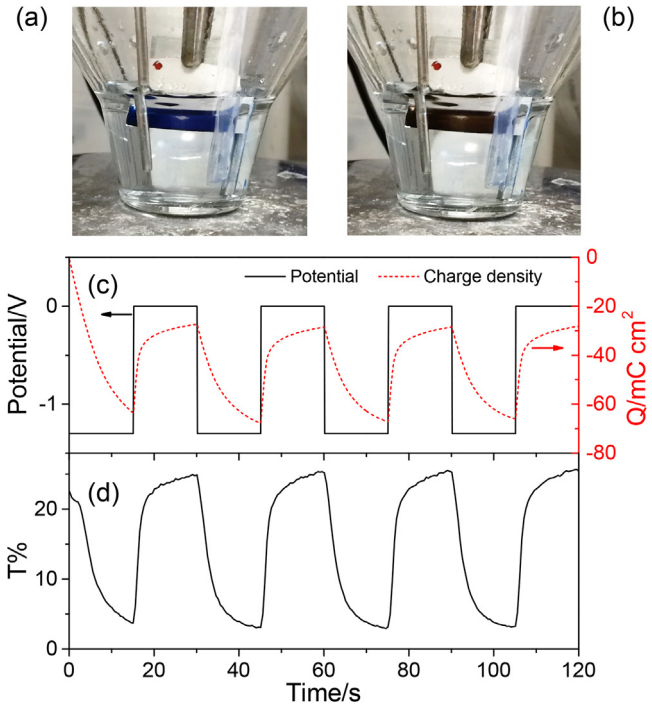


**Fig. 6.** Electrochromic switching of the V-Cr PBA from blue to black. Photographs of the films in the electrochemical cell (in aqueous solution of KCl) are shown in (a) at 0 V and in (b) for −1.3 V. The applied potential and corresponding charge density is presented in (c). The transmittance at 465 nm is shown in (d). (For interpretation of the references to colour in this figure legend, the reader is referred to the web version of this article.)

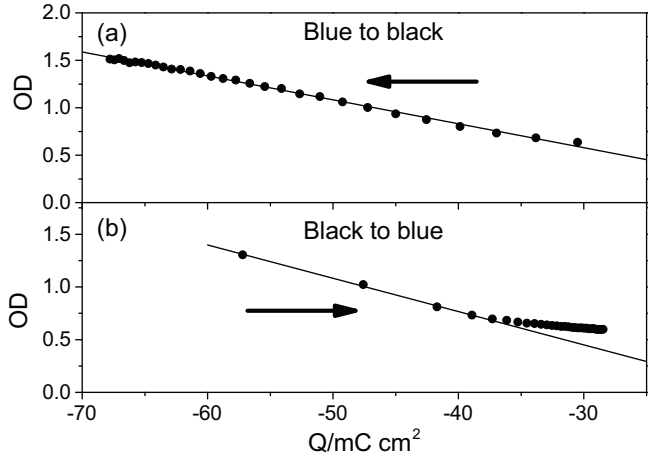


**Fig. 7.** The change in optical density as a function of applied charge density to the film in Fig. 5. The corresponding change from blue to black is shown in (a) and the change from black to blue is shown in (b). The chronological order of the applied charge density is indicated by the direction of the arrows.

properties of the films. The potential was cycled between 0 and −1.3 V and the charge density was recorded (Fig. 6 (c)). The transmittance at 465 nm was also recorded simultaneously. For the chosen film, the transmittance at 465 nm was T = 25 % while blue and could be reduced to ca. 3 % while black (Fig. 6 (d)). The colouration efficiency $\eta = \Delta OD/\Delta Q$ is typically used to characterise the efficiency of the switching process and relates to the change in optical density ($\Delta OD$) per unit charge density $\Delta Q$ passed through the material. We follow the convention of defining $\eta$ for absorbance (and therefore OD) instead of transmittance. The OD as a function of supplied charge density to the films can be plotted and the slope gives $\eta$, which is shown in Fig. 7 (a). A linear relationship of the optical density vs. charge density was found for the blue to black switching. This is because the films did not turn completely black within the time of the switching (cf. the spectroelectrochemical data in Fig. 5 (b) where the transmittance approaches $T \approx 0.2$ %). From the slope we found that $\eta = -25.2 \pm 0.2$ cm$^2$ C$^{-1}$. The switching process was rather slow and to switch from blue to black, corresponding to when the transmittance had reached 90% of its final value, took 6.6 s. In order to keep charge-neutrality in the reduced films, electrolyte counter ions have to diffuse into the lattice. On the other hand, the switching time is almost 1.5 times faster (4.7 s) when switching from black to blue colour. For switching from black to blue, the optical density saturates with applied charge density as is seen in Fig. 7 (b). The linear part of the curve was therefore fitted to obtain $\eta = -32 \pm 1$ cm$^2$ C$^{-1}$.

## 4. Conclusions

In conclusion, we have synthesised thin films of the V-Cr PBA using electrochemistry and studied their optical properties using spectroelectrochemistry. We have shown that we can reduce V(III) to V(II) and observe its effect on the optical spectrum due to the spectral sensitivity of the MMCT on V oxidation state. This can be useful for electrically fine-tuning the blue colour of V-Cr PBA films and its magnetic properties. By applying a more negative voltage, we can reduce the Cr ions and control the energy of the MLCT transition, shifting it from the UV to the visible region of the spectrum. This causes the film to turn black and the colour can be cycled repeatedly. In the electrosynthesis we can control the optical density of the films by increasing or decreasing the film thickness by adjusting the deposition time. We have found that potentiostatic deposition at large negative potential leads to

optically clear films with no $K^+$ counter ions and few vacant sites. We have demonstrated that we can electrically control and tune the colour of a room-temperature molecule-based magnet. Combining electrical, optical, and magnetic functionality of smart materials can potentially lead to new technologies such as magneto-optical data storage devices.

## Acknowledgements

The authors thank M. Verdaguer and C. Desplanches for helpful advice regarding the synthesis and characterisation of the materials, and D. Matselyukh for help with some of the measurements. This work was supported by funding from the Royal Society of Edinburgh and EPSRC (studentship to LH). JOJ is a Royal Society of Edinburgh/BP Trust research fellow.

## Appendix A. Supplementary data

Supplementary data associated with this article can be found, in the online version, at http://dx.doi.org/10.1016/j.electacta.2017.03.166.

## References

[1] P.R. Somani, S. Radhakrishnan, Electrochromic materials and devices: present and future, Mater. Chem. Phys. 77 (2003) 117–133, doi:http://dx.doi.org/10.1016/S0254-0584(01)00575-2.
[2] R.J. Mortimer, Electrochromic Materials, Annu. Rev. Mater. Res. 41 (2011) 241–268, doi:http://dx.doi.org/10.1146/annurev-matsci-062910-100344.
[3] T. Nuida, T. Hozumi, W. Kosaka, S. Sakurai, S. Ikeda, T. Matsuda, H. Tokoro, K. Hashimoto, S. Ohkoshi, Colored magnetic films composed of cyano-bridged metal assemblies and magneto-optical functionalities, Polyhedron. 24 (2005) 2901–2905, doi:http://dx.doi.org/10.1016/j.poly.2005.08.023.
[4] A. Llordés, Y. Wang, A. Fernandez-Martinez, P. Xiao, T. Lee, A. Poulain, O. Zandi, C.A. Saez Cabezas, G. Henkelman, D.J. Milliron, Linear topology in amorphous metal oxide electrochromic networks obtained via low-temperature solution processing, Nat. Mater. 15 (2016) 1267–1273, doi:http://dx.doi.org/10.1038/nmat4734.
[5] M. Verdaguer, G.S. Girolami, Magnetic Prussian Blue Analogs, in: J.S. Miller, M. Drillon (Eds.), Magn. Mol. to Mater., Wiley-VCH Verlag GmbH & Co. KGaA, Weinheim, Germany, 2005, pp. 283–346, doi:http://dx.doi.org/10.1002/9783527620548.ch9d.
[6] K. Itaya, T. Ataka, S. Toshima, Spectroelectrochemistry and electrochemical preparation method of Prussian blue modified electrodes, J. Am. Chem. Soc. 104 (1982) 4767–4772, doi:http://dx.doi.org/10.1021/ja00382a006.
[7] M. Mizuno, S. Ohkoshi, K. Hashimoto, Electrochemical Synthesis of High-Tc, Colored, Magnetic Thin Films Composed of Vanadium (II/III)–Chromium (II) Hexacyanochromate (III), Adv. Mater. 8904 (2000) 1955–1958, doi:http://dx.doi.org/10.1002/1521.
[8] S. Ohkoshi, M. Mizuno, G. Hung, K. Hashimoto, Magnetooptical Effects of Room Temperature Molecular-Based Magnetic Films Composed of Vanadium Hexacyanochromates, J. Phys. Chem. B. 104 (2000) 9365–9367, doi:http://dx.doi.org/10.1021/jp002002b.
[9] W.E. Buschmann, S.C. Paulson, C.M. Wynn, M.A. Girtu, A.J. Epstein, H.S. White, J. S. Miller, Reversed (Negative) Magnetization for Electrochemically Deposited High- T c Thin Films of Chromium Hexacyanide Magnets, Chem. Mater. 10 (1998) 1386–1395, doi:http://dx.doi.org/10.1021/cm970773v.
[10] E. Coronado, M. Makarewicz, J.P. Prieto-Ruiz, H. Prima-García, F.M. Romero, Magneto-optical properties of electrodeposited thin films of the molecule-based magnet Cr(5.5) (CN)(12)·11.5H(2) O, Adv. Mater. 23 (2011) 4323–4326, doi:http://dx.doi.org/10.1002/adma.201101513.
[11] J.P. Prieto-Ruiz, F.M. Romero, H. Prima-García, E. Coronado, Exchange coupling in an electrodeposited magnetic bilayer of Prussian blue analogues, J. Mater. Chem. C. 3 (2015) 11122–11128, doi:http://dx.doi.org/10.1039/C5TC01926E.
[12] P.M.S. Monk, R.J. Mortimer, D.R. Rosseinsky, Electrochromism by intervalence charge-transfer coloration: metal hexacyanometallates, in: Electrochromism and Electrochromic Devices, Cambridge University Press, Cambridge, 2007, pp. 282–302.
[13] O. Sato, T. Iyoda, A. Fujishima, K. Hashimoto, Electrochemically Tunable Magnetic Phase Transition in a High-Tc Chromium Cyanide Thin Film, Science (80-.) 271 (1996) 49–51, doi:http://dx.doi.org/10.1126/science.271.5245.49.
[14] O. Sato, Electrochromism and electrochemical magnetism in Ni-Fe Prussian blue, J. Solid State Electrochem. 11 (2007) 773–779, doi:http://dx.doi.org/10.1007/s10008-006-0203-2.
[15] Y. Mizuno, M. Okubo, K. Kagesawa, D. Asakura, T. Kudo, H. Zhou, K. Oh-ishi, A. Okazawa, N. Kojima, Precise Electrochemical Control of Ferromagnetism in a Cyanide-Bridged Bimetallic Coordination Polymer, Inorg. Chem. 51 (2012) 10311–10316, doi:http://dx.doi.org/10.1021/ic301361h.
[16] S. Ferlay, T. Mallah, R. Ouahès, P. Veillet, M. Verdaguer, A room-temperature organometallic magnet based on Prussian blue, Nature. 378 (1995) 701–703, doi:http://dx.doi.org/10.1038/378701a0.
[17] M. Verdaguer, M. Glavez, R. Garde, C. Desplanches, Electrons at Work in Prussian Blue Analogues, Electrochem. Soc. Interface. 11 (2002) 28.
[18] M. Verdaguer, A. Bleuzen, C. Train, R. Garde, F. Fabrizi de Biani, C. Desplanches, Room-temperature molecule-based magnets, Philos. Trans. R. Soc A Math. Phys. Eng. Sci. 357 (1999) 2959–2976, doi:http://dx.doi.org/10.1098/rsta.1999.0476.
[19] R. Garde, F. Villain, M. Verdaguer, Molecule-based room-temperature magnets: catalytic role of V(III) in the synthesis of vanadium-chromium Prussian blue analogues, J. Am. Chem. Soc. 124 (2002) 10531–10538, doi:http://dx.doi.org/10.1021/ja020528z. http://www.ncbi.nlm.nih.gov/pubmed/12197755.
[20] Ø. Hatlevik, W.E. Buschmann, J. Zhang, J.L. Manson, J.S. Miller, Enhancement of the Magnetic Ordering Temperature and Air Stability of a Mixed Valent Vanadium Hexacyanochromate(III) Magnet to 99 °C (372 K), Adv. Mater. 11 (1999) 914–918, doi:http://dx.doi.org/10.1002/(SICI)1521-4095(199908)11:11<914::AID-ADMA914>3.0.CO;2-T.
[21] K.D. Bozdag, J.-W. Yoo, N.P. Raju, A.C. McConnell, J.S. Miller, A.J. Epstein, Optical control of magnetization in a room-temperature magnet: V-Cr Prussian blue analog, Phys. Rev. B. 82 (2010) 94449, doi:http://dx.doi.org/10.1103/PhysRevB.82.094449.
[22] J.O. Johansson, J.-W. Kim, E. Allwright, D.M. Rogers, N. Robertson, J.-Y. Bigot, Directly probing spin dynamics in a molecular magnet with femtosecond time-resolution, Chem. Sci. 7 (2016) 7061–7067, doi:http://dx.doi.org/10.1039/C6SC01105E.
[23] S. Ohkoshi, Y. Einaga, A. Fujishima, K. Hashimoto, Magnetic properties and optical control of electrochemically prepared iron-chromium polycyanides, J. Electroanal. Chem. 473 (1999) 245–249, doi:http://dx.doi.org/10.1016/S0022-0728(99)00173-4.
[24] S. Ferlay, T. Mallah, R. Ouahes, P. Veillet, M. Verdaguer, A Chromium-Vanadyl Ferrimagnetic Molecule-Based Magnet: Structure, Magnetism, and Orbital Interpretation, Inorg. Chem. 38 (1999) 229–234, doi:http://dx.doi.org/10.1021/ic980109w.

## A.2 Observation of Excited State Absorption in the V-Cr Prussian Blue Analogue

Chemical Physics Letters 687 (2017) 125–130

Contents lists available at ScienceDirect

Chemical Physics Letters

journal homepage: www.elsevier.com/locate/cplett

Research paper

# Observation of excited state absorption in the V-Cr Prussian blue analogue

Luke Hedley [a], Michael D. Horbury [b], Florian Liedy [a], J. Olof Johansson [a,*]

[a] EaStCHEM, School of Chemistry, University of Edinburgh, David Brewster Road, EH9 3FJ, UK
[b] Department of Chemistry, University of Warwick, Gibbet Hill, CV4 7AL Coventry, UK

ARTICLE INFO

*Article history:*
Received 25 July 2017
In final form 31 August 2017
Available online 8 September 2017

*Keywords:*
Ultrafast spectroscopy
Prussian blue analogues
Charge-transfer transitions
Functional materials
Thin films
Spectroelectrochemistry

ABSTRACT

We present femtosecond transient transmission measurements of thin films of the $V^{II/III}$–$Cr^{III}$ Prussian blue analogue (V-Cr PBA) in the spectral range 330–675 nm after exciting the ligand-to-metal charge-transfer transition (LMCT) at 400 nm. A global analysis including three decay-times of $\tau_1 = 230$ fs, $\tau_2 = 1.38$ ps and $\tau_3 \gg 2$ ns could satisfactory describe the data. We observed an excited state absorption (ESA) at 345 nm, which was attributed to a charge-transfer transition from the $^2$E state on the Cr ions after fast intersystem crossing from the quartet manifold. An additional weak and short-lived ESA at 455 nm was also observed and was tentatively attributed to the initially populated $^4$LMCT state.



## 1. Introduction

Smart materials can be controlled using external perturbations to switch their electrical, optical and magnetic properties. Understanding the photophysics of charge-transfer (CT) transitions in these materials provides an interesting problem connecting light, charge and spin dynamics. For example, spin crossover (SCO) systems, which can be optically switched from low-spin to high-spin states, have been extensively studied for a number of years [1–4]. In Fe(II) complexes, where the SCO process is from the singlet ground state (S = 0) to a quintet meta-stable state (S = 2), it has been found that spin switching can occur in less than 100 fs [2,5,6]. Progress in this area can be important for future photonic devices combining optical control of electrical and magnetic properties. For achieving optical control of magnetically ordered materials, Prussian blue analogues (PBAs) have been extensively studied during the last twenty years [7,8]. These materials have a rock-salt structure with transition metal ions linked by cyanide bridging ligands (Fig. 1, inset). In particular, the V-Cr PBA is an interesting model system because of its high magnetic ordering temperature above room temperature [9–12]. The V-Cr PBA also displays interesting proton conductive [13], photomagnetic [14] and electrochromic [15,16] properties. There have been few ultrafast studies to date on PBAs in general [17–22] to probe the initial fs–ps dynamics after photoexcitation. The relatively large number of studies on the V-Cr PBA's static optical and magnetic properties means that it provides an interesting system for understanding both charge and spin dynamics after fs laser excitation in these systems. Here, we have explored transient transmission spectroscopy with the aim to study intermediate states important for the fast intersystem crossing (ISC) previously reported for various Cr-containing complexes and materials [21,23–28].

The optical spectrum of the V-Cr PBA (Fig. 1) is dominated by metal-to-metal charge-transfer (MMCT) transitions in the visible and ligand-to-metal (LMCT) and metal-to-ligand (MLCT) CT transitions in the UV. The MMCT transition takes place between localised electrons in $t_{2g}$ orbitals on the Cr and V ions (Fig. 2). A recent study employed ultrafast magneto-optical (MO) methods to directly study photo-induced spin dynamics in the V-Cr PBA after exciting at the LMCT transition [21]. The excitation in films of the V-Cr PBA appears to take place on localised sites in the lattice during the first few hundred fs [21], similarly to what is also observed in SCO crystals of Fe(II) complexes [29,30]. The ultrafast dynamics of $Cr(acac)_3$ in liquids, which has been extensively studied by Juban and McCusker [23], is therefore relevant for understanding the dynamics in thin films of the V-Cr PBA. The LMCT pump transition corresponds to transferring an electron from a $CN^-$ ligand to a Cr(III) site, thereby photo-reducing the ion transiently to a Cr(II) oxidation state (Fig. 2(b)). Back-electron transfer subsequently occurs very quickly and the Cr(III) oxidation state is formed again on a sub-100 fs timescale, similarly to the decay of the MLCT state in

* Corresponding author.
*E-mail address:* olof.johansson@ed.ac.uk (J.O. Johansson).

http://dx.doi.org/10.1016/j.cplett.2017.08.070

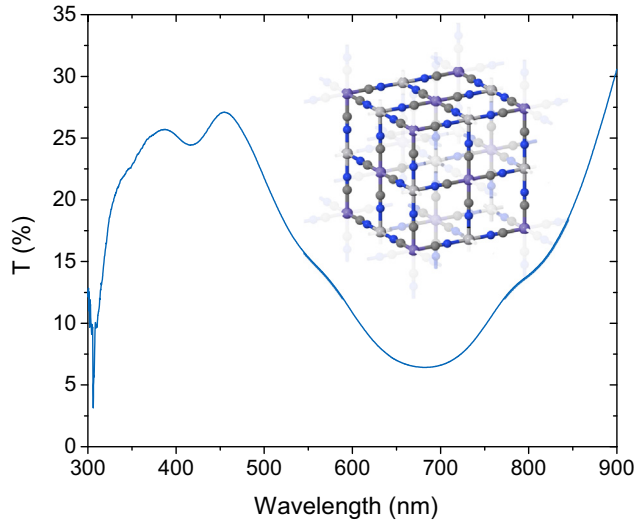


**Fig. 1.** Static transmission spectrum of the V-Cr PBA. The loss of transmission in the visible region is due to MMCT transitions between Cr(III)–V(II) at 540 nm (seen as a shoulder) and Cr(III)–V(III), which occurs closer to 670–690 nm for this particular film. LMCT/MLCT transitions occur ≤400 nm. Inset shows idealised crystal structure of the V-Cr PBA lattice.

Fe(II) SCO complexes in solution or crystals. However, a fraction of the Cr(III) sites are now formed in the $^2$E doublet state via fast ISC from the quartet manifold (Fig. 2(c)). The MO measurements could detect the formation of this doublet state on the Cr ion due to the change in the super-exchange interaction of this magnetically ordered material taking place as a result of the corresponding spin flip associated with the ISC [21]. The model describing this dynamics was inferred from the model developed by Juban and McCusker, who studied isolated $Cr(acac)_3$ ions in solution where a spectral broadening and red-shift of the excited-state absorption (ESA) from the $^2$E state could be followed and compared to ns results [23,25]. More recent studies using time-resolved IR techniques have shown that a relatively large fraction of the $^2$E state population decays back to the quartet manifold via back-ISC [24,27].

To understand the pathways involved in the fast ISC process, it is important to study the initially populated CT state, corresponding to the reduced Cr ion (Fig. 2(b)). We label this state $^4$LMCT, where the spin multiplicity corresponds to the total spin of the Cr ion and ligand to highlight that the total spin is conserved after absorbing a pump photon. In the previous ultrafast magneto-optical study, an increase in absorption at 480 nm could just be discerned at early delay times and was tentatively assigned to an ESA from the initially excited CT state [21]. It should be noted that the LMCT state in $Cr(acac)_3$ in solution has previously been shown to decay in less than 50 fs [23], making this state difficult to detect with the *ca.* 250 fs cross-correlation used in the magneto-optical study. Furthermore, the increase in absorption took place just at the blue edge of the white-light supercontinuum. In addition to the problem with the short-lived nature of the $^4$LMCT state, one still must find a clear optical signature of this state, which is not always trivial. In order to approach this more general problem, spectroelectrochemistry and transient absorption have previously been used to identify and study the dynamics of charge-transfer excited states in several systems (e.g. [31] and references therein). Inspired by our recent spectroelectrochemical study on thin films of the V-Cr PBA [16], we have in this letter investigated if a similar approach would be feasible. In the spectroelectrochemical study, we found that a new optical absorption peak arises at *ca.* 465 nm when the films were electrochemically reduced. This process corresponds to the reduction of $[Cr^{III}(CN)_6]^{3-}$ sites to $[Cr^{II}(CN)_6]^{4-}$ in

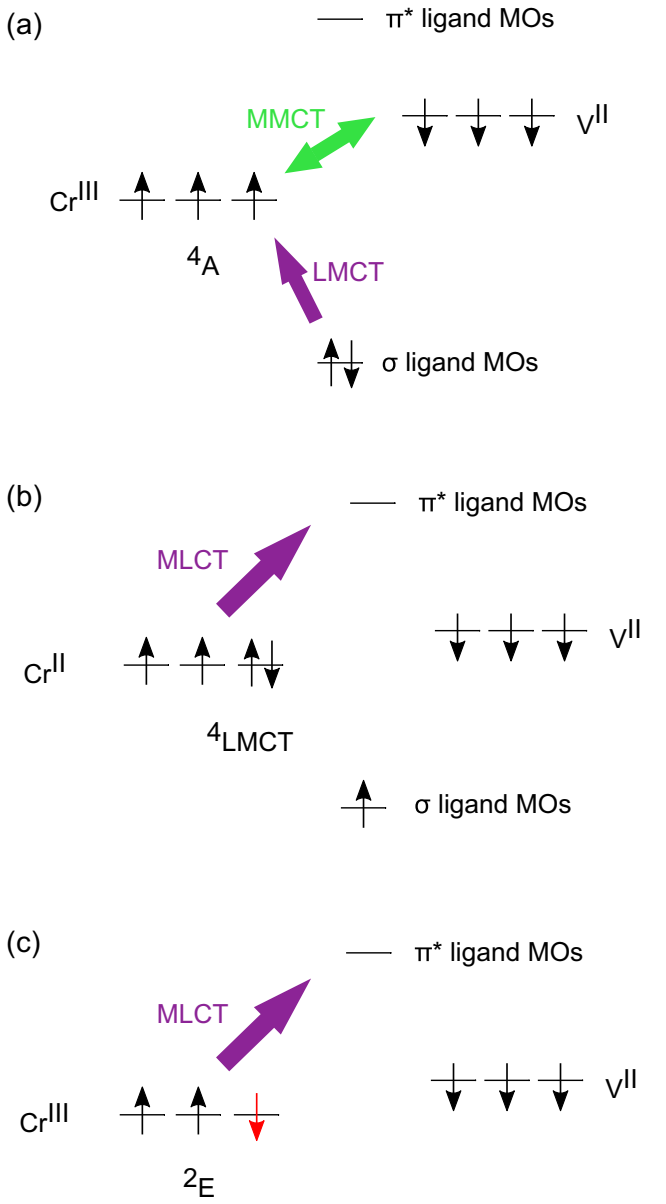


**Fig. 2.** Schematic diagram of orbital energy levels and optical transitions in the V-Cr PBA. (a) Ground-state electronic configuration, where only the $t_{2g}$ orbitals on the metal ions are shown ($e_g$ orbitals are not populated). Filled and empty $CN^-$ ligand orbitals are also shown. (b) After pumping at the LMCT, the Cr ion is reduced to Cr (II). The energy of the electrons localised on the ion is therefore increased closer to the empty $\pi^*$ ligand orbitals. This causes a red-shift of the MLCT transition. Spin multiplicity of $^4$LMCT refers to the total spin of the system in this case and implies spin is conserved after the LMCT excitation. (c) After the decay of the $^4$LMCT state and back-electron transfer, the Cr is formed as Cr(III) again. After ISC to the $^2$E state, one of the electrons on the Cr ion has changed its spin projection. Note that the transition energy of the MLCT is larger in (c) than (b) because the $^2$E state on Cr(III) is lower in energy than the $^4$LMCT state on Cr(II).

the PBA lattice, which in principle is similar to the LMCT photoexcitation process when the Cr sites are reduced by the transfer of an electron from the ligands. The absorption from the reduced Cr sites was attributed to a red-shift of a MLCT transition from Cr(II) to empty $\pi^*$ ligand orbitals, due to the increased energy of Cr(II) compared to Cr(III), pushing it closer in energy to the empty ligand orbitals. However, an ESA signal from the $^2$E or $^4$LMCT states has to date not been clearly observed in films of the V-Cr PBA. In this letter, we present a transient transmission study of the V-Cr PBA with the aim to observe ESA from the $^2$E state and to capture the

short-lived $^4$LMCT state on the photo-reduced Cr ions in the PBA lattice by probing with a wider spectral range, spanning 330–675 nm. We were able to observe a transient absorption centred at 345 nm, which we attribute to the $^2$E state. In addition, we also observed a weak and short-lived ESA at 455 nm, which is consistent with the spectroelectrochemical measurements of reduced Cr ions. The measured lifetime was less than 50 fs, in agreement with the short lifetime previously assigned to the LMCT state. Our findings are consistent with the model of fast ISC to the $^2$E state after pumping the $^4$LMCT state.

## 2. Methods

The synthesis of the films followed the procedure by Ohkoshi *et al.* [32] and has been described in more details in Ref. [16]. In short, cleaned glass substrates coated with fluorine-doped tin-oxide (FTO) were held under a constant potential of −1.2 V for 300 s in a solution of $K_3[Cr^{III}(CN)_6]$ and $VCl_3$ at 25 mM concentrations in an electrolytic solution of KCl (1.0 M) in water. The films are air sensitive so all the synthesis was carried out in a nitrogen environment. The films were dried in nitrogen flow and subsequently sealed with a cover glass slip and cyanoacrylate glue. In order to estimate the film thickness, we compared the transmittance with our previous study and could estimate the film thickness to be 600 ± 50 nm [16].

The transient absorption setup based at the University of Warwick has been described previously [33,34]. Briefly, the white-light continuum is generated in a $CaF_2$ plate and the probe spectrum is detected using an Avantes fibre-coupled spectrometer (AvaSpec-ULS1650F). The pump beam was relatively defocussed with a beam waist of 1.5 mm. The pump pulse energy was 400 nJ, which therefore corresponds to a fluence in the focal region of 22 μJ/cm$^2$. We monitored the pump-probe signal at 0 and 1000 fs delays between each scan to check for any film degradation. However, with the lower pump energy used, we could not observe any long-term changes to the signal. The pump pulse duration was 80 fs and the pump-probe beam angle was less than four degrees. The obtained transient transmittance was analysed in a sequential global-fit procedure using the Glotaran software [35].

## 3. Results and discussion

### 3.1. Overview of broadband transient transmission results

The transient transmission spectra obtained after pumping at 400 nm are presented in Fig. 3(a) as a function of pump-probe delay up to 5 ps. The time-delays were scanned up to 1.8 ns but we found that most of the dynamics had reached a plateau after *ca.* 5 ps, in agreement with previous work [21]. We therefore only show time-delays up to 5 ps in the 2D data. Kinetic traces for selected wavelengths for full delay times are presented in the Fig. 2(c). The signal around 400 nm observed in Fig. 2(a) is due to scattered pump light reaching the detector. In this time window this data is characterised by two specific features, namely a bleach, or increase of transmittance, for wavelengths above *ca.* 475 nm and a decrease in transmittance below this wavelength. The results in the visible region (500–700 nm) are similar to what was previously observed, *i.e.* bleach of the MMCT after pumping at the LMCT [21]. It should be noted that the position of the ground-state bleach (GSB) is red-shifted compared to our previous study (*ca.* 660 nm). However, we believe this is due to variability of the films used since the position of the MMCT can depend on the specific stoichiometry and morphology of the films, which can be different as a result of slightly different electrochemical deposition conditions [12]. The peak of the MMCT for the film in this study do

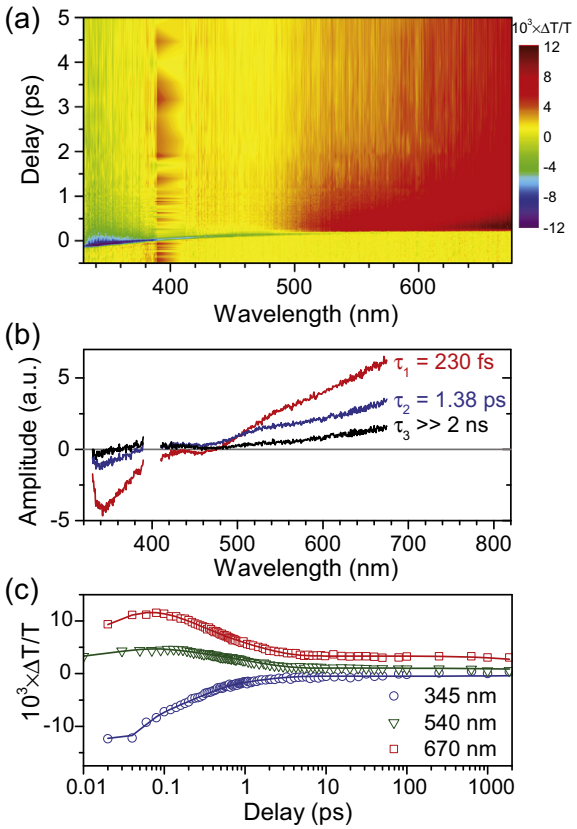


**Fig. 3.** Ultrafast dynamics of the V-Cr PBA after pumping at the LMCT transition. (a) Transient transmission results as a function of pump-probe delay time and wavelength. The signal at 400 nm is due to scattered pump light. The data has not been corrected for the white-light chirp (this has been done in all subsequent analysis). Fitted evolution associated difference spectra (EADS) from the global analysis are presented in (b). The pump signal at 400 nm has been removed for clarity. (c) Kinetic traces at selected wavelengths are shown on a semi logarithmic scale. Points are experimental data whereas solid lines are the results from the global analysis. The kinetic traces were averaged over a 10 nm bandwidth.

indeed occur at 680 nm, as seen in Fig. 1. The UV part of the spectrum was previously unexplored and so the finding of a decrease in transmittance in this spectral range is new. Although we have not measured the change in reflectance, we attribute the reduced transmittance to an ESA, which provides an interesting avenue to directly explore the nature of the excited state instead of solely relying on the GSB. This feature is discussed further in Section 3.2. The data was analysed using a sequential global fit procedure and three time-constants were found to describe the results adequately. We found two timescales of $\tau_1 = 230 \pm 40$ fs and $\tau_2 = 1.38 \pm 0.04$ ps. The third time-constant was larger than 2 ns and was thus equivalent to a constant offset.

### 3.2. Excited state absorption in the UV

The ESA in the UV can be seen in both the 2D transient transmittance data and the evolution associated difference spectra (EADS) resulting from the global fit in Fig. 3(a) and (b), respectively. Due to the larger spectral range, available with the $CaF_2$ supercontinuum generation, we were able to observe an ESA in the wavelength region around 330–350 nm. This ESA has previously not been observed for the V-Cr PBA. We have also carried out a measurement on the glass-substrate alone (including FTO, superglue and coverslip) but did not observe any ESA in this wavelength range (besides from the coherent signal at time-zero). The ESA was also present in the global analysis, but was

more dominated by the fast decay component ($\tau_1$ = 230 fs). The larger relative amplitude component of the fast channel compared to the MMCT bleach is clearly visible during the first 500 fs, which is demonstrated in Fig. 4. We have also shown the dynamics at 540 nm, corresponding to the MMCT of $V^{II}$–$Cr^{III}$, for comparison in Fig. 4. There is a constant plateau in the ESA decay similarly to the MMCT bleach, although it is just above the noise-level, as modelled by the non-zero $\tau_3$ component of the global analysis.

To attempt to identify the state giving rise to the UV-ESA, one must consider the model discussed in the introduction (Fig. 2). The spectral shapes of the bleach region and the ESA are rather similar for the three different time-constants obtained in the global analysis. This implies that there is not a large change in the electronic character of the excited state after the initial dynamics occurring during the rise time of the pump pulse. This argument was used by Juban and McCusker to conclude that the $^2$E state was formed on a very fast timescale (less than 100 fs) because the few-fs transient absorption spectrum matched that of the ns spectrum. Based on the physical model, whereby the intermediate $^4$LMCT state decays with a 20–50 fs time-constant to the $^2$E state, we attribute the ESA to the $^2$E state. Due to the short lifetime of the $^4$LMCT state, we do not see any delayed onset of the UV-ESA and we conclude that the $^2$E state is populated during the rise-time of the laser pulses. The transient transmission signal appears to be rather strong and comparable to the MMCT bleach. This could potentially suggest that it is a CT transition that is giving rise to the ESA in the V-Cr PBA instead of a metal-centred transition (d-d transition). The ESA could therefore originate from a red-shifted MLCT transition, in analogy to the assignment of the additional absorption of the reduced Cr sites observed in our recent spectroelectrochemistry study as discussed in the Introduction [16]. The red-shifted MLCT state in Cr(II) in the spectroelectrochemical study was observed at 465 nm while the ESA in the $^2$E state in this study was observed at *ca.* 345 nm. The MLCT transition energy difference is reasonable because it is expected that the $^2$E state is lower in energy than the reduced Cr(II).

A fraction of the $^2$E state population will decay back to the quartet manifold via back-ISC on a sub-100 fs timescale [24,25,27]. The EADS from the global analysis below 350 nm show a non-zero component of the $\tau_3 \gg$ ns component. This plateau corresponds to the fraction of the population trapped in the $^2$E state. However, this fraction is smaller than that expected from the plateau of the MMCT bleach and the signal above *ca.* 100 ps is in the noise level. It is therefore difficult to extract information about the plateau observed so clearly for the MMCT bleach. The $\tau_1$ to $\tau_2$ ratio is large in this wavelength range, which indicates that the majority of the $^2$E state population decays back to the quartet manifold on a 230 fs timescale. The 1.38 ps timescale then corresponds to vibrational cooling of the trapped $^2$E states. These new measurements therefore indicate that the $^2$E population after a few ps is lower than that estimated from the GSB.

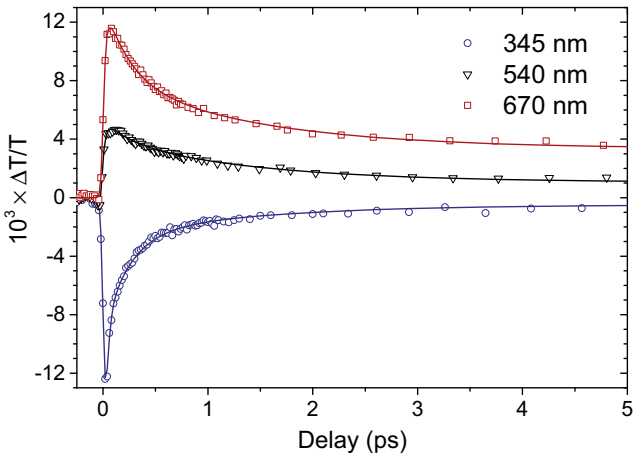


**Fig. 4.** Kinetic traces for selected wavelengths up to 5 ps (full time-delays are shown in Fig. 3(c)). Points are experimental data whereas solid lines are the results from the global analysis. The kinetic traces were averaged over a 10 nm bandwidth.

### 3.3. Observation of short-lived $^4$LMCT state

In order to test the hypothesis that the $^4$LMCT state could be observed during early time delays in the blue region of the spectrum, the transient spectra at early time-delays were more closely inspected in the narrow spectral range 420–480 nm. The corresponding result of the global analysis in this spectral region for the two short time-constants are shown in Fig. 5(a). The main difficulty with observing any signal at 455 nm is that this wavelength region falls between the rather intense ESA at shorter wavelength and the GSB at longer wavelengths. Nevertheless, there is an additional absorption feature that does not appear to be connected to the ESA in the UV or the GSB in the visible. The slight decrease in transmission, corresponding to increase in absorption, can be seen at 455 nm in Fig. 5(a). The spectral position of this peak is indeed close to 465 nm, which is measured in the spectroelectrochemical measurements [16]. The decay of this additional absorption feature is short-lived and so it becomes difficult to extract the time dynamics from the coherent artefact from the glass substrate and the chirp of the white-light continuum (Fig. S1). A shorter time-constant than 230 fs should in principle be included in the global analysis, but based on the aforementioned arguments, it becomes difficult to reliably extract relevant data from the global analysis for these conditions. We have therefore plotted the experimental data, averaged over a 10 nm wavelength range at 434, 455 and 465 nm in Fig. 5(b). For these three wavelengths, the coherent signal peak from the glass substrate can be seen as a decrease in transmittance around time-zero with a FWHM corresponding to the instrumental response function ($\Delta t_{FWHM} = 50$ *fs*). However, for the transient at 455 nm there is clearly a signal persisting for about 20–50 fs longer than the glass-substrate signal. Because the transient at 455 nm stands out from the adjacent wavelengths

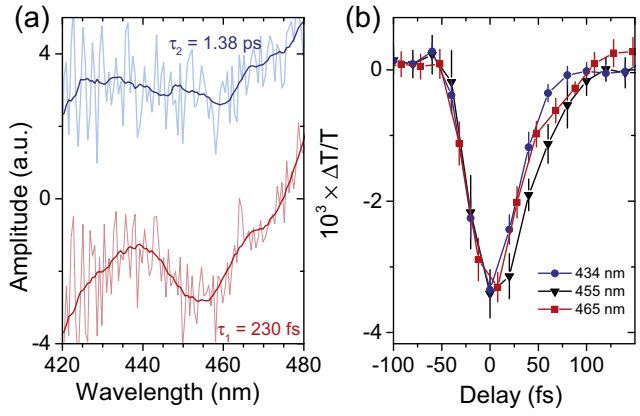


**Fig. 5.** Identification of intermediate charge-transfer state on photo-reduced Cr(II) sites. (a) The EADS from Fig. 3 (a) for $\tau_1$ = 230 fs and $\tau_2$ = 1.38 ps in a narrower spectral range. Due to the weak signal in this range, the EADS were smoothed to identify any additional absorption (corresponding to reduced transmittance). The $^4$LMCT ESA was attributed to the drop in the transmission coefficient in the EADS at 455 nm for the faster $\tau_1$ = 230 fs component. (b) The kinetic traces close to time-zero for three wavelength regions averaged over a 10 nm bandwidth. The error bars are from the standard deviation of the averaged 10 nm wavelength region. The decrease in transmission is due to the coherent signal of the glass substrate. The lingering signal at 455 nm is attributed to the short-lived $^4$LMCT state.

and is observed in the global analysis in Fig. 5(a), we exclude the possibility that this signal is simply an ultrafast artefact. However, further measurements using even shorter laser pulses are needed to study the ESA signal in more detail.

We tentatively assign the short-lived ESA at 455 nm to the $^4$LMCT state. Taking into account that the spectral position is in close agreement with spectroelectrochemical measurements, the appearance of the ESA at 345 nm from the $^2$E state at early time delays (and that this state is populated from the $^4$LMCT state) and the expected short lifetime, we believe that a tentative assignment of the $^4$LMCT state is reasonable. Based on the assignment in the spectroelectrochemical study mentioned in the introduction, we attribute the ESA to a MLCT transition, which is red-shifted with respect to the ground state absorption due to the higher energy of the photo-reduced Cr(II) compared to Cr(III). Of course, the spectral position in the transient transmission data does not necessarily have to be the same as in the spectroelectrochemical data because in that case the Cr ions are reduced by electrons from the electrode and subsequently $K^+$ counter ions (supplied from the electrolyte) are inserted into the films to maintain the charge-balance. In contrast, the transient transmission measurements are not carried out in an electrolyte and the source of electrons is not from an electrode, but rather from the cyanide ligand. We use this reason to justify the short lifetime of the photoexcited $^4$LMCT state compared to the stabilised lifetime of the electrochemically reduced Cr ions. The short lifetime of the intermediate $^4$LMCT is in agreement with that measured in $Cr(acac)_3$ by Juban and McCusker, who observed a time-constant of 50 ± 20 fs [23].

## 4. Conclusion

We conclude that the experimental results presented here are consistent with the formation of a short-lived $^4$LMCT state upon exciting at the LMCT transition, which subsequently decays to the $^2$E state on a sub-100 fs timescale. This state is characterised by a MMCT bleach in the visible and an ESA in the UV at 345 nm. The decay of the observed ESA signal for the $^2$E state at 345 nm, indicates that most of the $^2$E state population undergoes back-ISC on a 230 fs timescale but some part of the population is trapped in the $^2$E state. We could also observe a weak signal that was tentatively assigned to the short-lived $^4$LMCT state on the Cr ions, which is populated by the pump pulse. An ESA associated with this state was observed at 455 nm and could be due to a red-shifted MLCT transition, which is in good agreement with spectroelectrochemistry of reduced Cr sites in the V-Cr PBA lattice. The $^4$LMCT state subsequently decays to the $^2$E state. The fast decay implies that the ISC happens on the same fast timescale limited by the instrument-response function of *ca.* 50 fs. The ESA signals observed for both states should provide a more direct approach to further study the dynamics in this important molecular magnet without relying on the ground-state bleach. The results show that using spectroelectrochemistry to study femtosecond charge-transfer dynamics in PBAs is a powerful method and should be applicable to other inorganic coordination polymers cast in thin films.

## Acknowledgements

This work was supported by funding from the Royal Society of Edinburgh and EPSRC (studentship to LH). M. D. H. thanks the Leverhulme Trust for postdoctoral funding. The authors thank V. Stavros for use of the laser lab and N. Robertson for the use of the potentiostat for making films. J. O. J. is a Royal Society of Edinburgh/BP Trust research fellow.

## Appendix A. Supplementary material

Supplementary data associated with this article can be found, in the online version, at http://dx.doi.org/10.1016/j.cplett.2017.08.070.

## References

[1] S. Decurtins, P. Gütlich, C.P. Köhler, H. Spiering, A. Hauser, Light-induced excited spin state trapping in a transition-metal complex: the hexa-1-propyltetrazole-iron (II) tetrafluoroborate spin-crossover system, Chem Phys Lett 105 (1984) 1–4, http://dx.doi.org/10.1016/0009-2614(84)80403-0.
[2] J.E. Monat, J.K. McCusker, Femtosecond excited-state dynamics of an iron(II) polypyridyl solar cell sensitizer model, J. Am. Chem. Soc. 122 (2000) 4092–4097, http://dx.doi.org/10.1021/ja992436o.
[3] A. Cannizzo, C.J. Milne, C. Consani, W. Gawelda, C. Bressler, F. van Mourik, M. Chergui, Light-induced spin crossover in Fe(II)-based complexes: The full photocycle unraveled by ultrafast optical and X-ray spectroscopies, Coord. Chem. Rev. 254 (2010) 2677–2686, http://dx.doi.org/10.1016/j.ccr.2009.12.007.
[4] M. Halcrow, Spin-Crossover Materials: Properties and Applications, Wiley VCH, (2013).
[5] G. Auböck, M. Chergui, Sub-50-fs photoinduced spin crossover in [Fe(bpy)3]2+, Nat. Chem. 7 (2015) 629–633, http://dx.doi.org/10.1038/nchem.2305.
[6] H.T. Lemke, K.S. Kjær, R. Hartsock, T.B. van Driel, M. Chollet, J.M. Glownia, S. Song, D. Zhu, E. Pace, S.F. Matar, M.M. Nielsen, M. Benfatto, K.J. Gaffney, E. Collet, M. Cammarata, Coherent structural trapping through wave packet dispersion during photoinduced spin state switching, Nat. Commun. 8 (2017) 15342, http://dx.doi.org/10.1038/ncomms15342.
[7] M. Verdaguer, G.S. Girolami, Magnetic Prussian Blue analogs, in: J.S. Miller, M. Drillon (Eds.), Magn Mol Mater, Wiley-VCH Verlag GmbH & Co. KGaA, Weinheim, Germany, (2005): pp. 283–346. doi:10.1002/9783527620548.ch9d.
[8] S. Ohkoshi, H. Tokoro, Photomagnetism in Cyano-bridged bimetal assemblies, Acc. Chem. Res. 45 (2012) 1749–1758, http://dx.doi.org/10.1021/ar300068k.
[9] S. Ferlay, T. Mallah, R. Ouahès, P. Veillet, M. Verdaguer, A room-temperature organometallic magnet based on Prussian blue, Nature 378 (1995) 701–703, http://dx.doi.org/10.1038/378701a0.
[10] Ø. Hatlevik, W.E. Buschmann, J. Zhang, J.L. Manson, J.S. Miller, Enhancement of the magnetic ordering temperature and air stability of a mixed valent vanadium hexacyanochromate(III) magnet to 99 °C (372 K), Adv. Mater. 11 (1999) 914–918, http://dx.doi.org/10.1002/(SICI)1521-4095(199908)11:11<914::AID-ADMA914>3.0.CO;2-T.
[11] S.M. Holmes, G.S. Girolami, Sol−Gel Synthesis of KV II [Cr III (CN) 6 ]·2H 2 O: a crystalline molecule-based magnet with a magnetic ordering temperature above 100 °C, J. Am. Chem. Soc. 121 (1999) 5593–5594, http://dx.doi.org/10.1021/ja990946c.
[12] R. Garde, F. Villain, M. Verdaguer, Molecule-based room-temperature magnets: catalytic role of V(III) in the synthesis of vanadium−chromium Prussian blue analogues, J. Am. Chem. Soc. 124 (2002) 10531–10538, http://dx.doi.org/10.1021/ja020528z.
[13] S.I. Ohkoshi, K. Nakagawa, K. Tomono, K. Imoto, Y. Tsunobuchi, H. Tokoro, High proton conductivity in Prussian blue analogues and the interference effect by magnetic ordering, J. Am. Chem. Soc. 132 (2010) 6620–6621, http://dx.doi.org/10.1021/ja100385f.
[14] K.D. Bozdag, J.W. Yoo, N.P. Raju, A.C. McConnell, J.S. Miller, A.J. Epstein, Optical control of magnetization in a room-temperature magnet: V-Cr Prussian blue analog, Phys. Rev. B 82 (2010) 94449, http://dx.doi.org/10.1103/PhysRevB.82.094449.
[15] M. Verdaguer, M. Glavez, R. Garde, C. Desplanches, Electrons at work in Prussian blue analogues, Electrochem. Soc. Interface 11 (2002) 28.
[16] L. Hedley, N. Robertson, J.O. Johansson, Electrochromic thin films of the V-Cr Prussian blue analogue molecular magnet, Electrochim. Acta 236 (2017) 97–103, http://dx.doi.org/10.1016/j.electacta.2017.03.166.
[17] D.C. Arnett, P. Voehringer, N.F. Scherer, Excitation dephasing, product formation, and vibrational coherence in an intervalence charge-transfer reaction, J. Am. Chem. Soc. 117 (1995) 12262–12272, http://dx.doi.org/10.1021/ja00154a028.
[18] H. Kamioka, Y. Moritomo, W. Kosaka, S. Ohkoshi, Dynamics of charge-transfer pairs in the cyano-bridged Co2+-Fe3+ transition-metal compound, Phys. Rev. B 77 (2008) 180301, http://dx.doi.org/10.1103/PhysRevB.77.180301.
[19] D. Weidinger, D.J. Brown, J.C. Owrutsky, Transient absorption studies of vibrational relaxation and photophysics of Prussian blue and ruthenium purple nanoparticles, J. Chem. Phys. 134 (2011) 124510, http://dx.doi.org/10.1063/1.3564918.
[20] A. Asahara, M. Nakajima, R. Fukaya, H. Tokoro, S. Ohkoshi, T. Suemoto, Ultrafast dynamics of reversible photoinduced phase transitions in rubidium manganese hexacyanoferrate investigated by midinfrared CN vibration spectroscopy, Phys. Rev. B 86 (2012) 195138, http://dx.doi.org/10.1103/PhysRevB.86.195138.
[21] J.O. Johansson, J.W. Kim, E. Allwright, D.M. Rogers, N. Robertson, J.Y. Bigot, Directly probing spin dynamics in a molecular magnet with femtosecond time-resolution, Chem. Sci. 7 (2016) 7061–7067, http://dx.doi.org/10.1039/C6SC01105E.

[22] S. Zerdane, M. Cammarata, L. Balducci, R. Bertoni, L. Catala, S. Mazerat, T. Mallah, M.N. Pedersen, M. Wulff, K. Nakagawa, H. Tokoro, S. Ohkoshi, E. Collet, Probing transient photoinduced charge-transfer in Prussian blue analogues with time-resolved XANES and optical spectroscopy, Eur. J. Inorg. Chem. (2017), http://dx.doi.org/10.1002/ejic.201700657.
[23] E.A. Juban, J.K. McCusker, Ultrafast dynamics of $^2$E state formation in Cr(acac)3, J. Am. Chem. Soc. 127 (2005) 6857–6865, http://dx.doi.org/10.1021/ja042153i.
[24] E.M.S. Maçôas, R. Kananavicius, P. Myllyperkiö, M. Pettersson, H. Kunttu, Relaxation dynamics of Cr(acac) 3 probed by ultrafast infrared spectroscopy, J. Am. Chem. Soc. 129 (2007) 8934–8935, http://dx.doi.org/10.1021/ja071859k.
[25] J.N. Schrauben, K.L. Dillman, W.F. Beck, J.K. McCusker, Vibrational coherence in the excited state dynamics of Cr(acac)3: probing the reaction coordinate for ultrafast intersystem crossing, Chem. Sci. 1 (2010) 405, http://dx.doi.org/10.1039/c0sc00262c.
[26] H. Ando, S. Iuchi, H. Sato, Theoretical study on ultrafast intersystem crossing of chromium(III) acetylacetonate, Chem. Phys. Lett. 535 (2012) 177–181, http://dx.doi.org/10.1016/j.cplett.2012.03.043.
[27] E.M.S. Maçôas, S. Mustalahti, P. Myllyperkiö, H. Kunttu, M. Pettersson, Role of vibrational dynamics in electronic relaxation of Cr(acac)3, J. Phys. Chem. A 119 (2015) 2727–2734, http://dx.doi.org/10.1021/jp509905q.
[28] V.G. Sala, S. Dal Conte, T.A. Miller, D. Viola, E. Luppi, V. Véniard, G. Cerullo, S. Wall, Resonant optical control of the structural distortions that drive ultrafast demagnetization in $Cr_2O_3$, Phys. Rev. B 94 (2016) 14430, http://dx.doi.org/10.1103/PhysRevB.94.014430.
[29] M. Cammarata, R. Bertoni, M. Lorenc, H. Cailleau, S. Di Matteo, C. Mauriac, S.F. Matar, H. Lemke, M. Chollet, S. Ravy, C. Laulhé, J.F. Létard, E. Collet, Sequential activation of molecular breathing and bending during spin-crossover photoswitching revealed by femtosecond optical and X-Ray absorption spectroscopy, Phys. Rev. Lett. 113 (2014) 227402, http://dx.doi.org/10.1103/PhysRevLett. 113.227402.
[30] R. Field, L.C. Liu, W. Gawelda, C. Lu, R.J.D. Miller, Spectral signatures of ultrafast spin crossover in single crystal [FeII(bpy)3](PF6)2, Chem. A Eur. J. 22 (2016) 5118–5122, http://dx.doi.org/10.1002/chem.201600374.
[31] A.M. Brown, C.E. McCusker, J.K. McCusker, Spectroelectrochemical identification of charge-transfer excited states in transition metal-based polypyridyl complexes, Dalt. Trans. 43 (2014) 17635–17646, http://dx.doi.org/10.1039/C4DT02849J.
[32] S. Ohkoshi, M. Mizuno, G. Hung, K. Hashimoto, Magnetooptical effects of room temperature molecular-based magnetic films composed of vanadium hexacyanochromates, J. Phys. Chem. B 104 (2000) 9365–9367, http://dx.doi.org/10.1021/jp002002b.
[33] S.E. Greenough, G.M. Roberts, N.A. Smith, M.D. Horbury, R.G. McKinlay, J.M. Żurek, M.J. Paterson, P.J. Sadler, V.G. Stavros, S.E. Bradforth, M.N.R. Ashfold, J. Moan, P. Mroz, D. Nowis, J. Piette, B.C. Wilson, J. Golab, Ultrafast photo-induced ligand solvolysis of cis-[Ru(bipyridine)$_2$ (nicotinamide)$_2$ ] $^{2+}$ : experimental and theoretical insight into its photoactivation mechanism, Phys. Chem. Chem. Phys. 16 (2014) 19141–19155, http://dx.doi.org/10.1039/C4CP02359E.
[34] S.E. Greenough, M.D. Horbury, J.O.F. Thompson, G.M. Roberts, T.N.V. Karsili, B. Marchetti, D. Townsend, V.G. Stavros, C. Jouvet, S.E. Bradforth, M.N.R. Ashfold, Solvent induced conformer specific photochemistry of guaiacol, Phys. Chem. Chem. Phys. 16 (2014) 16187, http://dx.doi.org/10.1039/C4CP02424A.
[35] J.J. Snellenburg, S.P. Laptenok, R. Seger, K.M. Mullen, I.H.M. van Stokkum, Glotaran : a java -based graphical user interface for the R package TIMP, J. Stat. Softw. 49 (2012) 1–22, http://dx.doi.org/10.18637/jss.v049.i03.

## A.3 Electrochromic Bilayers of Prussian Blue and Its Cr Analogue

Journal of
Materials Chemistry C

PAPER

View Article Online
View Journal



Cite this: DOI: 10.1039/c7tc04521b

# Electrochromic bilayers of Prussian blue and its Cr analogue†

Luke Hedley, [a] Liz Porteous,[b] David Hutson, [b] Neil Robertson [a] and J. Olof Johansson *[a]

Multilayered thin films of functional materials play an important role in many applications in nanotechnology. The intense and tuneable colours of some molecular materials allow for the development of a unique spectral fingerprint of each layer in thin film heterostructures. Herein, we report on electrochromic switching of bilayer thin films composed of Prussian blue ($Fe^{III}Fe^{II}$) and its orange-coloured ($Fe^{II}Cr^{III}$) analogue. The films could be switched from green to orange by reducing the blue FeFe top layer. The distinct optical absorption spectra of the two layers allowed spectroelectrochemical measurements to probe the electrochemical activity of the individual layers during the switching of the Prussian blue layer. We found that for producing layers of equal optical density, the thickness of the layers had to be different due to a difference in oscillator strength for the metal-to-metal charge-transfer transition. The films used here had a thickness of 300 ± 70 nm and 30 ± 15 nm for the FeCr and FeFe sub-layers, respectively. The colouration efficiency was found to be 147.8 ± 0.8 $cm^2\ C^{-1}$ for the multilayered film. These results show that it is possible to obtain bilayers of Prussian blues that, with a unique optical spectral fingerprint of each sub-layer, retain the electrochromic functionality and therefore enable layer-sensitive studies of charge-transfer processes in thin film heterostructures of multifunctional materials.

Received 4th October 2017,
Accepted 28th November 2017

DOI: 10.1039/c7tc04521b

rsc.li/materials-c



## Introduction

Multilayered thin films and heterostructures are ubiquitous to a wide range of areas such as solar cells and spintronics. They can be used as smart materials because at the interface of nanoscale heterostructures, new phenomena can arise due to the large surface-to-volume ratio. However, it can be difficult to study charge-transfer and other processes of individual layers in multilayers and so a probe that is sensitive to all layers is desirable. Molecular-based materials that display strong optical charge-transfer transitions can often be modified to tune their absorption spectrum. Carefully choosing the layers such that each layer has a distinct optical spectrum, allows for obtaining a handle on each sub-layer in order to study charge transfer processes across interfaces in multilayers. In particular, electrochromic properties provide a visually pleasing example of achieving electrical control of the colour of the materials and to study the change in absorption spectrum after a redox process. Multilayers containing electrochromic components can be used in multi-coloured electrochromic devices, for applications in smart windows and displays.[1,2]

One of the most studied electrochromic materials is Prussian blue (PB), which can be switched from blue to transparent upon reduction. PB and its analogues are coordination polymers comprising transition metal ions linked by cyanide ligands in a rock-salt structure. A wealth of heterostructures exist which contain PB in combination with other materials, such as dye-sensitised titania[3] and conductive polymers.[4,5] There have also been a number of studies that employ multiple Prussian blue analogues (PBAs) to create heterostructures in the form of thin films or nanoparticles to study photo-induced magnetism[6,7] and magneto-structural effects.[8–10] Their electrochemical[11] and optical[12] properties have also been studied. In particular, Liao *et al.*[12] made a PB and NiFe PBA composite material using a conductive polymer matrix, which exhibited electrochromic switching. To date, layer-by-layer deposition has been the most common way of making heterostructures of PBAs due to the high degree of control of layer thickness this method allows, which is critical in applications such as ion sieving,[13,14] biosensing[15] and for the synthesis of electrochromic materials.[16] Notably, a sequential electrochemical approach was recently used by Prieto-Ruiz *et al.*[9] to combine two magnetically ordered analogues of PB.

The strong colour of some PBAs, and indeed PB itself, arises due to metal-to-metal charge-transfer (MMCT) transitions, which can be tuned by varying the transition metals and the stoichiometry of the films.[17,18] In this paper, we have tested the

[a] EaStCHEM, School of Chemistry, University of Edinburgh, David Brewster Road, EH9 3FJ, UK. E-mail: olof.johansson@ed.ac.uk
[b] School of Engineering and Computing, University of the West of Scotland, Paisley PA1 2BE, UK

† Electronic supplementary information (ESI) available. See DOI: 10.1039/c7tc04521b

possibility to fabricate multilayers of PBAs in order to provide a structure with distinct optical spectra for each layer. We have successfully deposited the FeFe PB (blue) on top of the FeCr PBA (orange) using successive electrochemical depositions. The resulting overall colour of the film was green. By applying alternating electrical potentials, we are able to selectively reduce and oxidise the FeFe layer resulting in an overall reversible colour change from green to orange due to the electrochromic properties of PB. By using the unique optical spectra as a handle on each of the sub-layers in the material we were able to observe the electrochromic switching of the FeFe layer as part of a FeFe–FeCr multilayered structure. These measurements open up the possibility to control the optical properties of multilayered functional materials and the layer-sensitivity enables ground-breaking studies of charge-transfer processes in important multilayers and heterostructures with applications for solar cells, spintronics and photonic devices.

# Experimental

### Electrochemistry

As a working electrode, 1 mm thick glass (aluminoborosilicate) substrates coated with a conductive fluorine-doped tin oxide (FTO) layer were used, with a sheet resistance of 8 $\Omega$ sq$^{-1}$. The substrates were cut to size (8 $\times$ 25 mm) and subsequently cleaned in water/detergent solution in an ultrasonic bath for 20 min. The process was repeated with isopropanol and methanol separately, rinsing with the previous solvent after each step to remove impurities on the surface. The cleaned substrates were then dried under a stream of nitrogen gas.

The electrochemical experiments were carried out using a Metrohm-Autolab μAUTOLAB III potentiostat with a saturated calomel reference electrode (SCE) and a Pt counter electrode used for the electrochemical depositions. For the FeCr deposition, concentrations of 37.5 and 25 mM of $FeCl_3$ and $K_3[Cr(CN)_6]$ were used, respectively. For the subsequent FeFe deposition, a concentration of 7.5 mM was used for both the $K_3[Fe(CN)_6]$ and the $FeCl_3$. For all results presented here, 1 M of $KCl_{(aq)}$ was used as an electrolyte. From previous work, it is known that a more negative voltage is needed to produce FeCr (around $-0.5$ V[9,19]), than to deposit the FeFe PB (around 0.2 V *vs.* Ag/AgCl,[20] although this varies slightly as the FeFe PB is best deposited with a constant current). The order in which the layers are deposited is important to avoid any substantial electrochemical modification of the first layer during the electrodeposition of the second layer. Therefore, deposition of the FeCr PBA was carried out first, using $FeCl_3$ and $K_3[Cr(CN)_6]$, potentiostatically at $-0.7$ V based on the work of Ohkoshi *et al.*[18] At this potential, solvated $Fe^{3+}$ ions are reduced to $Fe^{2+}$ at the surface of the electrode. This reduced cation subsequently binds to the hexacyanochromate anion to form the insoluble PBA directly on the substrate.

For FeFe deposition, the electrochemical cell is filled with $FeCl_3$ and $K_3[Fe(CN)_6]^{3-}$ along with the electrolyte. The FeCr film is used as an electrode in order to reduce the $[Fe(CN)_6]^{3-}$ ions in solution to $[Fe(CN)_6]^{4-}$, which subsequently reacts with $Fe^{3+}$ cations at the electrode surface. The product is the insoluble PB created on the FeCr electrode surface. In contrast to FeCr, where a potentiostatic deposition resulted in the optically clearest films, the PB films were deposited galvanostatically at $-40$ μA. This was previously found to yield the most homogeneous films,[21] which we also observed. After deposition, the films were thoroughly rinsed with distilled water and subsequently dried under continuous $N_2$ flow.

The spectroelectrochemical measurements were carried out using a halogen light source (Ocean Optics HL-2000-FHSA) which was coupled to a spectrometer (Ocean Optics HR2000+) through optical fibres. These optical fibres could be coupled to a cuvette holder where a 10 $\times$ 10 mm cuvette was used as the electrochemical cell. In order to fit all the required electrodes for the spectroelectrochemical measurements into the cuvette, the SCE reference and counter electrode were replaced with Pt wire electrodes. A previous investigation[22] of this arrangement of electrodes showed that the use of the pseudo-reference results in a shift of less than 0.02 V with respect to the SCE arrangement. Cyclic voltammograms were carried out on each of the layers individually and the bilayer structure in order to determine switching potentials to be used during the spectroelectrochemistry.

### Characterisation

Optical transmission spectra were recorded using a Shimadzu UV-1800 UV Spectrophotometer. IR spectra were collected using a Renishaw InVia Raman Microscope equipped with a reflection FTIR instrument. We found that the reflectivity of the FTO layer allowed for more sensitive IR measurements of the thin films than using an attenuated total reflectance instrument. Information on the thickness and crystal formation was gathered using various techniques. Atomic force microscopy (AFM) was used to measure the thicknesses of the films. The samples were prepared for AFM measurements using a razor blade drawn across the film in order to remove material from the electrode. This produces a 'valley' in the film which can be studied using the AFM tip. Several cross sections were taken in order to reliably assess the step height (Fig. S1, ESI†). Scanning electron microscopy (SEM) and energy dispersive X-ray spectroscopy (EDX) were used to study the individual layers in terms of their thickness and their elemental composition.

# Results and discussion

### Electrochemical formation of FeCr PBA

The FeCr PBA was first deposited on the FTO-coated glass substrate. The deposition time was adjusted to reach an optical transmission of *ca.* 35% at the peak of the MMCT band (corresponding to an absorbance of *ca.* 0.45), which occurred when the constant voltage was applied for 300 s. The resultant film on the FTO-coated glass substrate was orange (Fig. 1a) due to the MMCT absorption at 440 nm (Fig. 1b), in agreement with what has been described previously.[18] The IR spectrum showed the $CN^-$ asymmetric stretch at 2168 cm$^{-1}$, as expected[18,23] (Fig. 1c).

 

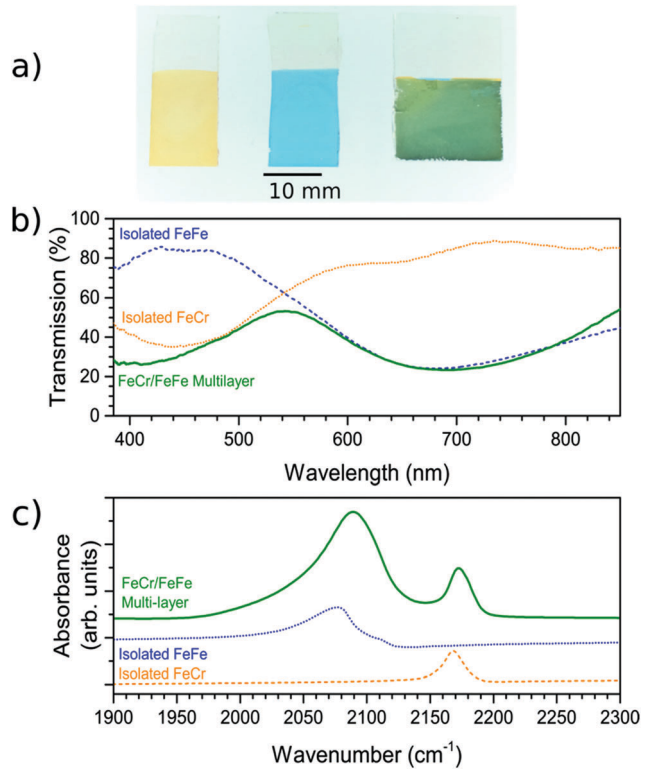


Fig. 1 Visible transmission and IR spectra of the individual and the bilayer films. (a) Photos of the FeCr (orange, left), FeFe (blue, middle) and FeCr–FeFe bilayer structure (green, right). (b) Transmission spectra for the FeCr, FeFe films and the bilayer material. (c) The IR spectra showing the $CN^-$ stretching frequencies of the FeCr and FeFe films, and those present in the bilayer. The IR spectra have been vertically offset for clarity.

The EDX spectrum of the film confirm the elemental composition (Fig. S2, ESI†).

These observations therefore lead us to conclude that we have successfully deposited the FeCr PBA on the FTO electrode. The SEM images of the films indicated that they were polycrystalline with cubic crystals of width *ca.* 1 μm (Fig. 2a and d). The thickness was determined from AFM and was found to be 300 ± 70 nm. The width of the crystals is larger than the height due to lateral growth of the crystals before growing vertically. Analysis of the SEM images allowed us to estimate that the FeCr layer covers *ca.* 70–80% of the FTO surface (Fig. S3, ESI†).

### Deposition of FeFe PB on FeCr PBA

Once the FeCr PBA film was made, cyclic voltammetry in KCl confirmed that there was no electrochemical activity at the voltage needed to make FeFe PB films, which is shown in Fig. 3a. The FeCr PBA is electrochemically active at more negative potentials around −1.0 V *vs.* SCE, as was shown by Ohkoshi *et al.*[19] After rinsing the FeCr film with deionised water, the deposition of the FeFe film was carried out on top of the FeCr film. The absorption from the FeFe PB could clearly be seen in the transmission spectra as a drop at *ca.* 685 nm, corresponding to the MMCT transition. The deposition times were tuned to produce films of a similar optical density to the FeCr layer, which resulted in green films (Fig. 1a and b). The optimum deposition time for the FeFe layer was found to be 60 s. The cyclic voltammogram together with a typical absorption spectrum, (Fig. 3a and b), IR spectrum ($CN^-$ stretch at 2077 $cm^{-1}$, Fig. 1c) and the EDX (Fig. S2, ESI†), were all in agreement with the literature and indicated that we had produced FeFe PB on the FeCr PBA surface. The colour of the resulting films ranged from orange (short deposition time), to green (intermediate) and blue (long deposition time).

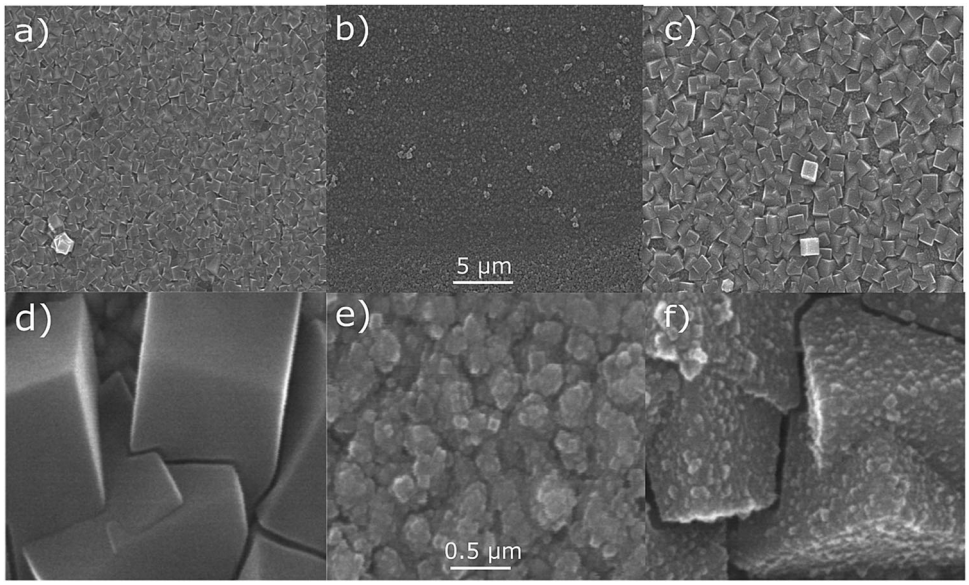


Fig. 2 SEM analysis at different zoom levels, showing the FeCr (a and d), FeFe (b and e) and the bilayer films (c and f). The FeFe film can be seen in image (f) as the smaller crystals on the surface of the larger FeCr crystals. The smaller structures visible below the FeCr crystals in (d) is the conductive FTO layer on the glass substrates. 5 μm scale bar refers to images a–c while the 0.5 μm scale bar refers to images d–f.

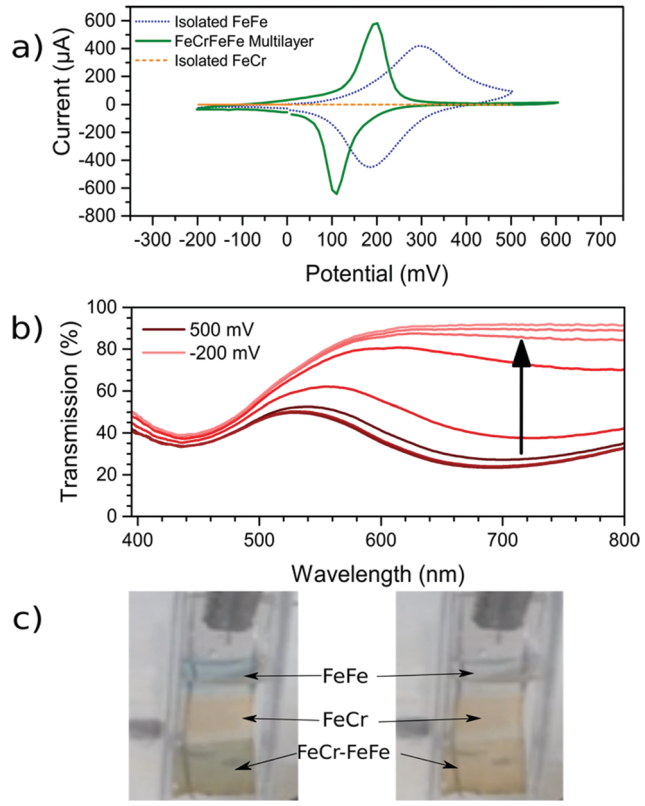


Fig. 3 Electrochemical analysis of the films. (a) CV scans (*vs.* SCE) of both the isolated FeFe film and the FeFe layer as part of the bilayer film. FeCr film shows negligible electrochemical activity over this range. The scan rate used for the three voltammograms was 0.01 V $s^{-1}$. (b) Spectroelectrochemistry of the bilayer film as the FeFe absorption (685 nm) is electrochemically reduced while the FeCr peak (440 nm) remains unchanged. (c) For demonstration purposes, a sample with FeFe, FeCr and the FeFe–FeCr bilayer was made on the same substrate. The sample was made by masking part of the substrate during the deposition using Teflon tape. When the FeFe layer is electrochemically reduced, the colour is switched from blue to transparent (ESI† video).

## Characterisation of bilayer

In order to confirm that a bilayer was formed, the CV was recorded and found to be slightly different compared to a bare FeFe PB film (Fig. 3a). These voltammograms were carried out using Pt pseudo-reference and counter electrodes as this replicates the conditions used in the spectroelectrochemical measurement. The electrochemical behaviour of the FeFe PB is maintained when it is deposited on top of the FeCr PBA film, although we see a shift when it is incorporated into the multilayer structure. The shift in potentials for the peaks could be due to the FeCr electrode having a different electrochemical behaviour to the FTO electrode. There is also a difference in the widths of the peak, the broader peaks of the isolated FeFe film suggest that the process is limited by the diffusion of ions in the solution whereas the switching in the multilayer is limited by the charge passing through the FeCr layer. The CVs do however demonstrate that we have deposited the FeFe PB layer on top of the FeCr film, which confirms that we have formed a true bilayer. This is also seen in the SEM images, where Fig. 2f clearly shows a bilayer with small FeFe crystal grains deposited on the larger FeCr crystal grains. The film-to-substrate ratio of the FeCr film should be even larger than that estimated from the SEM images and is probably larger than at least 80% due to the three-dimensional morphology of the FeCr crystal grains (Fig. S3, ESI†). The surface area of the electrode, which is subsequently used for FeFe PB deposition, is therefore mainly comprised of FeCr sites. This in turn implies that a bilayer is formed. The FeCr PBA is conductive enough, confirmed using tunnelling AFM, to allow the growth of the FeFe PB directly on top of the FeCr crystals (Fig. S4, ESI†). The IR spectrum shows the two peaks at 2077 $cm^{-1}$ and 2168 $cm^{-1}$, from the FeFe and FeCr respectively. The EDX also showed the correct composition for both the individual films and the bi-layered films. The FeFe layer thickness was 30 ± 15 nm, determined from AFM of individual films produced under identical conditions to the bilayer film and on an FTO electrode.

## Optical properties of bilayer

The bilayer films were generally transparent and optically very clear, which therefore make them suitable for optical applications. Interestingly, the SEM and AFM images showed an unexpected difference in the film thicknesses of the two layers despite that the optical density was similar for the two layers. We therefore studied the dependence of the optical density as a function of film thickness, which is shown in Fig. 4. It can be seen that the MMCT oscillator strength for the FeFe material is clearly higher than for the FeCr, which is due to the relative energies and overlap of the orbitals involved in the MMCT absorption.[24–26] Based on these data, it appears that

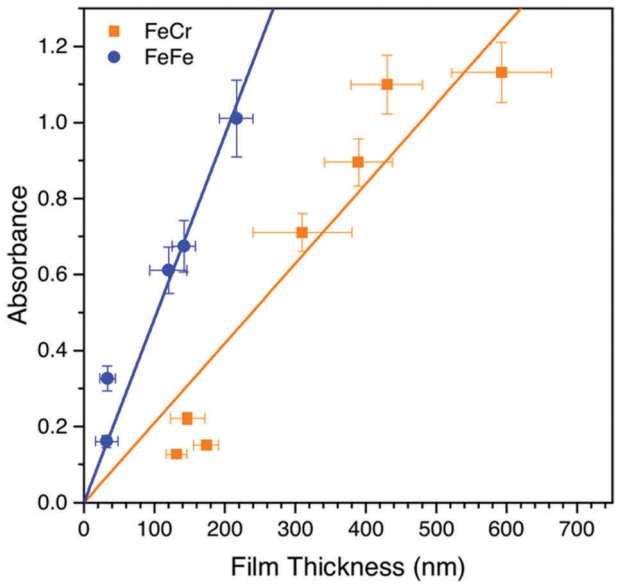


Fig. 4 The dependence of the optical density on the thickness of the film for the FeFe and FeCr Prussian blues. The error bars come from the AFM/UV-Vis analysis performed on the deposited samples, many cross sections/spots of the film were taken to reliably estimate these values. Note the error in absorption data increases with larger film thickness due to larger amount of scattered light as the crystals become larger.

the FeCr should be *ca.* 200 nm thicker than the FeFe films. This is in relatively good agreement with the AFM data, although the SEM images suggests a quite large difference in the size of the crystal grains in the film (Fig. 2f).

### Spectroelectrochemistry and electrochromic switching

During the CV scan, it was visually clear that the FeFe PB colour could be completely switched from blue to transparent (ESI† video). The dependence of the optical transmission spectrum on the applied reductive potential is shown in Fig. 3b. As the potential is swept from positive to negative, the absorbance feature at 685 nm, corresponding to the FeFe MMCT disappears as the film is reduced. As the potential is swept in the reverse direction, from negative to positive, the absorbance is restored. Throughout this reversible process, the FeCr film is not affected and retains its colour as it does not undergo any electrochemical redox processes. This can be observed in the CV scan of the isolated FeCr film in Fig. 3a. This therefore demonstrates the successful application of electrochromic PB layer in a PBA multilayered film. Because the vast majority of the FeFe PB crystals are deposited on top of FeCr crystals and because these can be completely reduced, as evidenced by the large colour-change, we conclude that charge is passed from the FeCr layer to the FeFe layer. This therefore implies that there is charge-transfer occurring between the two layers.

For the electrochromic switching, potentials of +0.5 V and −0.2 V were chosen from CVs in Fig. 3a, as this will drive the reduction and oxidation of the films to completion in order to measure the switching. The resulting modulation of the absorbance, measured at 685 nm, is shown in Fig. 5a. As can be seen, the colour could be reversibly switched for several cycles without degradation of the film. During the electrochromic switching, there appears to be a certain amount of charge building up in the material, this can be seen in the charge data for the switching process (Fig. S5, ESI†).

The colouration efficiency is a measure of the efficiency of the switching process and is defined as $\eta = \Delta OD/\Delta Q$. This relates the change in the optical density ($\Delta OD$) to the charge ($\Delta Q$) passed through the system. A plot of the absorbance against the supplied charge density will yield $\eta$ as the initial gradient, as shown in Fig. 5b. The value for $\eta$ was found to be $147.8 \pm 0.8$ cm$^2$ C$^{-1}$, for the blue to bleach process, which is of the same order of magnitude as reported in other studies employing the FeFe PB as part of an electrochromic device.[3,27–30] The switching times are defined here as the time taken for 90% of the switch completion. For the blue to bleached state transformation the switching time is $4.4 \pm 0.4$ s.

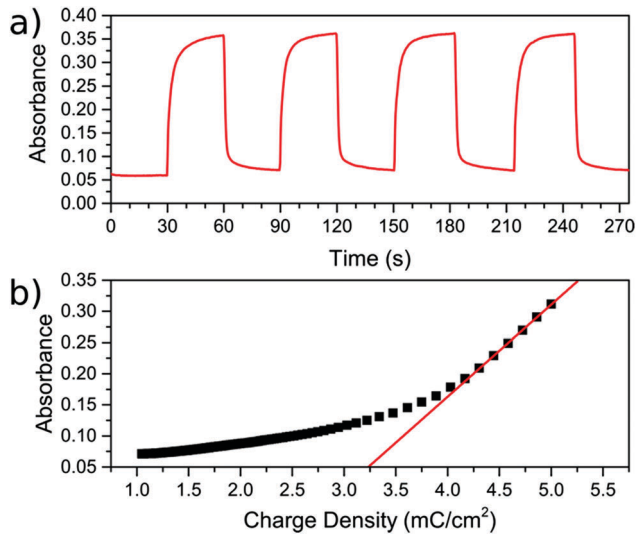


Fig. 5 Electrochromic switching and colouration efficiency of the FeCr–FeFe bilayer material. (a) The change in absorbance measured at 685 nm during the electrochromic switching by alternating the potentials between 0.5 to −0.2 V. (b) Colouration efficiency plot of the charge density against the absorbance. The initial gradient of the curve is the colouration efficiency.

## Conclusion

We have successfully made bilayers of the FeFe PB and FeCr PBA using electrochemical deposition. When bilayers of equal optical transmission were made, polycrystalline films with thicknesses of 300 nm and 30 nm for the FeCr and FeFe films, respectively, were produced. The crystal grain widths were *ca.* 1 μm and 30 nm for the FeCr and FeFe layers, respectively. The colour of the FeFe layer could be switched electrically and we found a colouration efficiency of $147.8 \pm 0.8$ cm$^2$ C$^{-1}$ and switching time of $4.4 \pm 0.4$ s for the blue to bleach switch.

The demonstration of layer-sensitivity in bilayers of PBAs opens up possibilities to study electron charge-transfer processes in a range of different multilayers of PBAs, some of which are electrochemically active, display high-temperature magnetic ordering, and have bright and chemically tuneable colours. Several PBAs, in addition to those presented here, can be deposited on ITO/FTO coated substrates such as the CrCr,[31] VCr[17] and CoFe[32] PBAs. Layer-sensitive measurements applied to PBAs with novel photomagnetic and optical properties will be of importance for developing applications for photonic and spintronic devices.

## Conflicts of interest

There are no conflicts to declare.

## Acknowledgements

The authors gratefully acknowledge funding from the Royal Society of Edinburgh, the Carnegie Trust (Collaborative Research Grant), EPSRC (studentship to L. H.), and the Royal Society (International Exchange Grant). J. O. J. is a RSE/BP Trust Research fellow.

## References

1 R. J. Mortimer, *Annu. Rev. Mater. Res.*, 2011, **41**, 241–268.
2 P. R. Somani and S. Radhakrishnan, *Mater. Chem. Phys.*, 2003, **77**, 117–133.

3 Z. Jiao, J. L. Song, X. W. Sun, X. W. Liu, J. M. Wang, L. Ke and H. V. Demir, *Sol. Energy Mater. Sol. Cells*, 2012, **98**, 154–160.
4 A. Pajor-Swierzy, M. Kolasinska-Sojka and P. Warszynski, *Colloid Polym. Sci.*, 2014, **292**, 455–465.
5 M. S. Fan, S. Y. Kao, T. H. Chang, R. Vittal and K. C. Ho, *Sol. Energy Mater. Sol. Cells*, 2016, **145**, 35–41.
6 M. F. Dumont, E. S. Knowles, A. Guiet, D. M. Pajerowski, A. Gomez, S. W. Kycia, M. W. Meisel and D. R. Talham, *Inorg. Chem.*, 2011, **50**, 4295–4300.
7 D. M. Pajerowski, M. J. Andrus, J. E. Gardner, E. S. Knowles, M. W. Meisel and D. R. Talham, *J. Am. Chem. Soc.*, 2010, **132**, 4058–4059.
8 J. T. Culp, J. H. Park, I. O. Benitez, M. W. Meisel and D. R. Talham, *Polyhedron*, 2003, **22**, 2125–2131.
9 J. P. Prieto-Ruiz, F. M. Romero, H. Prima-Garcia and E. Coronado, *J. Mater. Chem. C*, 2015, **3**, 11122–11128.
10 M. Fitta, H. Prima-Garcia, P. Czaja, T. Korzeniak, M. Krupinski, M. Wojtyniak and M. Balanda, *RSC Adv.*, 2017, **7**, 1382–1386.
11 R. C. Millward, C. E. Madden, I. Sutherland, R. J. Mortimer, S. Fletcher and F. Marken, *Chem. Commun.*, 2001, 1994–1995.
12 T. C. Liao, W. H. Chen, H. Y. Liao and L. C. Chen, *Sol. Energy Mater. Sol. Cells*, 2016, **145**, 26–34.
13 W. Q. Jin, A. Toutianoush, M. Pyrasch, J. Schnepf, H. Gottschalk, W. Rammensee and B. Tieke, *J. Phys. Chem. B*, 2003, **107**, 12062–12070.
14 M. Pyrasch, A. Toutianoush, W. Q. Jin, J. Schnepf and B. Tieke, *Chem. Mater.*, 2003, **15**, 245–254.
15 W. Zhao, J. J. Xu, C. G. Shi and H. Y. Chen, *Langmuir*, 2005, **21**, 9630–9634.
16 D. M. DeLongchamp and P. T. Hammond, *Chem. Mater.*, 2004, **16**, 4799–4805.
17 M. Mizuno, S. Ohkoshi and K. Hashimoto, *Adv. Mater.*, 2000, **12**, 1955–1958.
18 S.-I. Ohkoshi, A. Fujishima and K. Hashimoto, *J. Am. Chem. Soc.*, 1998, **120**, 5349–5350.
19 S.-I. Ohkoshi, Y. Einaga, A. Fujishima and K. Hashimoto, *J. Electroanal. Chem.*, 1999, **473**, 245–249.
20 V. D. Neff, *J. Electrochem. Soc.*, 1978, **125**, 886–887.
21 J. J. Garcia-Jareno, D. Benito, J. Navarro-Laboulais and F. Vicente, *J. Chem. Educ.*, 1998, **75**, 881–884.
22 L. Hedley, N. Robertson and J. O. Johansson, *Electrochim. Acta*, 2017, **236**, 97–103.
23 W. Kosaka, K. Nomura, K. Hashimoto and S.-I. Ohkoshi, *J. Am. Chem. Soc.*, 2005, **127**, 8590–8591.
24 M. B. Robin and P. Day, *Adv. Inorg. Chem. Radiochem.*, 1968, **10**, 247–422.
25 B. Mayoh and P. Day, *J. Chem. Soc., Dalton Trans.*, 1974, 846–852.
26 M. B. Robin, *Inorg. Chem.*, 1962, **1**, 337–342.
27 T.-S. Tung and K.-C. Ho, *Sol. Energy Mater. Sol. Cells*, 2006, **90**, 521–537.
28 M. Deepa, A. Awadhia, S. Bhandari and S. L. Agrawal, *Electrochim. Acta*, 2008, **53**, 7266–7275.
29 R. J. Mortimer and T. S. Varley, *Sol. Energy Mater. Sol. Cells*, 2012, **99**, 213–220.
30 Y. Rong, S. Kim, F. Su, D. Myers and M. Taya, *Electrochim. Acta*, 2011, **56**, 6230–6236.
31 O. Sato, T. Iyoda, A. Fujishima and K. Hashimoto, *Science*, 1996, **271**, 49–51.
32 O. Sato, Y. Einaga, T. Iyoda, A. Fujishima and K. Hashimoto, *J. Electrochem. Soc.*, 1997, **144**, L11.

 